VALIDATION OF MONTE CARLO-BASED CALCULATIONS FOR SMALL IRREGULARLY SHAPED INTRA-OPERATIVE RADIOTHERAPY ELECTRON BEAMS

A dissertation presented by

GRAEME LAWRENCE LAZARUS

To

THE DEPARTMENT OF MEDICAL PHYSICS, UNIVERSITY OF CAPE TOWN

In fulfilment of the requirements for the degree of

DOCTOR OF PHILOSOPHY

In the subject of

MEDICAL PHYSICS

UNIVERSITY OF CAPE TOWN, RONDEBOSCH, CAPE TOWN, SOUTH AFRICA

OCTOBER 2015

PLAGIARISM DECLARATION

I know the meaning of plagiarism and declare that all of the work in the dissertation, save for that which is properly acknowledged, is my own

Name: Graeme Lawrence Lazarus

Date: October 2015

Signature:

DEDICATION

I dedicate this dissertation to my dearly-departed mother, Theresa Veronica Lazarus, who died of cancer 20 years ago. I owe my successes to her for the many good values she instilled in me, for her belief that I could accomplish whatever I set my mind to, and for teaching me that the combination of hard work and a strong faith in our Lord Jesus Christ would always lead to me achieving my goals.

ACKNOWLEDGEMENTS

Mr L Strauss for his assistance in loading the Linux operating system and associated software on the computer used for performing the Monte Carlo simulations.

My co-supervisor, Dr F C P du Plessis, for his inspiration and for sharing his wealth of knowledge with me with regards all matters relating to Monte Carlo simulation methods. I am truly grateful for the expert advice he constantly gave me to ensure that a high standard was maintained throughout the course of the research project.

My supervisor Prof E Hering for affording me the opportunity to pursue the project through the University of Cape Town. I acknowledge his constant support, encouragement and expert advice on all matters relating to the successful completion of the thesis. I also thank him for his belief in my abilities and for always providing me with alternatives to solving the many problems encountered.

My employer, Inkosi Albert Luthuli Central Hospital (IALCH), for allowing me the use of the Radiotherapy and dosimetry equipment and associated software packages, without which this project would not have been feasible.

The University of Cape Town for accepting me as a PhD student.

Siemens, Germany for graciously providing me with detailed specifications of the components of the Siemens Primus Linear Accelerator that was used in this study. By omitting details of the material compositions of each of the components of the treatment head, I have ensured that I have not contravened the Non-Disclosure Agreement that I signed.

Mr Wayne Flowers (AEC Amersham, South Africa) for arranging the electron diode on loan from the manufacturer. To PTW, Freiburg, Germany, for agreeing to loan me the diode and for timeously shipping it to South Africa so that I may perform output factor measurements.

My loving wife Somantha Lazarus for her continued support and encouragement, especially during the times that I encountered problems that arose during the course of the study. I thank her also for allowing me to sacrifice our family time so that I may work on the project.

My ever-loving and adorable three year old daughter Izabella Veronica Lazarus for the joy and happiness she gives to me daily and for graciously accepting the fact that `daddy has to work'.

My eight-month-old son, Xander Daniel Graeme Lazarus, for unknowingly providing me with the encouragement and inspiration to complete the project timeously so that I may have the time to burp him and change his nappies.

THESIS STRUCTURE AND OVERVIEW

The objective of this project is to validate Monte Carlo-based calculations for small irregularly shaped intra-operative radiotherapy electron beams. Treatment is delivered using an electron beam passing through a commercially-available Intra-Operative Radiotherapy (IORT) cone system with a custom built irregularly-shaped alloy cut-out inserted at the end of the cone. The cut-out conforms to the shape of the tumour being irradiated. There is currently no commercially available treatment planning system that uses Monte Carlo calculations for the LINAC/cone-system used in this study. Over and above this, no publications were found where studies were performed with this exact combination. The uniqueness of the study was extended further by the introduction of custom-built alloy cut-outs at the end of the IORT cone.

CHAPTER 1 of this thesis describes the importance of the radiobiology concept of therapeutic ratio which is fundamental in the radiation therapy process. After a brief history of radiation therapy is given, the chapter proceeds to chronicle the evolution and advances made in this field, starting with 2-D treatment methods and ending with Volumetric Modulated Arc Therapy (VMAT).

CHAPTER 2 is dedicated to Intra-operative Radiation Therapy, which is the treatment technique focussed on in this study. The principles, history and various methods of IORT delivery is discussed. The cone system used in this study is shown. Pertinent electron beam characteristics (PDDs and profiles) are described in detail and the need for absolute dosimetry and measurement of cone and cut-out factors is explained. A brief description of monitor unit calculations for nominal and extended SSD treatments is given.

CHAPTER 3 describes the Monte Carlo method, the issue of electron transport and the manner in which modelling of the process may be accomplished using MC techniques.

CHAPTER 4 is dedicated to detailing the materials used in the study and describes the various processes and methodology that was employed. A description of the measurement procedure is provided. The software tools utilised for the Monte Carlo simulations is introduced. The Gamma Index evaluation method for comparison of measured and MC-calculation data is explained.

CHAPTER 5 describes in detail the BEAMnrc Monte Carlo commissioning of the linear accelerator. The commissioning is performed for the $10x10\ cm$ and $5\ cm$ circle electron applicators for 6, 12 and 18 MeV electron beams. A description of each component module utilised in building the accelerator in BEAMnrc is given. The phase-space file generated by the BEAM simulation is then used as the source for a phantom created in DOSXYZnrc.

Percentage Depth Doses (PDDs) and profiles at various depths are extracted from the 3-D dose distributions produced by the DOSXYZnrc Monte Carlo simulations. These are then compared with measured data using the Gamma Index (GI) evaluation method.

An analysis of the final energy spectra for each energy is performed using BEAMDP. Absolute dosimetry results utilising the TRS398 protocol are presented. MC-calculated output factors for the $5\ cm$ circle applicator relative to the reference $10x10\ cm$ applicator are compared to measurements.

In CHAPTER 6, separate Linear Accelerators are 'built' for each energy (6 MeV, 12 MeV and 18 MeV) by replacing, in turn, the standard applicator with Intra-Operative Radiotherapy cones of diameters 19 mm, 45 mm and 64 mm. The final energy spectra obtained for the reference $10x10\ cm$ applicator for each energy is used as the source for each build. The resulting MC-produced PDDs and profiles are compared with measured data using the GI evaluation method. Measured output factors are compared to that produced from the Monte Carlo simulations.

In CHAPTER 7, custom-made alloy cut-outs for each cone (19 mm, 45 mm and 64 mm) are then 'built' and 'inserted' into the last 2 cm at the end of the cone for each energy (6 MeV, 12 MeV and 18 MeV). The PDDs and profiles produced from the simulations for each energy are similarly compared to that of measured data using the GI evaluation method. The resulting measured cut-out factors are compared to that produced from Monte Carlo simulations.

CHAPTER 8 discusses future work with respect to cone factor and cut-out factor determination utilising Monte Carlo simulations for all the energies and cones available at the institution. This chapter also details further investigations that are necessary to ensure more accurate modelling of the LINAC.

CHAPTER 9 is dedicated to final discussions and conclusions.

A list of references is then given, followed by an appendix which details the method of MU calculation to be employed for treatment.

LIST OF TABLES

LIST OF FIGURES

GLOSSARY OF TERMS

3DCRT	3 Dimensional Radiation Therapy
AE	Production thresholds for electrons
AP	Production thresholds for photons
BCA	Boundary Crossing Algorithm
BEAMDP	Beam Data Processing
BEV	Beams Eye View
CDF	Cumulative Distribution Function
CF	Cone Factor
CH	Condensed History
CM	Component module
COF	Cut-out Factor
CS	Compton Scattering
CT	Computerised Tomography
DoN	%dose difference (in % of normalisation value)
DRR	Digitally reconstructed Radiograph
DTA	Distance to agreement
EBRT	External Beam Radiation Therapy
ECUT	Electron energy Cut-off
EGSnrc	Electron Gamma Shower (National Research Council of Canada)
GI	Gamma Index
GUI	Graphical User Interface
Gy	Gray
IAEA	International Atomic Energy Agency

ICRU	International Commission on Radiological Units and Measurements
IGRT	Image-guided Radiation Therapy
IMRT	Intensity-modulated Radiation Therapy
IORT	Intra-operative Radiation Therapy
keV	Kilo-electron volt
LAC	linear Attenuation Coefficient
LCA	Lateral Correlation Algorithm
LCRNG	Linear Congruently Random Number Generator
Linac	Linear Accelerator
MC	Monte Carlo
MCRNG	Multiplicative Congruently Random Number Generator
MERT	Modulated Electron Radiation Therapy
MeV	Mega-electron Volt
MLC	Multi-leaf Collimator
MU	Monitor unit
NTCP	Normal Tissue Complication Probability
OAR	Off-axis ratio
OMEGA	Ottawa Maddison Electron Gamma Algorithm
OPF	Output factor
PCUT	Photon energy Cut-off
PDD	Percentage Depth Dose
PDF	Probability Distribution Function
PE	Photo-electric Effect
PLC	Path Length Correction
PMMA	Poly-methyl Methacrylate

PP	Pair Production
PRESTA I and II	Parameter-reduced Electron Stopping Power Algorithm I and II
PSF	Phase-space file
SLAC	Stanford Linear Accelerator Centre
SSD	Source-surface-distance
TCP	Tumour Control Probability
TPS	Treatment planning System
VMAT	Volumetric Modulated Arc Therapy
VMC	Voxel Monte Carlo

Table of contents

CHAPTER 1

INTRODUCTION

The global incidence of cancer is expected to increase from 14 million in 2012 to 22 million in 2030 *(Stewart and Wild 2014)*. Africa, Asia, Central America and South America account for 70% of the world's cancer deaths *(de Martel et al 2012)*. The Centre for Disease Control and Prevention (CDC) states that globally, cancer kills more people than TB, AIDS and malaria combined. The Cancer Association of South Africa predicts that by the year 2030, the incidence of cancer in South Africa will increase by 78% to 178 000 new cases. One in six South African men and one in seven South African women will be inflicted by cancer during the course of their lives.

Currently, the main forms of treatment of cancer are radiation therapy, chemotherapy and surgery. The treatment of choice depends primarily on the type and staging of the cancer. Each of these modalities may be used as the sole mechanism of treatment. Any or all combinations of these modalities are common.

More than 40% of all cancer sufferers are treated with radiation therapy whereby a therapeutic dose of ionising radiation is delivered to a cancer site in the hope of eradicating the tumour. Radiation therapy treatment planning refers to the process involved in determining the optimal manner in which to achieve this goal.

1.1 Radiobiology

The basic unit of life is the cell, which contains the genetic material deoxyribonucleic acid (DNA). When normal cells become damaged or have reached the end of their life cycle, genes control their replacement in a controlled manner so that the body may remain in a healthy state. When DNA becomes damaged or altered, mutations may arise which affect normal cell

growth *(Hall & Giaccia 2006).* Various factors may influence the mutation of these genes, resulting in the uncontrolled proliferation of cells. These cells are then said to be cancerous and their proliferation results in a mass of cells that develop into a tumour.

The growth advantage of cancer cells relative to normal cells means that they are more likely to win the competition for nourishment and other resources necessary for cell survival, thereby further increasing their growth rate relative to normal cells. The tumours may cause the tissues or organs in which they reside to become dysfunctional or totally non-functional. The cancer cells may also break through the boundaries of the tissue and may migrate to neighbouring tissues and organs via the bloodstream or lymphatic system, creating secondary tumours at these new sites (metastasis).

1.1.1 Dose Response of tissue

The genetic effects of radiation as well as the induction of cancer by exposure to radiation was demonstrated in 1927 by Hermann Joseph Muller, who was awarded the Nobel Prize in 1946 for his findings. It is imperative that a high therapeutic ratio (tumour/normal tissue cell kill) be maintained *(Hall and Giaccia 2006)*. The ideal outcome would be complete eradication of the tumour with total sparing of healthy tissue to ensure viability and function of all essential tissues and organs.

The DNA present in cells is the critical target for radiation damage *(Steel 2002)*. Destruction of a tumour/cancerous cell population is accomplished by destruction of the reproductive capacity of the cell. Following a dose or course of radiation, a portion of cells will die whilst others will be unable to proliferate but will be capable of maintaining normal function. There are still others that will not be able to function normally.

For differentiated cells that do not proliferate eg. nerve and muscle, cell death refers to loss of specific function. For proliferating cells, cell death refers to the loss of capacity for sustained proliferation i.e. loss of reproductive integrity.

1.1.2 TCP and NTCP

Cell survival curves for a variety of tissue types were obtained experimentally by irradiating colonies of cells to a range of doses and measuring the survival fraction. This led to the introduction of the linear-quadratic model in which the α/β ratio was characteristic of each tissue type *(Dale 1985)*. The critical volume model was then introduced to determine the probability of killing all the cells in the tumour (tumour control probability, TCP) *(Niemierko and Goitein 1993)* and the probability that complications would arise in the normal tissue (normal tissue complication probability, NTCP) *(Niemierko and Goitein 1991)*.

These quantities are defined as:

$$TCP(D) = exp(-n_0 * exp(-D/D_0)) \quad (1.1)$$

$$NTCP(D) = 1/(1 + (\frac{D}{ED_{50}})^{-k}) \quad (1.2)$$

where: D is the absorbed dose,

n_0 is the number of clonogenic cells in the tumour mass,

D_0 is the mean lethal dose,

ED_{50} is the median effective dose which is the dose that produces death in 50 per cent of cell population and

k is the sensitivity constant.

The choice of dose delivered to the tumour is based on that which would result in the greatest TCP. Tolerance doses *(Emami et al 1991)* defined for organs at risk are based on the probability of complications (NTCP) arising in the normal tissues being irradiated.

Subsequent to this document, the QUANTEC (Quantitative Analysis of Normal Tissue Effects in the Clinic) review document *(Marks et al 2010)*, which served to update and refine the Emami guidelines, was produced. This document presents the most commonly used NTCP models and summarises available 3-d dose/volume/outcome data in a clinically useful manner. The objective of the QUANTEC document is to provide practical clinical guidelines for clinicians based on NTCP.

The therapeutic ratio may be defined as the ratio $TCP/NTCP$ *(Metcalfe et al 2007)*. The dose response curves for both normal tissue and cancerous cells are sigmoidal in nature *(Webb & Nahum 1993)* and may be represented graphically as the TCP and NTCP respectively. An unfavourable outcome would be one in which the TCP curve appears further along the dose axis than the NTCP curve *(figure 1.1)*. This would imply that tumour control would only be achieved after the dose delivered has exceeded that which would result in significant destruction of the normal tissue. A more favourable and common outcome, especially for situations in which the normal tissue is in close proximity to the tumour and cannot be avoided in the irradiation process, would be one in which the NTCP curve appears further along the dose axis than the TCP curve *(figure 1.2).* This would imply that for any given dose, the probability of tumour control would always be higher than the probability of normal tissue complications. The ideal situation would be one in which the NTCP curve appears further along the dose axis than the TCP curve and in which the curves do not have a point with a common dose value *(figure 1.3).* The main objective of all radiotherapy treatments is to obtain the highest possible value (TCP/NTCP) for the therapeutic ratio *(Metcalfe et al 2007).*

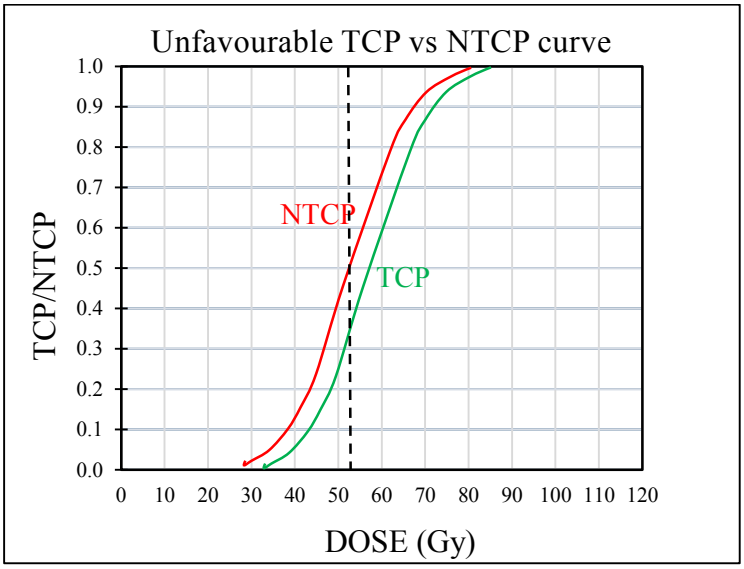

Figure 1.1 Unfavourable dose response curve for TCP vs NTCP

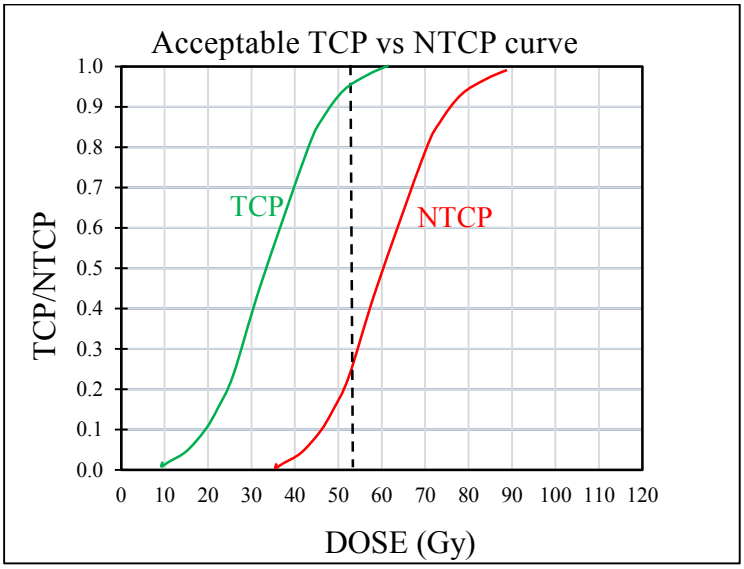

Figure 1.2 Acceptable dose response curve for TCP vs NTCP

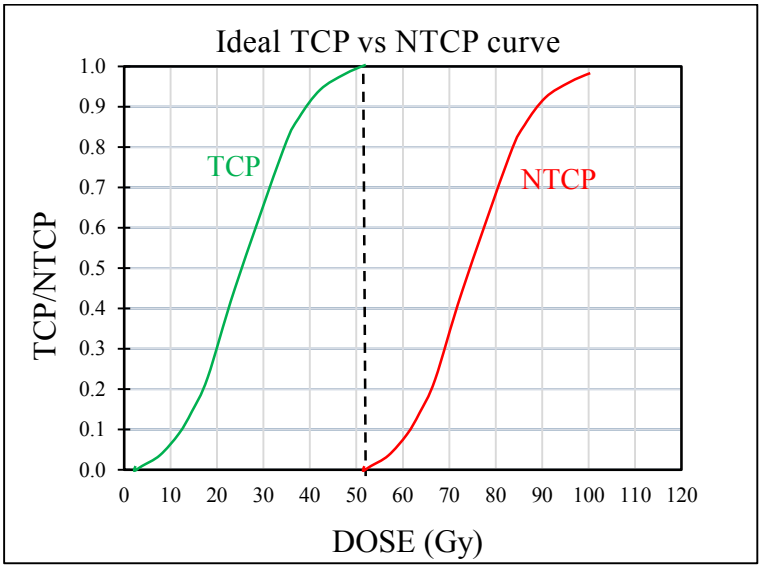

Figure 1.3 Ideal dose response curve for TCP vs NTCP

1.2 Radiation Therapy

1.2.1 History

In 1895, a German physicist, Wilhelm Conrad Roentgen, was performing experiments with cathode ray tubes involving the passing of current through gases at very low pressure, when he noticed a glow on a phosphorescent screen a distance away. He concluded that the electrical discharge underwent interactions that produced unknown rays, which he aptly named X-Rays *(Chodos and Ouellette 2001)*. He subsequently developed and image of his wife's hand using the X-Rays and demonstrated the differential attenuation/transmission of the beam by her tissue, bones and wedding ring. He concluded that X-Ray beams may be generated by the impact of cathode rays on material objects.

In 1896, a medical student in Chicago, Emile Grubbe, suffered radiation dermatitis of his hands and neck when exposed to X-Rays and concluded that radiation caused tissue damage. He convinced one of his superiors to allow him to irradiate a breast cancer patient in the hoping of killing the cancer cells. He thus became the first Radiation Oncologist and opened a treatment centre in Chicago in 1896.

1.2.2 Medical Linear Accelerators

In 1897, J J Thomson, through his exploration on the properties of cathode rays, discovered that the particles of the cathode ray were negatively charged and initially called them 'corpuscles'. He also found that they were an integral part of the atom and was thus credited with the discovery of the first sub-atomic particle. He won the Nobel Prize in 1906 for his discovery.

It is the use of these electrons in the treatment of cancer that is the focus of this study.

In 1952, Henry S Kaplan of Stanford University, together with Edward Ginzton, invented the first Medical linear accelerator (LINAC) for general radiotherapy use. In 1957, Gordon Isaacs was the first patient treated with a LINAC (for retinoblastoma).

Medical linear accelerators have evolved drastically since the 1960s *(Thwaites & Tuohy 2006)* and have become sophisticated and more efficient in their design and beam production methods. They are now capable of providing photon energies ranging from 6 MV to 25 MV and electron energies ranging from 4 MeV to 21 MeV. At present, the majority of LINACs being used clinically have 2 photon energies and 4 to 6 electron energies in the ranges mentioned. Although it is possible to have more than 2 photons energies available on any LINAC, there are cost implications. A combination of a single low and a single high photon energy on a LINAC has been found to be sufficient to adequately treat most cancers seen in the clinic. Electron energies evenly distributed (about 3 MeV apart) between the lowest and highest available energies have also proven to be sufficient for the electron treatments necessary.

1.2.3 Evolution of radiotherapy treatment modalities and techniques

The evolution of treatment modalities and techniques has been driven primarily by the need to obtain the highest therapeutic ratio possible. Beam shaping and the use of custom-built cut-

outs for the photon collimation systems and electron applicator systems were introduced to achieve this goal. Two of the main limitations of the 2-D techniques was the lack of realistic estimation of the tumour volumes and failure to calculate the dose distribution in the entire 3-D target volume.

A huge step forward was the introduction of 3-D Conformal Radiation Therapy (3DCRT) where Computerised Tomography (CT) scans of the treatment area were imported into the treatment planning systems (TPS). This made it possible to accurately delineate and display tumour volumes and organs at risk (OARs) and to calculate and display dose distributions in 3 dimensions. It thus became possible to shape the individual beams around the tumour with the assistance of a beams eye view (BEV), thereby increasing the therapeutic ratio. It also became possible to produce digitally reconstructed radiographs (DRRs), which utilises the attenuation information from the CT scan to digitally reconstruct a synthetic radiographic image in a plane perpendiculer to the beam. The projection of the beam outline and it's position relative to anatomical landmarks facilitates accurate setup and positioning of the patient for treatment. This is accomplished by comparing the DRR (plan radiograph) to a portal image of the patient in the proposed treatment position (treatment radiograph). The patient position is then altered until an acceptable coincidence of the two images is achieved.

In the 1990s, a pair of jaws was replaced by a multi-leaf collimator (MLC) to improve the efficiency of treatment delivery *(Biggs et al 2001).* MLCs consist of multiple leaves on each bank with each leaf capable of being moved independently to shape the beam along the leave's axis of motion *(Powlis et al 1993).*

With the introduction of inverse planning in 1988 *(Brahme 1988),* it became possible to deliver multi-segmented beams which results in a varied fluence across each beam. Although primarily used for photon therapy, studies have shown their effectiveness in shaping the

electron beams as well *(du Plessis et al 2006)*. Modulated Electron Radiotherapy (MERT) was also investigated for energy and intensity modulation of electron beams using a specially designed electron MLC *(Ma et al 2000)*.

Further development led to Volumetric Modulated Arc Therapy (VMAT) *(Teoh et al 2011)*, whereby the LINAC gantry is rotated through one or more arcs with the radiation continuously on, whilst varying some or all of the following parameters: MLC aperture shape, dose rate and gantry rotation speed.

In the more recent years, focus was also placed on the accuracy of treatment delivery with the introduction of Image Guided Radiation Therapy (IGRT) *(Verellen et al 2008)* whereby positional errors could be detected and corrected instantaneously by imaging of the patient in the treatment position.

Various respiratory gating techniques *(Podgorsak 2005)* were also introduced to improve the accuracy of treatment delivery. It allowed the patient's inspiration and expiration to be monitored so that the beam may only be switched on when the target volume was in the desired position.

1.3 Concluding remarks

The evolution of radiotherapy treatment modalities and techniques was influenced primarily by the need to obtain the highest therapeutic ratio possible. This was accomplished by the following: improving on immobilisation techniques thereby reducing the possibility of patient motion; making higher dose rates available for treatment thereby reducing the time the patient has to remain immobilised in the treatment position; introducing shielding and beam shaping devices into the beam; increasing the conformality of dose to the tumour with the

introduction of MLCs; introducing IMRT and VMAT for even greater conformality; introducing IGRT and respiratory gating.

These advances applied mainly to photon therapy, with the exception of MERT which is not commercially available at present. The most commonly-used mechanism available to increase the therapeutic ratio for electron treatments is the addition of electron cut-outs at the end of the electron applicator. This allows shaping of the beam as it exits the LINAC so that the beam conforms laterally to the shape of the tumour.

Another form of electron treatment introduced to increase the therapeutic ratio is Intra-Operative Radiation Therapy (IORT), which is the treatment technique focussed on in this study.

CHAPTER 2

INTRA-OPERATIVE RADIATION THERAPY (IORT)

Conventional external beam radiation therapy (EBRT) involves the use of medical linear accelerators for the treatment of tumours by externally exposing the patient to a dose of ionising radiation. In order to deliver an appreciable dose to deep seated tumours, higher doses of radiation are delivered to normal tissues or internal organs located proximal to the tumour. This results in an unfavourable therapeutic ratio *(section 1.1.2)*. In IORT, the tumour site is surgically exposed and the normal tissue and organs are displaced so that the tumour may be treated directly with a single dose of radiation in a sterile environment *(Biggs 1985)*. Irradiation may also take place after partial resection of the tumour. Normal tissue beyond the distal end of the tumour may be avoided by appropriate selection of available electron beams, which inherently display a rapid dose fall-off and have a finite range as compared with x-rays *(figure 2.1)*. The narrow build-up region of electron beams as opposed to photon beams makes them more suitable for treatment of superficial tumours.

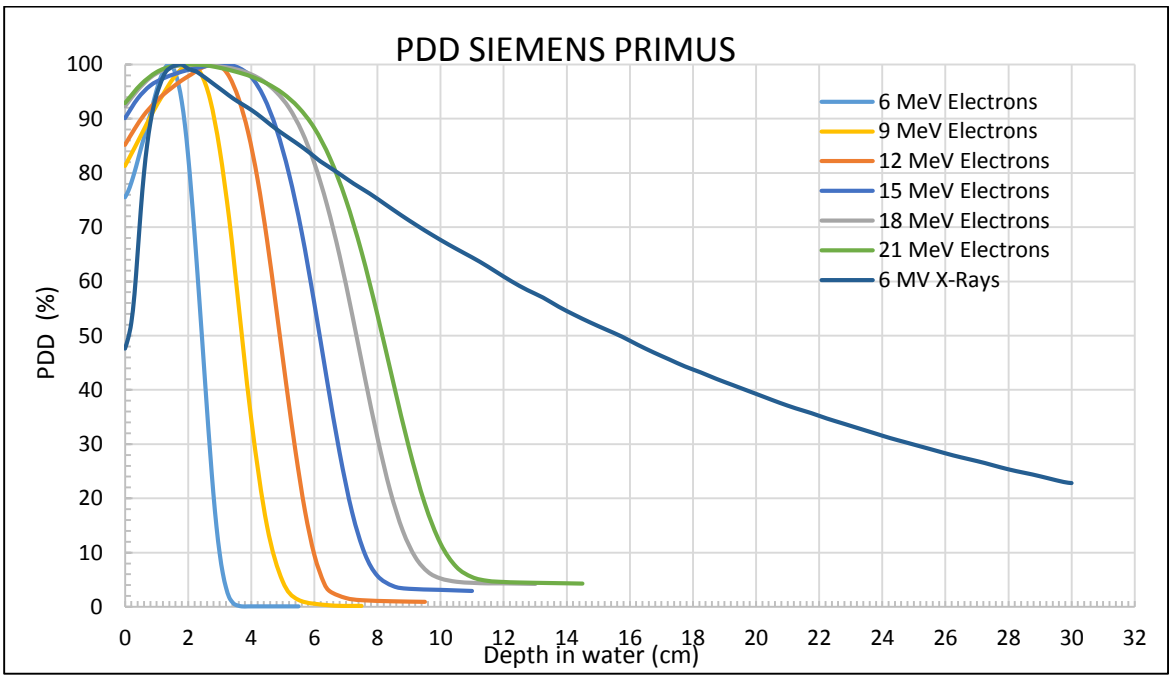

Figure 2.1 Measured percentage depth dose curves for the 6 MV X-Ray beam and the 6, 9, 12, 15, 18 and 21 MeV electron beams from the Siemens Primus linear accelerator used in this study.

Assuming that all the malignant cells in a particular tumour have equal radio-sensitivity, the lower the number of malignant cells, the higher the probability of achieving tumour control per given dose of radiation *(Calvo et al 2006)*. Delivery of EBRT a long while after surgery allows time for the growth of tumour cells, whereas with IORT, irradiation of the microscopic tissue remaining is performed immediately after resection of the tumour. In IORT, OARs and normal tissue may be shielded or moved out of the beam, allowing for dose escalation, thereby increasing the TCP/NTCP ratio. The single high doses delivered in IORT avoids the repopulation of the tumour cells that occurs with fractionated EBRT.

2.1 History

IORT was first used in 1909, less than 20 years after the discovery of x-rays *(Beck C 1909 and Finsterer H 1915 cited in Palta et al 1995)*. At the time, only low energy x-ray beams were available for radiotherapy. This posed an additional problem in that the normal tissue beyond the tumour bed was then unnecessarily exposed to radiation resulting in a decreased therapeutic ratio.

With the introduction (1950s) of the more penetrable megavoltage x-ray beams capable of treating the deep seated tumours, IORT treatment became relatively non-existent *(Palta 1995)*. Skin dose was also reduced due to the build-up effect in MV beams not present in the lower energy kV beams. However, organs at risk in close proximity to the tumours were still being irradiated unnecessarily. For treatment of the deeper seated tumours situated well beyond the build-up region, normal tissue proximal to the tumour still received high doses of radiation *(Abe & Takahashi 1984)*.

Based on these factors, as well as the fact that microscopic disease may also be treated during surgery *(Fraass et al 1985)*, it was realised that adequate tumour control with high therapeutic

ratios would better be served by simultaneous surgery and treatment rather than using these modalities independently *(Abe et al 1975)*.

IORT was revived at the University of Kyoto, Japan in the early 1960s *(Calvo et al 2006)* with the first patients being treated for advanced abdominal cancers using Cobalt-60 beams. In 1965, the Japanese used electrons produced by a Betatron for IORT *(Abe 1984)*.

Electron beams, by nature, have a rapid fall-off and finite range which would imply that the underlying tissues would be spared to a much larger degree than the more penetrating kilo-voltage and megavoltage photon beams. The dose-rate advantage of electron beams over ortho-voltage x-ray beams meant that treatments were accomplished in a much shorter time. It was also possible to more efficiently shield normal tissue or OARs with lead strips *(Giarratano et al 1975)* placed at the lateral extents of the tumour when using electrons. There is also less differential absorption between tissues of varying densities with electrons relative to photons *(Palta et al 1995)*.

IORT then gained popularity and was introduced into the United States at Howard University in 1976 *(Goldson 1981)*. Numerous centres started their own programmes: Massachusetts General Hospital (1978) *(Gunderson et al 1982)*; National Cancer Institute (1979); Mayo Clinic (1981) *(Rich et al 1984)*.

Popularity of IORT spread to Europe in the 1980s and programmes were started in France (1983), Spain (1984), Italy (1985) and Germany (1986) *(Calvo et al 2006)*. Other European countries followed suit.

To date, there are no centres in Africa that have IORT programmes.

2.2 The IORT technique

Megavoltage electron beams produced by LINACs is the modality of choice for IORT treatments *(Ellis et al 2000, Calvo 2006)*. The range of electron energies available and the

finite range of each of these beams affords the opportunity of selection of the appropriate penetrating power necessary to adequately treat the distal end of the tumour with minimal irradiation of normal tissue that exists beyond this point.

Existing treatment couches are devoid of a tilt function which would improve accuracy of the alignment of the beam with the tumour. New couches with this capability have been manufactured by various institutions *(Nyerick et al 1991; Palta & Suntharalingam 1989).*

Initial collimation of the electron beam is provided by the movable photon collimator Y-jaws and MLC. Depending on the coding mechanism of the LINAC, these settings may be automatic depending on the cone-energy combination, or may be set by the user *(Biggs et al 1981).* The square-sided electron applicators routinely supplied with LINACs are inappropriate for IORT as they are too large ($5x5\ cm$ to $25x25\ cm$ in steps of $5\ cm$). Even the smallest $5x5\ cm$ applicator would require large surgical incisions so that the sides of the applicator would be able to be placed in direct contact with the surgically exposed tumour. The preferred mechanism for beam collimation in IORT is with circular applicators.

Figure 2.2 Example of an IORT procedure for the treatment of breast cancer showing the positioning of the circular IORT cone placed directly on the tumour bed. *(Reprinted from Mihailescu & Borcia 2014)*

2.3 Challenges in IORT

One of the main challenges in IORT is the need for the patient to be in a sterile environment throughout the surgical and treatment procedures. In many instances, the operating theatres are situated a distance from the LINAC bunker. This poses a problem of the patient being moved post-surgery through unsterile environments for their treatment, which would increase the chance of infection of the open wound. The patient would also have to be transferred from the operating bed to the treatment couch *(Palta 1995)*. IORT treatments are few and far between whereas LINACs are routinely utilised for external beam treatments throughout the day. The treatment room would also have to be sterilised prior to delivering the radiation. This would mean that all other routine treatments scheduled for that day would have to be postponed.

A second option utilised by many centres is to have an operating theatre adjoining the LINAC bunker *(Palta 1995)*. Whilst this scenario ensures that the patient is not exposed to unsterile environments, the issue of sterilising the LINAC bunker prior to treatment and postponing scheduled treatments for that day still exists. The patient would still have to be transferred to the treatment couch.

Another option used would be for the operating theatre facilities to be installed in an existing LINAC bunker and for the surgery to be performed on the treatment couch *(Palta 1995)*. The room could be sterilised the night before so that the surgery and treatment could commence the next morning. This would once again mean that all other routine treatments scheduled for that day would have to be postponed. This would appear to be the least time-consuming and would reduce the duration that the patient would need to be anaesthetised. This is the option available at the institution in which this study was performed.

Mobile electron LINACs with reduced shielding requirements have been developed and are gaining popularity for IORT *(Beddar et al 2006)*. These units may be used in existing operating theatres *(Beddar & Krishnan 2005)* and provide a suitable solution to the challenges mentioned above.

2.4 Mobile Linear Accelerators

The first mobile linear accelerator dedicated to IORT was manufactured towards the end of 1990 *(Mihailescu & Borcia 2014)*. The Mobetron (IntraOp Medical Incorporated, USA) produces electron beams with nominal energies of 4, 6, 9 and 12 MeV and is supplied with circular applicators of diameters 3, 5, 6, and 10 cm. The NOVAC 7 (Hitesys, Italy) is equipped with 3, 5, 7 and 9 MeV electron beams and is supplied with circular applicators of diameters 4, 6, 8 and 10 cm *(Fantini et al 1997)*.

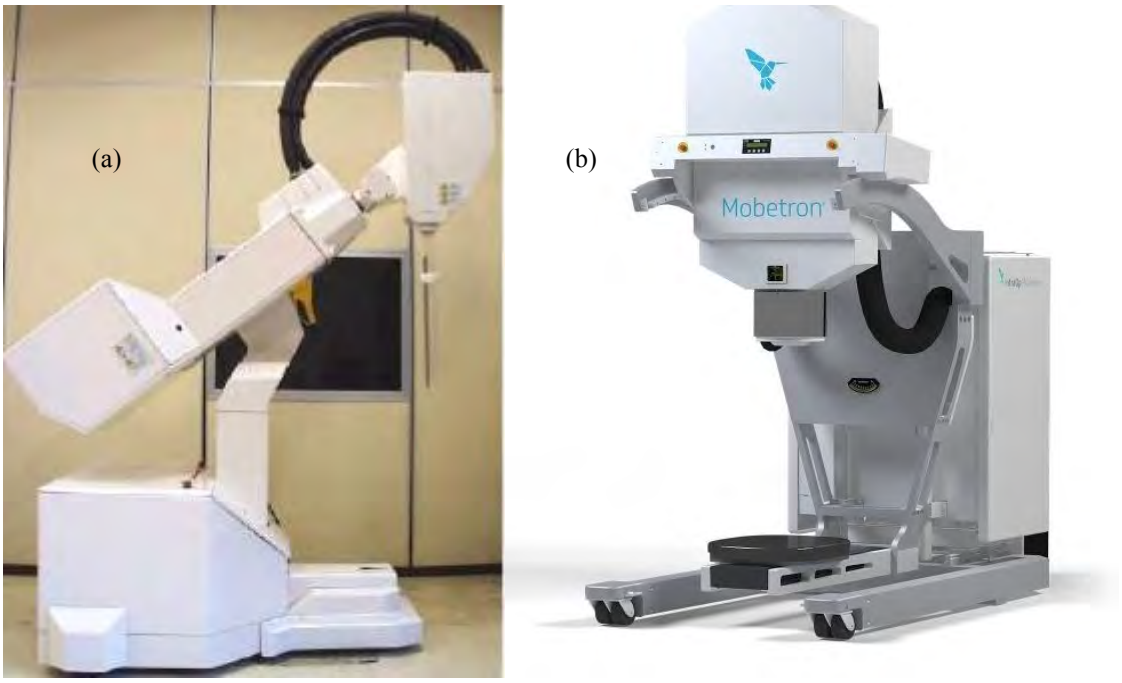

Figure 2.3 The first mobile accelerators routinely used for Intra-Operative Radiation Therapy: (a) NOVAC 7 (b) Mobetron

Whilst IORT with both conventional and mobile LINACs may achieve the same endpoints in terms of clinical outcomes, there are many practical aspects that need to be considered before deciding on which treatment modality to obtain. Some of the more important similarities and

differences as well as advantages and disadvantages of each modality is tabulated below *(table 2.1)*.

Table 2.1 Comparison of conventional and mobile linear accelerators for IORT treatments

Conventional Linear Accelerators	Mobile Linear Accelerators
Shallow penetrating electron beams	Shallow penetrating electron beams
Circular applicators	Circular applicators
Beam-shaping cut-outs	Beam-shaping cut-outs
Single fraction	Single fraction
Shielding of OARs possible	Shielding of OARs possible
High machine cost	Less expensive unit
Patient transported from operating room to bunker (risk of infection)	Treatment performed in operating theatre (reduced risk of infection)
Protracted operating/anaesthetic times	Shorter operating/anaesthetic times
Sterilisation of bunker required	Operating theatre fully sterile
Unit unavailable for routine EBRT from time of initial sterilisation to completion of treatment	Unit dedicated to IORT in operating theatre
Unit installed in a fully shielded room	Unit may be used in un-shielded operating theatre
Number of patients treated per day/week not restricted by shielding provided	Number of patients treated per day/week restricted by reduced shielding provided
Maximum energy not limited to 12 MeV, thereby allowing greater depth of target coverage.	Maximum energy limited to 12 MeV due to possible exposure in adjacent rooms
No beam stop exists	Beam stop (available on some units) may interfere with patient treatment
Unit in bunker – no additional storage room required	Storage room for unit required
Large, fixed and immovable	Smaller and lighter unit – may easily be transported between rooms
Limited range of motion of treatment head – patient set-up more challenging	Greater flexibility in range of motion of treatment head – easier patient set-up

Experiences and clinical outcomes for a variety of sites treated with IORT (utilising either modality) may be found in the publications cited below:

Pancreas *(Farrell et al 1997, Crane et al 2003)*

Rectal *(Nag et al 1997, Wiig et al 2000)*

Stomach *(Krämling et al 1997)*

Gynaecological tumours *(Garton et al 1993, del Carmen 2003)*

Soft tissue sarcomas *(Gunderson et al 1993, Oxenberg et al 2014)*

Breast *(Palta et al 1995, Veronesi et al 2001)*.

2.5 IORT cone system

The most common and appropriate collimation system consists of a set of circular applicators with diameters ranging from about 2 cm for smaller tumours to about 10 cm for larger treatment areas. Modifications of the existing LINAC are not necessary to accommodate the cones. Most cone systems in use are incorporated into the existing LINAC structure by adaptor plates that fit into the accessory slot of the treatment head. Most commercial systems are similar in structure and design. In order to describe the IORT technique, only the IORT cone system (Radiation Products Design Inc., Albertville, USA) used for this study is described.

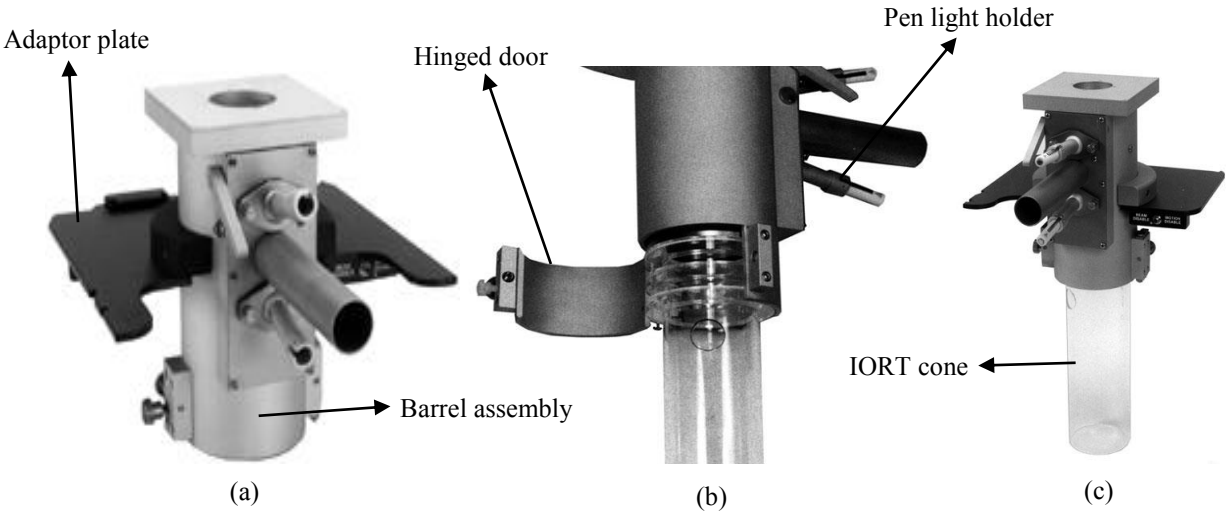

Figure 2.4 The IORT cone system used in this study depicting: (a) The adaptor plate and barrel assembly (b) The hinged door for lateral docking of the cone and pen light holder for viewing of the treatment site (c) the fully assembled cone system *(Courtesy of Radiation Products Design Inc., Albertville, USA)*

The Intra-Operative Periscopic Cone system may be used on any LINAC by the inclusion of a coded adapter plate that fits into the accessory slot of that particular LINAC *(figure 2.4(a))*. The barrel assembly with a periscopic viewer is attached to the adapter plate. The bottom end of the barrel assembly has a hinged door *(figure 2.4(b))* facilitating lateral insertion of the cone into position so that the presence of the patient on the treatment couch does not interfere with the process of insertion of the cone. Utilisation of the stainless steel locking knob ensures the electron cone is held in the desired position. In this system, it is possible for the cone to

slide up to about 20 cm into the periscopic barrel assembly if treatment at shorter SSDs is desired. Washers and screws need to be adjusted to ensure that the barrel assembly and electron cone are centred along the central axis of the beam.

There is a spring-loaded movable mirror inside the barrel assembly that may be used to assist in accurately docking the cone whilst viewing the treatment area. The spring mechanism ensures that the mirror is automatically retracted out of the field during treatment. Viewing of the treatment area is optimised by the presence of two pen light holders on swivel sockets. A 0.005 cm thick Mylar sheath is secured at the top of the barrel assembly to ensure that no foreign particles fall into the surgically exposed treatment area.

Bevelled applicators are also available to facilitate apposition of the cone with the tumour. Further field shaping may be accomplished by placing lead pieces adjacent to the tumour to avoid unnecessary irradiation of normal tissues or organs in close proximity to the tumour. The lead should be thick enough to reduce the dose to below 5% of the maximum dose being delivered.

Custom-designed alloy cut-outs may also be fitted into the end of the cone to shape the beam so that it conforms to the shape of the tumour. The use of these cut-outs is the focus of this study. The method of manufacture and insertion of the cut-outs is described in detail in section 7.1.

2.6 Electron beam characteristics

It is essential that the following comprehensive set of measurements be performed to accurately determine the dose characteristics of each possible cone-energy combination to be used for IORT: central axis percentage depth dose; beam profiles at multiple depths; isodose contours; surface dose determination; absolute dosimetry under reference conditions;

applicator (output) factors; cut-out factors; air gap factors; lead transmission factors; alloy transmission factors *(Fraas et al 1985, Palta et al 1995, Beddar et al 2006)*.

The measurements relevant to this study are discussed in greater detail below.

2.6.1 Percentage depth dose (PDD)

The Percentage Depth Dose (PDD), expressed as a percentage, at depth z for a beam of energy E with field size x and SSD = f is defined as:

$$PDD(z, E, x, f) = \frac{D_z}{D_{max}} * 100 \qquad (2.1)$$

where D_z is the absorbed dose at point z on the central axis and D_{max} is the absorbed dose at the depth R_{max} of maximum dose. *(Podgorsak 2005; Khan 2003)*.

There are several pertinent parameters *(figure 2.5)* characteristic of each electron beam that may also be used to differentiate one from the next in the absence of visual PDD plots of the beams. These range parameters may be defined thus *(Brahme 1976)*:

R_{100} (R_{max}) is the depth of maximum dose,

R_{80} is defined as the depth interval from the surface to the depth of 80% of the absorbed dose and is chosen to coincide with the target volume. (R_{85} and R_{90} are sometimes used for this purpose).

R_{50} is the depth of the 50% dose.

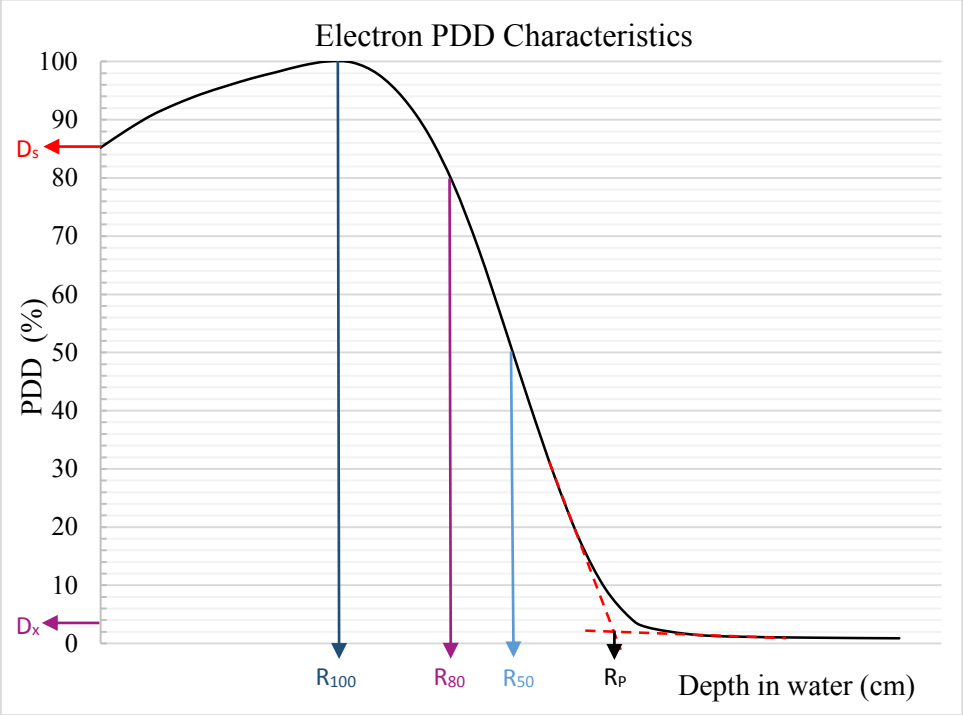

Figure 2.5 A typical electron beam PDD depicting distinguishing parameters that characterise the beam

For photon beams, dose deposition along the beam central axis gives a good indication of the beam quality by providing information of the manner in which the beam is attenuated relative to the depth in the phantom/patient.

For electron beams, the depth of the 50% dose R_{50} is related to the mean electron energy $\overline{E_0}$ by the relationship *(Brahme 1976)*

$$\overline{E_0} = C * R_{50} \qquad (2.2)$$

where C = 2.33 MeV/cm for water *(Podgorsak 2005)*.

The practical range R_p is defined as the depth at which the line projected backwards along the bremsstrahlung tail intersects the tangent line through the steepest portion of the PDD curve *(figure 2.5)*.

The mean energy of the spectrum decreases approximately linearly with depth and is given by the Harder equation *(Harder D 1965 cited in Khan 2003)*

$$\overline{E_z} = \overline{E_0}\left(1 - \frac{z}{R_p}\right) \quad (2.3)$$

D_s refers to the surface/skin dose relative to the dose D_{max} which occurs at depth R_{100}.

D_x represents the dose from the Bremsstrahlung component of the beam relative to D_{max}.

R_{80} is the depth of 80% dose. The most suitable electron beam energy used for treatment would be one in which the distal end of the tumour is coincident with d_{80}. The R_{80} is thus called the therapeutic range and is approximately E/3 (cm). In some clinics, the therapeutic range of R_{90} is used – R_{90} is approximately E/4 (cm) *(Khan 2003)*.

The following characteristics of electron beams may be observed from the PDD plots in figure 2.1 above.

There is a build-up of dose between the surface and R_{100} which is a consequence of the scattering interactions between the incident electrons and the atoms of the phantom material as well as due to the production of secondary electrons. The surface dose increases with increasing electron energy. This is due to the fact that relatively lower energy electrons and δ-rays are scattered away from the central axis to a much larger degree than the relatively higher energy electrons. Dose therefore builds up more rapidly resulting in the ratio of surface dose to maximum dose being lower for the lower energy beam *(Klevenhagen 1985)*.

Electron beams display a high dose plateau from 90% to 100% that increases in depth with increasing beam energy and falls off steeply distally *(figure 2.1)* and laterally *(figure 2.6)* *(Hogstrom 2006)*.

This rapid falloff of dose beyond R_{100} is due to continuous energy loss and scattering. The lower the energy, the steeper the dose falloff since the lower energy electrons are scattered away from the central axis to a larger degree.

Bremsstrahlung production occurs with interactions of the incident electron beam with the components of the LINAC head, the air and the phantom, resulting in the photon contamination tail observed at the distal end of the beam. As observed in figure 2.1, the higher the energy, the greater the amount of bremsstrahlung production.

The practical range R_p of the electron beam is also observed to increase with increasing energy. It is worth noting that beam-characteristic factors such as R_{100}, R_{80} and R_{50} increase as the field size increases to a point where lateral electronic equilibrium is achieved. The practical range, R_p, however is preserved for each electron energy and invariant with change in field size *(Podgorsak 2005)*.

2.6.2 Beam profiles

In-plane (radial) and cross-plane (transverse) profiles are also essential to comprehensively characterise electron beams and are used in conjunction with the central axis PDDs to determine 2-D dose distributions. If 3-D dose distributions are required, off-axis profiles must also be obtained so that the beam may be characterised accurately in 3 dimensions. The profiles are measured at multiple depths perpendicular to the beam axis.

Due to the continuous energy loss and scattering of the electron beam as it traverses the medium, the scattering angle of the lower energy electrons increase, thereby causing the beam to diverge at depth. Penumbra is the term used to quantify the degree of divergence and is defined as the distance between the 80% and 20% dose values in the profile *(figure 2.6) (Podgorsak 2005).* The width of the penumbra is dependent on the depth of measurement, field size, energy of the beam and collimation used *(Podgorsak 2005)*. Since the depth of the profile has the greatest effect on the width of the penumbra, IEC *(Khan 2003)* recommends that the profile used to quantify any particular electron beam penumbra be that acquired at $d_{80}/2$, where d_{80} is the depth of the 80% dose on the central axis.

Dose uniformity may be quantified by determination of the flatness and symmetry properties of the beam profiles. Specification of the flatness of the beam gives an indication of the homogeneity of the beam. Flatness is quantified by the difference between the D_{max} and D_{min} values ($D_{max} - D_{min}$) in the central 80% of the beam profile *(Khan 2003)*. Care must be taken to minimise noise *(depicted in figure 2.6),* especially in the flattened portion of the scan in order to achieve more accurate flatness and symmetry results *(Das et al 2008)*.

The symmetry of the beam is quantified, from the profile at R_{max}, by the maximum ratio of doses of any two points symmetric about the central axis of the beam *(Khan 2003)*.

Measurement of beam profiles near the water surface may lead to a ripple effect observed in the central portion of the profile. It is not a property of the beam but is caused by wave-motion displacement effects of the water by the scanning arm as the chamber travels across the beam. This may be avoided by using slow scan speeds especially for low energy beams at depths beyond R_{max} *(Das et al 2008)*.

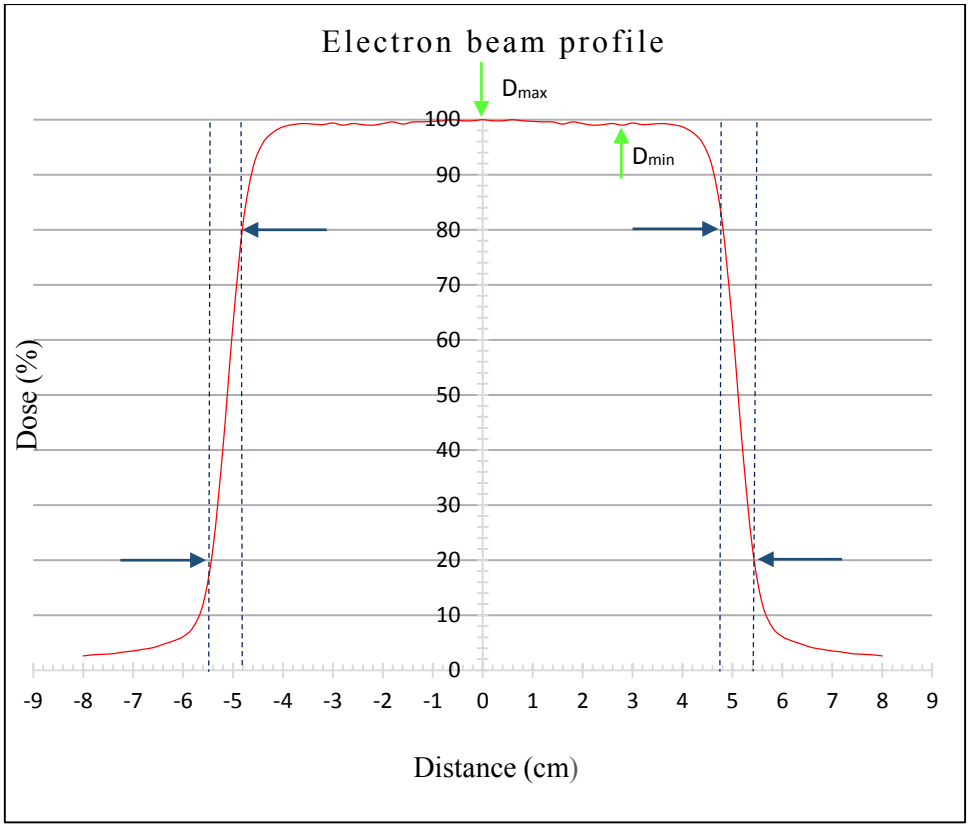

Figure 2.6 Typical electron beam profile showing the defining points for flatness and symmetry determination.

2.6.3 Absolute dosimetry

All electron energies available are routinely calibrated to deliver 1 cGy per monitor unit (MU) at a specified depth (usually R_{max}) on the central axis for the $10x10$ cm applicator at an SSD of 100 cm.

A detailed description of the calibration technique is presented in section 5.3.1.

2.6.4 Cone factor (CF) and Cut-out factor (COF)

It is necessary to determine the MU required to deliver a prescribed dose with the IORT cone in place. This is accomplished by measuring the dose per MU for the IORT cone and determining a cone factor by relating it to the dose per MU for the calibration geometry.

The cone factor (CF) used in this study is defined as *(Verhaegen et al 2001)*:

$$CF = \frac{D_{max}(E,X,100cm)}{D_{max}(E,10x10cm,100cm)} \quad (2.4)$$

where the numerator is the maximum dose on the central axis for a beam of energy E and cylindrical cone of size of diameter X for 100 cm source to surface distance. The denominator is the maximum dose for 100 cm SSD for the same beam energy, E, with the $10x10\ cm$ applicator in place (reference geometry). Both numerator and denominator must be determined for the same number of monitor units. Note that the depth of the maximum dose, R_{max}, for each beam differs due to the fact that it decreases with decreasing field size implying that each measurement must be performed at their respective R_{max} depths *(Verhaegen 2001)*.

Equation 2.4 applies in an identical manner when irregularly shaped cut-outs are introduced into the beam. The cut-out factor COF is therefore given by:

$$COF = \frac{D_{max}(E,X,100cm)}{D_{max}(E,10x10cm,100cm)} \quad (2.5)$$

2.6.5 Monitor Unit (MU) calculations

2.6.5.1 Nominal SSD (100 cm)

The MU required to deliver the prescribed dose at depth z with the IORT cone or cut-out X in place may then be calculated using the following equation *(Biggs 1981)*:

$$MU_X = \frac{Prescribed\ dose\ (Gy) * 100MU/Gy}{CF*PDD_z} \quad (2.6)$$

where prescribed dose is the prescription dose at depth z for the cone or cut-out and PDD_z is the $PDD/100$ at depth z obtained from the cone or cut-out PDD curve.

2.6.5.2 Electron treatments at extended SSD

The pencil electron beam exiting the vacuum window has a small but finite radial and angular spread. Due to the multiple Coulomb scattering events that occur as the beam traverses the various treatment head components to the applicator/cone end, the beam is broadened, but appears to emanate from a point *(Khan et al 1991)*.

In order to be able to utilise the inverse square law for MU calculations for extended SSD electron beams, the effective source to surface distance (SSD_{eff}), which is the distance between the virtual source position and the isocentre, must be determined.

To illustrate the process of SSD_{eff} determination, measurements of dose at d_{max}, for gaps between the applicator end and the water surface varying from 0 to 15 cm at 1 cm intervals, were performed *(Podgorsak 2005, Khan 2003)* for the $10\ x\ 10\ cm$ applicator for 6 MeV, 12 MeV and 18 MeV beams.

If I_0 is the dose with gap = 0 and I_g is the dose with gap = g,

$$I_0/I_g = [(SSD_{eff} + d_{max} + g\ /(SSD_{eff} + d_{max})]^2 \quad (2.7)$$

resulting in

$$(I_0/I_g)^{(1/2)} = 1 + g/(SSD_{eff} + d_{max}) \quad (2.8)$$

Plotting $(I_0/I_g)^{(1/2)}$ against g results in a straight line *(figure 2.7)*, the slope of which is:

$$Slope = 1/(SSD_{eff} + d_{max})$$

or

$$SSD_{eff} = (1/slope) - d_{max} \quad (2.9)$$

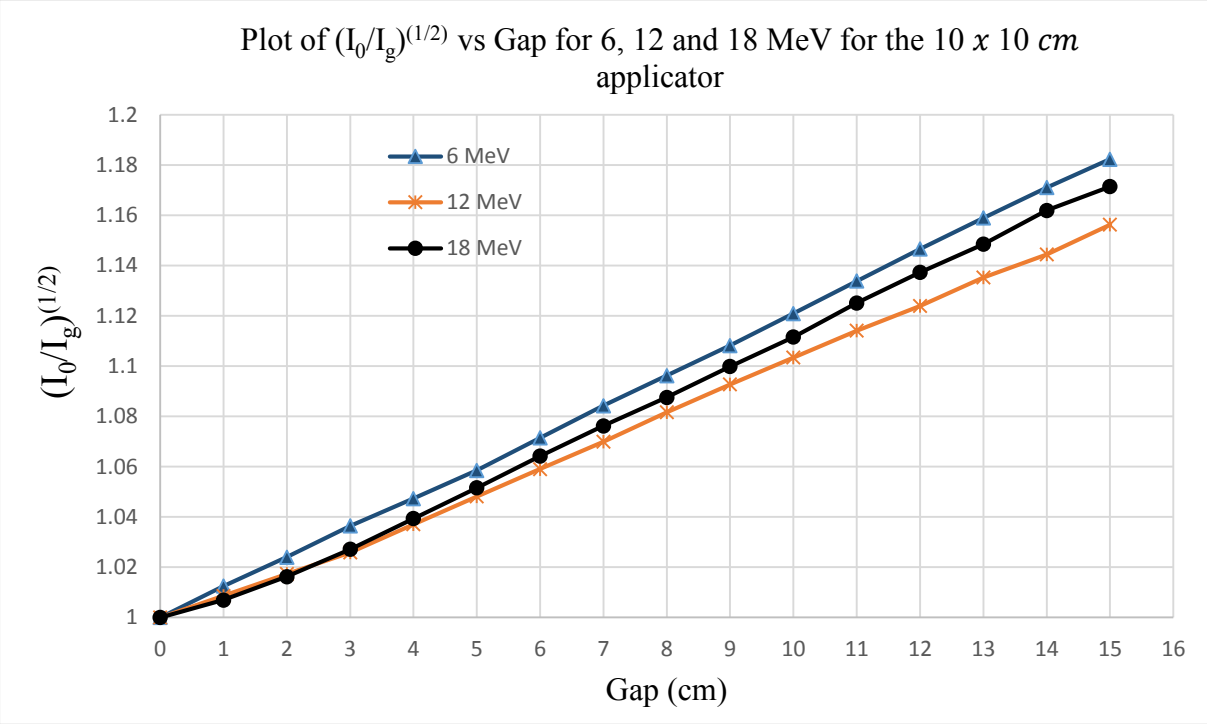

Figure 2.7 Effective SSD (SSD_{eff}) determination for 6 MeV, 12 MeV and 18 MeV electron beams for the $10\ x\ 10\ cm$ applicator

By substituting the value of the slope obtained for each curve into equation 2.9, the following effective SSD for each energy was obtained.

Table 2.2 Effective SSD (SSD_{eff}) for energies 6 MeV, 12 MeV and 18 MeV for the $10\ x\ 10\ cm$ applicator. *(Measurement uncertainty = ±0.6%)*

Energy (MeV)	**6**	**12**	**18**
SSD_{eff} (cm)	80.7	92.1	82.6

In situations where the applicator or cone end cannot make direct contact with the tumour surface and treatment at extended SSDs is necessary, an inverse square law factor utilising the SSD_{eff} may be applied to equation 2.6 to obtain the MU with a gap (g):

$$MU_x = \frac{Prescribed\ dose * 100MU/Gy}{CF * PDD_z} * \left(\frac{SSD_{eff}+g}{SSD_{eff}}\right)^2 \quad (2.10)$$

Note that CF in equations 2.6 and 2.10 must be replaced by COF for the cases with cut-outs. In this study, the cone end was placed at 99 cm with 1 cm clearance between the cone end and the patient surface. The SSD therefore remained at 100 cm with no stand-off corrections necessary.

SSD_{eff} is known to also vary with field size *(Khan 1991, Cygler 1997, Das 1995)*. It would thus be necessary to obtain the SSD_{eff} for each energy/applicator, energy/cone and energy/cut-out combination for conventional electron treatments utilising extended SSDs.

In IORT, however, the tumour site is surgically exposed and the normal tissue and organs are displaced so that the tumour may be treated with the applicator or cone in direct contact with the exposed tumour site. Since it is highly unlikely that extended SSDs for IORT treatments will be necessary in our clinic, determination of SSD_{eff} for the above-mentioned combinations was not included in this study.

CHAPTER 3

MONTE CARLO TECHNIQUES IN RADIOTHERAPY

The basis and origin of the Monte Carlo method of calculation is described by the following statement made by Stan Ulam in 1983 *(Eckhardt 1987)*:

> "The first thoughts and attempts I made to practice [the Monte Carlo method] were suggested by a question which occurred to me in 1946 as I was convalescing from an illness and playing solitaires. The question was what are the chances that a Canfield solitaire laid out with 52 cards will come out successfully? After spending a lot of time trying to estimate them by pure combinatorial calculations, I wondered whether a more practical method than "abstract thinking" might not be to lay it out say one hundred times and simply observe and count the number of successful plays. This was already possible to envisage with the beginning of the new era of fast computers, and I immediately thought of problems of neutron diffusion and other questions of mathematical physics, and more generally how to change processes described by certain differential equations into an equivalent form interpretable as a succession of random operations. Later... [in 1946], I described the idea to John von Neumann and we began to plan actual calculations.

Ulam and von Neumann decided to use this statistical sampling technique to estimate neutron multiplication rates to predict the behaviour of neutron chain reactions in fission devices that were being designed at the time. Due to the technique's similarity to games of chance, he named the method 'Monte Carlo' after the casino city in the principality of Monaco."

The Monte Carlo method is any process where random sampling from probability distribution functions is used to construct solutions to problems. Application of the Monte Carlo method was introduced to the field of radiation therapy in the 1970s *(Andreo 1991)* and experienced a slow start mainly due to the low computational speeds of computers available. Major advances in computer technology and the development of faster codes to simulate the transport of electrons and photons in matter have made the MC method a more acceptable alternative to solving complex transport equations analytically *(Chetty et al 2007)*.

It is virtually impossible to accurately obtain a solution to the radiation transport of photons and electrons in a medium in a single analytical expression *(Rogers & Bielajew 1990)*. This is mainly due to the fact that the interactions of the electrons with the atoms of the material they encounter may produce bremsstrahlung photons and secondary or knock-on electrons, and the photons may produce both electrons and positrons. There is also a large degree of scattering that occurs with photons and electrons. Further challenges are experienced with oblique incidence of the electron beam and the presence of inhomogeneities in the material being traversed by the beam. Attempts were made to find simple analytical expressions for essential transport parameters *(Brahme 1975)*. Further work was done to improve the accuracy of the algorithms *(Shiu & Hogstrom 1991)* but large dose discrepancies still existed in certain instances *(Boyd et al 2001)*, more specifically in the handling of patient heterogeneities.

The majority of treatment planning systems still utilise analytical algorithms which apply formulas to explicitly calculate dose deposition in a medium *(Hogstrom et al 1981)*. The Monte Carlo method has shown great potential in solving the problems associated with use of these algorithms in treatment planning systems *(Reynaert et al 2007).*

An accuracy of about 5% in dose delivery is required to effectively treat certain types of cancers and to reduce complications *(ICRU 24 1976 and ICRU 42 1988)*.

The beauty of the MC simulation of radiation transport is that it models the real physics of the processes that occur during interactions of radiation with matter. MC-based systems take into account the trajectory and history of each and every particle present in the incident beam which makes for extremely accurate calculations *(Ma et al 1997, Jiang et al 2000, Sempau et al 2000)*

It has therefore become the gold standard for determining absorbed dose in a medium from clinical radiotherapy beams and has been extensively benchmarked *(Sheikh-Bagheri &*

Rogers 2002a, Sheikh-Bagheri & Rogers 2002b). Computation time for simulations has been the biggest drawback in the routine use of MC simulations for the determination of absolute dose in a treatment planning system, but as technology has progressed, faster computers and higher quality processors have become available making it a more viable option *(Chetty 2007)*. Variance reduction options are also available in the code used in this study (section 4.3.3) and aid in efficiency whilst maintaining accuracy *(Rogers et al 2005)*.

3.1 The Monte Carlo Method

Monte Carlo codes were introduced to simulate the interactions of photons and electrons with the materials they encounter along their path. The scientifically obtained probability distributions governing these interactions are well documented *(Mayles et al 2007)* and are used to simulate the history of each particle as they traverse the materials they encounter. Variables defining the properties (e.g. energy and direction) of the particle and the properties (e.g. density) of the materials it interacts with will determine the type of interaction and subsequently the products of the interaction based on the known probability distribution function that is sampled *(Raeside 1976)*. Variables defining the properties of the products of the interaction are then stored and these products also become the objects of the ensuing simulation process. The particle history ends once it has lost all its energy or once it has exited the geometry of interest *(Kawrakow & Rogers 2003)*.

The following example is used to illustrate the principle of the Monte Carlo simulation process in order to calculate the dose to a point in the medium from a photon beam.

Photons (and electrons) interact with various components (targets) of matter, such as electrons, nuclei etc. The cross sectional area of these components in a plane perpendicular to the incident photon direction is used to estimate the probability of interaction and is termed the cross section, σ *(Mayles et al 2007).*

The linear attenuation coefficient (LAC) μ is defined as the probability per unit length for an interaction to occur and is dependent on the properties of the medium and the photon energy *(Raeside 1976)*. It is related to the total cross section by:

$$\mu = N\,\sigma \tag{3.1}$$

where

$$N = (N_A/A) * \rho \tag{3.2}$$

where N_A is Avagadro's number, A is the relative atomic mass of the absorber and ρ is its density.

The average distance λ travelled by a photon before it interacts is called the mean free path and is given by the equation *(Nahum 2002)*:

$$\lambda = \int_0^\infty x e^{-\mu x} dx = \frac{1}{\mu} \tag{3.3}$$

which implies that the mean free path is the inverse of the LAC.

The first step in the application of the MC simulation is to generate the random distances that the photon travels before an interaction occurs *(Raeside 1976).*

Note that:

$$R = \int_a^x PDF(x')dx' = CDF(x) \tag{3.4}$$

where: R is a random number in the interval (0,1)

PDF is the normalised probability distribution function

CDF is the cumulative distribution function

The probability that no interaction occurs for a photon that has travelled a distance x is given by

$$exp\,(-\mu x) \tag{3.5}$$

where μ is the total LAC.

The probability of an interaction occurring between the distances x and x+dx is *(Nahum 2002)*:

$$\mu\, exp(-\mu x)\, dx \tag{3.6}$$

The cumulative distribution function F(x) is

$$F(x) = \int_0^x \mu \exp(-\mu x)\, dx$$

$$= 1 - exp(-\mu x) \tag{3.7}$$

The distance x travelled by the photon may be solved by random sampling of the cumulative probability distribution function $F(x)$ by the generation of a random number R_1 which implies that

$$x = -\frac{1}{\mu} ln\,(1 - R_1) \tag{3.8}$$

Since $(0 < (1 - R_1) < 1)$ and since R_1 is a random number that has the same probability as $(1 - R_1)$, the distance x travelled by the photon before the next interaction may be written as *(Raeside 1976, Rogers 2002)*.

$$x = -\frac{1}{\mu} ln\,(R_1) \tag{3.9}$$

The next step would be to determine the interaction type that occurs once the photon has travelled to the interaction site. Assume that only the three main interaction processes Compton Scattering (CS), Photoelectric Effect (PE) and Pair Production (PP) may occur with associated interaction cross-sections σ_{cs}, σ_{pe} and σ_{pp} respectively. The total cross section is the sum of the cross sections for the individual processes *(Johns 1983)*:

$$\sigma_{total} = \sigma_{cs} + \sigma_{pe} + \sigma_{pp} \tag{3.10}$$

This equation may therefore be seen to describe the probability distribution for the interactions that may occur. The probability of PE, CS and PP occurring is respectively given by

$$\frac{\sigma_{cs}}{\sigma_{total}}, \quad \frac{\sigma_{pe}}{\sigma_{total}} \quad and \quad \frac{\sigma_{pp}}{\sigma_{total}} \tag{3.11}$$

Assume that the known probability for the interaction type of a photon in a particular medium is arbitrarily given as follows: 60% Compton Scattering (CS), 10% Photoelectric Effect (PE) and 30% Pair Production (PP). This implies that

$$\frac{\sigma_{cs}}{\sigma_{total}} = 0.6, \quad \frac{\sigma_{pe}}{\sigma_{total}} = 0.1 \quad and \quad \frac{\sigma_{pp}}{\sigma_{total}} = 0.3 \tag{3.12}$$

Suppose 8 random numbers R_2 through to R_9 are then generated in the interval (0, 1). Their positions in the interval defines the interaction type that occurs.

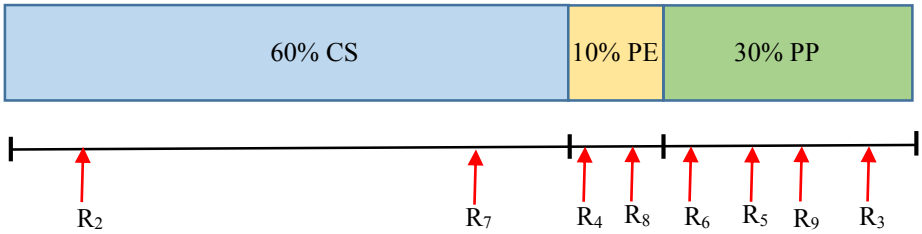

Figure 3.1 Representation of determination method of interaction type

In this example, 25% of the interactions would be Compton scattering interactions, 25% Photoelectric Effect interactions and 50% Pair Production interactions. This is obviously not a true reflection of the of the real life situation based on the known probability distribution functions. The reason for this is that the number of random numbers generated to sample the probability distribution function is far too low to provide accurate simulation results. If the number of histories were increased to the order of 10^7 *(Walters et al 2002)*, for instance, the interaction results of the simulation would conform to the real life situation viz. CS:PE:PP would be 0.6:0.1:0.3. The statistical uncertainty of the result is dependent on the number of histories N and decreases as $\frac{1}{\sqrt{N}}$, which means that to reduce the uncertainty to half its original value, 4 times as many histories must be used.

Whilst the interaction type is sampled from the branching ratios such as that depicted in figure 3.1, different sampling methods are used to determine other dynamical variables (such as energy and angular distribution) of the products of the interactions.

One of the main attractions of the MC simulation of radiation transport is that it models the real physics of the processes that occur during interactions of radiation with matter using random sampling techniques *(Rogers 2006)*. Modelling the stochastic nature of radiation

transport in this manner requires a large amount of history data to calculate the expectation value for the dynamic variable being sought after. It is thus a very accurate method of modelling. It has therefore become the gold standard for determining absorbed dose in a medium from clinical radiotherapy beams. It can provide solutions to complex radiation transport near and at interfaces and boundaries between tissues with large density and atomic composition differences. Computation time for simulations has been the biggest drawback in the routine use of MC simulations for the determination of absolute dose in a treatment planning system, but as technology has progressed, faster computers and higher quality processors have become available making it a more viable option. Variance reduction options are also available in the code (section 4.3.3) and may be employed to reduce computational time.

3.2 Electron transport

3.2.1 Electron interactions with matter

Collisional losses (inelastic scattering) and radiative losses that occur as an electron traverses matter are dependent on the energy of the electron and the distance of the electron from the atom *(Attix 1986)*. Collisional losses may be either soft or hard.

Soft collisional losses occur when this distance is much greater that the atomic radius. The presence of the electron in the coulomb field of the atom may cause the atom to become excited and an electron may jump from an inner orbital shell to an outer orbital shell. The ejection of an orbital electron may also occur (ionisation). The excited or ionised atom then returns to its ground state by the emission of characteristic radiation or by the emission of Auger electrons. Approximately half of the energy transferred by electrons to a medium occur via soft collisions *(Attix 1986)*.

Hard collisions occur when the distance of approach of the electron is roughly equal to the atomic radius. The probability of an interaction of the electron with an orbital electron increases. The energy transferred to the orbital electron may be sufficient to overcome its

binding energy thereby ejecting it from the atom (ionisation) and giving it enough kinetic energy to travel a distance away from the point of interaction *(Khan 2003)*. Once again, characteristic radiation and/or Auger electrons may be emitted. The ejected electron may be responsible for further ionisations and excitations along an independent track.

When the distance of approach is much less than the atomic radius, the electron may interact with the electromagnetic field of the atomic nucleus resulting in radiative losses. The energy lost by the electron causes it to decelerate and be deflected from its original path. This energy is known as bremsstrahlung. Bremsstrahlung production is the dominant energy-loss process at high energies, whilst collisional losses are more significant at low energies *(Attix 1986, Hendee et al 2005)*.

The interaction of the electron with the nucleus may also result in elastic scattering whereby the electron is deflected from its original path without the transfer of energy. The probability of this interaction process increases as the square of the atomic number of the atom involved in the interaction.

3.2.2 Monte Carlo modelling of electron transport

In the Monte Carlo simulation example described in section 3.1, the transport of photons was accomplished by first calculating the distance that the photon travels without interaction and then transporting the particle to the interaction site. The interaction type was then determined and the interaction was simulated. This analogue approach works well for photons since they deposit their energy in discrete steps.

Electrons and positrons, however, undergo collisional and radiative losses in an almost continuous manner with much smaller mean free path lengths. They may undergo as much as 10^4 inelastic and 10^5 elastic collisions with atomic nuclei and electrons before their energies fall below a pre-determined cut-off at which the remaining energy is locally absorbed *(Berger*

& Wang 1988). Due to this excessively large number of interactions, the analogue approach of simulation of electron interactions is highly impractical as it would increase simulation times to unacceptable levels.

Since the majority of electron interactions lead to small changes in electron energy and angular distribution, the condensed history (CH) approximation method introduced by Berger has become the basis of MC simulation of electron transport in matter *(Berger 1963)*. In this model, each electron track is subdivided into a series of track segments (steps). Instead of modelling each interaction individually, the interactions are statistically grouped and the cumulative energy loss due to elastic collisions and angular scattering due to elastic collisions are sampled once for each condensed step.

The sampling of energy loss is accomplished by either Class I or Class II condensed history algorithms *(Berger 1963)* and differ by how they deal with individual interactions that produce bremsstrahlung photons or knock-on electrons. In class I models, the energy and direction of the incident electron are not affected by the creation of secondary particles. Energy losses (and angular deflections) associated with all interactions are grouped together. In class II models, energy thresholds are specified. Secondary electrons and photons produced above this energy threshold are simulated explicitly, whilst the effects of secondary particles produced below this threshold are grouped together *(Kawrakow & Rogers 2003)*. Particle histories are terminated for particles with kinetic energies below ECUT for electrons and PCUT for photons. Secondary particles produced with energies greater than AE (low energy threshold for the production of knock-on electrons) for electrons and AP (low energy threshold for the production of secondary bremsstrahlung photons) for photons is modelled explicitly.

Energy cut-offs (ECUT and PCUT) are used for both class I and class II algorithms and production thresholds (AE and AP) are used for class II algorithms only. The choice of these values is not a function of the actual physical processes but rather a function of the code. EGSnrc uses class II algorithms for sampling energy losses *(Rogers & Bielajew 1990)*.

3.3 Random numbers

Particle-particle interactions have a random probability distribution that may be analysed statistically and hence have a stochastic nature *(Kawrakow 2000)*. The objective of MC calculations in radiotherapy is to simulate these interactions from the known particle interaction cross sections. In order to achieve this goal, a source of random numbers is essential. True randomness is seen, for example, in the time intervals between decays of a radioactive substance. In order to use the randomness from such a phenomenon, one would have to either interface hardware producing the random number to the computer performing the simulation, or store on a computer a sufficiently long random number sequence thus produced, of which neither is practical *(Bielajew 2001)*.

The alternative is to use mathematical algorithms on a computer to produce random numbers. When random numbers are generated in this deterministic manner, they are aptly called pseudo-random numbers and have been found to be suitable for MC simulations of radiation transport. Care needs to be taken to ensure that the distinct number of elements produced (period) is large enough so that the sequence does not repeat itself *(Bielajew 2001)*. It is acceptable for the sequence to repeat itself as long as the initial random number (seed) does not repeat during a particular history which would result in duplication of that history. Since it is not possible to know when there is repetition of the cycle, it is advisable not to exhaust the sequence or even approach the sequence length.

A random number generator commonly used in MC calculations is the Linear Congruently Random Number Generator (LCRNG) of the form *(Bielajew 2001)*

$$R_{n+1} = (aR_n + c) modulus 2^k \quad (3.13)$$

Where R_n is the n^{th} random number, a is a multiplier, c is the increment ($0 \leq c < 2^k$) and k is the number of bits in the integers of the computer. When $c = 0$, the RNG assumes the form

$$R_{n+1} = (aR_n) modulus 2^k \quad (3.14)$$

and is called a Multiplicative Congruently Random Number Generator (MCRNG) which is the type is used in EGSnrc.

The multiplier a is a positive integer such that $0 \leq a < 2^k$. An optimum multiplier determined experimentally *(Ehrman 1981)* is 663608941 and with k = 32, can yield up to 10^9 random numbers per cycle.

It is best for the seed R_0 to be a large prime number or at least an odd number. If the seed is an even number, the cycle length will be reduced proportionally to the number of times the seed can be divided by 2. The random number R_{n+1} is converted to a floating point real number in the interval (0,1) by dividing it by 2^k. RANLUX *(Demchik 2011, James 1994)*, the default MCRNG provided with EGSnrc, was used for this study.

3.4 Efficacy for the use of EGSnrc MC Code

Subsequent to the introduction of the MC method to the field of radiation therapy in the 1970s *(Andreo 1991),* most of the initial studies were devoted to photon beams *(Mohan et al 1985).* Interest in the simulation of electron beams began in the 1980s *(Ding et al 1996, Udale 1988)*.

The Monte Carlo method has been found to be the most accurate method in dose calculation of from electron beams *(Ma & Jiang 1999)*. The greatest dose-calculation advantage has been observed in the manner in which the method handles heterogeneities in patient tissues where

the effects of electron transport are not accurately computed using conventional analytical dose calculation algorithms *(Chetty et al 2007).* Currently, all absolute dose calculation codes of practice use stopping power ratio data derived from MC simulations *(Almond et al 1999).*

Various Monte Carlo codes are available for modelling of medical linear accelerators and/or performing radiation transport simulations:

MCNP is a general-purpose Monte Carlo N–Particle code that can be used for neutron, photon, electron, or coupled neutron/photon/electron transport *(Briesmeister 2000)*.

Penelope (PENetration and Energy Loss of Positrons and Electrons in matter) *(Baro et al 1995).*

GEANT4 (GEometry ANd Tracking) *(Agostinelli et al 2003).*

ETRAN *(Seltzer 1991).*

PEREGRINE *(Hartman et al 2001).*

EGSnrc (Electron Gamma Shower National Research Council of Canada) *(Rogers et al 1995, Rogers et al 2005, Rogers et al 2011)*.

Monte Carlo calculation algorithms for planning of electron treatments are commercially available in a variety of treatment planning systems. The Oncentra Masterplan TPS uses Voxel Monte Carlo VMC^{++} *(Kawrakow 2001)* and handles electron beams from all clinical LINACs. The beam modelling cannot be performed in-house and is handled by the supplier of the system. The CMS Xio TPS is based on the XVMC Monte Carlo code *(Kawrakow et al 1996)* and is also capable of performing MC calculations from clinical electron beams. Beam modelling is performed by the vendor. The Varian Eclipse TPS uses eMC (electron Monte Carlo) for dose calculation from electron beams and was initially implemented for only Varian 23EX LINACs *(Neuenschwander & Born 1992)* with the beam modelling performed by the vendor.

The availability these codes show that there are many different ways of modelling the same real-life physical processes on a computer. It is essential that the most suitable code for the radiotherapy application being studied is selected, as different programmes may yield different results based on the application and not all available codes are suitable for all applications *(Poon & Verhaegen 2005)*.

Motivation for this study was provided by the fact that none of the commercially available MC-based treatment planning systems modelled the Siemens Primus LINAC S/N 3606 (Siemens Medical Solutions, Malvern, USA) together with the Radiation Products Design Inc. IORT cones for electron IORT treatments. Out of all of the codes mentioned above, the BEAMnrc Monte Carlo code is the one that most focusses on all aspects of the modelling of medical linear accelerators, radiation transport from clinical radiotherapy beams and calculations of dose distribution in a phantom or in a patient using acquired patient data. Extensive documentation, user manuals and publications exist on the use of BEAMnrc. User-friendly graphical user interfaces (GUIs) are provided to facilitate input of relevant geometries and parameters vital for correct simulation of the treatment planning process. The code has been extensively benchmarked *(Sheikh-Bagheri & Rogers 2002a, Sheikh-Bagheri & Rogers 2002b)* for clinical radiotherapy applications and is therefore the code of choice for this study.

CHAPTER 4

MATERIALS AND METHODOLOGY

4.1 General

It is envisaged that an Intra-Operative Radiation Therapy programme be implemented at the institution in which this study was performed. Since IORT treatments involve the treatment of surgically exposed tumours or organs, it is essential that accurate dose distributions are obtained for the individual treatment sites. These sites will vary in size and shape in all 3 physical dimensions. These dimensions will only be known after the tumour or organ is exposed following the surgical procedure.

The study involves the validation of Monte Carlo-based calculations for small irregularly shaped intra-operative radiotherapy electron fields. The shape of these fields will be determined by the dimensions of the site to be treated as well as the proximity of normal tissue to the treatment area so that a high therapeutic ratio is maintained. In order to achieve this goal, it is essential that the beams produced by the Monte Carlo simulations conform to the linear accelerator beams.

The LINAC built for this study is the Siemens Primus LINAC S.N 3606 currently used clinically at the Inkosi Albert Luthuli Central Hospital (IALCH) in Durban, South Africa. In compliance with the Non-Disclosure Agreement, intimate details of the material composition and exact dimensions of the components of the LINAC have been omitted in this report. Instead, diagrams (not drawn to scale) are included.

This LINAC has the capability of delivering radiation treatments of 6 MV and 23 MV X-Ray beams as well as 6 MeV, 9 MeV, 12 MeV, 15 MeV, 18 MeV and 21 MeV electron beams. Only the 6 MeV, 12 MeV and 18 MeV beams were used for this study. This was deemed to be adequate in determining the feasibility of utilising the MC dose distribution calculations

for all available electron energies as it covered an appropriate range. The details of the treatment head components (dimensions and material composition) were obtained from the vendor.

Although additional applicators ($15x15\ cm$, $20x20\ cm$ and $25x25\ cm$) are available for this treatment unit, only the standard $10x10\ cm$ and $5\ cm$ circle applicators were used for the Monte Carlo commissioning of the electron beams in question. This was regarded as being adequate as the maximum IORT cone diameter used in this study is 64 mm.

The Intra-Operative Periscopic Cone system (Radiation Products Design Inc., Albertville, USA) model 1100-00 is the IORT cone system used for this study. A more detailed description of the cone system may be found in section 2.5. Thirteen clear circular Poly-MethylMethAcrylate (PMMA) cones of length 30.5 cm each with inner diameters of 19 mm, 25 mm, 32 mm, 38 mm, 45 mm, 51 mm, 57 mm, 64 mm, 70 mm, 76 mm, 83 mm and 95 mm were supplied, of which only the 19 mm, 45 mm and 64 mm were used for this study.

The Par Scientific hot-wire cutter and associated software (Par Scientific A/S, Odense, Denmark) software and was used in the manufacturing process of irregularly-shaped cerrobend cut-outs that were fitted into each of the IORT cones (19 mm, 45 mm and 64 mm). A more detailed description of the process is presented in section 7.1.

4.2 Measurements

For commissioning purposes, central axis percentage depth doses (PDDs) and profiles at a variety of depths were obtained for the $10x10$ cm open and $5\ cm$ circle standard applicators utilising the MP3 therapy beam analyser (PTW, Freiburg, Germany) which is controlled by the Mephysto mc^2 version 2.0 software. The waterproof Pinpoint ionisation chamber (PTW type 31006, Freiburg, Germany) with a measuring volume of 0.015 cm^3 was used as the field

chamber to minimise errors due to the small fields used in this study. The chamber wall is composed of 0.56 mm of Poly-Methylmethacrylate ($C_5H_8O_2$) and 0.15 mm of graphite (C) with densities of 1.19 g/cm^3 and 1.82 g/cm^3 respectively. The steel electrode is 0.18 mm in diameter and 4.5 mm in length. The chamber is specifically designed for relative measurements of small radiation fields. The semi-flex chamber (PTW type 31010, Freiburg, Germany) with a nominal sensitive volume of 0.125 cm^3 was used as the reference chamber and was placed at the corner of the last scraper of the applicator *(figure 4.1)*.

Although utilising parallel-plate chambers is widely recommended for obtaining PDDs *(Almond et al 1999, IAEA 2000, Thwaites et al 2003),* the cylindrical pinpoint chamber may be used with the inclusion of a correction for the effective point of measurement *(Das et al 2003, IAEA 2000)*. It is also recommended *(Das et al 2008)* that small field profiles (≤ 4 cm x 4 cm) similar to some of the beams used in this study should be measured with micro-chambers such as stereotactic field diodes or pinpoint chambers.

The effective point of measurement for cylindrical chambers *(IAEA 1997, IAEA 2000, Das et al 2003)* is situated closer to the source by a distance of (0.5 * r_{cyl}), where r_{cyl} is the radius of the chamber cavity. Based on the fact that the cavity diameter for the pinpoint chamber is 2 mm, the chamber axis was set to coincide with the water surface, moved deeper into the water by 0.5 mm and then zeroed so that the effective point of measurement coincided with the water surface. This point was used as the zero reference depth for all PDD and profile scans.

Due to the chamber wall being made of material different in density to the phantom material (water), attenuation of the charged particle electron beam by the wall would differ from the attenuation of the beam by the same thickness of water *(IAEA 2000)*. Using the PMMA and graphite densities, the difference between the water-equivalent thickness of the wall and the phantom is calculated to be 0.23 mm. Since the required adjustment is small and may be

neglected *(IAEA 2000)*, the water-equivalent thickness of the wall was not taken into account when performing the PDD and profile measurements. Implications of this omission will be discussed later.

The PDD scans were performed from depth to surface with step sizes of 1 mm and a scan speed of 2 mm/s. The step sizes for the beam profile scans were 2 mm with a scan speed of 2 mm/s. The delay time and sampling time was set as 0.2 s for both the PDD and profile scans. The step sizes were chosen as such so that the measured data points corresponded to the MC data points which is defined by the voxel dimensions in DOSXYZnrc *(section 5.2.1)*.

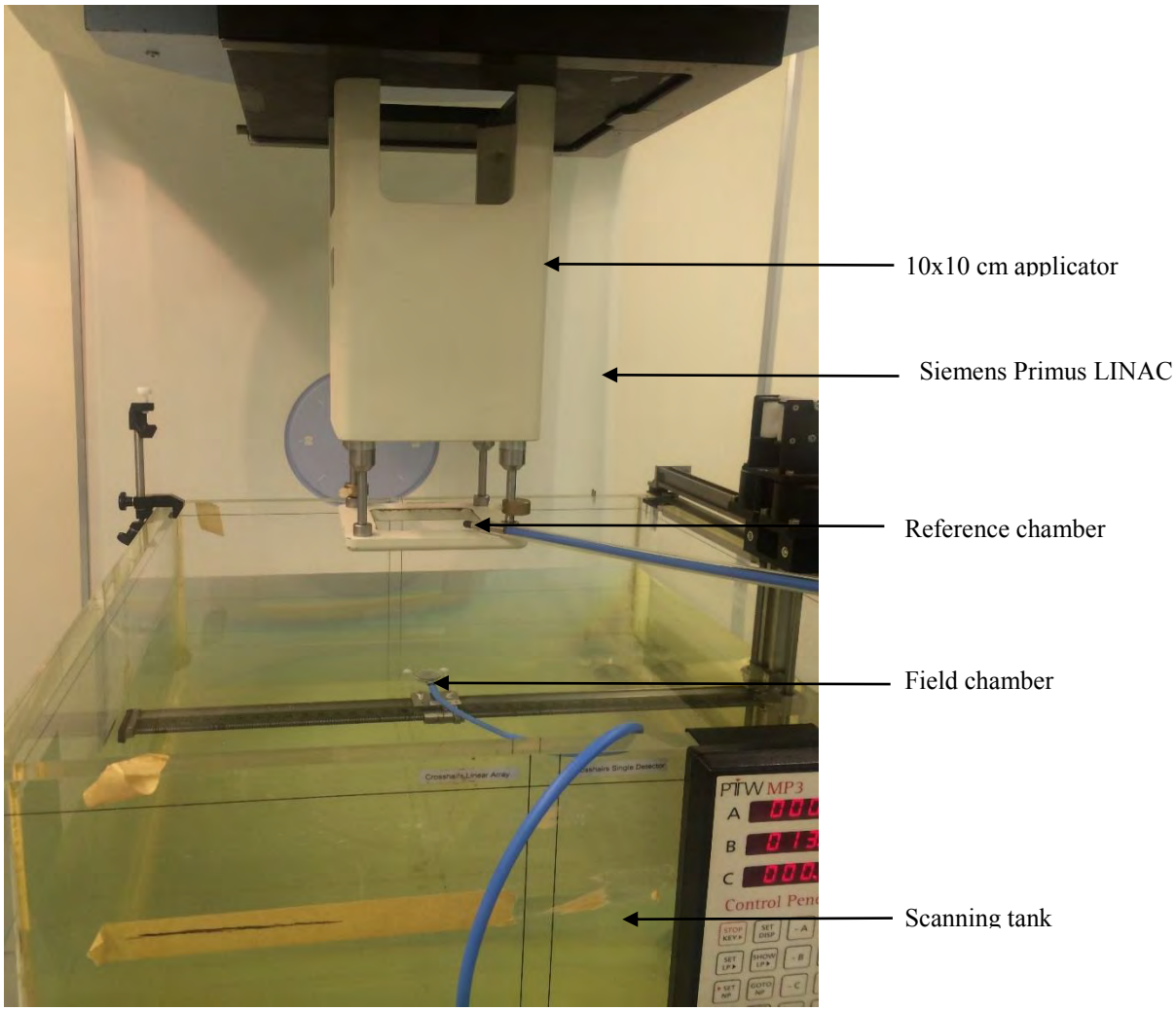

Figure 4.1 Measurement set-up for electron PDD and profile acquisition from the Siemens Primus LINAC for the $10x10\ cm$ applicator using the PTW MP3 therapy beam analyser.

The gantry was set to 0° with the central axis of the beam directed along the geometrical centre of the water tank. The $10x10$ cm standard and 5 cm circle applicators were used with the applicator end at 95 cm from the source (100 cm SSD, 5 cm air gap).

The resulting PDDs and profiles were smoothed using the three-point algorithm inherent in Mephysto and the PDDs were converted from ionisation to dose using the IAEA TRS398 stopping power ratios before being exported to an Excel spreadsheet. The data was then incorporated in separate files readable by the Verisoft version 4.2 software (PTW, Freiburg, Germany).

The Y jaws and MLC (X jaws) symmetric field sizes were set to 19.0 cm for the $10\,x10$ cm applicator and 13.0 cm for the 5 cm circle applicator, which are the default field sizes for each applicator. The default jaw size is larger than the field size defined by the applicator so as to reduce the variation of secondary collimator scatter.

The depths for profile measurements were selected so that they covered a range from near-R_{100} to approximately R_{50} for each of the energies:

The data was then incorporated into a file in .mcc format so that it could be read by the Verisoft software for evaluation and analysis *(figure 4.3)*. Each 1-D data set was copied to 2 off axis distances symmetric about the central axis, since Verisoft requires a 2-D matrix in its input files for data comparison.

PDDs and profiles were similarly obtained and analysed with each of the three IORT open cones in place.

The cut-outs were then inserted into the same cones (19 mm, 45 mm and 64 mm) and PDDs and profiles were once again obtained and analysed as above.

Measured applicator factor *(section 5.4.2.3)*, cone factors *(section 6.3.3)* and cut-out factors *(section 7.5.3)* were obtained using Electron Dosimetry Diode E (PTW type T60017, Freiburg, Germany) in the MP1 tank (PTW, Freiburg, Germany).

Absolute dosimetry *(section 5.3.1)* was performed in the MP1 tank using the waterproof Advanced Markus ionisation chamber (PTW type 34045, Freiburg, Germany) with a measuring volume of 0.02 cm^3. The chamber was cross calibrated with the 0.6 cm^3 Farmer Chamber (PTW type 30013, Freiburg, Germany) with traceable calibration performed at the National Metrology Institute of South Africa (NMISA) standards laboratory. The dose-rate (cGy/MU) was obtained for each beam used in this study.

4.3 Monte-Carlo Simulations

The openSuse 13.1 Linux operating system was installed on a Dell Inspiron laptop with 2nd generation Intel Core i7 dual quad core processors of 2.20 GHz. This meant that up to 8 Monte Carlo simulations could be independently run, one with each processor. The EGSnrc Monte Carlo Code system was then installed on the system and used to perform simulations.

4.3.1 EGSnrc

The original Electron-Gamma Shower (EGS) code system for Monte Carlo simulation of the coupled transport of electrons and photons was developed by Walter Ralph Nelson and Richard Ford of the Stanford Linear Accelerator Centre (SLAC) in the mid 1970's (*Rogers et al 1995)*.

The system is a general purpose package for the Monte Carlo simulation of the coupled transport of electrons and photons with energies ranging from a few keV up to 100 GeV. (*Rogers et al 1995)*.

A collaboration in the eighties between the National Research Council of Canada (NRC) and SLAC led to EGS being capable of functioning in the energy range of 10 keV to 50 MeV, which is the energy range of interest in Medical Physics. EGSnrc is currently maintained by the Ionisation Radiation Standards Group at the NRC and is the code system used in this report.

One of the user codes of the EGSnrc system is BEAMnrc, which has built-in Component Modules (CMs) that provide the ability to model complex geometries of the treatment head of Linear Accelerators. There are also several CMs available as part of the code to build accessories such as applicators and beam modifiers (eg alloy cut-outs). Specifying the z coordinate of the start of each CM ensures that their relative positions along the beam axis are maintained. Input of the details of each component is facilitated by the BEAMnrc Graphical User Interface (GUI).

EGSnrc was used for this study for a variety of reasons. It is the most widely published and used MC code for modelling medical linear accelerators. It has been extensively benchmarked and has been used to model all types of commercially available LINACs. The component modules available in the code make it possible to model all the treatment head components accurately. The users have the option of writing their own code for component modules that do not exist as part of the original system. The graphical user interfaces available make for a comfortable user-friendly environment.

EGSnrc is therefore an all-encompassing Monte Carlo code system that accurately deals with the real physics involved in radiation transport and provides an efficient and effective method of building and modelling linear accelerators being investigated.

4.3.2 PEGS4

PEGS4 is a Pre-processor code for EGS (*Nelson et al 1985)* which produces the cross section data for BEAMnrc. Data in the existing distribution of PEGS4 were based on density effect corrections in ICRU report 37.

The alloy used for the cut-outs did not exist in the existing PEGS4 data files. The production of cross section data for the alloy was facilitated by using the EGSnrc_MP (EGSnrc multi-platform) GUI *(figure 4.2),* which simplified the process spelt out in the SLAC265 document *(Nelson et al 1985)*.

Material specification options of element, compound and mixture *(Kawrakow & Rogers 2003)* are available. The mixture option was chosen for the alloy, whereby relative atomic proportions are given by weight. The mass density in g/cm^3 as well as values of AE and AP were needed as inputs. UE and UP are used to define the upper energy limits for the interval over which electrons and photons are transported, resulting in the electron energy interval (AE,UE) and photon energy interval (AP,UP). The data subsequently created was appended to an existing PEGS4 data set. *(Kawrakow & Rogers 2003, Nelson et al 1985)*

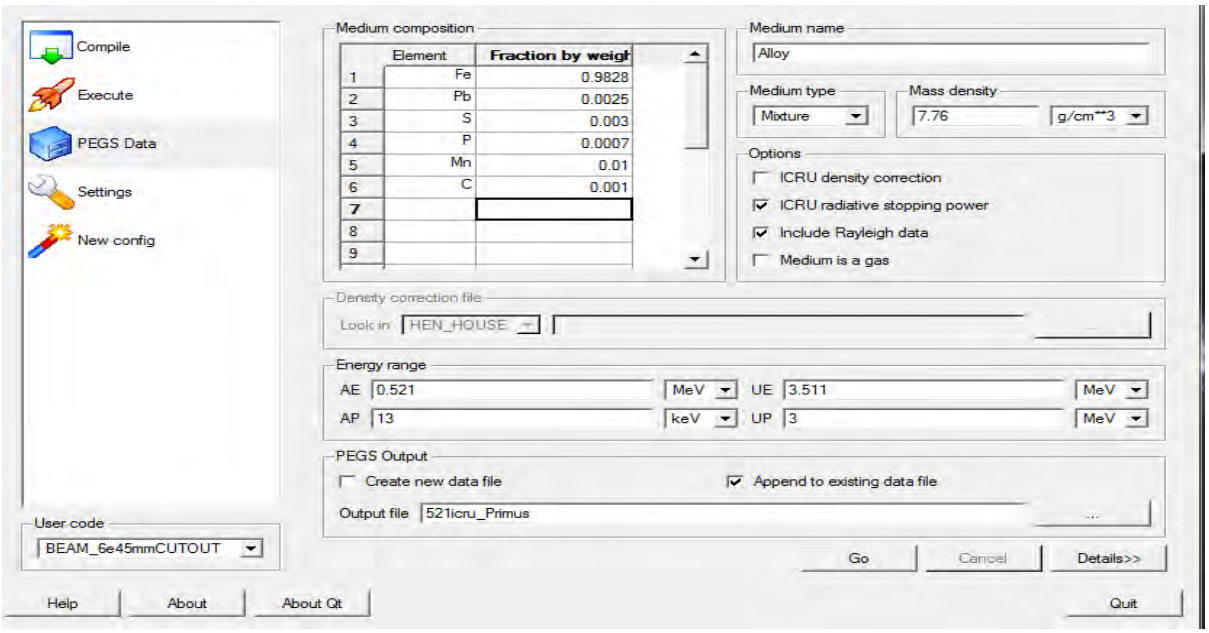

Figure 4.2 PEGS4 Graphical User Interface (GUI)

4.3.3 Variance Reduction

In the migration from the BEAM MC code system *(Rogers et al 1995)* to BEAMnrc, the method of estimating the uncertainty in dose and fluence calculations was changed from splitting calculations into statistical batches to implementation of a history by history method. In this method, an estimator s^2 of the true variance σ^2 for the scored quantity (eg dose) may be written as *(Walters et al 2002)*:

$$s^2 = \frac{1}{N-1}\left(\frac{\sum_{i=1}^{N} X_i^2}{N} - \left(\frac{\sum_{i=1}^{N} X_i}{N}\right)^2\right) \quad (5.1)$$

where X_i is the quantity scored for history *i,* and N is the number of histories.

This implies that

$$s^2 \propto \frac{1}{\sqrt{N}} \quad (5.2)$$

This means that in order to reduce the variance by half, the number of histories must increase by a factor of 4.

The efficiency of a MC simulation may be defined as *(Kawrakow & Fippel 2000, Ali & Rogers 2007)*

$$\in = \frac{1}{T\,s^2} \quad (5.3)$$

where T is the time taken for a simulation and s^2 is the variance.

Since both Ns^2 and T/N are almost constant, the efficiency is roughly independent of the number of histories simulated. According to equation 5.3, increasing the efficiency would mean that Ts^2 has increased, implying that the time to achieve a given variance has decreased, or the variance achieved in a given time has been reduced. Techniques employed to achieve this are known as variance reduction techniques *(Rogers et al 1995)* which are designed to increase efficiency by not necessarily reducing the variance, but by reducing the time to achieve the same variance.

Variance reduction techniques that may be employed in the code are discussed below. The latter two, although not applicable to electron transport focussed on in this study, were included for completeness sake.

4.3.3.1 Electron Range Rejection

Electron range rejection is one of the variance reduction techniques *(Rogers et al 1995)* that saves computational time. The code calculates the residual range of the electron. If the electron cannot leave a region with energy greater that the cut-off energy ECUT, the history is terminated and the energy is deposited locally. The problem with this is that the electron could still have produced bremsstrahlung photons that would now not exist if the electron history is terminated by the range rejection technique *(Rogers et al 1995)*. To minimise the effect of this approximation, an energy threshold, ESAVE, is specified by the user and the histories of particles that have energies higher than ESAVE are not terminated. The higher energy electrons may then still produce bremsstrahlung photons that leave the region even if the electrons in question do not.

4.3.3.2 Bremsstrahlung splitting

If bremsstrahlung splitting is selected as a variance reduction technique, an approximation of the angular distribution of the bremsstrahlung photons created by electron interactions is made. Justification for using the approximation is that at high energies, the angular distribution is peaked in the forward direction and will not affect the results in a significant manner. At low energies, the photon distribution will be negligible with respect to the multiple scattering of the electron striking the material. When bremsstrahlung splitting is switched on, user-defined splitting factors are requested. It has been shown that optimal selection of splitting factors can reduce computational time by a factor of 4.

4.3.3.3 Photon forcing

Photon interactions are minimal in low density materials or in thin slabs of any material. In order to improve statistics of scattered photons, the user has the option of forcing photons to interact in specified component modules. The user is required to input the first and last CM in which photon interactions must be forced.

4.3.4 Monte Carlo data acquisition

BEAMnrc was utilised to model the LINAC for the $10\,x10$ cm standard applicator. This formed the initial part of the commissioning process.

DOSXYZnrc *(section 5.2)* was used to calculate 3D dose distributions in a voxel-based phantom using the individual phase space files obtained from the BEAMnrc simulations as the source.

The BEAMDP (beam data processing) programme was used to extract spectral distributions from the simulations.

The MCSHOW programme was used to extract 3D dose distributions from the DOSXYZnrc simulations of the standard $10\ x\ 10\ cm$.

The PDDs and profiles were displayed in the Grace plotting programme and the individual data points were exported to an excel spreadsheet.

The data was then incorporated in separate files readable by the Verisoft software.

The energy spectra describing each of the sources comprised 5 energy bins each with varying relative intensities. The relative intensities were adjusted *(section 5.1.4.1)* until the measured and MC-produced PDDs and profiles satisfied the GI criteria set.

Once acceptable comparisons *(section 4.4)* were obtained between measurements and calculations for the $10\ x\ 10\ cm$ applicator, the identical workflow above was used to obtain the PDDs and profiles for the $5\ cm$ circle in order to complete the commissioning process.

The accepted incident electron energy spectra was used as input for each of the energies modelled.

The 19 mm, 45 mm and 64 mm IORT open cones were then modelled in BEAMnrc and resulting dose distributions were obtained using DOSXYZnrc. The same data-extraction tools (MCSHOW, Grace, Excel and Verisoft) were used to obtain and analyse the results for the IORT open cones *(section 6.3)*.

The manufactured cut-outs for the 19 mm, 45 mm and 64 mm cones *(section 4.1 and 7.1)* were similarly modelled and simulated utilising BEAMnrc and DOSXYZnrc. Data extraction was performed in the same manner as for the open cones.

Monte Carlo-calculated output factors were obtained by analysing the 3-D dose distributions in STATDOSE *(McGowan et al 2007)*. The absorbed dose in the voxel at d_{max} for each of the beams evaluated in this study was obtained and the applicator output factor ($5\,cm$ circle standard applicator), cone factors (19 mm, 45 mm and 64 mm IORT open cones) and cut-out factors (19 mm, 45 mm and 64 mm IORT cones with cut-outs) were determined by relating these doses to the MC-calculated dose at d_{max} for the $10x10\ cm$ applicator.

The simulation of 10^7 histories in BEAMnrc and 1.2 x 10^8 histories in DOSXYZnrc for all simulations were deemed to be sufficient to reduce the statistical variance of all MC calculations to below 1% *(du Plessis et al 2001, Sempau et al 2001, Walters et al 2002, Walters et al 2005)*. Latent variance in the phase space files was therefore not an issue *(Sempau et al 2001)*.

4.4 Comparison between measuremets and MC-calculated data

4.4.1 Gamma index evaluation method

In order to commission the Monte Carlo based treatment planning system being developed, differences between the measured and MC-calculated dose distributions are essential. A qualitative evaluation may be obtained by superimposing the measured and calculated isodose distributions. The maximum dose differences exhibited in regions of highest disagreements may be used to evaluate the accuracy of the calculation method prior to acceptance *(Low et al 1998)*.

In low dose gradient regions dose differences may be calculated by direct comparison and the calculation method may be deemed to be acceptable *(Harms et al 1998)* if the differences satisfy a user-defined tolerance level which depends on the level of accuracy required. However, large disagreements in the penumbral regions, where the dose gradients are high, may easily be seen for small insignificant spatial errors in either the measured or calculated data *(van Dyk et al 1993)*. It is therefore essential that a more rigid quantitative method of evaluation be employed to ascertain the suitability of the calculation method being proposed *(Bakai et al 2003, Depuydt et al 2002)*.

In an attempt to find a solution to this problem, a method called the GI method *(Low et al 1998)* was introduced. The concept of Distance to Agreement (DTA) was introduced to assist in performing this evaluation function efficiently. The DTA is the distance between a measured data point and the nearest point in the calculated dose distribution that has exactly the same dose value. Analagously, dose difference refers to the absolute difference in dose at the same spatial point in the measured and calculated data sets. The dose difference and DTA evaluation methods are used in a complementary fashion to quantitatively evaluate the acceptability of the dose calculation method. In the earlier analysis methods *(Harms et al*

1998), points that fail set criteria for both the dose difference and DTA were displayed as fail, implying that the two individual quantities were not displayed independently.

The GI evaluation technique introduced by Low provides a numerical value related to the pass/fail criteria set. It gives an indication of the measure of disagreement in the regions that fails the set acceptance criteria and also gives a measure of agreement in regions that pass the set criteria. The suitability of the calculation method may then be easily evaluated from a graphical display *(figure 4.3).*

As pointed out below *(section 5.4.2)*, if 3-D dose distributions are required, PDDs, central axis profiles and off-axis profiles must be obtained so that the beam may be characterised accurately in 3 dimensions. This study focusses on the comparison of measured and calculated PDDs and central axis profiles for each beam which are essentially one-dimensional in nature. PDDs are obtained by measuring dose along the depth (z) axis whilst profiles are obtained by measuring along either the x or y axis perpendicular to the beam. The theory associated with determining the GI when comparing measured and calculated data is therefore reserved to the 1-dimensional case in the explanation below *(Jiang et al 2006, Low et al 1998, Harms et al 1998)*.

The objective of the evaluation method is to quantify the differences between a measured dose distribution D_m and a calculated dose distribution D_c *(figure 5.13)*. The measured data is used as the reference data. At a comparison point x, the measured data has a dose value $D_m\ (x)$ and the calculated data has a dose value $D_c\ (x)$. Comparisons performed in both the spatial and dose domains consider this single measured dose value $D_m\ (x)$ relative to all calculated points in the neighbourhood of $D_m\ (x)$ to see if the agreement is within a user-specified tolerance. The horizontal axis indicates the spatial location x, the vertical axis is the dose axis D, and the origin is the point $(x, D_m\ (x))$.

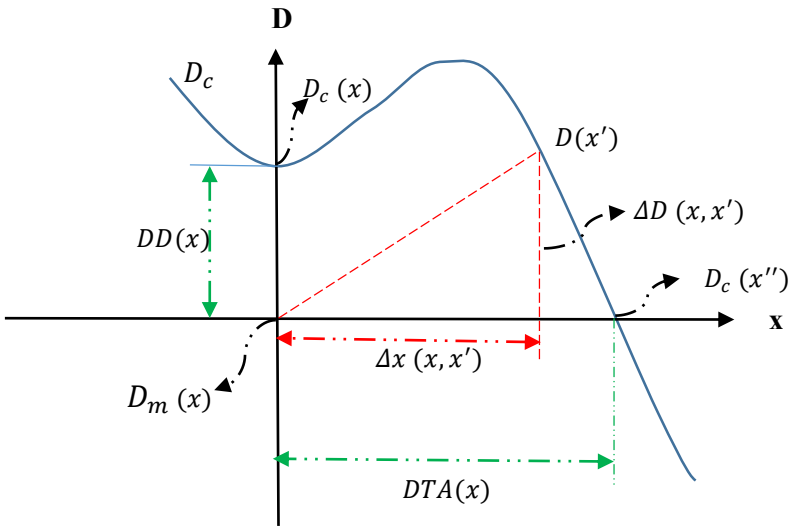

Figure 4.3 Illustration of variables used to define the GI. D_c represents the calculated curve and $D_m\ (x)$ represents the comparison point of the measured curve *(Redesigned from Jiang et al 2006)*.

The difference between the calculated dose at an arbitrary point x′ on the calculated curve and the measured dose value at the comparison point x is

$$\Delta D\ (x,\ x')\ =\ D_c\ (\ x'\ )\ -\ D_m\ (x) \tag{5.4}$$

The dose difference between the measured and calculated distributions at the comparison point x (i.e. $x'= x$) is given by

$$DD(x)\ =\ D_c\ (x)\ -\ D_m\ (x) \tag{5.5}$$

The spatial distance between an arbitrary point x′ on the calculated curve and the comparison point x is

$$\Delta x\ (x, x')\ =\ |\ x'\ -\ x| \tag{5.6}$$

The closest distance between point x and x'(viz. x'') where the dose at point x is equal to the dose on the calculated curve (i.e. $\Delta D\ (x, x'\ )\ =\ 0$) is defined as the distance to agreement (DTA) and is given by *(Jiang et al 2006)*

$$DTA(x)\ =\ min\ [\Delta x\ (x, x')] \tag{5.7}$$

If $|DD(x)|$ is less than a user-defined dose tolerance δD_0, the comparison satisfies the dose-difference criterion and passes in the dose domain at point x.

If $DTA(x)$ is less than a user-defined spatial tolerance δx_0, the comparison satisfies the distance-to-agreement criterion and passes in the spatial domain at point x.

By first normalising $\Delta D\ (x, x')$ to δD_0 and $\Delta x(x, x')$ to δx_0, the GI at the comparison point x is given by *(Low et al 1998)*

$$\gamma(x) = min_{x'}\left[\sqrt{\left(\frac{\Delta x(x,x')}{\delta x_0}\right)^2 + \left(\frac{\Delta D(x,x')}{\delta D_0}\right)^2}\right] \tag{5.8}$$

For a given δD_0 and δx_0, the comparison passes when $\gamma \leq 1$ and fails when $\gamma > 1$.

The tolerances values used when performing gamma analysis are usually expressed as $\delta x_0 / \delta D_0$ in mm and % respectively (eg 3 mm/3%). Selection of this value is important as it will determine the accepted accuracy of the comparison. The gamma criteria used in this study is 3 mm/3%.

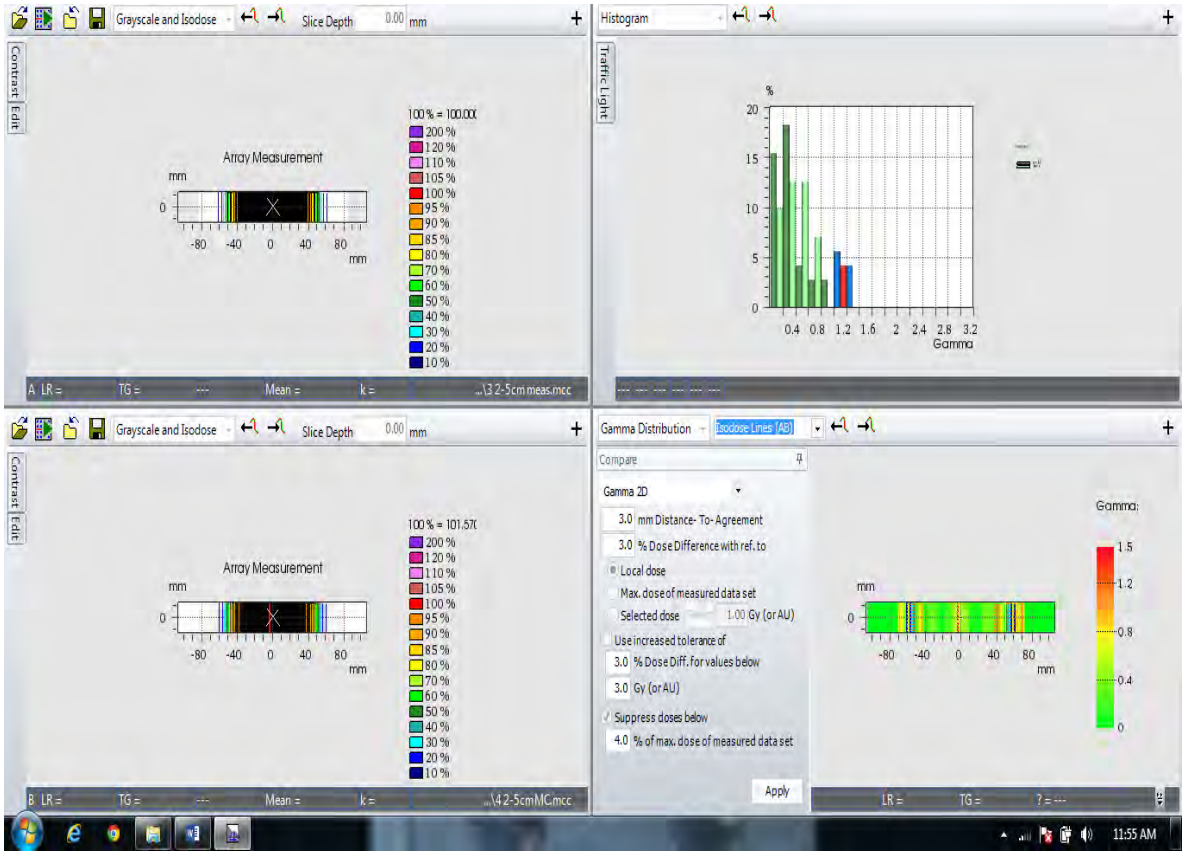

Figure 4.4 Verisoft Graphical User interface (GUI) showing sample input data used for comparison, comparison criteria used and gamma index output histogram

4.4.2 Workflow

The measured and MC data for the PDDs and profiles for the $10x10\ cm$ applicator was compared in Verisoft using the GI evaluation method, with the measured data as the reference data. The initial mono-energetic sources used for each energy in BEAMnrc did not produce favourable comparisons. Poly-energetic sources were then used for each source for each of the energies being investigated. The energy spectra describing each of the sources comprised 5 energy bins each with varying relative intensities. The relative intensities were adjusted *(section 5.1.4.1)* until the measured and MC-produced PDDs and profiles satisfied the GI criteria set.

The accepted incident electron energy spectra was used as input for all further BEAMnrc simulations.

The measured and Monte Carlo-calculated PDDs and profiles for the $5\ cm$ circle *(sections 5.4.2.1 and 5.4.2.2 respectively)*, IORT open cones *(sections 6.3.1 and 6.3.2 respectively)* and IORT cones with cut-outs *(sections 7.5.1 and 7.5.2 respectively)* were compared and analysed in Verisoft using the GI evaluation method inherent in the Verisoft programme.

Direct comparisons of measured and MC-calculated applicator factor *(section 5.4.2.3)* cone factors *(section 6.3.3)* and cut-out factors *(section 7.5.3)* were done and presented in both tabular and graphical forms.

CHAPTER 5

MONTE CARLO COMMISSIONING OF THE LINAC

5.1 BEAMnrc build of the Siemens Primus Linear Accelerator

5.1.1 Introduction

BEAMnrc is a Monte Carlo simulation code that may be used to model medical linear accelerators. In order to accurately model the accelerator, the user must be knowledgeable of the theory behind the various input parameters required *(section 5.1.2 and 5.1.3)* so that appropriate selections are made. An intimate knowledge of the various treatment head components is also required. This includes the exact physical dimensions and compositions of each component as well as their relative positions in space.

Each component may be built by selecting an appropriate Component Module (CM) inherent in the code. Each CM available may be used more than once in the build but must have a unique name. CMs are not allowed to overlap. If the CM is composed of a material not found in the PEGS4 data file, the data for that material may be produced by the user *(section 4.3.2)*.

Phase space data files may be requested at the back of any scoring plane. This PSF may then be used as the input source for the rest of the accelerator build. This feature can greatly reduce computational time e.g. if a variety of applicators are modelled, the PSF at the back of the CM preceding the applicator may be used to complete the modelling for each applicator without having to perform the full simulation for each case (assuming the field sizes are unchanged).

Either mono-energetic or poly-energetic incident particles (electrons, photons or positrons) may be used as the source. Several options for source geometries are provided.

Since the code keeps track of each particles history, separate dose components may be scored for charged particle or photons exclusively, for any CM selected by the user e.g. the dose from electrons scattered off the applicator may be obtained.

5.1.2 Main Input Parameters

Table 5.1 list the main input parameters used for the modelling of the Primus LINAC. If the total energy of the electron falls below the global electron cut-off energy ECUT specified by the user, the electrons history is terminated and the energy is locally deposited. PCUT is the ECUT equivalent for photons. Higher ECUT and PCUT values may be set for individual regions. ECUT = 0.521 MeV and PCUT = 0.01 MeV are recommended for general-purpose LINAC modelling. If the values in these regions are set to be lower than the global values, the global values are used.

Electron range rejection is used to save computing time. This variance reduction technique was turned off for these simulations in order to obtain more accurate results due to the approximations *(section 4.3.3.1)* that are introduced when switched on.

Bremsstrahlung splitting and photon forcing *(sections 4.3.3.2 and 4.3.3.3 respectively)* are variance reduction techniques applicable to photon simulations and were switched off as they were not relevant to this study.

Table 5.1 Main BEAMnrc input parameters

MAIN INPUT PARAMETERS	
Number of histories	10^7
Random number seed 1	33
Random number seed 2	97
Bremsstrahlung splitting	None
Bremsstrahlung cross section enhancement	Off
Global electron cut-off energy ECUT	0.521 MeV
Global photon cut-off energy PCUT	0.01 MeV
Electron range rejection	Off
Photon forcing	Off

5.1.3 EGSnrc parameters

PRESTA (Parameter Reduced Electron Step Transport Algorithm) *(Bielajew & Rogers 1986)* was introduced into the EGS code system to improve the accuracy of modelling of electron transport. PRESTA consists of algorithms that calculate lateral and longitudinal corrections (path-length correction PLC and the lateral correlation algorithm LCA) *(Bielajew & Rogers 1986)* to account for elastic scattering in a CH electron step *(section 3.2.2)*. A boundary crossing algorithm (BCA), which transports electrons more accurately in the vicinity of medium interfaces, was also introduced in PRESTA. The newer more accurate algorithm introduced into EGSnrc was PRESTA II, which is the default.

Options for the boundary crossing algorithm (BCA), which determines how electrons are transported across region boundaries, are either PRESTA I or EXACT. Skin Depth for BCA is defined as the perpendicular distance (in mean free paths) to the region boundary at which the electrons will be transported in single elastic scattering mode *(Bielajew & Rogers 1986)*. If PRESTA I is selected, the LCA is not used if the perpendicular distance of the electron to the boundary is less than the Skin Depth for BCA. As soon as the electron reaches the boundary, a multiple scattering event is forced *(Bielajew & Rogers 1986)*.

If the EXACT BCA is chosen, electrons are transported in single elastic scattering mode as soon as they reach a distance from the boundary defined by the Skin depth for BCA. The default value of 3 mean free paths is recommended to give peak efficiency. If the skin depth for BCA is a very large number, all electrons will be transported in single elastic scattering mode.

If PRESTA II and EXACT are selected, the default maximum step size should be accepted.

For accurate electron transport, it is advised that the value for the maximum fractional energy loss per electron step (ESTEPE) should not exceed 25% and that it not be changed unless the electron step algorithm is PRESTA I.

The maximum first multiple elastic scattering moment per electron step (XIMAX) is approximately half the average multiple scattering angle squared. The default value of 0.5 is recommended.

If spin effects are turned on, elastic scattering cross sections that take into account spin effects are used. Whilst this increases calculation time, it provides more accurate results and is essential for acceptable backscatter calculations *(Rogers et al 2005).*

The emission angle of bremsstrahlung photons is determined by the selection of the bremsstrahlung angular sampling option. The default (Simple) would imply that only the leading term of the Koch and Motz equation *(Bielajew et al 1989)* is used. Using the entire equation is recommended at low energies and does not increase simulation time appreciably *(Rogers et al 2005)*.

The choices of bremsstrahlung cross sections to be used for bremsstrahlung interactions has negligible difference for energies >10 MeV.

The pair angular sampling method option determines the method used in sampling the electron/positron emission angles (relative to the incoming photon) in a pair production event.

The cross-sectional data used for pair production may also be chosen.

The photoelectron angular sampling input signifies the sampling method used to determine the angle of emission of the photoelectrons. If switched off, the photoelectron is emitted in the direction of the incident photon.

Rayleigh scattering need only be simulated for energies less than 1 MeV whilst atomic relaxations need only be used for low energy applications *(Rogers et al 2005)*.

Table 5.2 EGSnrc input parameters

EGSnrc PARAMETERS	
Maximum step size	1e10
Maximum fractional energy loss per step	0.25 cm
XImax	0.5
Boundary Crossing Algorithm (BCA)	Exact
Skin depth for BCA	3
Electron Step algorithm	PRESTA II
Spin effects	Off
Electron impact ionisation	Off
Bremsstrahlung angular sampling	Simple
Bremsstrahlumg cross sections	Bethe Heitler
Bound Compton scattering	Off
Compton cross sections	Off
Pair angular sampling	Simple
Pair cross sections	Bethe Heitler
Photoelectron angular sampling	Off
Rayleigh scattering	Off
Atomic relaxations	Off
Photon cross sections	Si
Photon cross section output	Off

5.1.4 LINAC head components

A full schematic diagram of all the components of the treatment head detailing their relative positions is given in figure 5.9.

5.1.4.1 Source

A parallel circular beam (option Source = 0) incident from the front of the first component of the accelerator head was used for input of a poly-energetic electron source for the BEAMnrc user code. Values of 0.1 cm and (0, 0, 1) were used for the source diameter and the (x, y, z) direction cosines respectively.

The parameters and format of the file defining the energy spectrum are as follows:

SPEC_TITLE
NENSRC, ENMIN, IMODE
ENSRCD(i), SRCPDF(i)

Where SPEC_TITLE is the spectrum title,

NENSRC is the number of energy bins in the spectrum,

ENMIN is the lower energy of the first bin,

IMODE is set to 0 for histogram counts/bin and set to 1 for counts/MeV,

ENSRCD(i) is the upper energy (MeV) of bin (i)

SRCPDF(i) is the probability of finding a particle in bin (i)

It was not necessary to normalise SRCPDF(i). The energies of the incident particles are randomly distributed across each energy bin by BEAMnrc.

The energy spectra describing the source for 6, 12 and 18 MeV beams had 5 energy bins each with varying relative intensities. The energy bins ranged from 6.75 MeV to 8.5 MeV for the 6 MeV source, 11.2 MeV to 16.4 MeV for the 12 MeV source and 17.2 MeV to 23.5 MeV for the 18 MeV source. These values were obtained by varying the relative intensities of the energy bins until acceptable PDD comparisons were obtained with the measured data. Similar approaches were used in other studies *(Antolak et al 2002, Verhaegen et al 2001)* whereby an improved calculated guess was made to determine the incident electron energy spectra based on comparisons of resulting R_{50} and R_p values.

5.1.4.2 Primary Scattering Foil

The primary scattering foil is responsible for spreading out the narrow pencil beam of electrons that exit the window of the accelerator tube. It is also responsible for obtaining a uniform electron fluence across the treatment field *(Karzmark 1993)*. Whilst most of the electrons are scattered, a small fraction does interact with the primary scattering foil producing bremsstrahlung, which results in x-ray contamination of the electron beam *(Karzmark 1993)*.

The FLATFILT CM was used to build the primary scattering foil. This CM provides the ability to model treatment head components that consist of coaxial cones by specifying the top and bottom radii and material composition of each cone. It is also possible to have more than one cone at each z level, with z denoting the distance from the source.

The dimensions of the primary scattering foil differ for each energy for this LINAC model and consist of various combinations of brass, lead alloy, and gold. For each energy, the foil consists of 4 layers with 3 conical sections in the 3rd layer and 2 conical sections in the other layers. The electron and photon cut-off energies for this CM were set to 0.521 MeV and 0.01 MeV respectively. Diagrams of this component, as built in BEAMnrc for each energy, appear below.

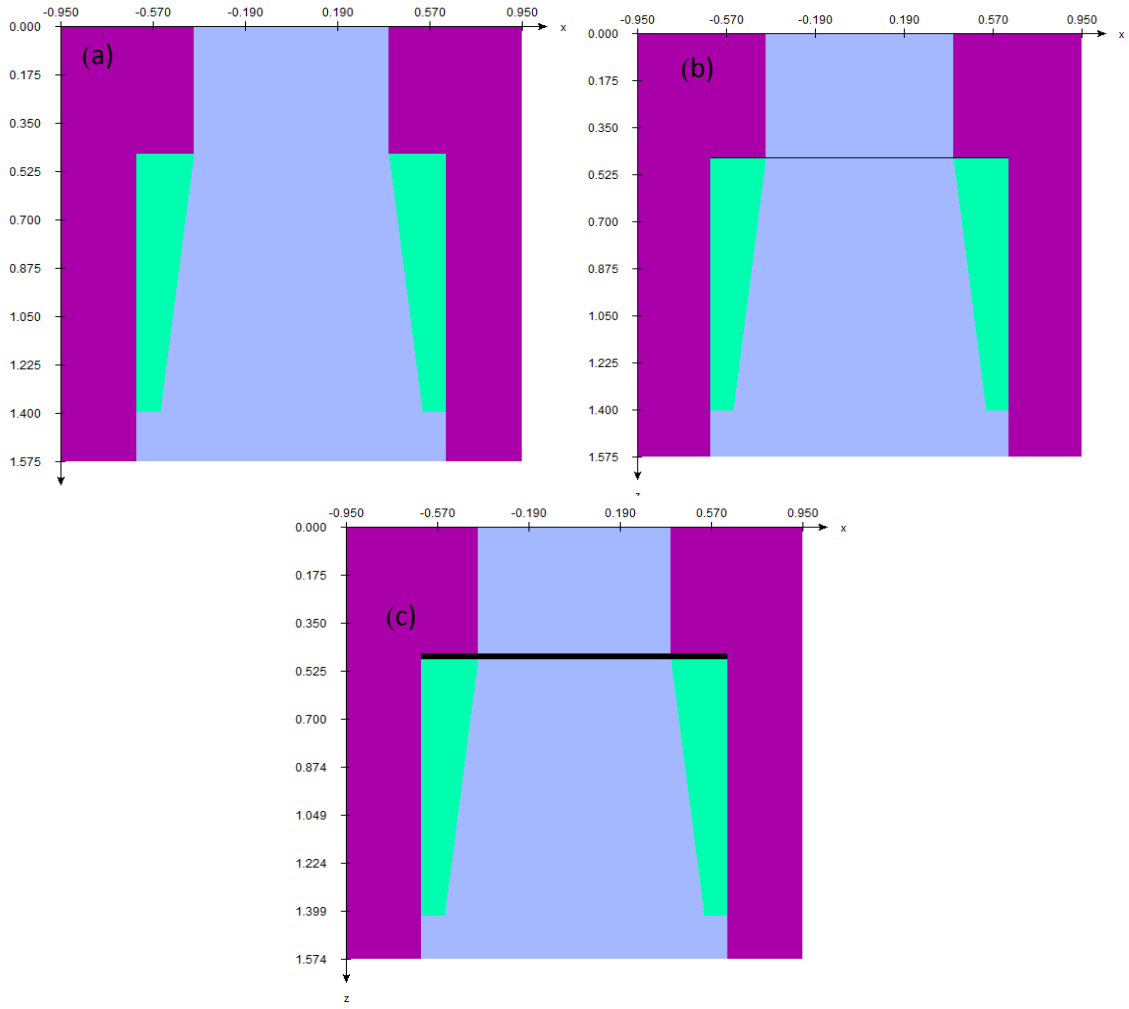

Figure 5.1. Primary scattering foil for (a) 6 MeV (b) 12 MeV and (c) 18 MeV

5.1.4.3 Primary Collimator

The fixed primary collimator defines a maximum circular field by collimating the beam scattered by the primary scattering foil. The FLATFILT CM was used to build the primary collimator, which consists of 6 layers of tungsten with 2 conical sections in each layer. The code requires cylindrical symmetry if the FLATFILT CM is used, which makes the outer

boundaries circular instead of rectangular. The differences are insignificant since the outer boundaries make no difference to the treatment area. The electron and photon cut-off energies for this CM were set to 0.521 MeV and 0.01 MeV respectively.

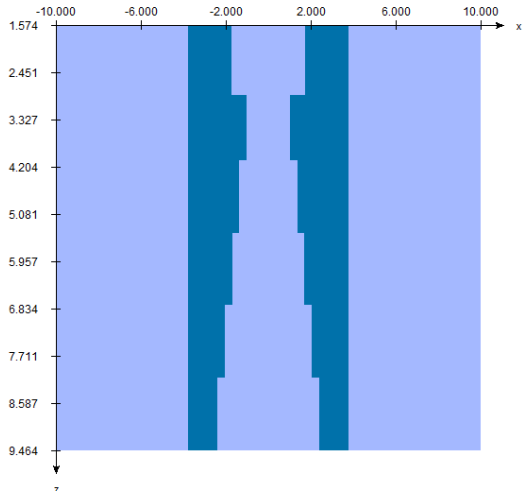

Figure 5.2 Primary Collimator

5.1.4.4 Secondary Scattering Foil

The secondary scattering foil scatters the beam further and may produce more bremsstrahlung. The FLATFILT CM was used for the secondary scattering foil, which consist of 5 layers with 2 conical sections in the top and bottom layers and 3 conical sections in the middle layers. The same foil is used for all the electron energies and are composed of aluminium and Kapton. The electron and photon cut-off energies for this CM were set to 0.521 MeV and 0.01 MeV respectively.

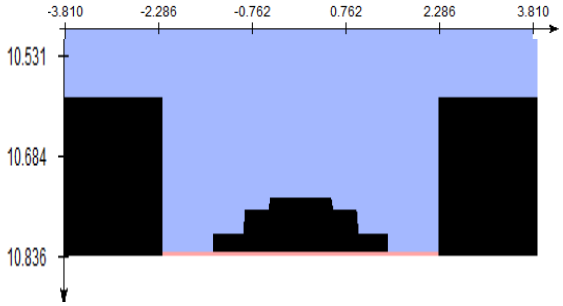

Figure 5.3 Secondary Scattering Foil

5.1.4.5 Chamber

The dose monitoring chamber consist of several ion chambers that monitor electron dose rate and field flatness and symmetry in the transverse and radial directions. The chamber is sealed

and is not affected by temperature and pressure changes. BEAMnrc allows the direct calculation of charge in the chamber.

The CHAMBER CM, which has cylindrical symmetry, defines this treatment head component. Use of only the central region of this CM is necessary to model the chamber for this LINAC. Subsequent to input of the inner and outer radii of the chamber wall and the inner radius of the container wall, each of the 17 layers are defined by their thickness (in the z direction). The chamber is composed of gold and kapton. The electron and photon cut-off energies for this CM were set to 0.521 MeV and 0.01 MeV respectively.

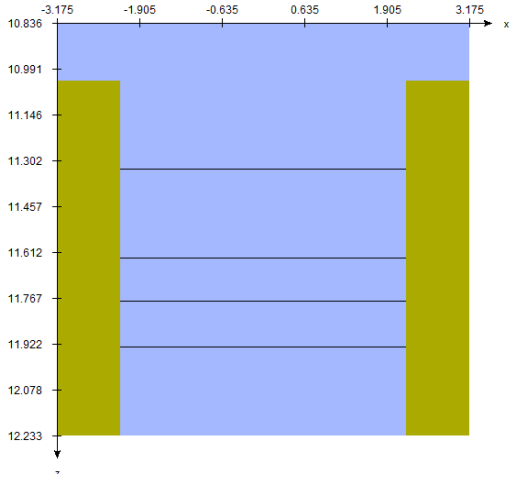

Figure 5.4 Chamber

5.1.4.6 Mirror

A field-defining light is produced by a light source striking a highly polished mirror placed at 45° to the beam axis. The light field illuminates an area defined by the adjustable jaw and MLC *(section 5.1.4.7 and section 5.1.4.8)* so that the coincident radiation treatment area may be visible on the patient prior to turning the beam on. This aids in accurate setup of the patient so that the radiation field will be delivered in the desired position.

Replication of the mirror in BEAMnrc is accomplished using the MIRROR CM and by defining the x and z coordinates at the top and bottom of the mirror, as well as the 2 materials that the mirror is composed of. It is aligned along the gun-target axis (in-plane) and tilts

towards the gun. The electron and photon cut-off energies for this CM were set to 0.521 MeV and 0.01 MeV respectively.

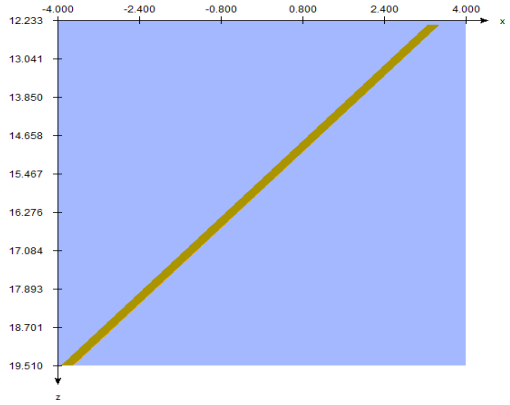

Figure 5.5 Mirror

5.1.4.7 Y Collimator

The beam is further collimated by a moveable pair of upper Y jaws, the opening of which is set by the operator. The opening projects a field along the Y axis at the isocentre that ranges from 0 to 40 cm. Assymetric jaw setting are also possible with each jaw pivoting on two linear tracks with both jaws coincident with the beam central axis when set at 0 cm.

The JAWS CM is used to define the Y collimator, which consists of a single pair of bars that define the field size in the y direction. The collimator is specified by input of the y and z coordinate at the top and at the bottom of each bar. The y coordinates used define a field size, symmetric about the z axis, of 19.0 cm at 100 cm source-to-isocentre distance, which is the default jaw size for the $10x10$ cm applicator. The jaws are composed of tungsten. The electron and photon cut-off energies for this CM were set to 0.521 MeV and 0.01 MeV respectively.

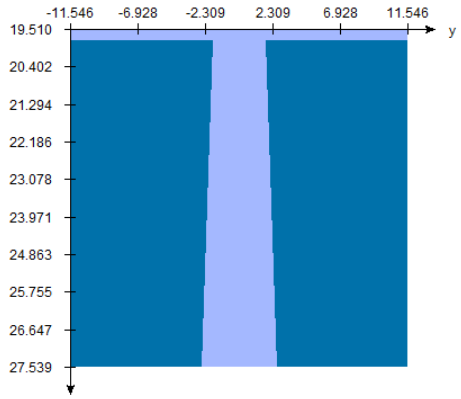

Figure 5.6 Y Collimator

5.1.4.8 Multi-leaf Collimator (MLC)

There are no X collimators on the Siemens Primus LINAC as collimation along this axis is performed purely by the multi-leaf collimator. The MLC consists of 29 Tungsten blades/leaves on each bank, all of which move along a concentric arc. Its presence creates the possibility of providing irregularly shaped treatment fields by moving each leaf independently to a desired position. The MLC resolution in this LINAC is 1 cm at isocentre.

The MLC CM is used to define the multi-leaf collimator. The number, thickness and total width of the leaves is required as input parameters. The x coordinate used for each leaf position defines a symmetric field size of 19.0 cm at 100 cm SSD, which is the default field size for the $10x10\ cm$ applicator. The CM also provides the ability to set each leaf position independently so that arbitrary field shapes in the x direction may be modelled. Input of the z focus ensures correct divergence of the inner portion of the leaves. The electron and photon cut-off energies for this CM were set to 0.521 MeV and 0.01 MeV respectively.

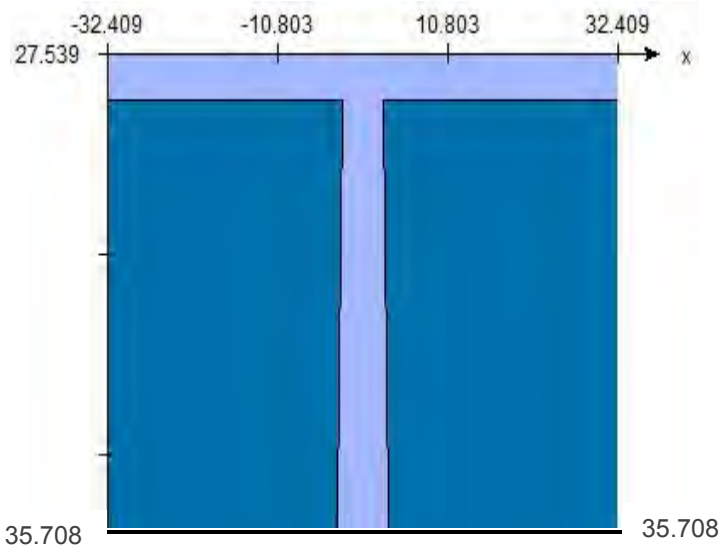

Figure 5.7 Multi-leaf Collimator (MLC)

5.1.4.9 $10x10\ cm$ Applicator

Due to the extensive scattering of electrons in air, it is necessary to collimate the beam in close proximity to the skin surface. The bottom of the MLC ends at approximately 35.6 cm, which implies that there is an air gap of approximately 64.4 cm before the electrons reach the patient (100 cm SSD). Collimation of the electron beam is accomplished by the inclusion of an applicator, with its top end at 56.0 cm and ending at 95 cm, implying the existence of an air gap of 5 cm.

The $10x10\ cm$ applicator was modelled using the APPLICAT CM. there are 5 scrapers present with the first, second and fourth scraper composed of aluminium, the third scraper composed of stainless steel and the last scraper composed of brass. The following dimensions, together with the z coordinate of bottom of the last scraper, were specified for each of the 5 scrapers present:

Z coordinate of front of scraper; thickness of scraper; half-width of inner opening in x and y directions; width of scraper and material composition.

The electron and photon cut-off energies for this CM were set to 0.521 MeV and 0.01 MeV respectively. A representation of the applicator may be seen in figure 5.8 below.

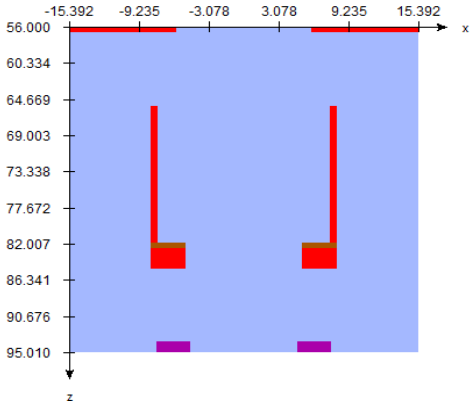

Figure 5.8 10x10 cm Applicator

5.1.5 Phase-space file

A phase-space file (PSF) of a MC simulation can be thought of as the collection of all particles together with all relevant properties of each particle present. The file contains details of the energy, position, direction, charge and history tag for each particle. There can be an arbitrary number of scoring planes requested, with each residing at the back of any component module of the LINAC being modelled. The PSF for the BEAMnrc simulation performed is chosen to be directly below the end of the 10x10 cm applicator (z = 95 cm) *(figure 5.9)*. Some of the main variables defining the properties of the particles produced and/or transported following the interactions of the initial electron source as it traversed the treatment head and exited the end of the 10x10 cm applicator appear in the table 5.3 below *(Capote et al 2006)*.

Table 5.3 Variables associated with the phase-space file

VARIABLE	DESCRIPTION
X	Position in X direction (cm)
Y	Position in Y direction (cm)
Z	Position in Z direction (cm)
U	Direction cosine along X
V	Direction cosine along Y
Sign of W	W=Direction cosine along Z, where $U^2+V^2+W^2=1$
E	Kinetic energy (MeV)
Particle_type	Type of particle
Statistical	Particle statistical weight
Is_new-history	Indicates if particle belongs to a new history

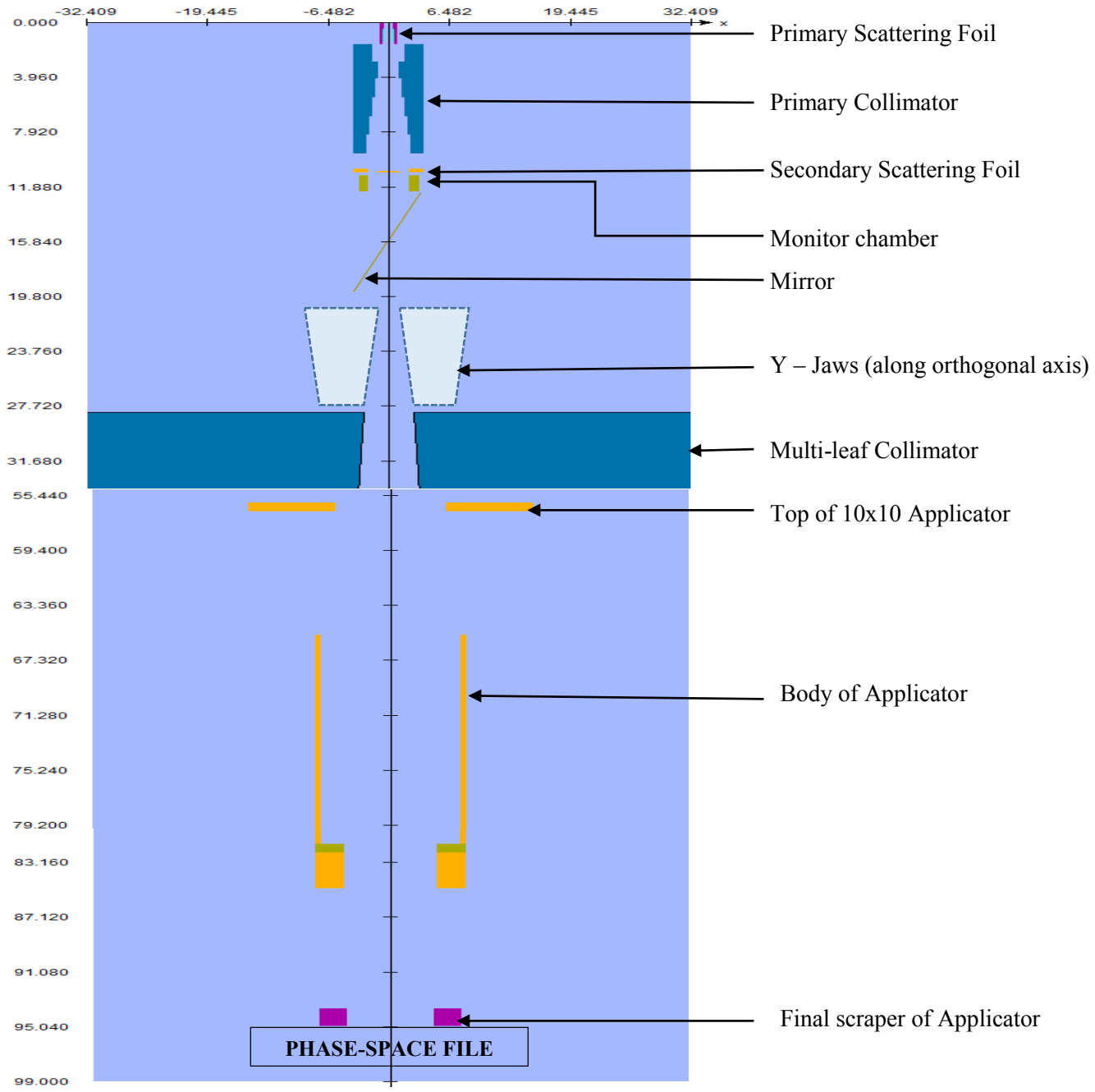

Figure 5.9 The complete Primus LINAC detailing the position of each component of the treatment head together with the $10x10$ cm applicator and phase-space file position

5.1.6 Energy spectra analysis

5.1.6.1 Input parameters

The spectral distributions for the 6, 12 and 18 MeV electron beams for the $10x10$ cm applicator was derived using the BEAM Data Processor (BEAMDP) programme, which was

originally developed for the Ottawa Madison Electron Gamma Algorithm (OMEGA) project. *(Rogers et al 2005).*

The PSF files at the end of the applicator for each energy is used as input for BEAMDP. 50 energy bins (N_{bin}) within a spatial annular region of R_{min} to R_{max} of 0 to 20 were used for the analysis. The kinetic energy ranges selected were E_{min} = 0 and E_{max} = 9 MeV, 16 MeV and 25 MeV for the 6 MeV, 12 MeV and 18 MeV beams respectively. E_{max} was chosen to be greater than the maximum energy of the particles in the phase-space data for each energy. Real estimated fluence (and not planar fluence) was scored. This ensured that the angle at which the particle strikes the scoring plane is taken into account. This is accomplished by dividing each particle weight by cos(θ), where θ is the angle at which the particle strikes the scoring plane. If θ > 85°, cos(85°) is used to avoid division by 0 for angles close to 90° *(Ma & Rogers 2005)*

5.1.6.2 Results

The data for the electron (I_Q = -1) and photon (I_Q = 0) spectral distributions for each PSF was exported to an excel spreadsheet and plotted *(figures 5.10 – 5.12).* Table 5.4 gives a summary of the particles in the PSF as obtained from analysis using BEAMDP *(Ma & Rogers 2005).*

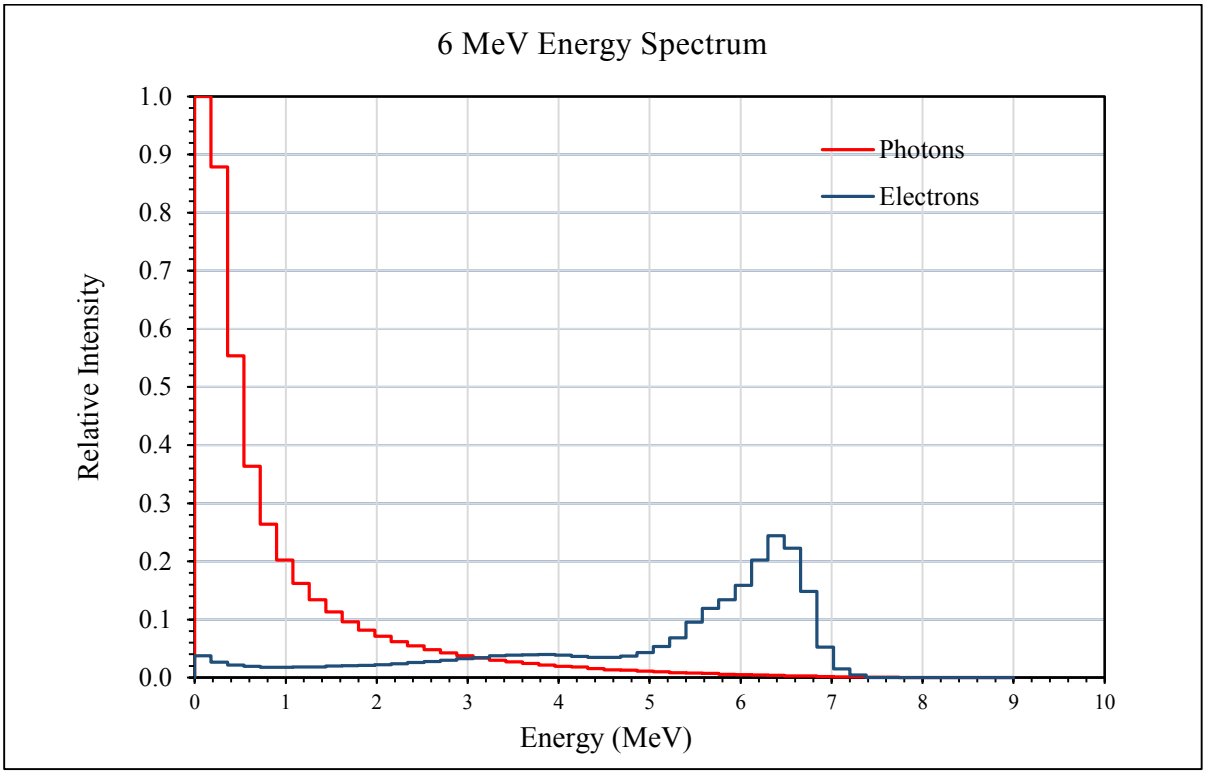

Figure 5.10 6 MeV energy spectrum normalised to the maximum photon fluence

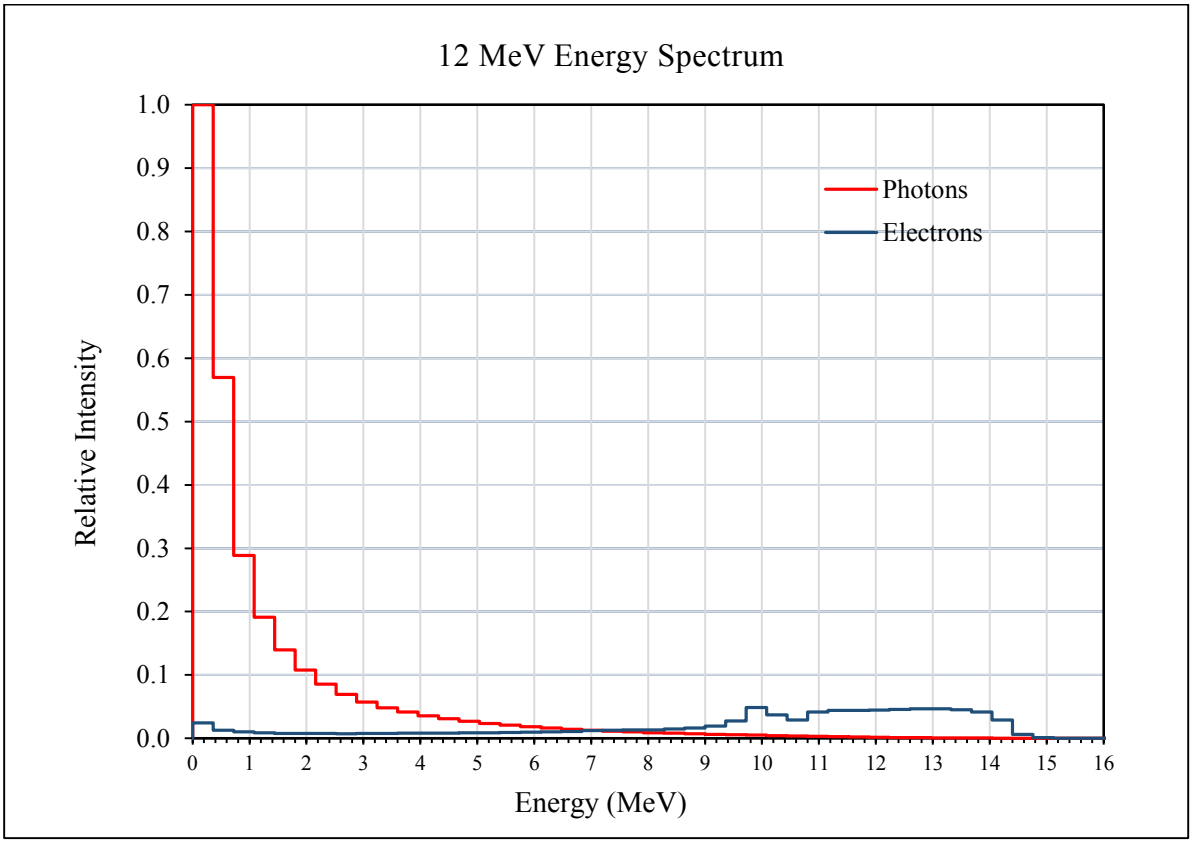

Figure 5.11 12 MeV energy spectrum normalised to the maximum photon fluence

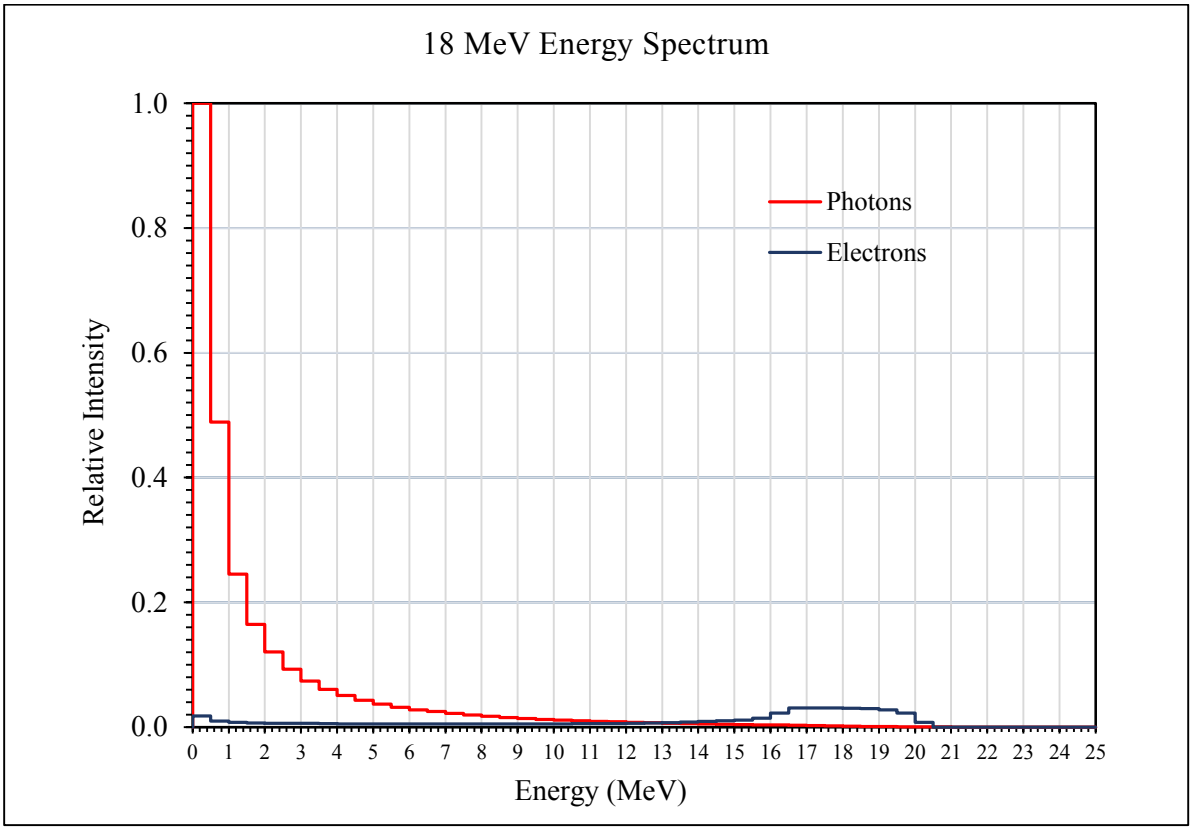

Figure 5.12 18 MeV energy spectrum normalised to the maximum photon fluence

Table 5.4 Summary of particles in the Phase-Space file for the $10x10$ cm applicator

ENERGY (MeV)	Total number of particles	Total number of photons	% Photons	% electrons/positrons	Max kinetic energy (MeV)
6	1 027 597	653 756	63.6	36.4	8.142
12	2 293 376	1 715 699	74.8	25.2	15.606
18	3 043 463	2 567 168	84.3	15.7	21 647

5.1.6.3 Analysis and discussion

Fluence (radiant energy per unit cross-sectional area) values greater than 50% of maximum fluence occur between 5.94 MeV and 6.84 MeV, 9.72 MeV and 14.22 MeV and 16.5 MeV and 20 MeV for the 6, 12 and 18 MeV beams respectively.

As the nominal energy of the poly-energetic input source for each beam increases from 6 to 12 to 18 MeV, the number of particles exiting the applicator increases from 10.3% to 22.9% to 30.4% respectively. The percentage photon contamination produced by the interactions of the electron source as it encounters the metallic components of the LINAC increases from

63.6% to 74.8% to 84.3% for the 6, 12 and 18 MeV beams respectively. The remaining particles in each PSF are electrons and positrons.

5.2 DOSXYZnrc

5.2.1 Phantom construction

DOSXYZnrc is an EGSnrc MC user-code capable of calculating 3-dimensional dose distributions in a user-defined rectilinear voxel phantom, by scoring energy-deposition in each voxel. It has the added capability of converting (by a programme called 'ctcreate') a CT data set of Hounsfield units into an appropriate format so that DOSXYZnrc may simulate dose distribution in a phantom with the relevant materials and densities specified in each voxel. *(Walters et al 2005).*

A homogeneous water-equivalent phantom, with the following voxel dimensions, was constructed for this study:

X voxels: 105 voxels of 0.2 cm each ranging from -10.5 cm to +10.5 cm for all energies

Y voxels: 105 voxels of 0.2 cm each ranging from -10.5 cm to +10.5 cm for all energies

Z voxels (6 MeV): 50 voxels of 0.1 cm each to a depth of 5.0 cm

Z voxels (12 MeV): 90 voxels of 0.1 cm each to a depth of 9.0 cm

Z voxels (18 MeV): 125 voxels of 0.1 cm each to a depth of 12.5 cm

The phantom was designed so that a group of voxels are centred along the central axis in the z direction up to a depth that extends beyond the practical range for each electron energy simulated. This ensures that dose may be scored along the central axis so that suitable PDDs are obtained from the simulation. The extent of the phantom in the lateral x and y directions ensure that suitable cross-plane and in-plane profiles may be obtained at a variety of depths.

5.2.2 Simulation parameters

The DOSXYZnrc input parameters are as follows:

Table 5.5 DOSXYZnrc Input parameters

INPUT PARAMETERS	
Incident particle	All
Number of histories	1.2×10^8
Random number seed 1	33
Random number seed 2	97
ECUT	0.521 MeV
PCUT	0.01 MeV
Range rejection	Off
Medium surrounding phantom	Air
Incident beam size	15
NRCYCL	0
HOWFARLESS	On

All the particles that exist in the PSF were included in the DOSXYZnrc simulations.

Particle histories are terminated for particles with kinetic energies below 0.521 MeV (ECUT) for electrons and 0.01 MeV (PCUT) for photons.

The incident beam size selection of 15 cm implies that any phase space particles that fall outside the square field of 15 cm will be discarded by DOSXYZnrc *(Walters and Kawrakow 2007)*.

The maximum field size simulated in this study is a 10 cm square field which makes this selection acceptable.

The HOWFARLESS transport algorithm was introduced into DOSXYZnrc to increase simulation efficiency of calculations in homogeneous phantoms *(Walters & Kawrakow 2007).* This is accomplished by the fact that the algorithm only considers the distance to the extreme outer boundaries of the homogeneous phantoms, thereby ignoring individual voxel boundaries which would have increased computational time.

The value NRCYCL indicates the number of times that each particle from a phase space source is reused each time it is read. Recycling particles becomes necessary when phase space data is sparse so that adequate statistics are obtained. Setting NRCYCL = 0 (as was the case for this study) allows DOSXYZnrc to automatically calculate NRCYCL based on the number of histories and number of particles in the phase space source. When the simulation has used all the particles in the source, the phase space source is automatically restarted. Restarting may lead to underestimates in the uncertainty of the results *(Walters et al 2002)*. However, if there is only one restart and if only a small fraction of the source is used in the second pass, the impact on the estimated uncertainty is not significant *(Walters et al 2005)*. Each simulation performed was inspected (via the .egslst file) to determine if restarts occurred and are reported on in the relevant sections below.

5.2.3 Source parameters

The PSF file obtained from the BEAMnrc simulation for each energy (6, 12 and 18 MeV) was used as the input source for DOSXYZnrc, utilising the 'source type 2' option. This provides the possibility of the source entering the phantom from any direction.

The required input parameters defining the source position relative to the phantom are as follows:

$(x, y, z)_{iso}$ = (0, 0, 0) represents the coordinates of the isocentre which is centred on the surface of the phantom at a distance of 100 cm from the BEAMnrc source.

Theta is defined as the angle between the +z direction, and the line joining the centre of the beam where it strikes the phantom surface, to the isocentre. Since the beam is orthogonal to the phantom and the isocentre is centred on the surface, theta = 180°.

Phi is the angle between the +x direction and the projection on the x-y plane of the line joining the centre of the beam on the phantom surface to the isocentre on the x-y plane. Since the beam is orthogonal to the phantom surface and the isocentre lies on the surface, phi = 0°.

d_{source} is the absolute distance from the origin of the phase-space plane (source origin) to the isocentre. Since the Psf is at the end of the applicator and the phantom surface is at 100 cm, d_{source} = 5 cm.

phi_{col} is the angle by which the source is rotated in the source plane about the beam-direction axis. Phi_{col} =180°.

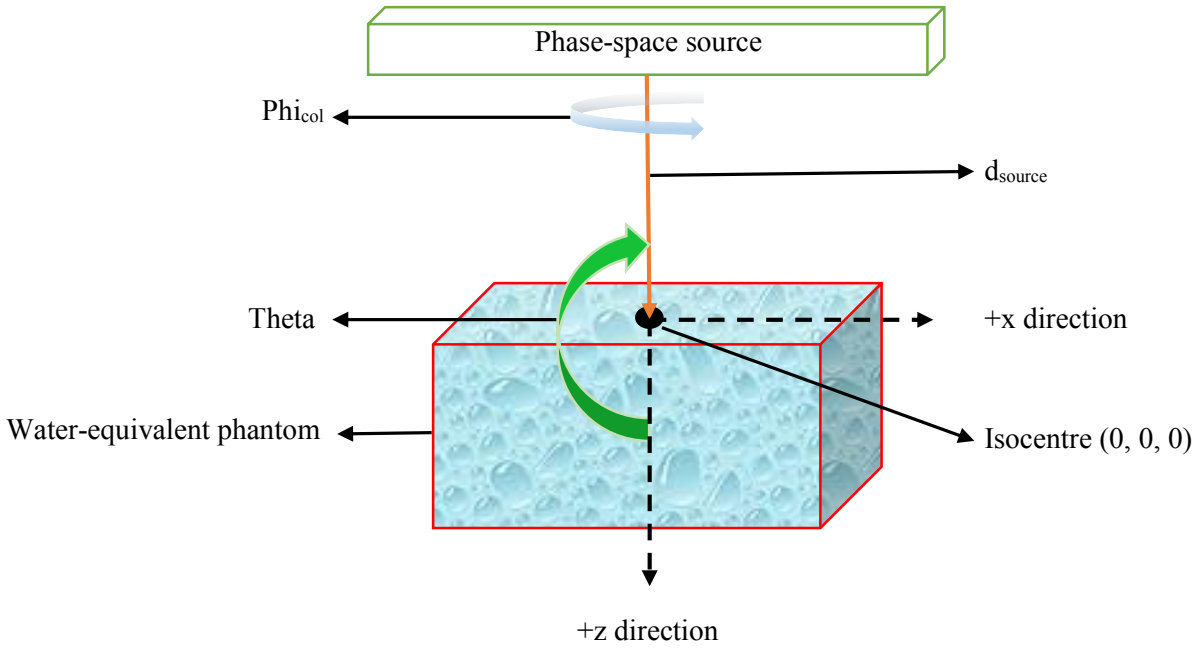

Figure 5.13 Description of the source parameters for DOSXYZnrc input

5.2.4 DOSXYZnrc Simulation results

The result of the simulation performed in DOSXYZnrc is a 3-D dose distribution with dose points at the centre of each voxel of the phantom created. Extraction of the dose data is achieved by invoking the MCSHOW programme that uses the dose output file (xxx.3ddose) and the phantom file (xxx.egs4phant) to generate plots of the calculation results in the plotting programme, Grace. PDDs were extracted for each of the 3 beam energies simulated and compared to measured data. The energy spectrum for each BEAMnrc source *(section 5.1.4.1)* was adjusted by altering the upper energy of the bins and/or altering the probability of finding a particle in the respective bins before re-simulating with the new spectrum. The process was

repeated until suitable comparisons, that satisfied the gamma Index (GI) evaluation criteria, were achieved. The final energy spectrums accepted for the full simulation of the 6, 12 and 18 MeV electron beam for the $10x10$ cm applicator were used as the BEAMnrc input source for all subsequent simulations for each of the energies.

5.3 Results

5.3.1 Absolute Dosimetry *(IAEA 2000)*

An error of 5% in absolute dose measurement may lead to a change in TCP of up to 20% or to a change in NTCP of up to 30% *(Papanikolaou et al 2004, Orton et al 1984)* if the prescribed dose falls along the steepest region of the dose response curves. It is therefore critical to maintain the highest level of accuracy in absolute dose measurement and calculation.

Based on the TRS398 *(IAEA 2000)* absolute dosimetry protocol, the absorbed dose to water at a reference depth z_{ref} for an electron beam of quality Q (under reference conditions) is given by

$$D_{w,Q} = M_Q * N_{D,w} * k_Q \tag{5.9}$$

where z_{ref} is the depth of measurement,

M_Q is the reading for energy Q of the dosimeter corrected for temperature and pressure, ion recombination and polarity,

$N_{D,w}$ is the calibration coefficient in terms of absorbed dose to water for the dosimeter in Co-60 and is obtained from the standards laboratory.

k_Q is a chamber specific factor which corrects for differences between the reference beam quality (Co-60) and the actual beam quality Q.

The following modified notation has been introduced in this study.

M_Q^x is the notation used in the rest of this section to denote the corrected reading for energy Q and chamber x.

$N_{D,w,Q}^x$ is the notation used in the rest of this section to denote the absorbed dose to water calibration coefficient for the dosimeter x and electron beam energy Q. If Q is Co-60, Q will be omitted in the notation.

k_{Q,Q_i}^x is the notation used in the rest of this section to denote the chamber specific factor which corrects for differences between the reference electron beam quality Q_i and the actual beam quality Q for chamber x.

For the purposes of this study, the objective in calibrating each electron beam is to ensure that the dose per 100 MU at the depth of maximum dose of the beam under reference conditions (10x10 applicator, 100 cm SSD) is 1.00 Gy. Equation 5.9 therefore needs to be divided by the PDD at z_{ref} in order to convert the dose at z_{ref} to the dose at z_{max}.

$R_{50,ion}$ is the half-value of the depth ionisation distribution in water (g/cm^2) and is obtained from the measured depth ionisation curve. R_{50} is the half-value of the depth dose distribution in water and is given by

$$R_{50} = 1.029 * R_{50,ion} - 0.06 g/cm^2 \quad (5.10)$$

The cylindrical chamber and parallel plate chambers used in this study (chapter 4) are abbreviated to cyl and pp respectively for the rest of this section.

For parallel plate chambers, z_{refpp} for each beam is determined from R_{50} by the relationship *(Burns et al 1996)*

$$z_{refpp} = 0.6 * R_{50} - 0.1\ g/cm^2 \quad (5.11)$$

For cylindrical chambers, the reference depth for measurement is given by *(IAEA 2000)*

$$z_{refcyl} = z_{refpp} + 0.5 * r_{cyl} = (0.6 * R_{50} - 0.1 + 0.5 * r_{cyl}) \ g/cm^2 \quad (5.12)$$

where r_{cyl} is the inner radius of the cylindrical chamber.

The TRS398 code of practice recommends that all electron beams that have $R_{50} < 4\ g/cm^2$ be calibrated using a parallel plate chamber, since accurate k_Q values are only available for electron beams with $R_{50} \geq 4\ g/cm^2$. This is due to inaccuracies at low energies in p_{wall}, which is a factor that corrects for the fact that the chamber wall is not equivalent to the medium in which measurements are performed. p_{wall} is used in the determination of k_Q.

Since $N_{D,w}$ is only available for the cylindrical chamber, cross calibration is necessary in order to determine $N_{D,w}$ for the parallel plate chamber.

Cross calibration is performed using the highest electron energy available – this is the 21 MeV beam (R_{50} = 8.298 g/cm^2) for the LINAC used in this study and is called the cross-calibration energy Q_{cross} = 21e.

A measurement is performed for energy Q_{cross} with the cylindrical chamber (cyl) at depth z_{refcyl} given by equation 5.12. This the value $M_{Q_{cross}}^{cyl} = M_{21e}^{cyl}$.

A measurement is then performed for energy Q_{cross} with the parallel plate chamber (pp) at depth z_{refpp} given by equation 5.11. This is the value $M_{Q_{cross}}^{pp} = M_{21e}^{pp}$

k_Q is obtained for the cylindrical chamber for energy 21 MeV (R_{50} = 8.298 g/cm^2) from Table 18 in the TRS398 document.

$N_{D,w,Q_{cross}}^{x} = N_{D,w,21e}^{pp}$ is the calibration coefficient in terms of absorbed dose to water for the parallel plate chamber for the 21 MeV beam and is thus given by

$$N_{D,w,21e}^{pp} = \left[\frac{M_{21e}^{cyl}}{M_{21e}^{pp}}\right] * \left[N_{D,w}^{cyl}\right] * \left[k_{21e}^{cyl}\right] \quad (5.13)$$

where the terms of the equation have been defined above.

In order to simplify the presentation of data in the code of practice document, an intermediate energy Q_{int} with R_{50} = 7.5 g/cm^2 is introduced. The objective is to obtain a calibration coefficient

N_{D,w,Q_i}^{pp} for each user energy Q_i. This is accomplished by utilising Q_{int} in the following manner

$$N_{D,w,Q_i}^{pp} = N_{D,w,21e}^{pp} * k_{Q_i,Q_{21e}}^{pp}$$

$$= N_{D,w,21e}^{pp} * \left[\frac{k_{Q_i,Q_{int}}^{pp}}{k_{Q_{21e},Q_{int}}^{pp}}\right] \quad (5.14)$$

Where the factors $k_{Q_i,Q_{int}}^{pp}$ and $k_{Q_{21e},Q_{int}}^{pp}$ are obtained from the relevant tables in the TRS398 code of practice.

The absorbed dose to water at z_{max} for each energy Q_i is therefore

$$D_{w,Q_i} = \frac{M_{Q_i}^{pp} * N_{D,w,Q_i}^{pp}}{PDD_{Q_i,z_{ref}}} \quad (5.15)$$

where $M_{Q_i}^{pp}$ is the corrected parallel plate chamber reading at z_{refpp} for energy Q_i

N_{D,w,Q_i}^{pp} is obtained from equation 5.14, and

$PDD_{Q_i,z_{ref}}$ is the PDD at z_{ref} for electron energy Q_i and is obtained from the relevant measured PDD curve.

The output of each electron beam (10x10 cm applicator, 100 cm SSD) was measured and soft-pots were adjusted so that the absolute dose at z_{max} was 1.00 Gy per 100 MU. The estimated relative standard uncertainty in determination of D_{w,Q_i} utilising the TRS398 protocol is quoted as 1.6% *(IAEA 2000)*.

5.3.2 Percentage Depth Dose (PDD) Results

3 dimensional isodose distributions are obtained by combining measured PDDs and central and off-axis profiles at various depths for each beam. Accuracy of the resulting 3-D isodose distributions depends on the number of data points measured as well as the interpolation algorithms inherent in the software. It therefore makes more sense to quantitatively evaluate the one-dimensional primary measured components (viz. PDDs and profiles) independently rather than using the software generated isodose distributions.

The goal of dose calibration accuracy of 2%/2 mm *(Chetty et al 2006)* and overall accuracy of 5%/5 mm *(Faddegon et al 1998)* has been regarded as being realistic and feasible. It is suggested that ideal agreement between measurement and calculation would be within 2% or 2 mm of the beam normalisation value whilst levels of 3% and/or 3 mm would be regarded as acceptable *(Mayles et al 1999).* For more complex geometries, 4% or 4 mm is specified as the limit *(Van Dyk et al 1993).* Agreements of 3% for low dose gradient regions and 3 mm for high dose gradient regions for complex geometries (eg MLC or blocks) are suggested by Venselaar et al 2001.

Whilst 2%/2 mm may be ideal, the relative dose comparison (gamma index) criteria between measurement and calculation for this study was selected as 3%/3 mm due to the existence of these complex geometries.

Table 5.6 below shows the absolute differences of pertinent characteristic MC-calculated points (defined in section 2.6.1) relative to measurements for 6 MeV, 12 MeV and 18 MeV PDD curves for the $10x10cm$ applicator.

The source parameters were repeatedly adjusted *(section 5.1.4.1)* until acceptable matches were obtained.

Table 5.6 Absolute differences between measured and MC-calculated characteristic points on the PDD curve for the $10x10cm$ Open Applicator for energies 6, 12 and 18 MeV.

	6 MeV			12 MeV			18 MeV		
	Meas	**MC**	**Diff**	**Meas**	**MC**	**Diff**	**Meas**	**MC**	**Diff**
D_s (%)	79.6	78.7	**-0.9**	91.0	88.7	**-2.3**	95.4	90.2	**-5.2**
R_{max} (cm)	1.32	1.35	**0.03**	2.28	2.35	**0.07**	1.40	1.45	**0.05**
R_{90} (cm)	1.82	1.78	**-0.04**	3.47	3.55	**0.08**	4.72	4.75	**0.03**
R_{80} (cm)	2.02	2.01	**-0.01**	3.94	3.95	**0.01**	5.65	5.70	**0.05**
R_{50} (cm)	2.44	2.44	**0.00**	4.86	4.87	**0.01**	7.14	7.20	**0.06**

For the GI PDD comparisons for 6, 12 and 18 MeV *(figures 5.14, 5.15 and 5.16)* below, the %dose difference, DoN (in % of normalisation value of the reference matrix) parameter was used. DoN is defined as

$$DoN = \frac{C_{i,j} - M_{i,j}}{M_{i_0,j_0}} \tag{5.16}$$

where $C_{i,j}$ is the value at point (i,j) of the calculated matrix

$M_{i,j}$ is the value at point (i,j) of the measured matrix

$M_{i_0 j_0}$ is the value at the normalization point (i_0,j_0) of the measured matrix

The passing criteria set was $DoN \leq 3.0\%$. If more than 90% of the evaluated dose points are $\leq$ 3% DoN, the bars in the histogram will be green. If more than 75% of the evaluated dose points are $\leq 3\%$ DoN, the bars in the histogram will be yellow.

The statistical variance was less than 1% for all Monte Carlo PDD calculations *(section 4.3.4)*.

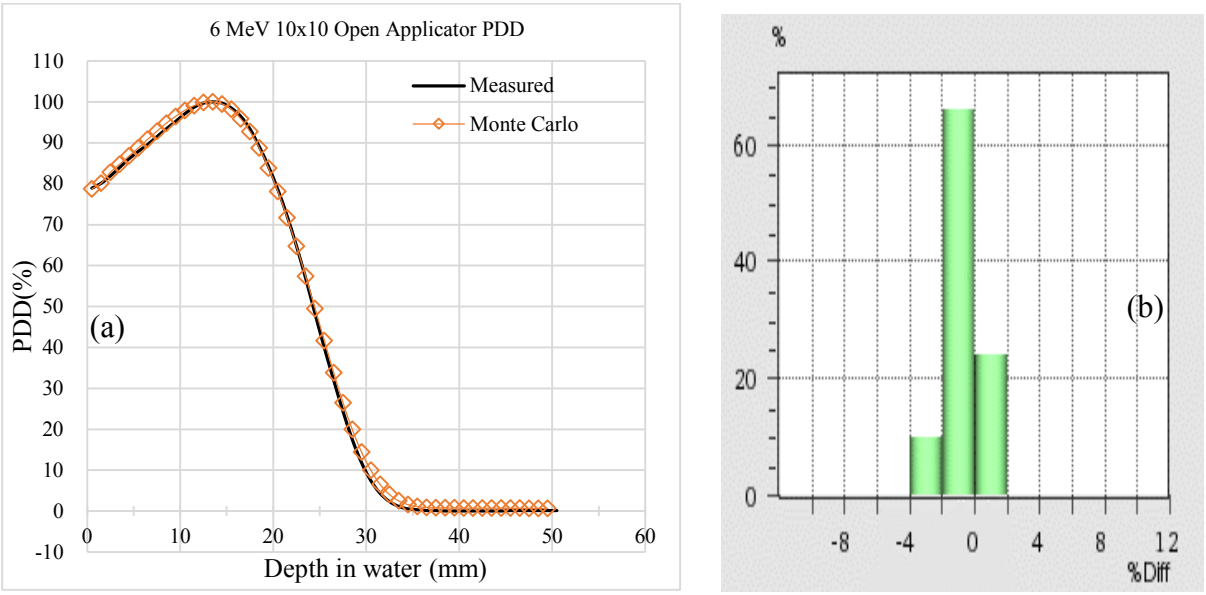

Figure 5.14 Comparison of measured and MC PDDs for 6 MeV $10x10$ *cm* open applicator: (a) PDD (b) % dose difference histogram.

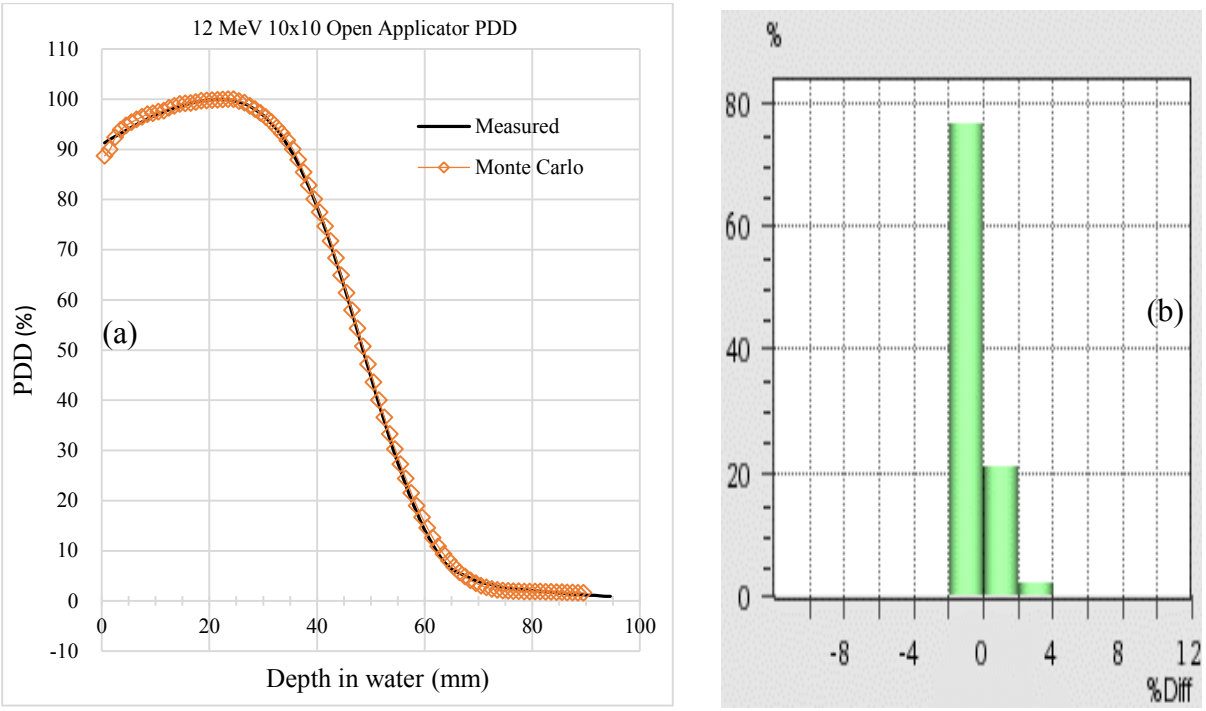

Figure 5.15 Comparison of measured and MC PDDs for 12 MeV $10x10$ *cm* open applicator: (a) PDD (b) % dose difference histogram

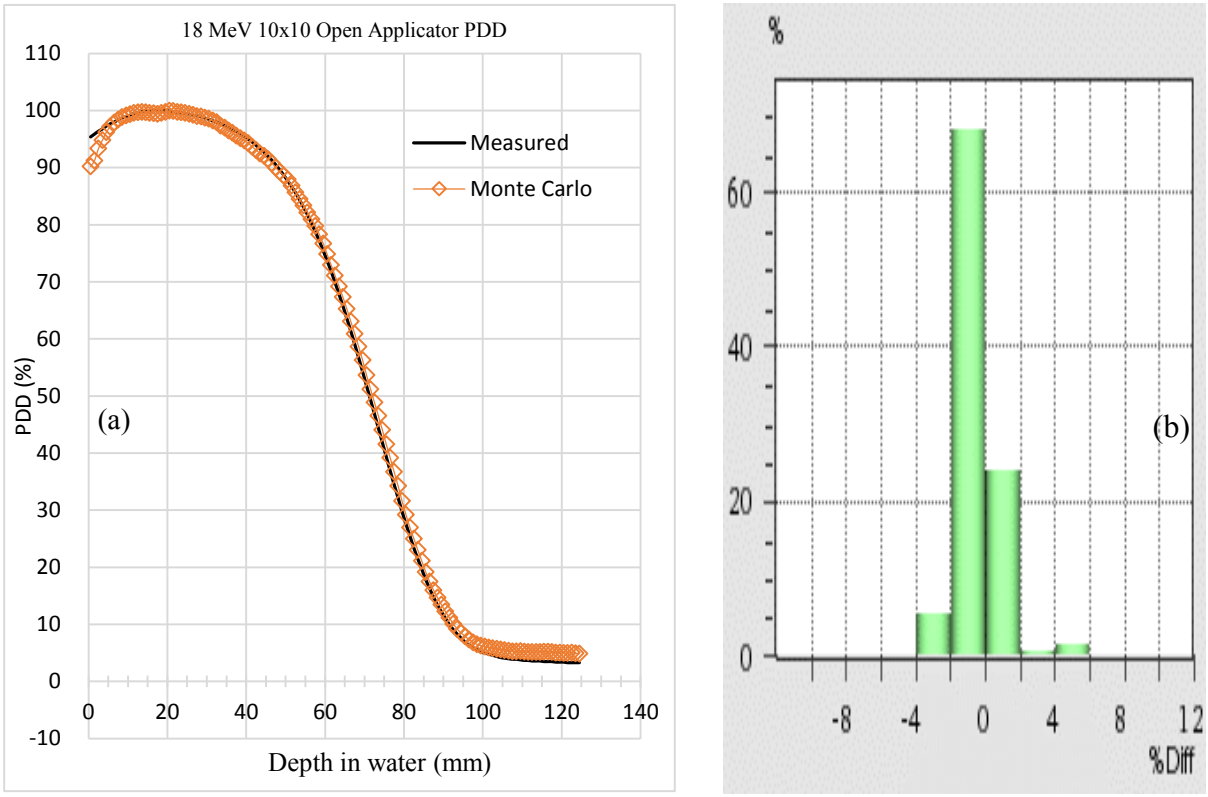

Figure 5.16 Comparison of measured and MC PDDs for 18 MeV 10*x*10 *cm* open applicator: (a) PDD (b) % dose difference histogram

5.3.2.1 Analysis

Direct comparison of the depths R_{max}, R_{90}, R_{80}, and R_{50} *(table 5.6)* show differences of less than 0.8 mm for all energies. The MC-calculated depths were larger for all PDDs with the exception of d_{90} and d_{80} for the 6 MeV beam. As the energy increased, differences between measured and calculated surface doses increased with only the 18 MeV displaying a dose difference higher than 3%. However, this dose difference decreased to 0% within the first 2.5 mm *(figure 5.16(a))* for this beam. The calculated surface doses were lower than measurement for all energies *(discussed in section 5.5)*. The values between R_{max} and R_{20} for all energies compared favourably. For all the energies, the measured PDD fell off more rapidly than the calculated PDDs but were still within the acceptance criteria. The discrepancies in this region increased with increasing energy. The bremsstrahlung tail for the calculated curve is higher for both 6 MeV and 18 MeV but still fell within the acceptance criteria.

5.3.3 Beam Profile Results

In-plane and cross-plane profiles were measured with step sizes of 2 mm at the following depths for each of the energies:

Table 5.7 Profile depths acquired for 6 MeV, 12 MeV and 18 MeV beams for the $10x10\ cm$ applicator

	Depth 1 (cm)	**Depth 2 (cm)**	**Depth 3 (cm)**	**Depth 4 (cm)**
6 MeV	1.4	2.0	-	-
12 MeV	2.5	3.5	4.5	-
18 MeV	2.5	4.0	5.0	7.0

The comparison, with the MC simulation data, of the measured in-plane and cross-plane profiles yielded similar results, so for brevity, only the cross-plane results are reported below.

The measured data was used as the reference matrix with the MC data as the secondary data set. All profiles were normalised to 100% on the central axis.

For the profile comparisons, the following 2D GI parameters were used:

3.0 mm Distance – To – Agreement (DTA)

3.0% Dose Difference with reference to local dose

Increased tolerance of 4.0 % Dose Difference for values below 3.0 %. This implies that for any dose points in the profile that is less than 3% of the maximum dose (extreme ends of the penumbra), the pass/fail GI criteria is increased to 4%.

The associated GI histograms appear adjacent to each set of plotted data.

The percentage that satisfy the passing criteria of Gamma ≤ 1.0 are represented by light green and dark green bars for MC values greater than the measured values (hot) and for MC values less than the measured values (cold) respectively.

The percentage that fail and have GI > 1.0 are represented by red and blue bars for MC values greater than the measured values (hot) and for MC values less than the measured values (cold) respectively.

The red and blue ellipses on the plotted profile curves represent the point(s) on the curve that fail the GI criteria according to the colour nomenclature in the associated histogram.

The statistical variance was less than 1% for all Monte Carlo profile calculations *(section 4.3.4)*.

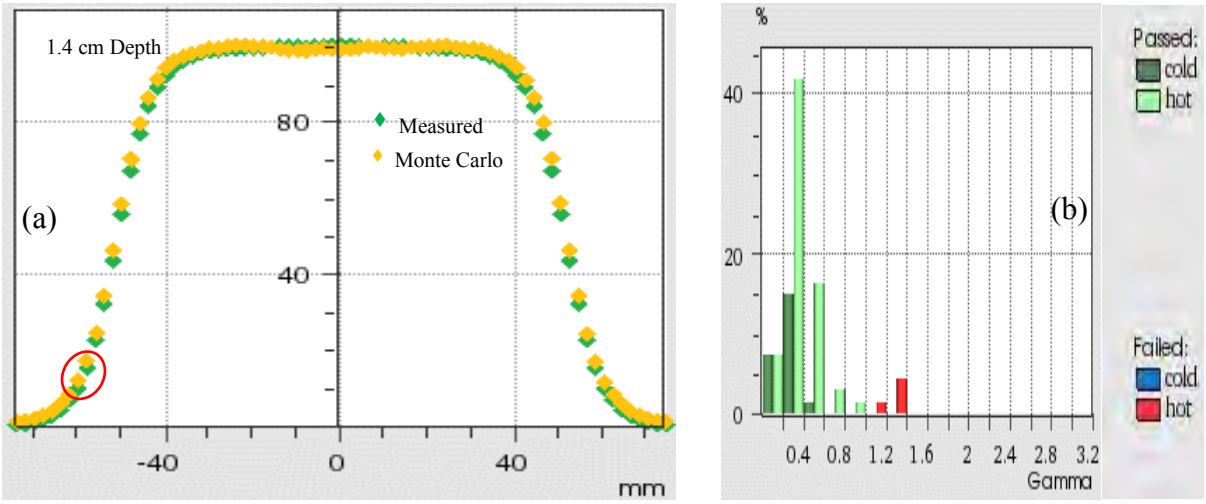

Figure 5.17 Comparison of measured and MC profiles at 1.4 cm depth for 6 MeV $10x10$ cm open applicator: (a) Profile (b) Gamma Index histogram

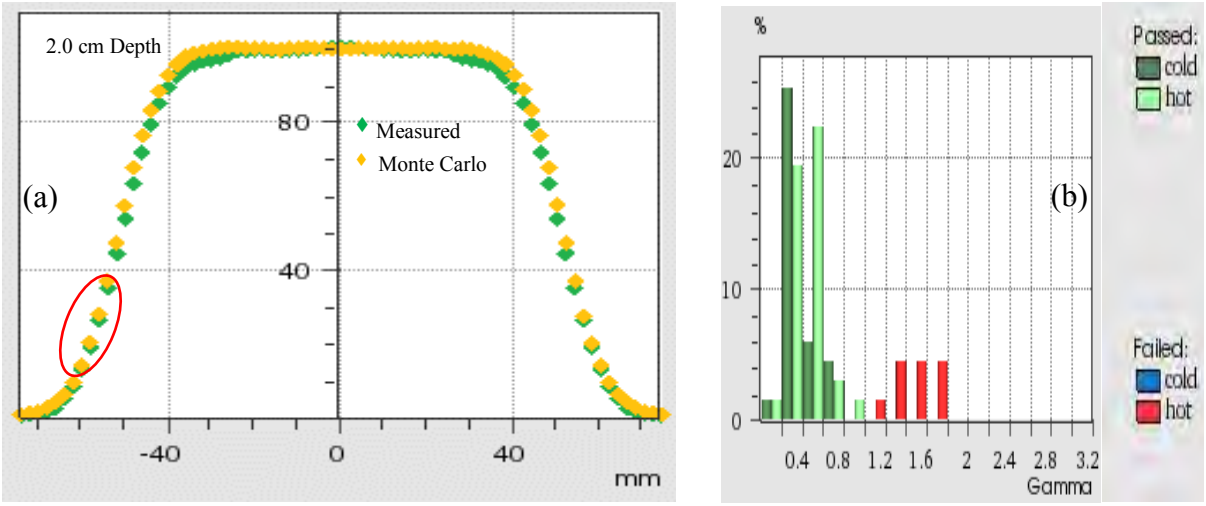

Figure 5.18 Comparison of measured and MC profiles at 2.0 cm depth for 6 MeV $10x10$ cm open applicator: (a) Profile (b) Gamma Index histogram

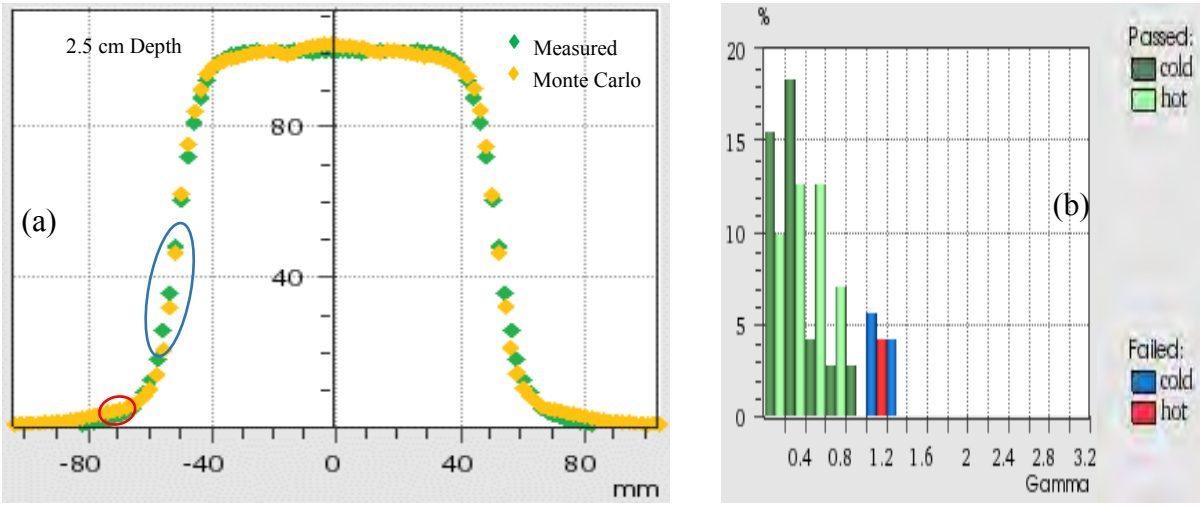

Figure 5.19 Comparison of measured and MC profiles at 2.5 cm depth for 12 MeV $10x10$ *cm* open applicator: (a) Profile (b) Gamma Index histogram

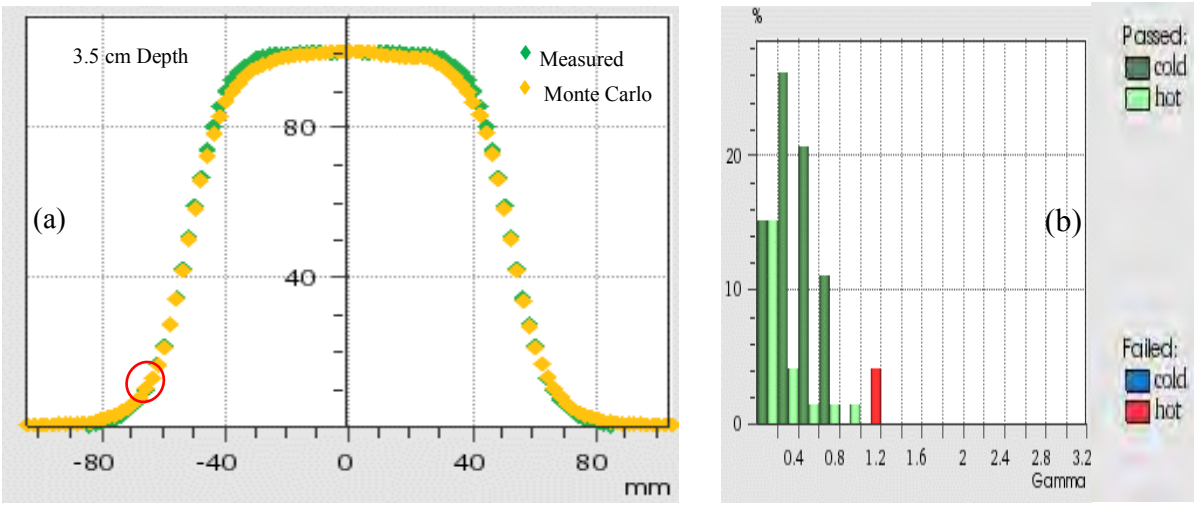

Figure 5.20 Comparison of measured and MC profiles at 3.5 cm depth for 12 MeV $10x10$ *cm* open applicator: (a) Profile (b) Gamma Index histogram

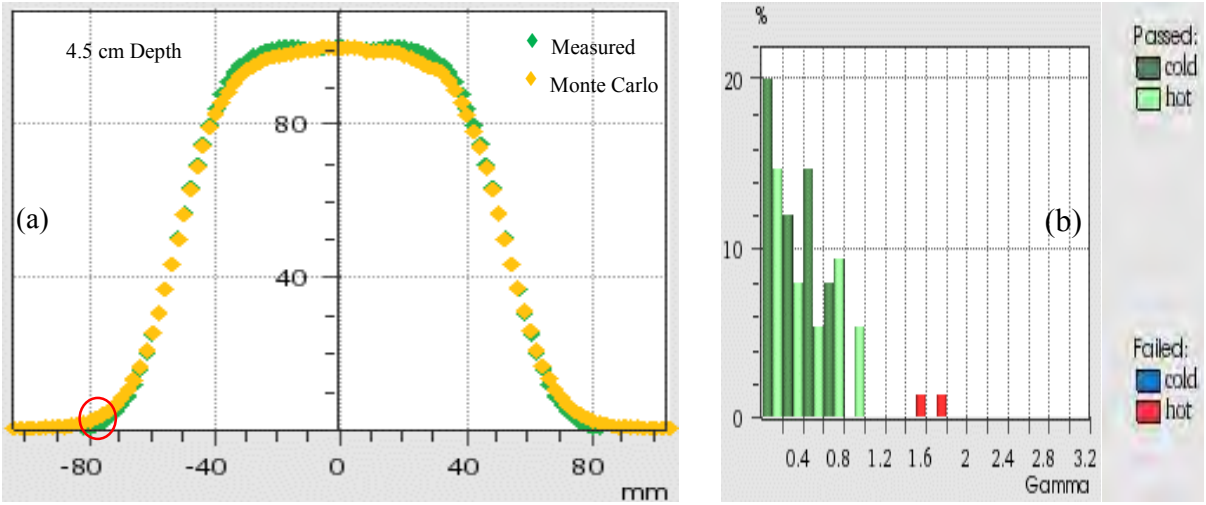

Figure 5.21 Comparison of measured and MC profiles at 4.5 cm depth for 12 MeV $10x10$ *cm* open applicator: (a) Profile (b) Gamma Index histogram

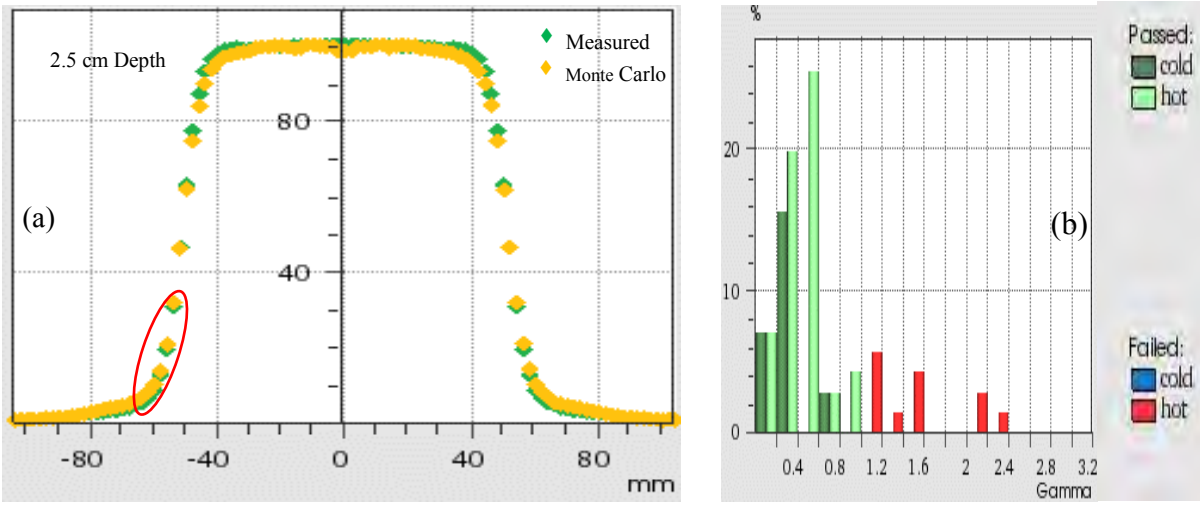

Figure 5.22 Comparison of measured and MC profiles at 2.5 cm depth for 18 MeV $10x10$ *cm* open applicator: (a) Profile (b) Gamma Index histogram

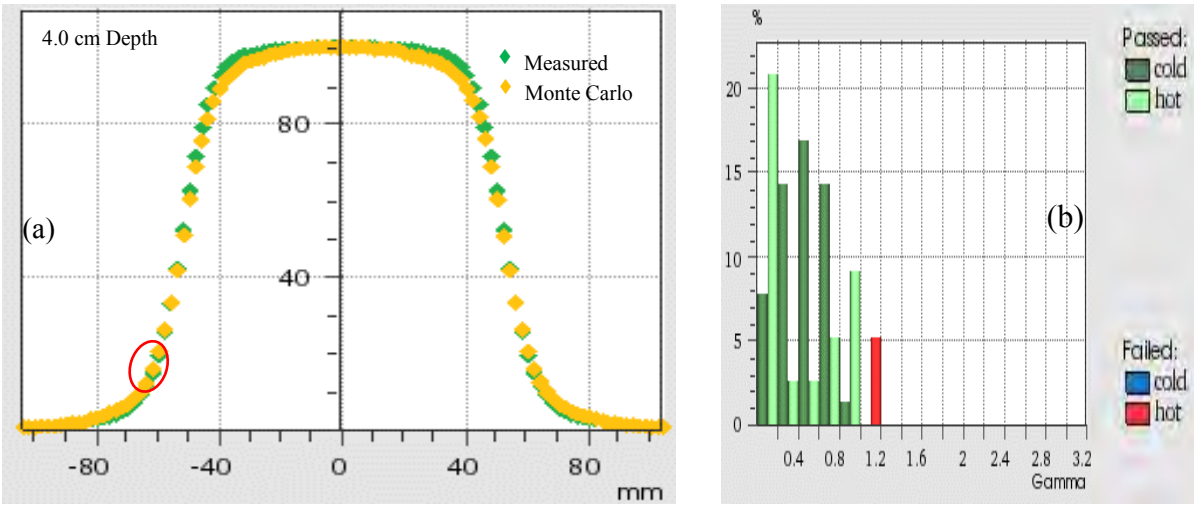

Figure 5.23 Comparison of measured and MC profiles at 4.0 cm depth for 18 MeV $10x10$ *cm* open applicator: (a) Profile (b) Gamma Index histogram

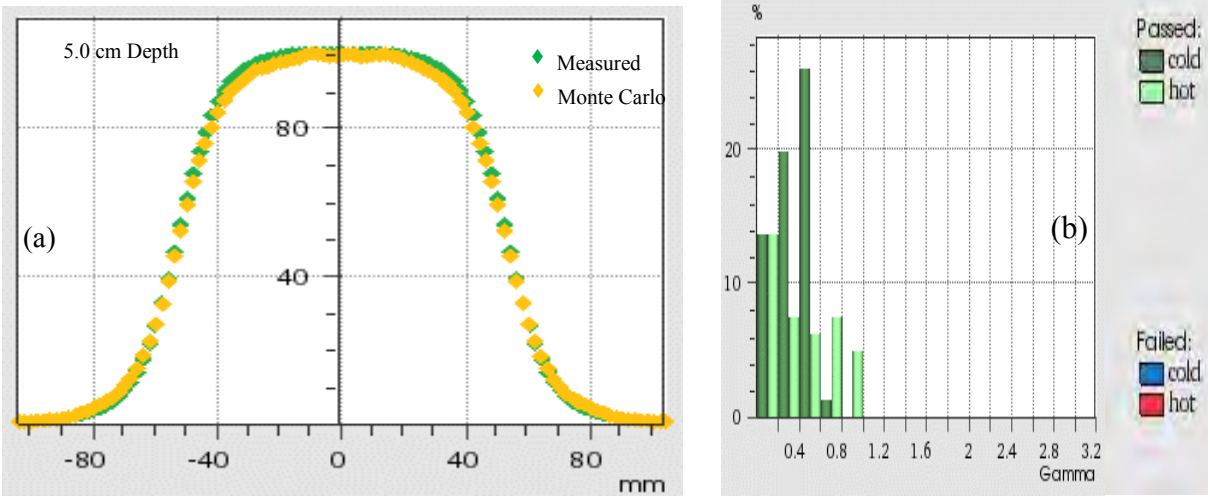

Figure 5.24 Comparison of measured and MC profiles at 5.0 cm depth for 18 MeV $10x10$ *cm* open applicator: (a) Profile (b) Gamma Index histogram

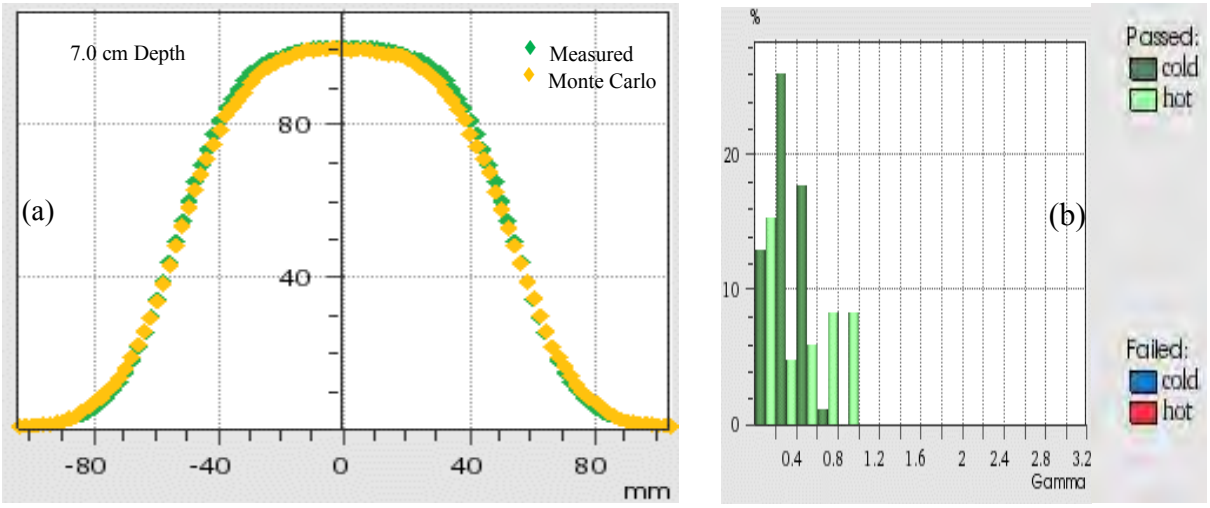

Figure 5.25 Comparison of measured and MC profiles at 7.0 cm depth for 18 MeV $10x10\ cm$ open applicator: (a) Profile (b) Gamma Index histogram

5.3.3.1 Analysis

6 MeV beam profile at 1.4 cm depth: The 5% of the points that failed had a maximum γ of 1.4 in the 20% dose region at a lateral distance greater than 5.5 cm.

6 MeV beam profile at 2.0 cm depth: 4% of the failed points had a maximum γ of 1.8 in the 10% to 40% dose region at lateral distance greater than 5.5 cm.

12 MeV beam profile at 2.5 cm depth: 6% and 4% of the failed points were colder in the 20% to 50% dose regions with γ of 1.1 and 1.3 respectively at lateral distance >5 cm. 4% of points were hotter in the 5% dose region at 7 cm lateral distance with γ of 1.2.

12 MeV beam profile at 3.5 cm depth: 4% of the failed points had γ of 1.2 in the 15% dose region at lateral distance > 5 cm.

12 MeV beam profile at 4.5 cm depth: Only 1% of the points failed with a maximum γ of 1.8 in the <5% dose region at lateral extent >7.5 cm.

18 MeV beam profile at 2.5 cm depth: Less than 2% of the points failed with maximum γ of 2.4 in the 5% to 35% dose region at lateral extent >5 cm. The maximum number of failed points was 5% with γ of 1.2 in the same lateral region.

18 MeV beam profile at 4.0 cm depth: Less than 2% of the points failed with a maximum γ of 1.2 in the dose range 10% to 20% at lateral extent > 6 cm

18 MeV beam profile at 5.0 cm depth: All points passed the GI evaluation for this profile.

18 MeV beam profile at 7.0 cm depth: All points passed the gamma evaluation for this profile.

Discussion and conclusions based on the results and analysis of the commissioning with the $10x10\ cm$ applicator are reserved for the end of the chapter *(section 5.5)* after completion of the MC commissioning of the 5 cm circle applicator.

5.4 Monte Carlo commissioning of the 5 cm circle applicator

5.4.1 General information

The reference $10x10\ cm$ applicator used was replaced in the build by the standard 5 cm circle applicator. The same main input parameters *(table 5.1)*, EGSnrc parameters *(table 5.2)* and source for each energy *(section 5.1.4.1)* as for the $10x10\ cm$ applicator case was used as input. The jaw and MLC sizes were changed from $19x19\ cm$ to $13x13\ cm$, which is the default field size for this standard applicator.

The 5 cm circle standard applicator was 'built' *(figure 5.26)* in BEAMnrc utilising 3 different component modules available in the code.

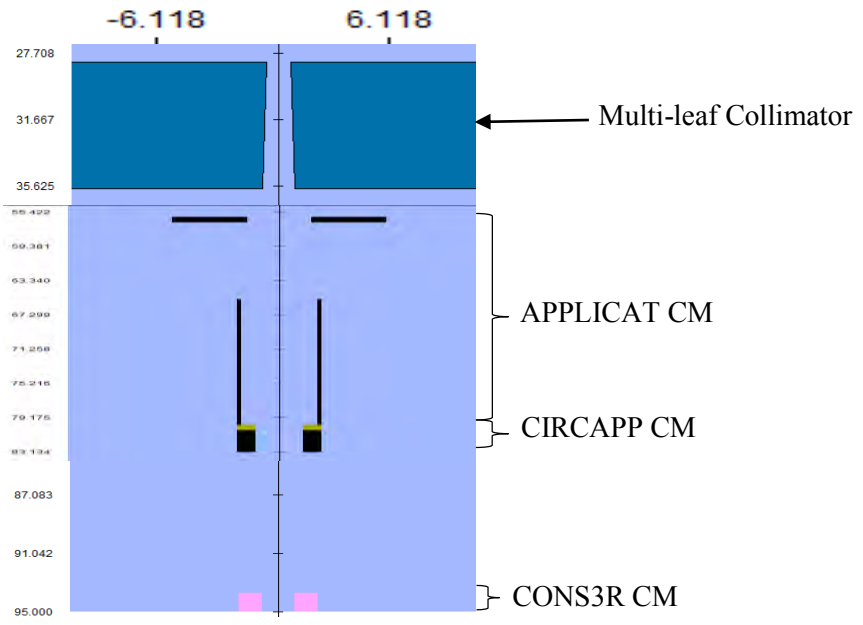

Figure 5.26 BEAMnrc build of the standard 5 cm circle applicator depicting the 3 different component modules that were used in the construction.

The APPLICAT CM was used to build the first part of the $5\,cm$ circle applicator and consisted of 2 Aluminium scrapers starting at z = 56.0 cm and ending at 80.005 cm.

The CIRCAPP CM was used to build the second part of the applicator and consisted of 2 scrapers starting at z = 80.026 cm and ending at 83.186 cm.

The third part of the applicator was built using the CONS3R CM and consisted of a 1.27 cm thick lead disc with a 4.75 cm diameter aperture ending at z = 95.0 cm.

A PSF from the simulation was obtained at the applicator end and was subsequently used as the input source for DOSXYZnrc so that dose distributions may be obtained. The lateral dimensions of the phantom constructed for the $5\,cm$ circle applicator simulations was decreased from the $10x10cm$ applicator simulations due to the reduced field size. The individual voxels sizes in each of the 3 dimensions of the phantom were kept the same as for the $10x10cm$ applicator case. The voxel dimensions were as follows:

X voxels: 127 voxels of 0.2 cm each ranging from -12.7 cm to +12.7 cm for all energies

Y voxels: 127 voxels of 0.2 cm each ranging from -12.7 cm to +12.7 cm for all energies

Z voxels (6 MeV): 50 voxels of 0.1 cm each to a depth of 5.0 cm

Z voxels (12 MeV): 90 voxels of 0.1 cm each to a depth of 9.0 cm

Z voxels (18 MeV): 125 voxels of 0.1 cm each to a depth of 12.5 cm

The simulation parameters and source parameters used were identical to that described in sections 5.1.2 and 5.1.3 respectively. The DOSXYZnrc simulation results were obtained as per section 5.2.4 and were evaluated using the GI evaluation method *(section 4.4.1)*.

Table 5.8 Summary of particles in the Phase-Space file for the 5 cm circle applicator

ENERGY (MeV)	Total number of particles	Total number of photons	% Photons	% electrons/positrons	Max kinetic energy (MeV)
6	427 732	366 360	85.7	14.3	8.212
12	2 217 917	2 002 955	90.3	9.7	15.471
18	664 163	592 095	89.1	10.9	21.557

5.4.2 Results

5.4.2.1 Percentage Depth Dose (PDD) Results

Table 5.9 below shows the absolute differences of pertinent characteristic MC-calculated points (defined in section 2.6.1) relative to measurements for 6 MeV, 12 MeV and 18 MeV PDD curves for the 5 cm circle applicator.

Table 5.9 Absolute differences between measured and MC-calculated characteristic points on the PDD curve for the 5 cm circle applicator for energies 6, 12 and 18 MeV.

	6 MeV			12 MeV			18 MeV		
	Meas	**MC**	**Diff**	**Meas**	**MC**	**Diff**	**Meas**	**MC**	**Diff**
D_s (%)	77.5	76.5	**-1.0**	91.0	88.6	**-2.4**	94.0	91.0	**-3.0**
R_{max} (cm)	1.45	1.40	**0.05**	2.05	2.05	**0.00**	1.75	1.65	**0.10**
R_{90} (cm)	1.85	1.80	**-0.05**	3.41	3.46	**-0.05**	4.25	4.26	**0.01**
R_{80} (cm)	2.03	2.06	**-0.03**	3.88	3.86	**-0.02**	5.10	5.12	**0.02**
R_{50} (cm)	2.46	2.44	**-0.02**	4.78	4.76	**-0.02**	6.73	6.77	**0.04**

For the GI PDD comparisons for 6, 12 and 18 MeV *(figures 5.27, 5.28 and 5.29)* below, the %dose difference, DoN, as defined in section 5.3.2, was used.

The statistical variance was less than 1% for all Monte Carlo PDD calculations *(section 4.3.4)*.

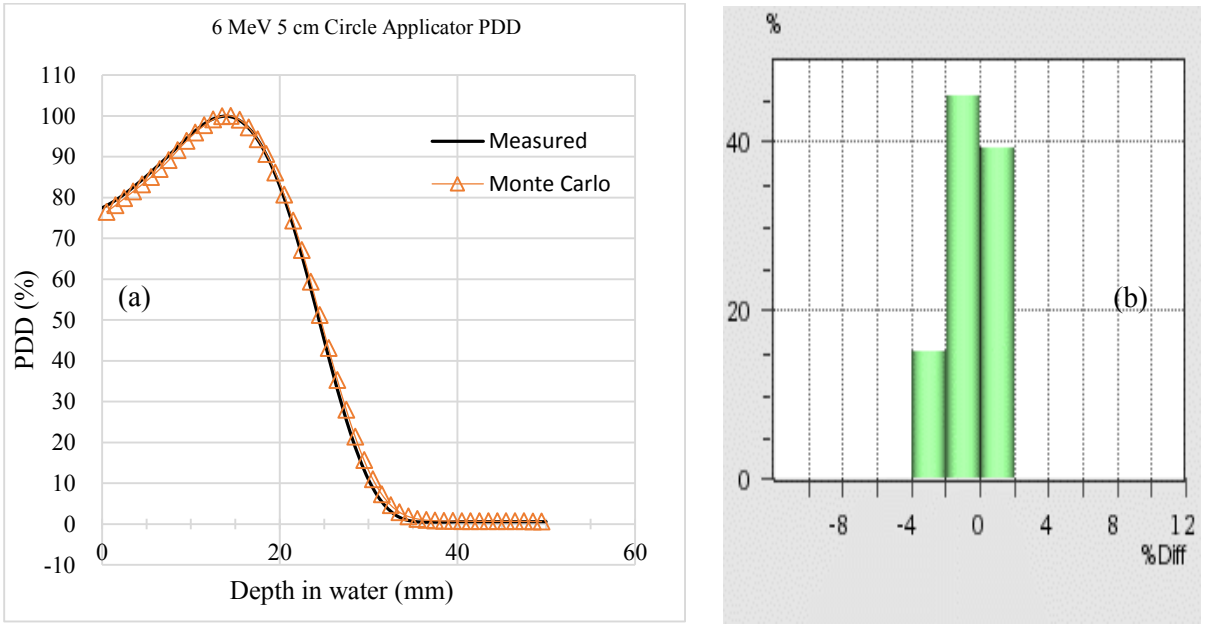

Figure 5.27 Comparison of measured and MC PDDs for 6 MeV 5 *cm* circle applicator: (a) PDD (b) % dose difference histogram

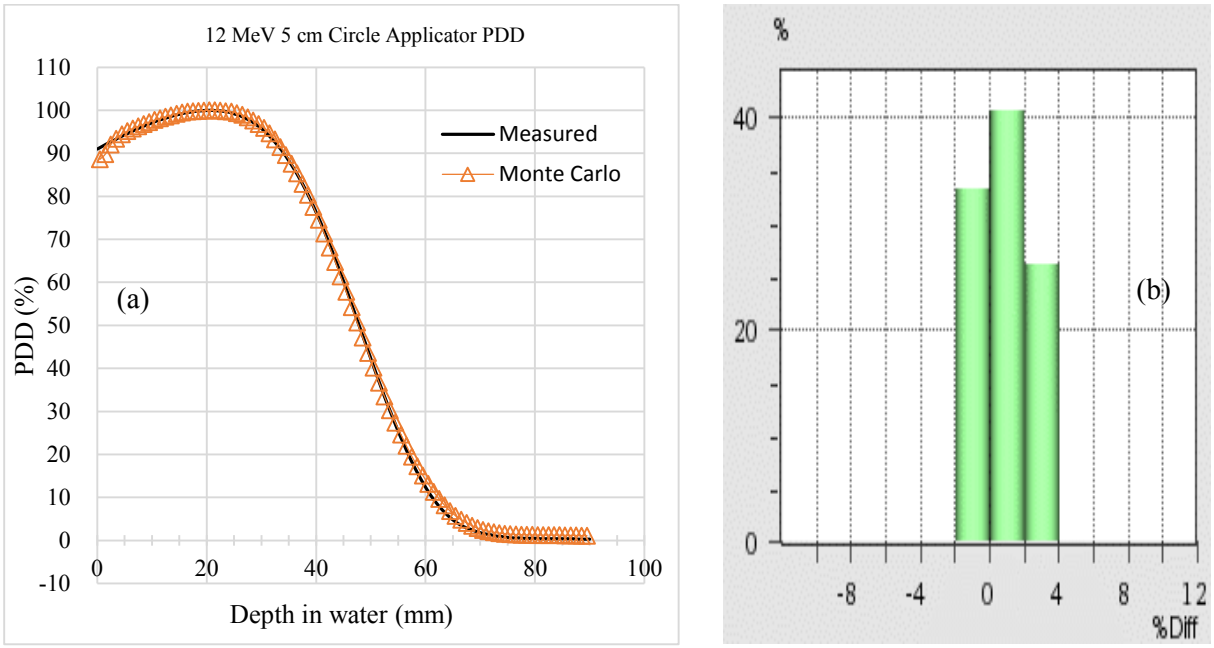

Figure 5.28 Comparison of measured and MC PDDs for 12 MeV 5 *cm* circle applicator: (a) PDD (b) % dose difference histogram

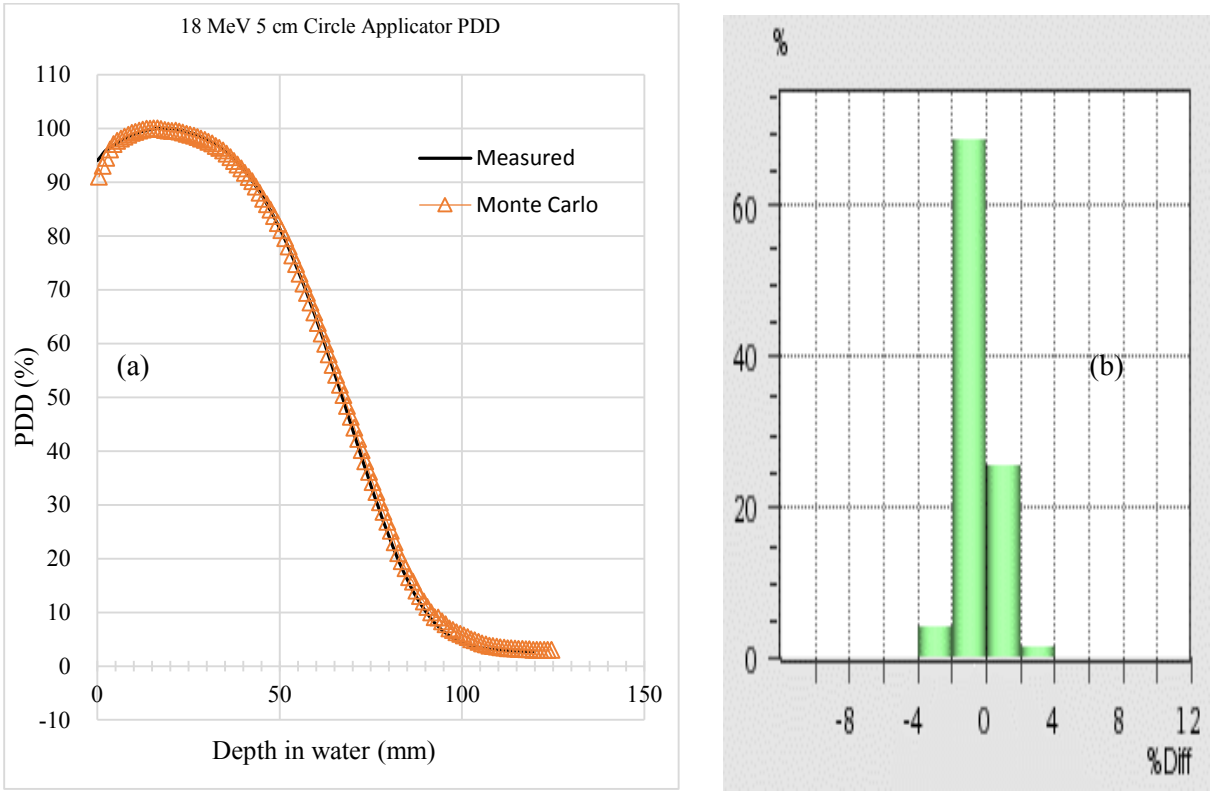

Figure 5.29 Comparison of measured and MC PDDs for 18 MeV 5 *cm* circle applicator:
(a) PDD (b) % dose difference histogram

5.4.2.1.1 Analysis

Direct comparison *(table 5.9)* of the surface dose showed an increase in differences in surface dose with an increase in energy. The maximum difference in surface dose was for the 18 MeV beam with the calculated value being 3.0% lower than measurement. This dose difference decreased to 0% within the first 2.5 mm *(figure 5.29(a))* for this beam. The calculated surface doses were lower than measurement for all energies.

Direct comparison of the depths R_{max}, R_{90}, R_{80}, and R_{50} resulted in a maximum difference of 0.05 mm observed for the R_{max} and R_{90} for the 6 MeV beam and R_{90} for the 12 MeV beam. The values between R_{max} and R_{20} for all energies compared favourably. The bremsstrahlung tail for all energies displayed acceptable results.

5.4.2.2 Beam Profile Results

In-plane and cross-plane profiles were measured with step sizes of 2 mm at the following depths for each of the energies:

Table 5.10 Profile depths acquired for 6 MeV, 12 MeV and 18 MeV beams for the 5 *cm* circle applicator

	Depth 1 (cm)	**Depth 2 (cm)**	**Depth 3 (cm)**	**Depth 4 (cm)**
6 MeV	1.4	2.0	-	-
12 MeV	2.5	3.5	4.5	-
18 MeV	2.5	4.0	5.0	7.0

The statistical variance was less than 1% for all Monte Carlo profile calculations *(section 4.3.4)*.

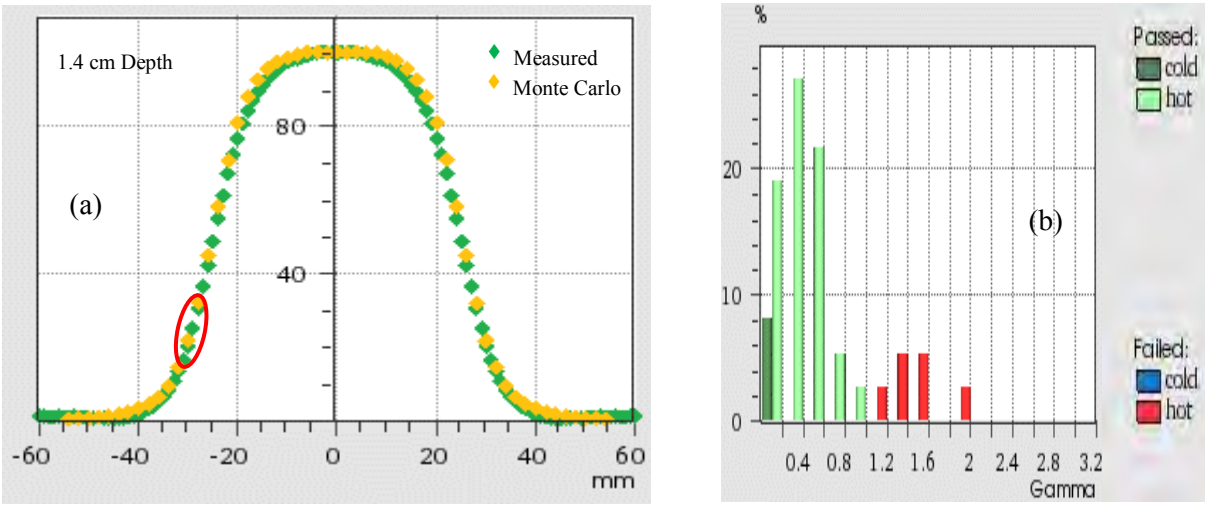

Figure 5.30 Comparison of measured and MC profiles at 1.4 cm depth for 6 MeV 5 *cm* circle applicator: (a) Profile (b) Gamma Index histogram

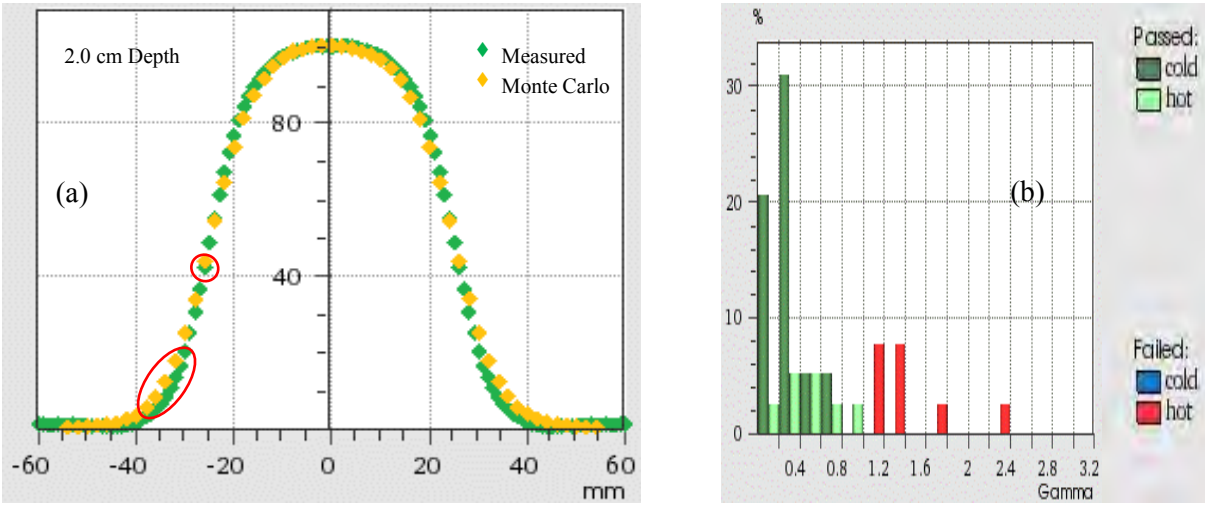

Figure 5.31 Comparison of measured and MC profiles at 2.0 cm depth for 6 MeV 5 *cm* circle applicator: (a) Profile (b) Gamma Index histogram

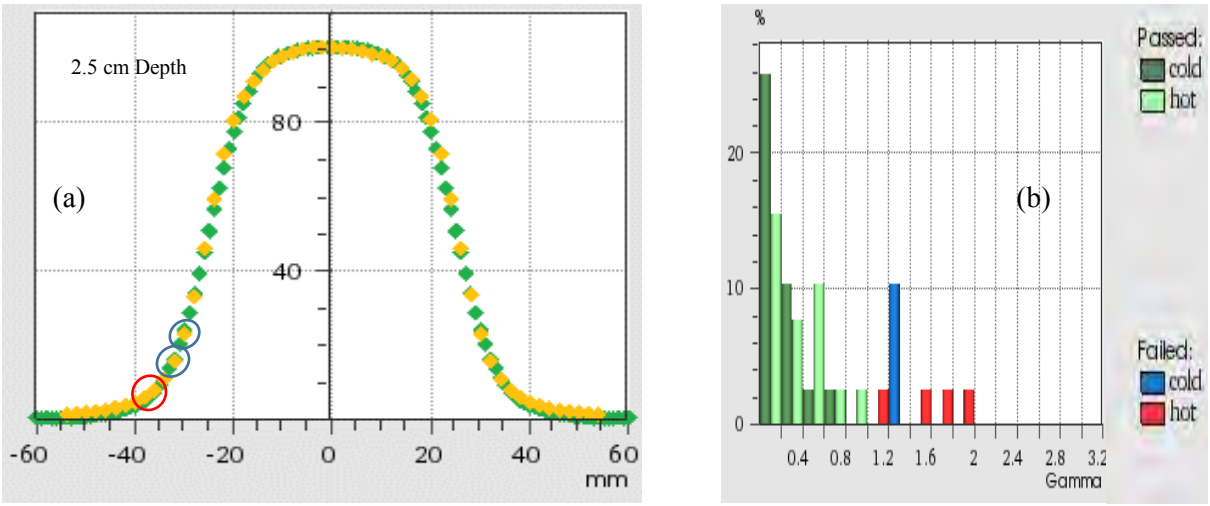

Figure 5.32 Comparison of measured and MC profiles at 2.5cm depth for 12 MeV 5 *cm* circle applicator: (a) Profile (b) Gamma Index histogram

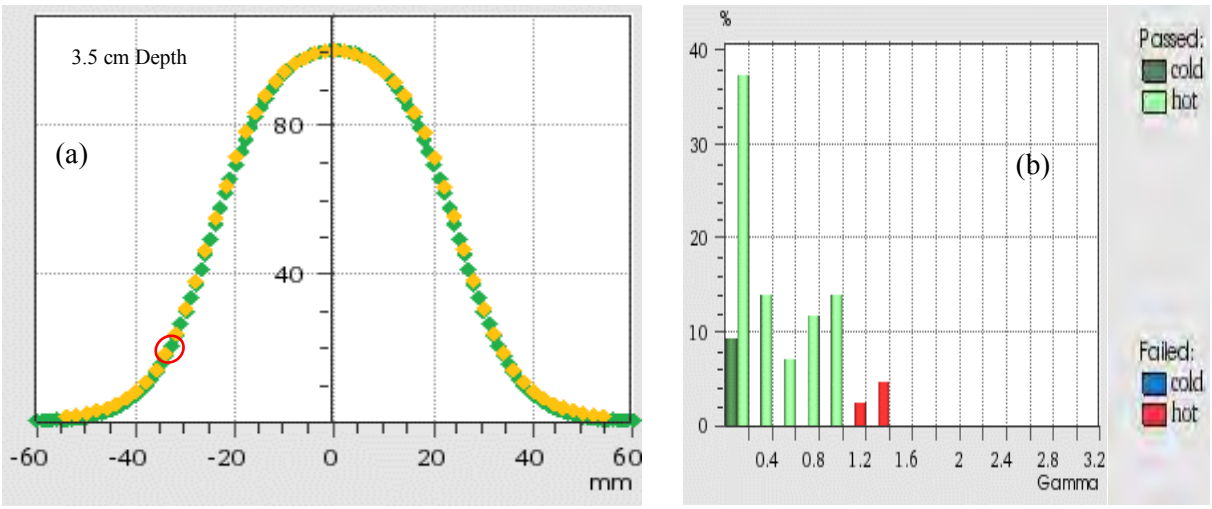

Figure 5.33 Comparison of measured and MC profiles at 3.5 cm depth for 12 MeV 5 *cm* circle applicator: (a) Profile (b) Gamma Index histogram

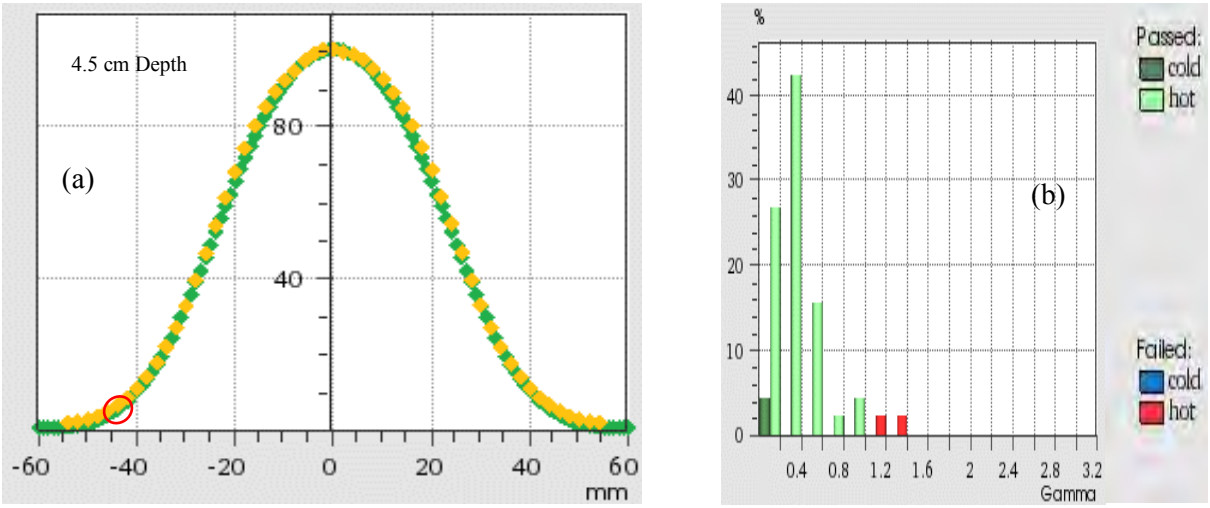

Figure 5.34 Comparison of measured and MC profiles at 4.5 cm depth for 12 MeV 5 *cm* circle applicator: (a) Profile (b) Gamma Index histogram

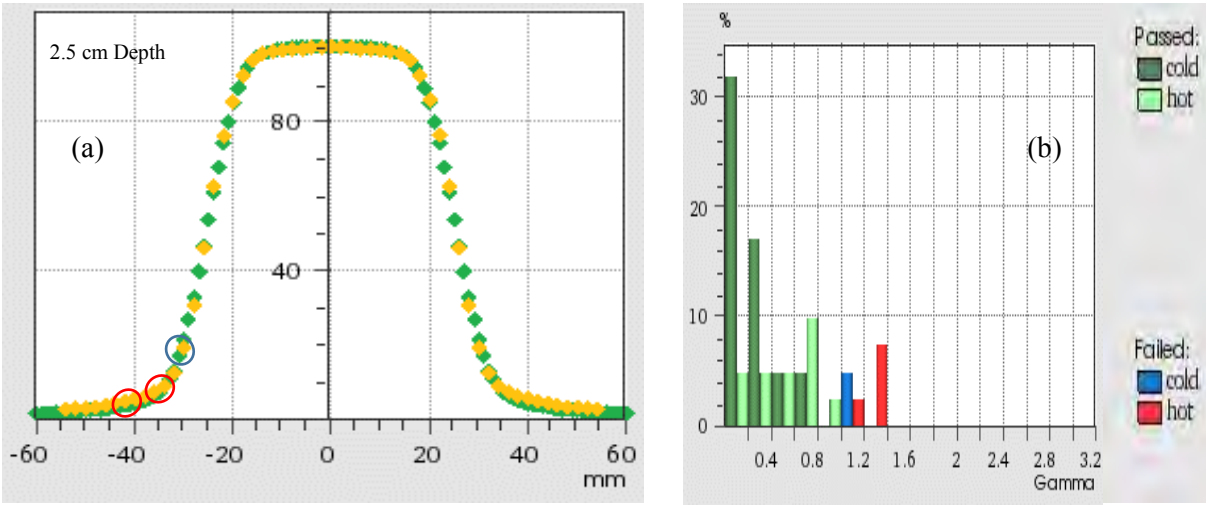

Figure 5.35 Comparison of measured and MC profiles at 2.5 cm depth for 18 MeV 5 *cm* circle applicator: (a) Profile (b) Gamma Index histogram

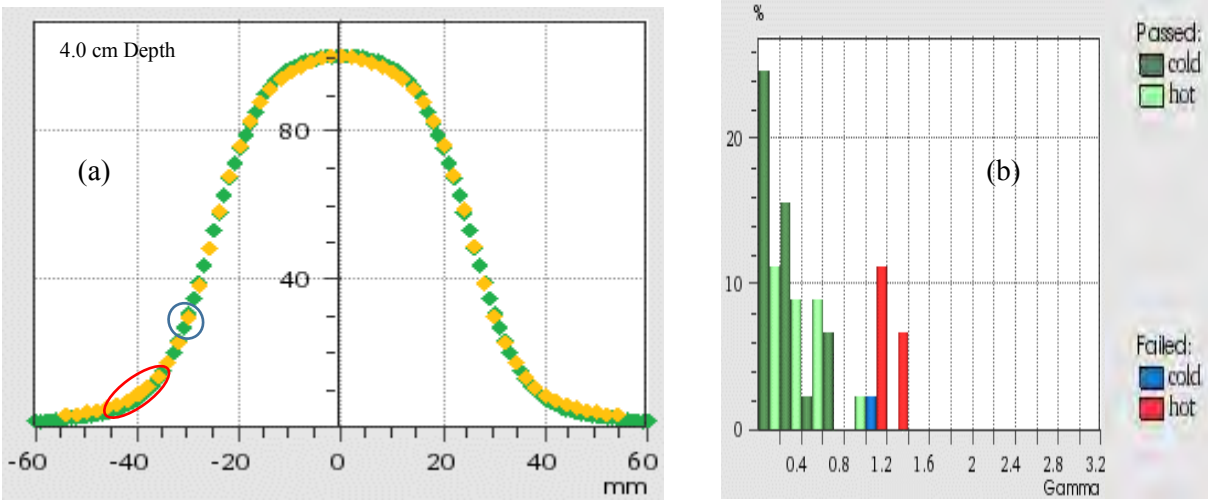

Figure 5.36 Comparison of measured and MC profiles at 4.0 cm depth for 18 MeV 5 *cm* circle applicator: (a) Profile (b) Gamma Index histogram

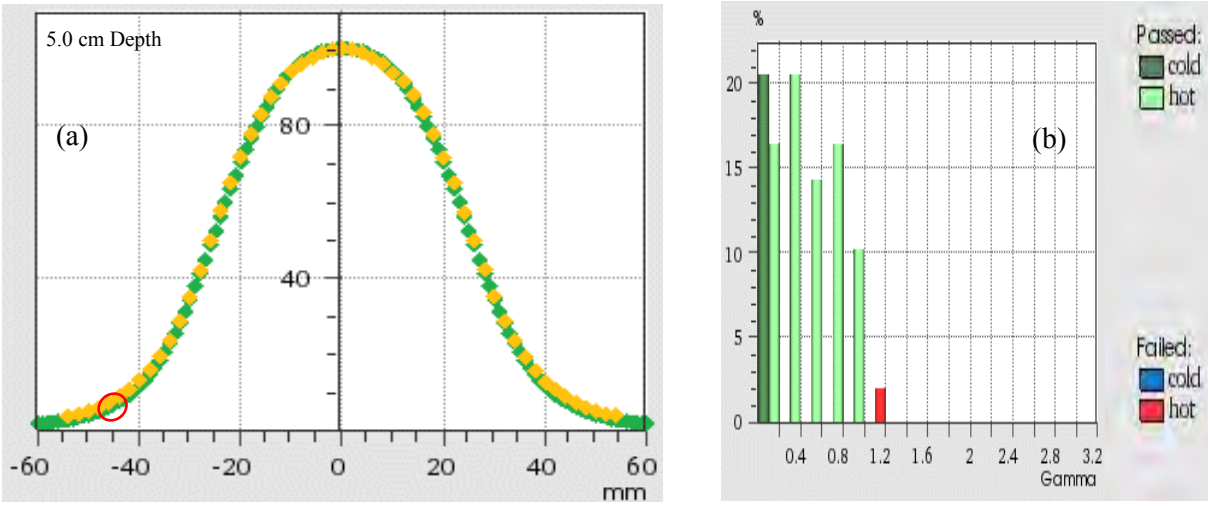

Figure 5.37 Comparison of measured and MC profiles at 5.0 cm depth for 18 MeV 5 *cm* circle applicator: (a) Profile (b) Gamma Index histogram

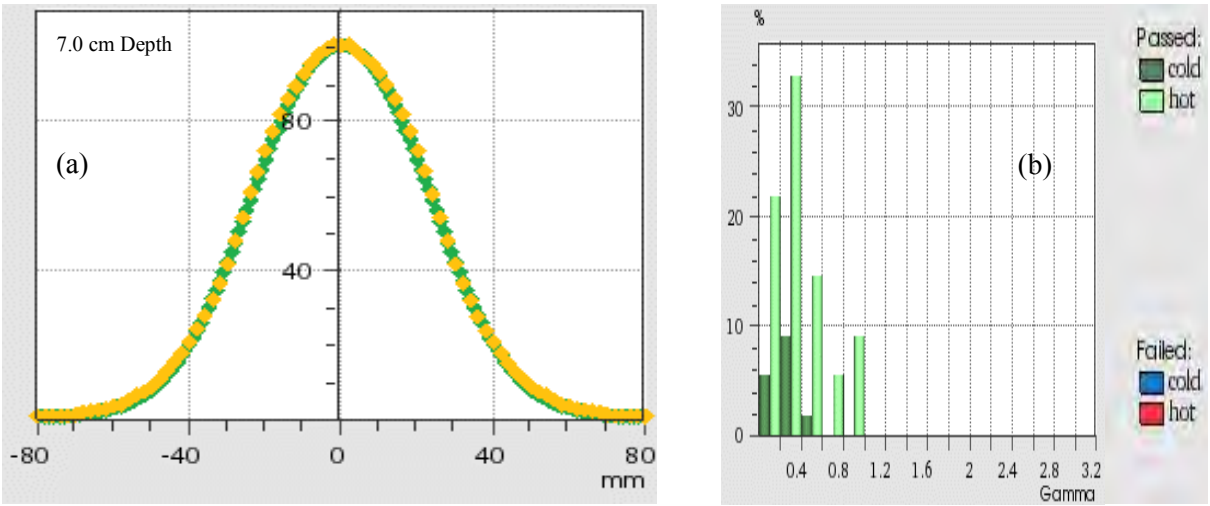

Figure 5.38 Comparison of measured and MC profiles at 7.0 cm depth for 18 MeV 5 *cm* circle applicator: (a) Profile (b) Gamma Index histogram

5.4.2.2.1 Analysis

6 MeV beam profile at 1.4 cm depth: Less than 3% of the points failed with a maximum γ of 2.0 beyond the field edge (lateral distance greater than 2.5 cm), where the calculated points were hotter than the measured points.

6 MeV beam profile at 2.0 cm depth: 8% of the failed points were hotter in the 40% dose region with γ of less than 1.4 at lateral distance 2.5 cm. A maximum γ of 2.4 is observed in the 3.5 cm to 4.0 cm range where calculated points were higher than measurement.

12 MeV beam profile at 2.5 cm depth: 2% of the failed points were hotter in the 8% dose regions with γ of less than 2.0 at lateral distance 3.5 cm. 10% of the failed points were colder in the 10% to 25% dose regions at lateral distances ranging from 2.8 cm to 3.2 cm.

12 MeV beam profile at 3.5 cm depth: 4% of the failed points were hotter in the 25% dose regions with γ of less than 1.4 at lateral distance 3.2 cm.

12 MeV beam profile at 4.5 cm depth: 2% of the failed points were hotter in the 5% dose regions with γ of less than 1.4 at lateral distance 0f 4.2 cm.

18 MeV beam profile at 2.5 cm depth: A maximum γ of 1.4 for 7% of the points is observed in the 3.2 cm to 4.8 cm range where calculated points were higher than measurement. 5% of failed points (γ of 1.1) were lower than measurement in the 15% to 20% dose regions at a lateral distance of 3.0 cm.

18 MeV beam profile at 4.0 cm depth: A γ of 1.4 and 1.2 for 7% and 11% of the points respectively is observed in the 3.5 cm to 4.5 cm range where calculated points were higher than measurement. A γ of 1.1 is observed for 2% of the points 255 to 30% dose regions at lateral distance of 3.0 cm.

18 MeV beam profile at 5.0 cm depth: A maximum γ of 1.2 for 4% of the points is observed in the 8% dose region at lateral distance of 4.5 cm where calculated points were higher than measurement.

18 MeV beam profile at 7.0 cm depth: All points passed the GI criteria for this profile

Further discussion and conclusions based on these results are reserved for the end of the chapter *(section 5.5).*

5.4.2.3 Applicator factors

When an applicator in the beam differs from the applicator used for the absolute dose reference calibration, the MU required to deliver a prescribed dose may be determined with the use of an applicator output factor (OF). This is accomplished by measuring the dose per

MU for the non-reference applicator (5 cm circle) and relating it to the dose per MU for the calibration geometry. The applicator output factor (OF) is defined as:

$$OF = \frac{D_{max}(E,X,100cm)}{D_{max}(E,10x10cm,100cm)} \quad (5.17)$$

where the numerator is the maximum dose on the central axis for a beam of energy E and applicator size X for 100 cm source to surface distance. The denominator is the maximum dose for 100 cm SSD for the same beam energy, E, with the $10x10cm$ applicator in place (reference geometry). Both numerator and denominator must be determined for the same number of monitor units.

The MU required to deliver the prescribed dose at depth z with the applicator X in place may then be calculated using the following equation:

$$MU_X = \frac{Prescribed\ dose\ (Gy) * 100MU/Gy}{OF * PDD_z} \quad (5.18)$$

where prescribed dose is the prescription dose at depth z for the applicator and PDD_z is the $PDD/100$ at depth z obtained from the applicator PDD curve.

In situations where extended SSDs are required and a gap (g) is necessary, an inverse square law factor may be applied to equation 5.18 using the effective SSD *(section 2.6.5.2)* to obtain the MU. Equation 5.18 thus becomes

$$MU_X = \frac{Prescribed\ dose * 100MU/Gy}{OF * PDD_z} * \left(\frac{SSD_{eff}+g}{SSD_{eff}}\right)^2 \quad (5.19)$$

The electron Dosimetry Diode E (PTW type 60017, Freiburg, Germany) was used to measure the applicator factors for the 5 cm circle applicator. Measurements were performed at d_{max} for the non-reference field (5 cm circle applicator) and the reference field ($10x10$ cm open applicator). The resulting applicator factor for each energy *(table 5.11)* was calculated as per equation 5.17 above.

Three measurements were taken for each energy and the standard deviation for each set of measurements was calculated according to the following equation:

$$SD = \sqrt{\left(\frac{\sum_{i=1}^{n}(x_i - \bar{x})^2}{(n-1)}\right)} \quad (5.20)$$

where SD is the standard deviation

x_i is the i^{th} measurement

$\bar{x}$ is the mean of the three measurements

n is the total number of measurements

Since the applicator factor is a ratio of the mean of each set of measurements, the standard deviation for the resulting applicator factors is given by summing the standard deviation of each set of measurements.

The MC-calculated output factor was obtained by analysing the 3-d dose distribution for the $10x10cm$ and 5 cm circle applicators in STATDOSE and relating the doses at the respective d_{max} depths as per equation 5.17. A comparison between the measured and MC-calculated output factors for the 5 cm circle applicator appear in table 5.11 below, with the uncertainty in measurements being determined utilising equation 5.20.

The statistical variance was less than 1% for all output factors determined by Monte Carlo calculations *(section 4.3.4)*.

Table 5.11 Comparison of measured and MC-calculated Applicator factors for the 5 cm circle applicator for energies 6, 12 and 18 MeV.

	6 MeV			**12 MeV**			**18 MeV**		
	Meas	**MC**	**%Diff**	**Meas**	**MC**	**%Diff**	**Meas**	**MC**	**%Diff**
Applicator Factor	0.797 ±0.003	0.789	-1.00	0.930 ±0.003	0.920	-1.08	0.975 ±0.002	0.969	-0.62

The variation of measured and calculated applicator factor with energy for the 5 cm circle applicator is shown in figure 5.39 below.

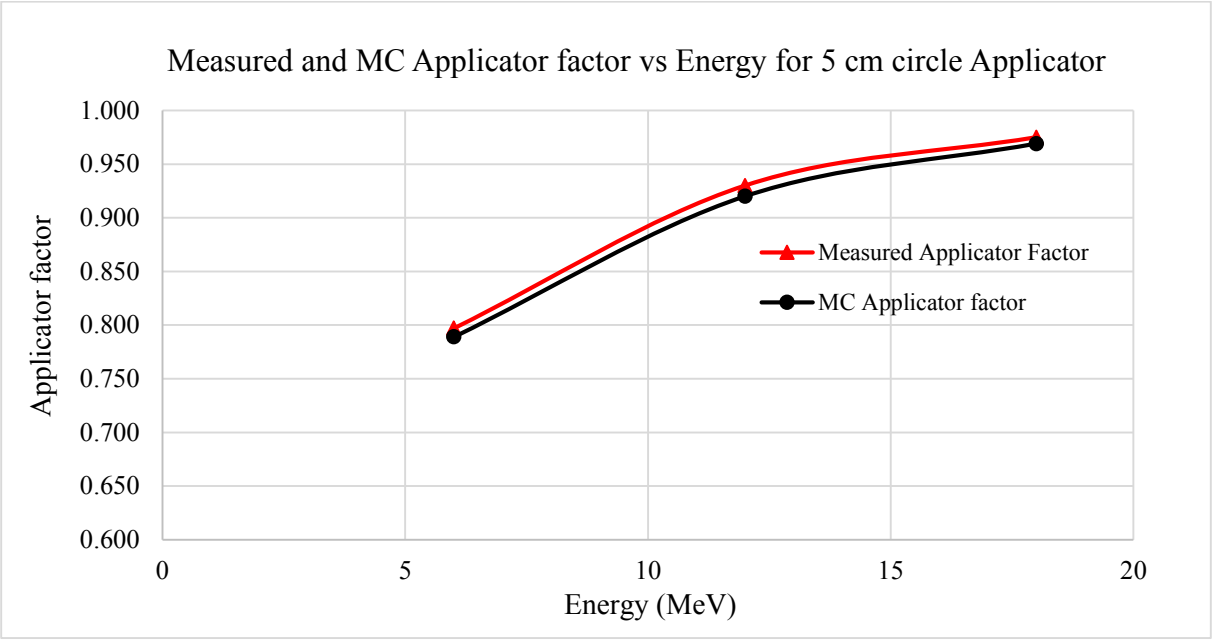

Figure 5.39 Plot of measured and MC-calculated Applicator factor vs electron energy for the 5 cm circle standard applicator.

5.4.2.3.1 Analysis

A maximum difference of 1.08% in applicator factor is observed (12 MeV) with all calculated factors being lower than measurement. The applicator factor increased with an increase in energy.

5.5 Discussion and Conclusion

The objective of this chapter was to perform Monte Carlo commissioning of the Siemens Primus LINAC for 6 MeV, 12 MeV and 18 MeV electron beams using the standard $10x10\ cm$ and $5\ cm$ circle applicators. The commissioning process involves obtaining acceptable comparisons between the MC-calculated beam data and measurements using acceptance criteria based on clinically accepted beam data tolerances *(Antolak 2002)*. The MC commissioning task was accomplished by first building the accelerator in BEAMnrc with the aid of the component modules available in the code. Detailed descriptions of the dimensions and material composition of each of the treatment head components as supplied by the vendor were used to facilitate the process. The phase space file from the BEAMnrc simulation was used as the input source for DOSXYZnrc. This MC simulation code produced 3-d dose

distributions from which the relevant PDD and profiles were obtained for comparison with measured data.

Methodologies in achieving high levels of accuracy in matching MC calculations with measurements have been published *(Faddegon et al 2000)*. Unacceptable comparisons would imply the need to firstly further investigate the accuracy and validity of the measurements. If this is found to be error-free and as accurate as possible, the entire MC modelling process would need to be scrutinised to ensure that the CMs and input parameters used in the MC build of the accelerator are correct *(Antolak 2002)*. Acceptable agreements would suggest successful completion of the commissioning process which would justify subsequent use of the method and input parameters for further investigations.

The incident electron energy has been found to be the primary tuning parameter for electron beam simulations *(Chetty et al 2007),* where it is stated that a 0.2 MeV change in electron energy results in a 1 mm change in beam range. For this study, numerous failed attempts at getting acceptable PDD and profile comparisons using mono-energetic sources led to the use of incident electron energy spectra as input. The relative intensities of each of the 5 energy bins of each spectrum were manipulated *(section 5.1.4.1)* until acceptable comparisons were obtained. Acceptable comparisons were only obtained after 35, 7 and 22 attempts for the 6 MeV, 12 MeV and 18 MeV beams respectively. This tedious process may be circumvented by deriving electron spectra from depth dose distributions *(Faddegon & Blevis 2000)*.

The MC-calculated PDDs initially obtained in the course of this study yielded unacceptable comparisons whereby there was a considerable lack of dose in the bremsstrahlung tail. Upon further investigation, it was found that the primary scattering foil had been inadvertently left out of the build in BEAMnrc. This error was corrected and the results subsequently obtained satisfied the acceptance criteria for the $10x10\ cm$ applicator.

The PDD comparison for the $10x10\ cm$ applicator proved to be favourable as direct comparison of R_{max}, R_{90}, R_{80}, and R_{50} yielded differences of less than 1 mm.

For the $5\ cm$ circle applicator, a maximum difference of 1 mm was observed in R_{max} for the 18 MeV beam, with all other differences being less than 0.5 mm.

For the $10x10\ cm$ applicator, the calculated surface dose for 18 MeV fell below the acceptance criteria. This difference was reduced within the first 2.5 mm of the beam and would not have an appreciable effect on clinical outcomes. A 3.0% difference in surface dose was observed for the $5\ cm$ circle applicator case. This was also reduced within the first 2.5 mm of the beam.

The comparisons in the therapeutic range and from R_{80} to R_{20} satisfied the acceptance criteria for all the beams, even though the measured PDD fell off more rapidly than the calculated PDDs for the $10x10\ cm$ applicator.

The discrepancies observed at dose levels below 10% may be ignored since this portion of the curve is attributed to contaminant photons (bremsstrahlung) and falls well beyond the therapeutic range. Care must however be taken to ensure that critical structures at the distal end of the beam are avoided. The PDD comparisons showed acceptable results satisfying the GI criteria in this portion of the beam.

The differences in the PDD curves at the surface and in the build-up regions are generally attributed to scattered electrons from the phantom, chamber type, and the choice of the effective point of measurement *(Omer 2012).* The high dose gradient in this region makes ionisation chamber measurements unreliable *(Hosntalab et al 2012)*. Perturbation of the absorbed dose due to the finite size of the ionisation chamber is yet another source of error *(Siebers et al 1999).* Accurate tuning of the incident electron energy spectrum may also be a source of error *(Chetty et al 2007).* Discrepancies may also be due to inaccurate determination

of the true zero depth. The effective point of measurement for the pinpoint chamber was taken into account for all measurements *(section 4.2)*. The equivalent thickness of the chamber wall was determined to be 0.23 mm *(section 4.2)* and was not taken into account in detector positioning for the PDDs as it was deemed to be negligible *(IAEA 2000)*. Inclusion of this parameter would have decreased the measured surface doses, thereby decreasing the differences between measurement and calculation. It may be noted that despite the mismatch at these points, the differences in general are within the 3%/3 mm range.

For the $10x10\ cm$ applicator, the comparison of the generated profiles with measured data showed discrepancies only in the high dose gradient regions at the extreme lateral extents of the beams. The minimum lateral distance displaying this discrepancy was 5 cm for the 12 MeV profile at 2.5 cm depth. The maximum number of points that failed the GI criteria for the profile comparisons was 6%. The GI was 1.1 for his case. There were no points in the -60% to +60% range that failed the GI criteria of 3%/3 mm. The beam profiles for the $10x10\ cm$ applicator was therefore deemed to be acceptable as discrepancies were outside the useful portion of the beam.

Similar results were observed for the $5\ cm$ circle standard applicator, where the minimum lateral distances displaying discrepancies was 2.5 cm for the 6 MeV profile at 2.0 cm depth. All other failed points occurred beyond the lateral distance of 3.0 cm. There were no points in the central 80% region of the beam that failed the GI criteria of 3%/3 mm.

Applicator factors for the $5\ cm$ circle applicator increased with an increase in energy. The differences in calculated and measured applicator factors for the $5\ cm$ circle standard applicator were negligible (maximum of 1.08% for the 12 MeV beam) with calculated values being lower than measured values for all three energies *(figure 5.39)*. These results would imply that the MC-calculated applicator factor may therefore be used for MU calculations for the $5\ cm$ circle applicator.

It is well documented that greater accuracy is achieved with appropriately small voxel sizes *(Chetty et al 2007)*, by simulating an adequate number of histories *(Rogers et al 1995)*, and by modifying the energy spectrum of the source *(Ma & Jiang 1999)*. In this study, the voxel sizes are deemed to be appropriate and sufficient histories were simulated in both BEAMnrc and DOSXYZnrc to reduce the statistical variance to below 1%. It may therefore be concluded that the differences between measurement and calculation are systematic and arise due to the inaccurate modelling of the LINAC. Inaccuracies may result from the fact that the actual input electron source geometry and spectral distribution is not known in detail. Inaccurate set-up of the scanning system and in-accurate placement of the ionisation chamber may also lead to discrepancies in the commissioning process *(Chetty et al 2007)*. It is also imperative that the treatment head component details provided by the vendor be accurate *(Rogers et al 1995, Bieda et al 2001)*. Modifications made to these components subsequent to the supply of data must be incorporated into the build.

Specifications of the treatment head components as supplied by vendors have been found in many cases to be unreliable *(Rogers et al 1995)* and sometimes incomplete *(Verhaegen 2001)*. This has been attributed mainly to the reluctance of vendors to divulge detailed specifications necessary for accurate MC modelling due to the commercial value of the accelerator parts *(Ma & Jiang 1999).*

The results presented above provide acceptable agreement with measured data and the conclusion is that the Monte Carlo commissioning of the Siemens Primus LINAC for 6 MeV , 12 MeV and 18 MeV electron beams was successful and may be used to perform further calculations for more complex geometries *(Chapters 6 and 7)*.

CHAPTER 6

COMPARISON OF MC SIMULATIONS AND MEASUREMENTS WITH IORT OPEN CONES

The Intra-Operative Periscopic Cone system (Radiation Products Design Inc., Albertville, USA) model 1100-00 was used on the Siemens Primus LINAC for this study. A detailed description of the system is given in section 2.5.

6.1 BEAMnrc modelling of the IORT accelerator with open cones

Building of the LINAC with the IORT open cones in place is accomplished by replacing the $10x10\ cm$ applicator, which starts at z = 56 cm, by each of 3 open IORT cones, which start at z = 42 cm. The 3.1 mm thick clear PMMA cones utilised in this study had inner diameters of 19 mm, 45 mm and 64 mm along their 30.5 cm lengths.

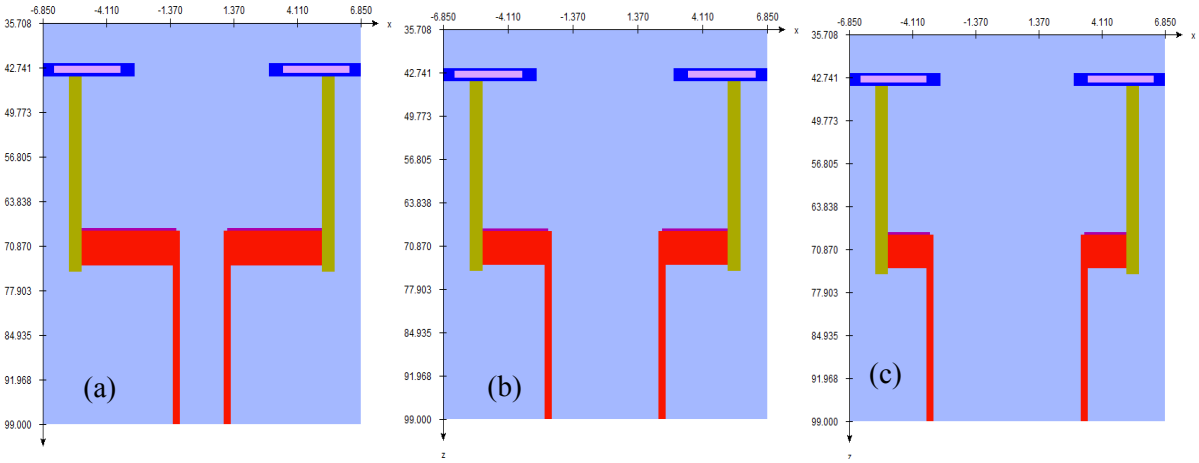

Figure 6.1 BEAMnrc build of the IORT cones used in this study (a) 19 mm cone (b) 45 mm cone and (c) 64 mm cone

The same main input parameters *(table 5.1)*, EGSnrc parameters *(table 5.2)* and source for each energy *(section 5.1.4.1)* as for the $10x10\ cm$ applicator case was used as input for the IORT open cone cases. Use of these sources produced PDDs *(section 5.3.2)* and beam profiles *(section 5.3.3)* for the $10x10\ cm$ applicator that compared favourably with measured data and were thus deemed to be acceptable for further investigations.

The exact same primary scattering foil for each energy, primary collimator, secondary scattering foil, chamber and mirror modelled for the $10x10\ cm$ applicator case was used to model the IORT accelerator. The $10\ x10\ cm$ applicator was replaced by each cone in turn. The Y-jaw and MLC setting was kept at $19\ cm\ x\ 19\ cm$.

The FLATFILT CM was used to build the cones in BEAMnrc. Each cone consists of 9 layers with varying numbers of conical sections in each layer.

The same jaw settings (Y = 19.0 cm and MLC(X) = 19.0 cm) used for the MC simulation for the $10x10\ cm$ applicator was used for each cone. The dimensions and material composition of the various components of the cone were obtained from the manufacturer. The top of the barrel assembly has a 1.27 cm lead plate with a circular hole inside it to provide initial collimation of the electrons exiting the treatment head. Each cone consists of a 4.8 mm thick brass plate (with a centre hole of diameter slightly larger than the cone inner diameter) at the top to collimate the beam to prevent electrons from penetrating the PMMA spacer rings.

For this study, the cone was slid 1 cm into the barrel assembly so that the open end of the cone was at a z distance of 99 cm, resulting in a 1 cm gap between the cone end and the isocentre.

Monte Carlo simulations were performed for each energy (6 MeV, 12 MeV and 18 MeV) for each cone (19 mm, 45 mm and 64 mm). Phase-space files were scored at the open end of the cone.

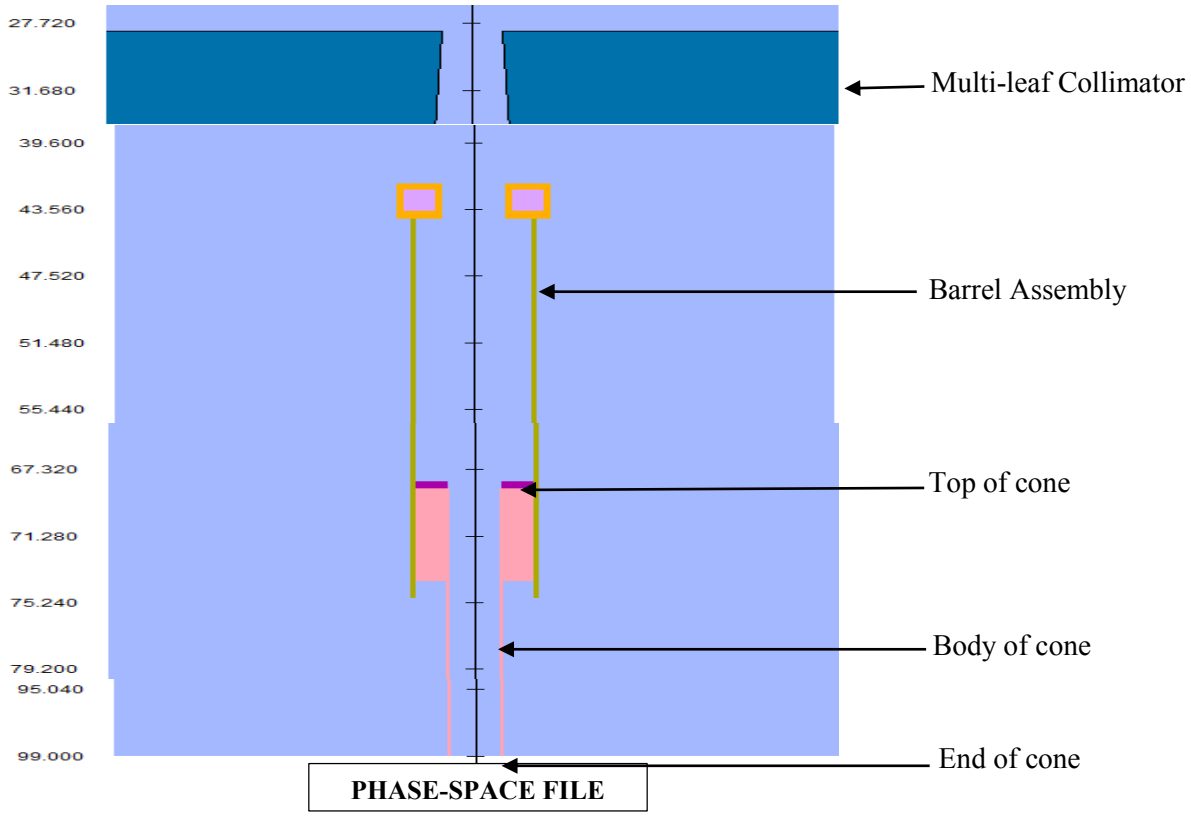

Figure 6.2 BEAMnrc representation of the 45 mm IORT cone position relative to the MLC and phase space file.

Each PSF was used, in turn, as the input source in DOSXYZnrc. The homogenous water equivalent phantom and source parameters were unchanged from the previous DOSXYZnrc simulations. 3-D dose distributions were obtained from the simulations for each energy/cone combination.

Table 6.1 Summary of particles in the Phase-Space file for the 19 mm IORT open cone

ENERGY (MeV)	Total number of particles	Total number of photons	% Photons	% electrons/positrons	Max kinetic energy (MeV)
6	752 035	734 639	97.7	2.3	8.277
12	1 152 802	1 126 839	97.7	2.3	16.149
18	1 642 937	1 612 751	98.2	1.8	21.517

Table 6.2 Summary of particles in the Phase-Space file for the 45 mm IORT open cone

ENERGY (MeV)	Total number of particles	Total number of photons	% Photons	% electrons/positrons	Max kinetic energy (MeV)
6	456 097	387 011	84.9	15.1	8.228
12	1 275 516	1 138 383	89.2	10.8	15.937
18	2 167 441	2 029 535	93.6	6.4	21.747

Table 6.3 Summary of particles in the Phase-Space file for the 64 mm IORT open cone

ENERGY (MeV)	Total number of particles	Total number of photons	% Photons	% electrons/positrons	Max kinetic energy (MeV)
6	1 742 332	1 285 004	73.6	26.4	8.245
12	1 408 549	1 146 504	81.4	18.6	15.799
18	2 281 001	2 033 067	89.1	10.9	21.643

6.2 Measured data of the IORT accelerator with open cones

The MP3 3-D therapy beam analyser (PTW, Freiburg, Germany) operated by Mephysto mc^2 software was used to acquire the relevant data for the 6 MeV, 12 MeV and 18 MeV electron beams for each IORT cone of diameter 19 mm, 45 mm and 64 mm. The waterproof Pinpoint ionisation chamber (PTW type 31006, Freiburg, Germany) with a measuring volume of 0.015 cm^3 was used as the field chamber to minimise errors due to the small fields used in this study. The semi-flex chamber (PTW type 31010, Freiburg, Germany) with a nominal sensitive volume of 0.125 cm^3 was used as the reference chamber and was placed at the top of the barrel assembly *(figure 6.3)*.

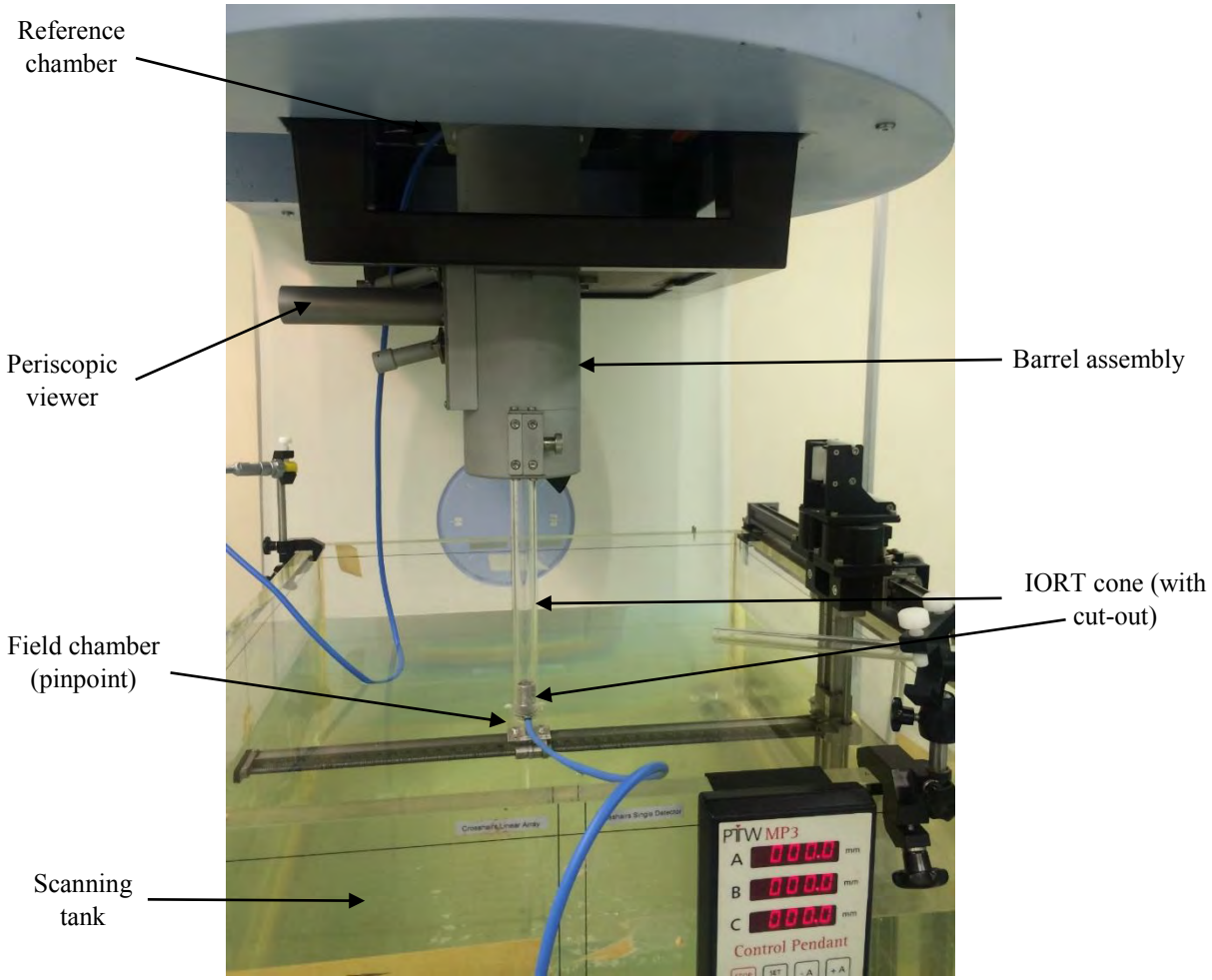

Figure 6.3 Measurement set-up for electron PDD and profile acquisition for the Siemens Primus LINAC with an IORT cone (with cut-out) using the PTW MP3 therapy beam analyser.

Central axis percentage depth dose (PDD) curves and in-plane and cross-plane profiles were measured with step sizes of 1 mm for the PDDs and 2 mm for the profiles for each of the 3 energies. This was done so that the measured data points corresponded to the MC data points which is defined by the voxel dimensions in DOSXYZnrc *(section 5.2.1)*.

The depths at which the profiles were acquired are specified in table 6.4 below

Table 6.4 Profile depths acquired for 6 MeV, 12 MeV and 18 MeV beams for the IORT open cones

	Depth 1 (cm)	Depth 2 (cm)	Depth 3 (cm)	Depth 4 (cm)
6 MeV	1.4	2.0	-	-
12 MeV	2.5	4.0		-
18 MeV	2.5	4.5	5.5	6.5

The MC and measured data was modified and converted as described in chapter 4.

6.3 Results

6.3.1 Percentage Depth Dose (PDD) results

Tables 6.5, 6.6 and 6.7 below show the absolute differences of pertinent characteristic MC-calculated points (defined in section 2.6.1) relative to measurements for the 19 mm, 45 mm and 64 mm IORT cones respectively for 6 MeV, 12 MeV and 18 MeV PDD curves.

Table 6.5 Absolute differences between measured and MC-calculated characteristic points on the PDD curve for the 19 mm IORT Open cone for energies 6, 12 and 18 MeV.

	6 MeV			12 MeV			18 MeV		
	Meas	**MC**	**Diff**	**Meas**	**MC**	**Diff**	**Meas**	**MC**	**Diff**
D_s (%)	95.1	90.7	**-4.4**	93.7	92.3	**-1.4**	94.9	92.2	**-2.7**
R_{max} (cm)	0.60	0.75	**0.15**	1.20	1.15	**-0.05**	1.35	0.95	**0.40**
R_{90} (cm)	1.19	1.33	**0.14**	2.21	2.10	**-0.11**	2.70	2.64	**0.06**
R_{80} (cm)	1.48	1.58	**0.10**	2.60	2.48	**-0.12**	3.28	3.17	**0.11**
R_{50} (cm)	2.05	2.13	**0.08**	3.50	3.44	**-0.06**	4.53	4.51	**0.02**

Table 6.6 Absolute differences between measured and MC-calculated characteristic points on the PDD curve for the 45 mm IORT Open cone for energies 6, 12 and 18 MeV.

	6 MeV			12 MeV			18 MeV		
	Meas	**MC**	**Diff**	**Meas**	**MC**	**Diff**	**Meas**	**MC**	**Diff**
D_s (%)	78.6	76.5	**-2.1**	90.6	87.6	**-2.4**	93.9	88.3	**-5.6**
R_{max} (cm)	1.20	1.25	**0.05**	2.10	1.95	**-0.15**	1.95	2.05	**0.10**
R_{90} (cm)	1.81	1.77	**-0.04**	3.31	3.34	**0.03**	4.32	4.25	**-0.07**
R_{80} (cm)	1.99	1.93	**-0.06**	3.78	3.75	**-0.03**	5.02	4.94	**-0.08**
R_{50} (cm)	2.39	2.37	**-0.02**	4.65	4.66	**0.01**	6.60	6.47	**-0.13**

Table 6.7 Absolute differences between measured and MC-calculated characteristic points on the PDD curve for the 64mm IORT Open cone for energies 6, 12 and 18 MeV.

	6 MeV			12 MeV			18 MeV		
	Meas	**MC**	**Diff**	**Meas**	**MC**	**Diff**	**Meas**	**MC**	**Diff**
D_s (%)	78.0	77.1	**-0.9**	84.6	87.2	**2.6**	95.1	93.5	**-1.6**
R_{max} (cm)	1.30	1.35	**0.05**	2.60	2.45	**-0.15**	1.80	0.95	**-0.95**
R_{90} (cm)	1.75	1.77	**0.02**	3.71	3.46	**-0.25**	4.50	4.36	**-0.14**
R_{80} (cm)	1.95	1.97	**0.02**	4.08	3.90	**-0.18**	5.38	5.30	**-0.08**
R_{50} (cm)	2.37	2.38	**0.01**	4.83	4.81	**-0.02**	6.87	6.85	**-0.02**

For the GI PDD comparison, the %dose difference, DoN (in % of normalization value of the reference matrix) parameter was used. The measured data was used as the reference matrix with the MC data as the secondary data set.

The passing criteria set was DoN ≤ 3.0%. Green bars in the histogram represents the %pass at each %difference level (x axis).

The statistical variance was less than 1% for all Monte Carlo PDD calculations *(section 4.3.4)*.

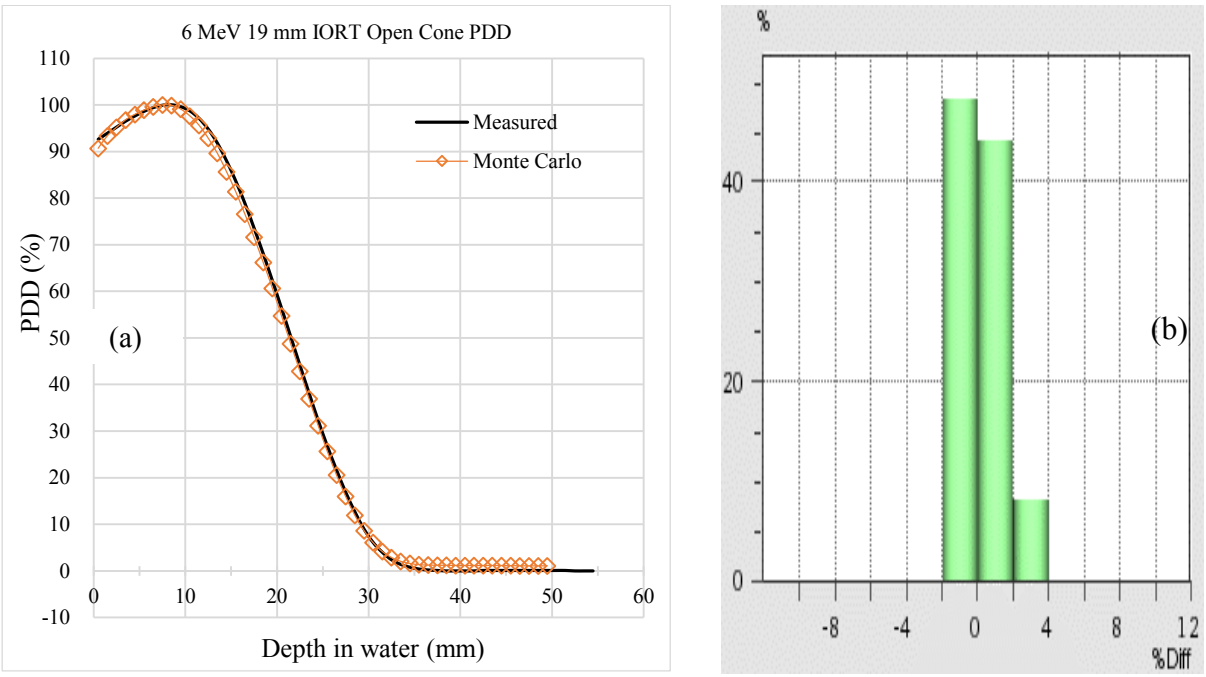

Figure 6.4 Comparison of measured and MC PDDs for 6 MeV 19 mm IORT Open Cone: (a) PDD (b) % dose difference histogram

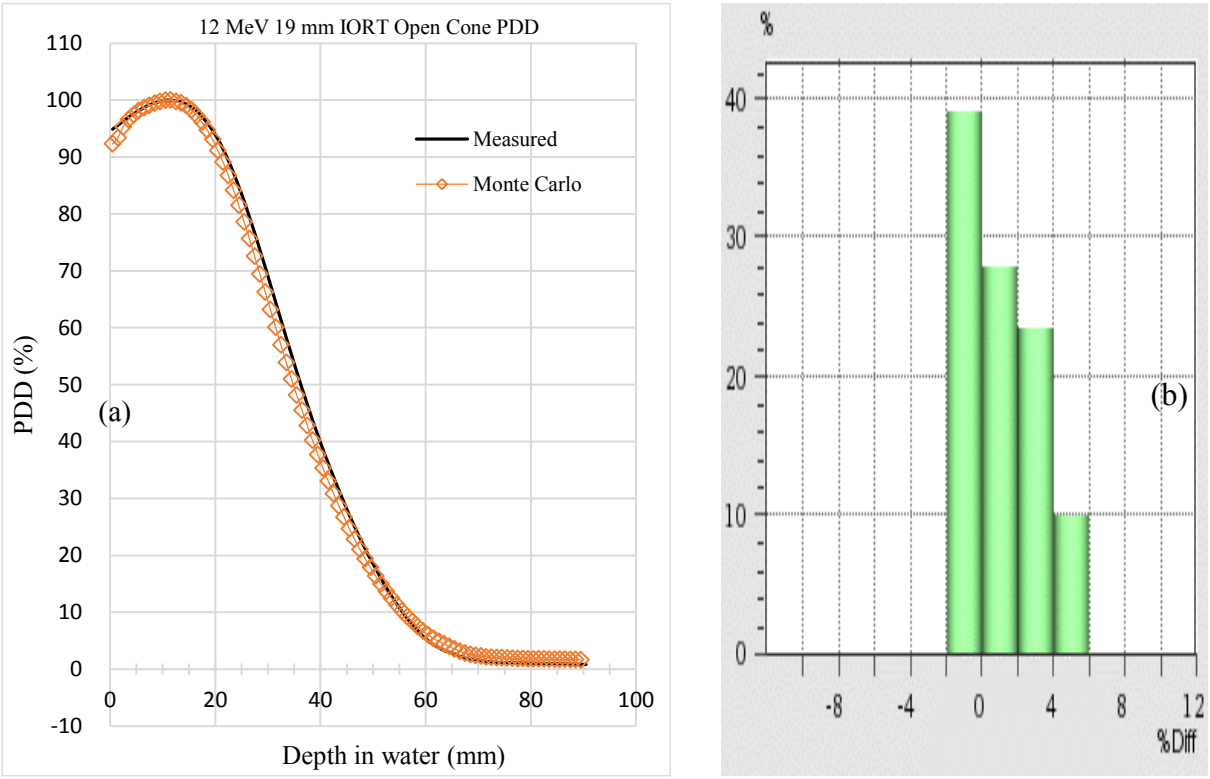

Figure 6.5 Comparison of measured and MC PDDs for 12 MeV 19 mm IORT Open Cone: (a) PDD (b) % dose difference histogram

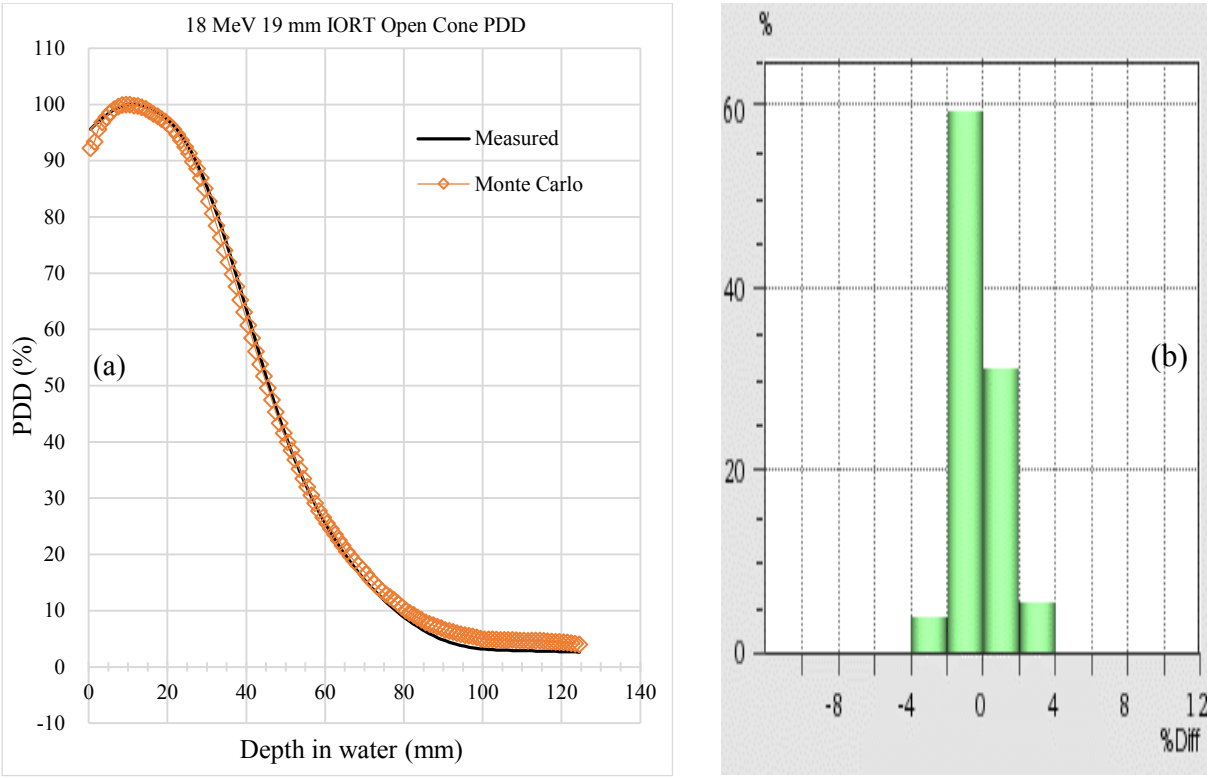

Figure 6.6 Comparison of measured and MC PDDs for 18 MeV 19 mm IORT Open Cone: (a) PDD (b) % dose difference histogram

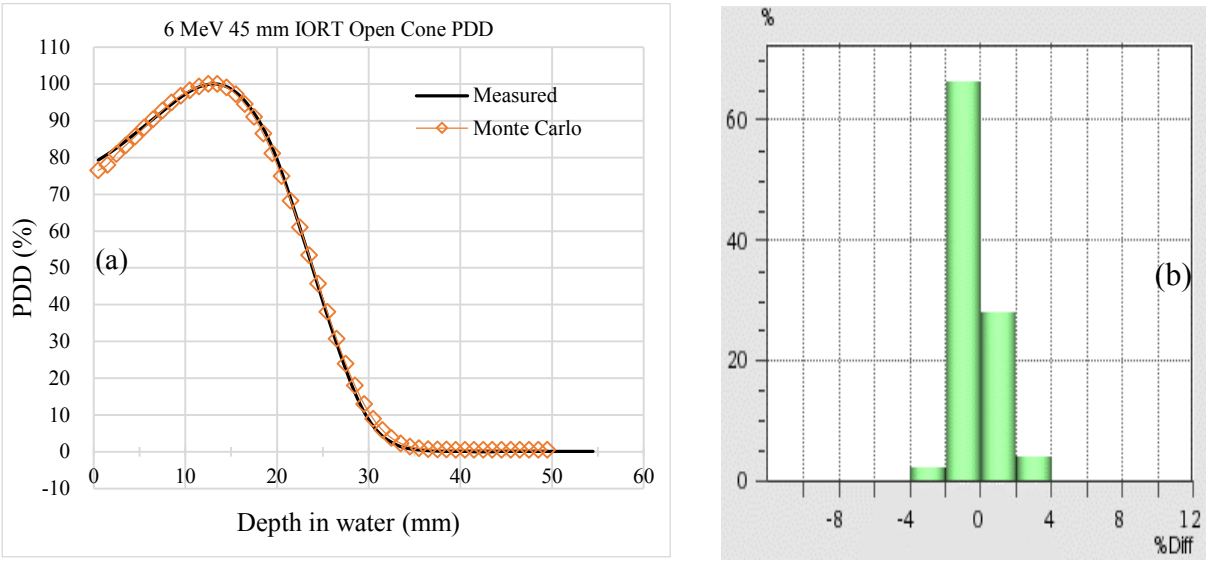

Figure 6.7 Comparison of measured and MC PDDs for 6 MeV 45 mm IORT Open Cone: (a) PDD (b) % dose difference histogram

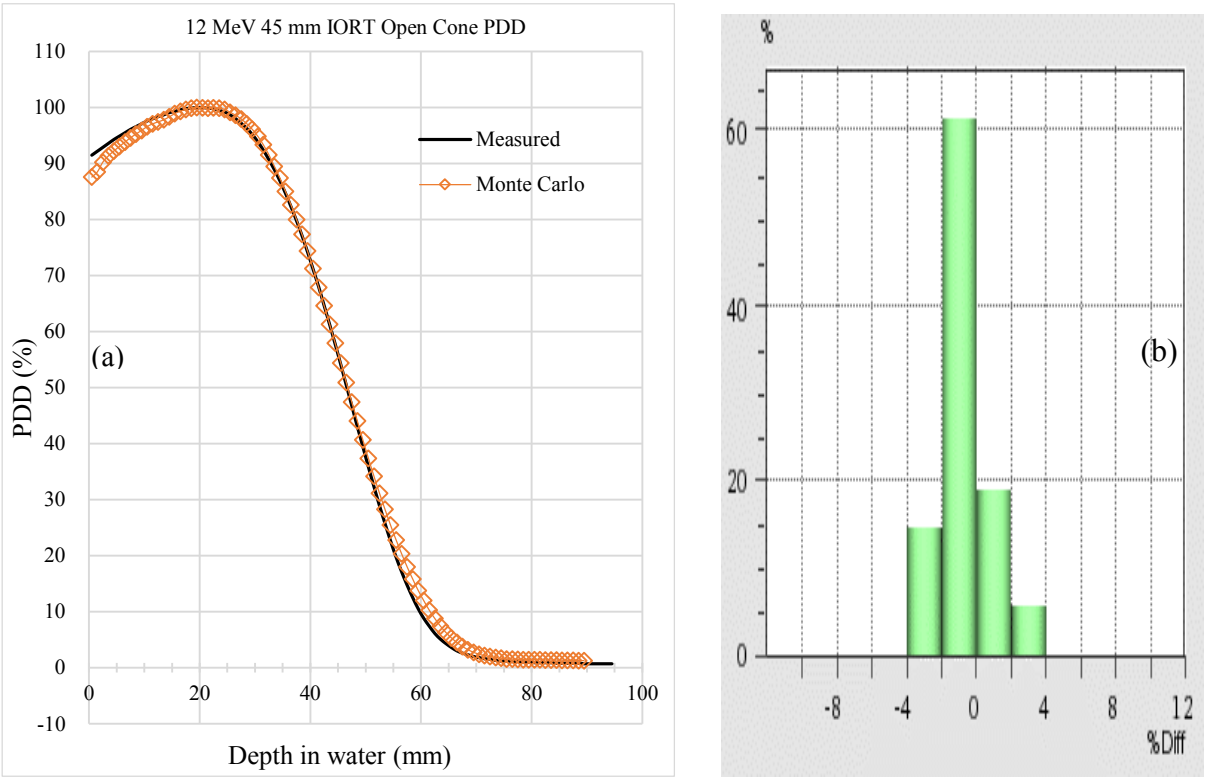

Figure 6.8 Comparison of measured and MC PDDs for 12 MeV 45 mm IORT Open Cone: (a) PDD (b) % dose difference histogram

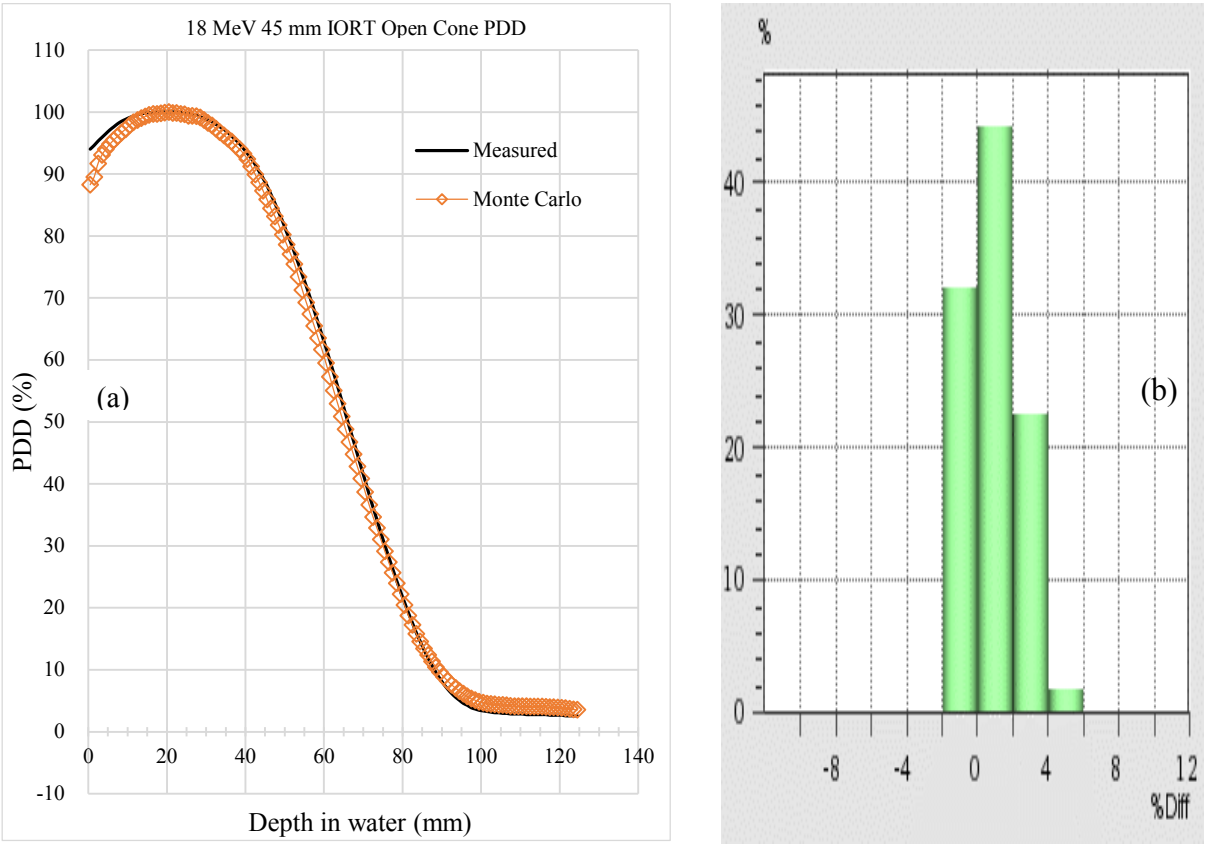

Figure 6.9 Comparison of measured and MC PDDs for 18 MeV 45 mm IORT Open Cone: (a) PDD (b) % dose difference histogram

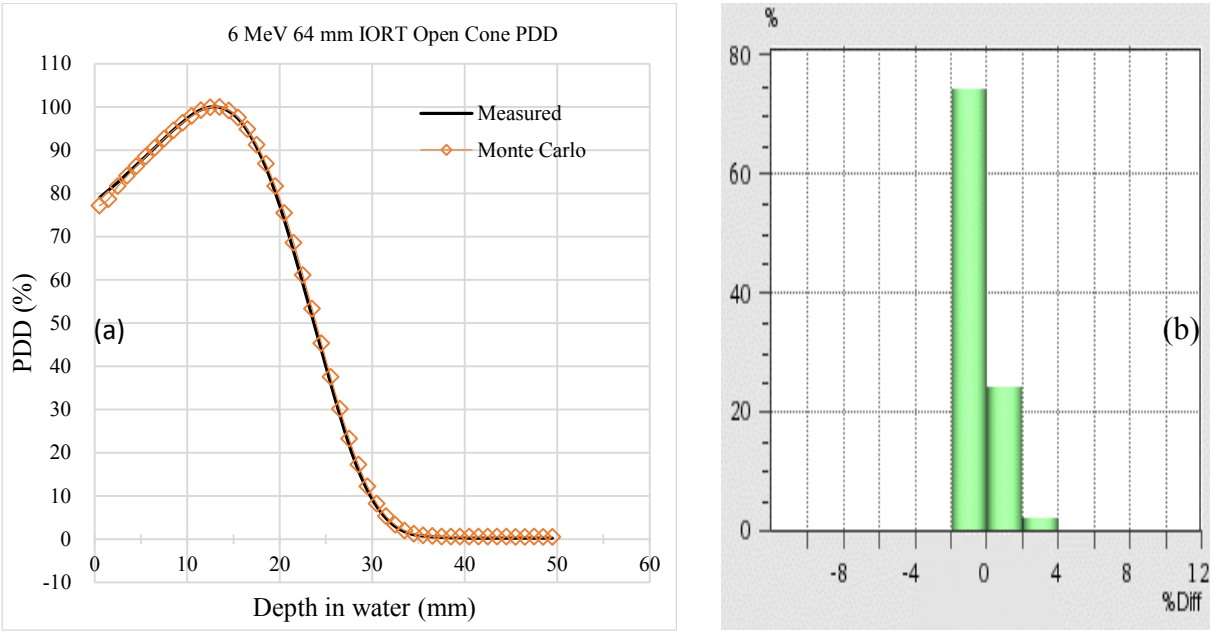

Figure 6.10 Comparison of measured and MC PDDs for 6 MeV 64 mm IORT Open Cone: (a) PDD (b) % dose difference histogram

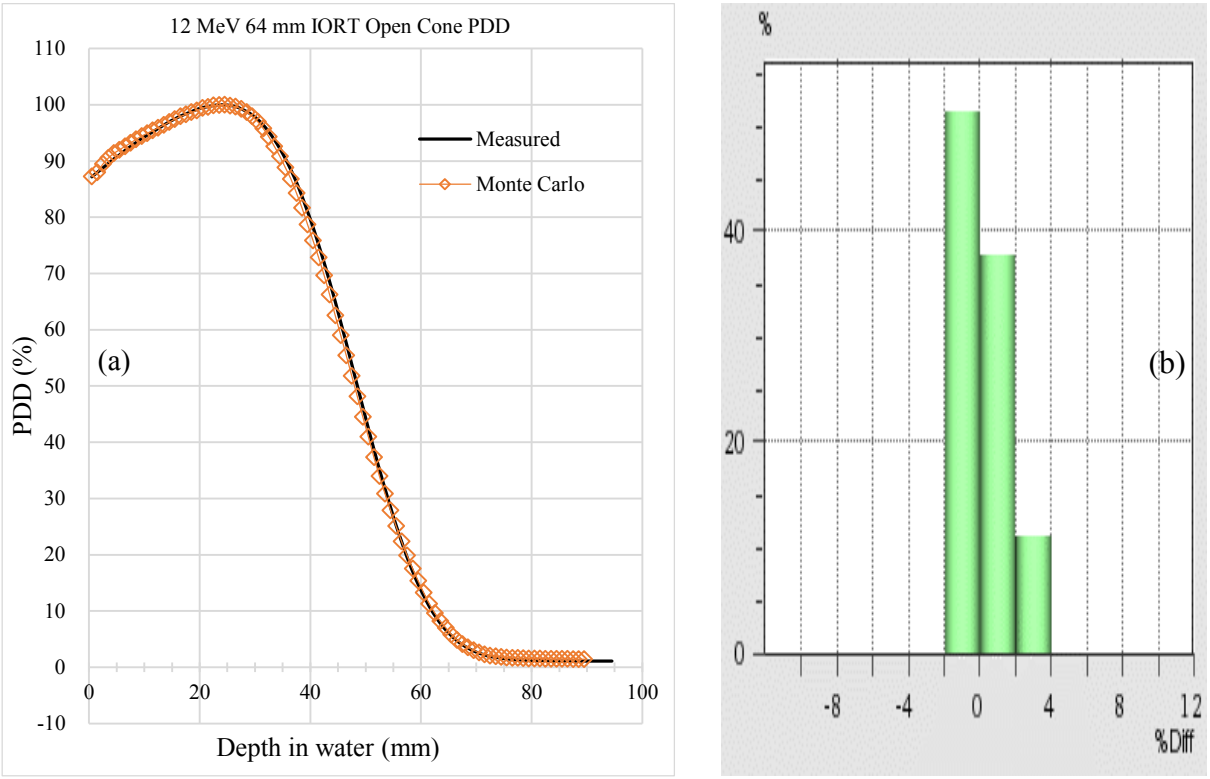

Figure 6.11 Comparison of measured and MC PDDs for 12 MeV 64 mm IORT Open Cone: (a) PDD (b) % dose difference histogram

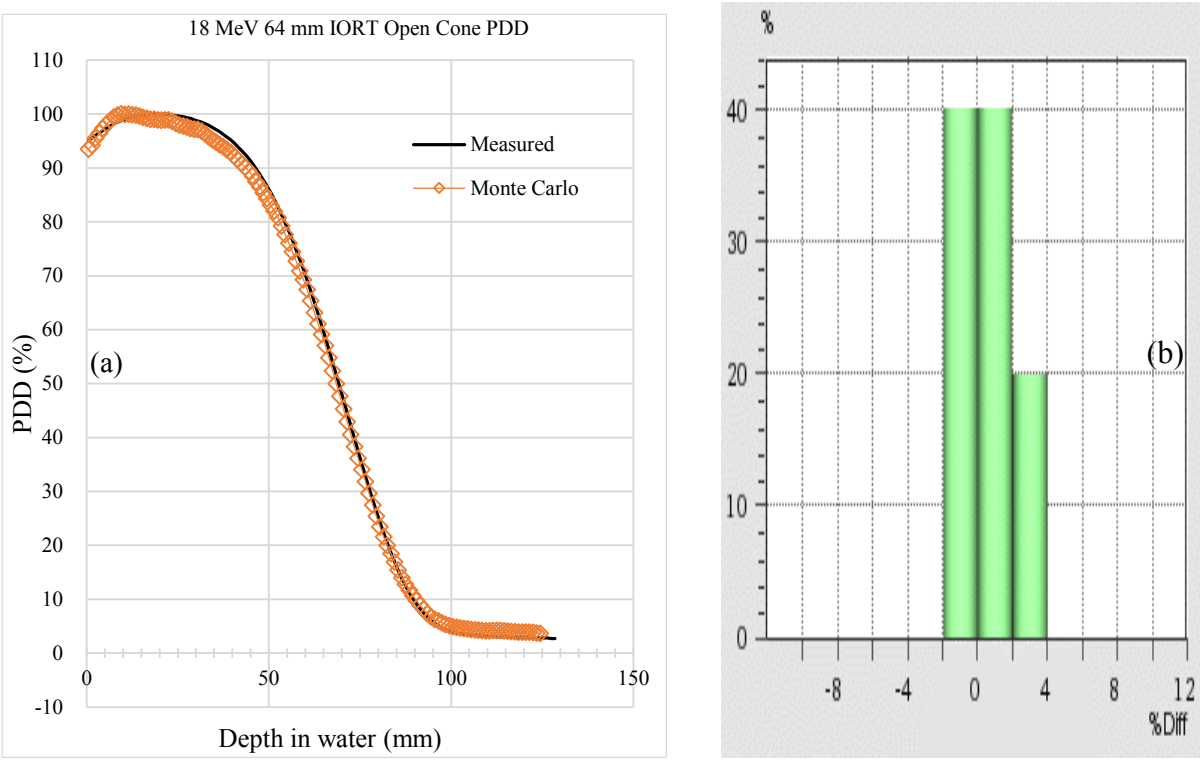

Figure 6.12 Comparison of measured and MC PDDs for 18 MeV 64 mm IORT Open Cone: (a) PDD (b) % dose difference histogram

6.3.1.1 Analysis

For the 19 mm IORT cone, direct comparison of the depths R_{max}, R_{90}, R_{80}, and R_{50} *(table 6.5)* show differences of less than 1.5 mm for all energies with the exception of R_{max} for the 18 MeV beam. All MC-calculated depths were larger for 6 MeV and 18 MeV beams and smaller for the 12 MeV beam. The surface dose for the 6 MeV beam showed a difference of 4.4%. However, this dose difference decreased to 0% within the first 1.5 mm *(figure 6.4(a))* for this beam. The calculated surface doses were lower than measurement for all energies. The values between R_{max} and R_{20} for all energies compared favourably. The bremsstrahlung tail for the calculated curve is higher for 6 MeV and 18 MeV but still fell within the acceptance criteria.

For the 45 mm IORT cone, direct comparison of the depths R_{max}, R_{90}, R_{80}, and R_{50} *(table 6.6)* show differences of less than 1.0 mm for all energies with the exception of R_{max} for the 12 MeV beam and R_{50} for the 18 MeV beams. The points still fell within the acceptance criteria. The surface dose for the 18 MeV beam showed a difference of 5.6%. However, this dose difference decreased to 0% within the first 1.5 mm *(figure 6.9(a))* for this beam. The calculated surface doses were lower than measurement for all energies. The values between R_{max} and R_{20} for all energies compared favourably. The calculated bremsstrahlung tail was higher than measurement for all energies but still fell within acceptable levels.

For the 64 mm IORT cone, direct comparison of the depths R_{max}, R_{90}, R_{80}, and R_{50} *(table 6.7)* show differences of less than 1.0 mm for all energies with the exception of R_{max} and R_{90} for the 18 MeV beam. The surface dose for the 12 MeV beam showed a difference of 2.6%. The values between R_{max} and R_{20} for all energies compared favourably. The bremsstrahlung tail for the calculated curve is higher for all 6 MeV and 18 MeV but still fell within the acceptance criteria.

6.3.2 Beam Profile Results

The depths for profile measurements are as specified in table 6.4

For the profile comparisons, the following 2-D GI parameters were used:

3.0 mm Distance – To – Agreement (DTA)

3.0% Dose Difference with reference to local dose

Increased tolerance of 4.0 % Dose Difference for values below 3.0 %. This implies that for any dose points in the profile that is less than 3% of the maximum dose (extreme ends of the penumbra), the pass/fail GI criteria is increased to 4%.

The associated GI histograms appear adjacent to each set of plotted data. The percentage that satisfy the passing criteria of GI $\leq$ 1.0 are represented by light green and dark green bars for MC values greater than the measured values (hot) and for MC values less than the measured values (cold) respectively.

The percentage that fail and have GI > 1.0 are represented by red and blue bars for MC values greater than the measured values (hot) and for MC values less than the measured values (cold) respectively.

The red and blue ellipses on the plotted profile curves represent the point(s) on the curve that fail the GI criteria according to the colour nomenclature specified above.

The comparison, with the MC simulation data, of the measured in-plane and cross-plane profiles at the depths specified in table 6.4 yielded similar results, so for brevity, only the cross-plane results are reported below.

The measured data was used as the reference matrix with the MC data as the secondary data set.

The statistical variance was less than 1% for all Monte Carlo profile calculations *(section 4.3.4)*.

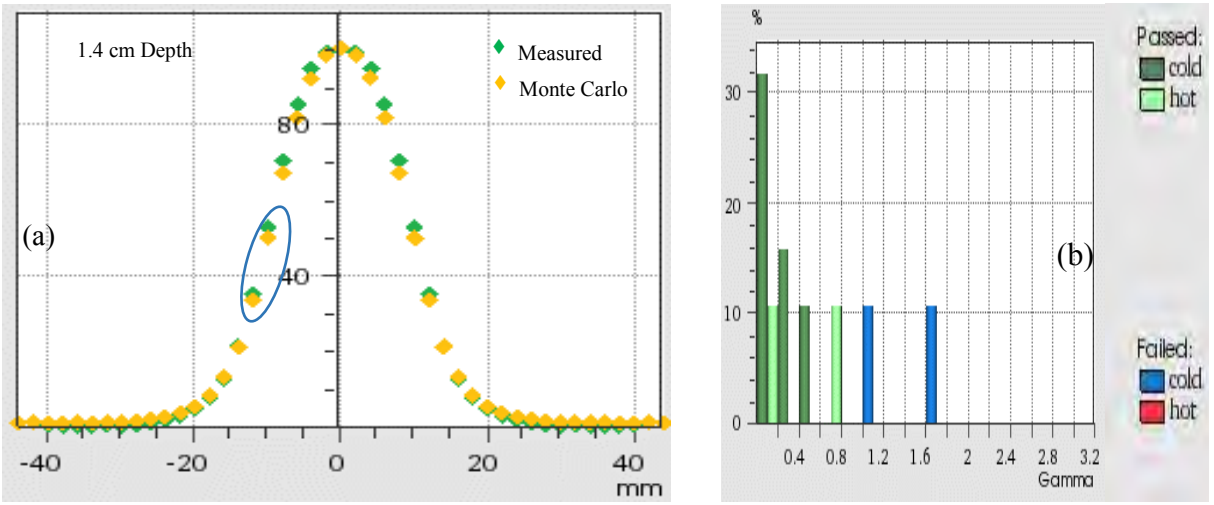

Figure 6.13 Comparison of measured and MC profiles at 1.4 cm depth for 6 MeV 19 mm IORT Open Cone: (a) Profile (b) Gamma Index histogram

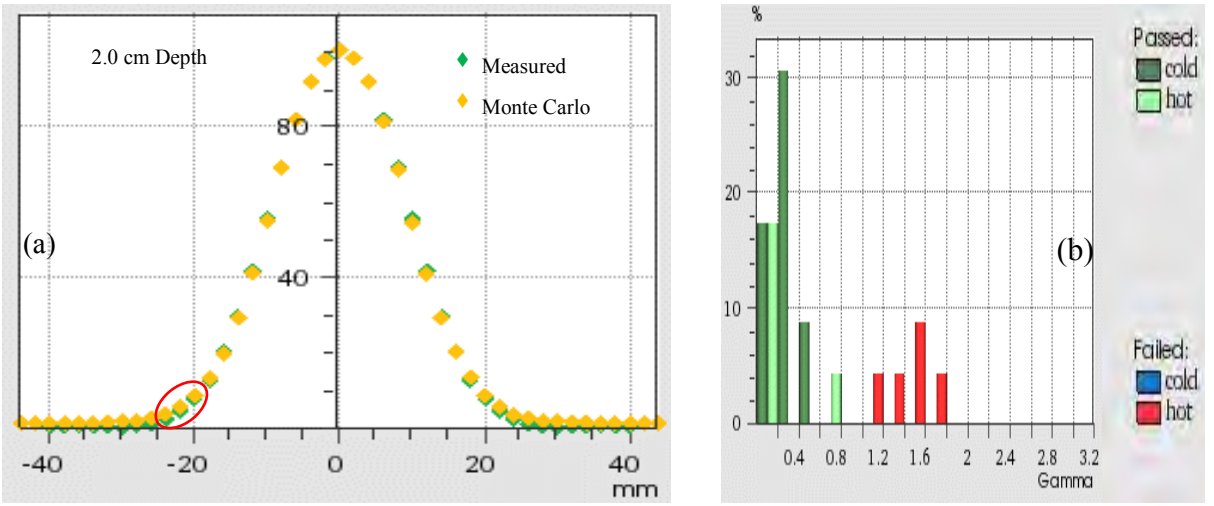

Figure 6.14 Comparison of measured and MC profiles at 2.0 cm depth for 6 MeV 19 mm IORT Open Cone: (a) Profile (b) Gamma Index histogram

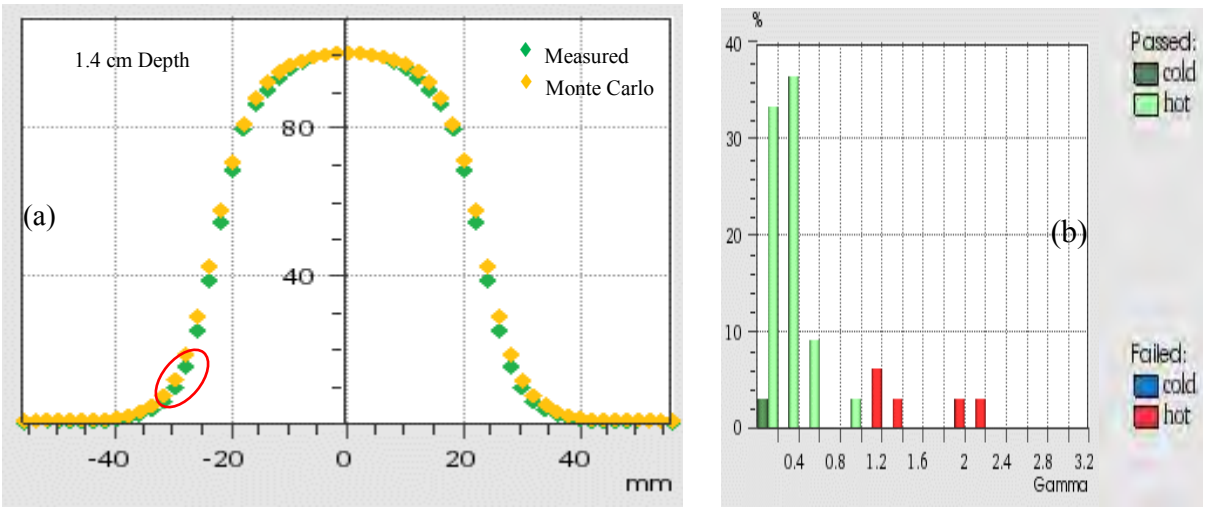

Figure 6.15 Comparison of measured and MC profiles at 1.4 cm depth for 6 MeV 45 mm IORT Open Cone: (a) Profile (b) Gamma Index histogram

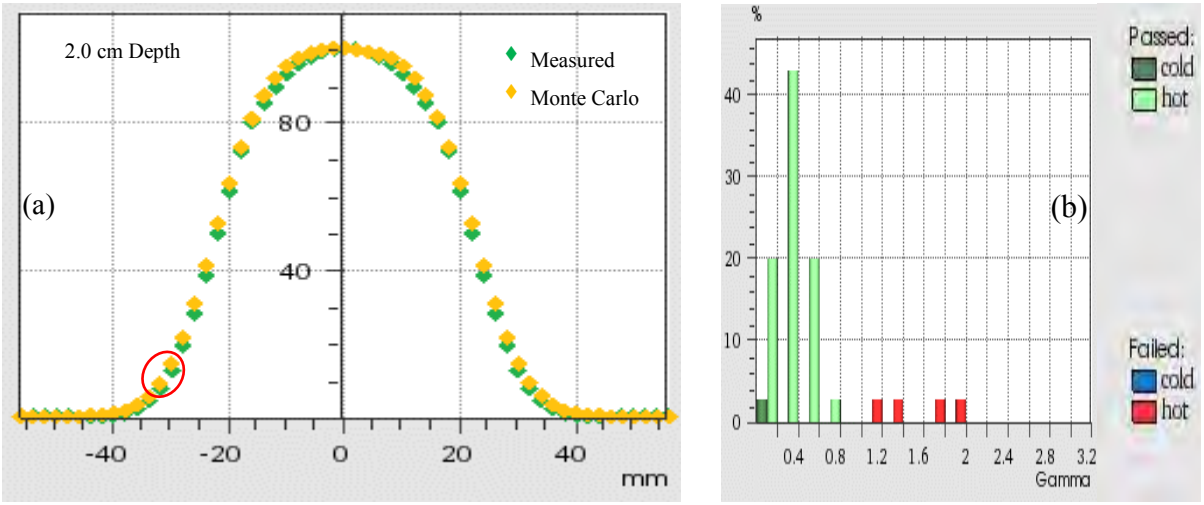

Figure 6.16 Comparison of measured and MC profiles at 2.0 cm depth for 6 MeV 45 mm IORT Open Cone: (a) Profile (b) Gamma Index histogram

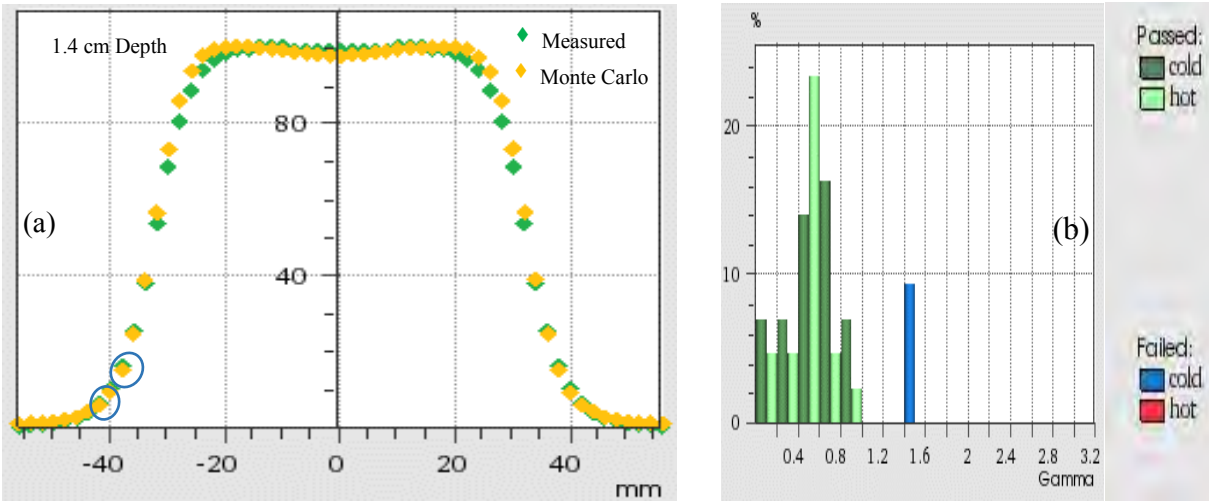

Figure 6.17 Comparison of measured and MC profiles at 1.4 cm depth for 6 MeV 64 mm IORT Open Cone: (a) Profile (b) Gamma Index histogram

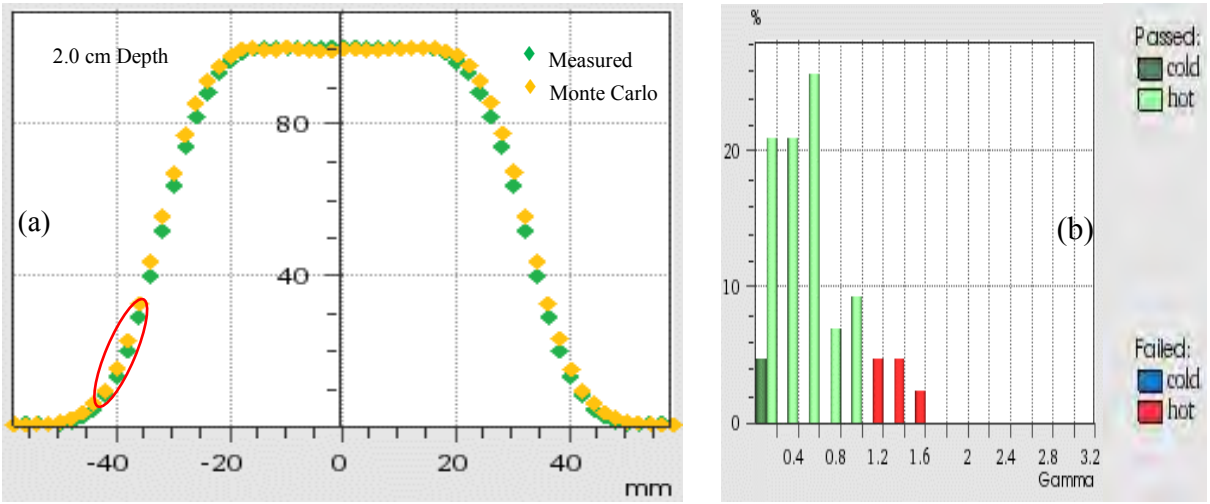

Figure 6.18 Comparison of measured and MC profiles at 2.0 cm depth for 6 MeV 64 mm IORT Open Cone: (a) Profile (b) Gamma Index histogram

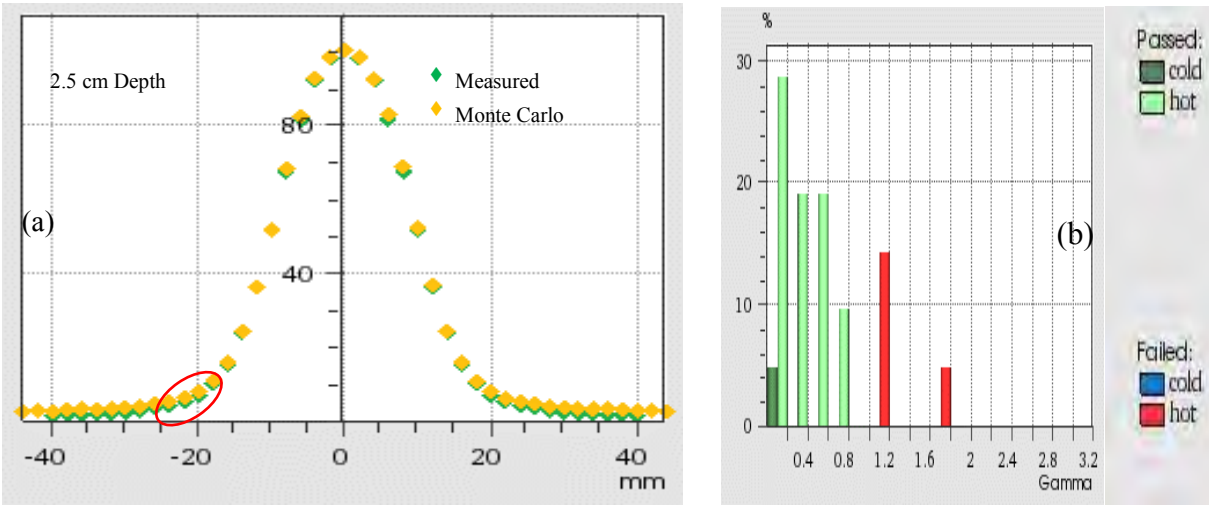

Figure 6.19 Comparison of measured and MC profiles at 2.5 cm depth for 12 MeV 19 mm IORT Open Cone: (a) Profile (b) Gamma Index histogram

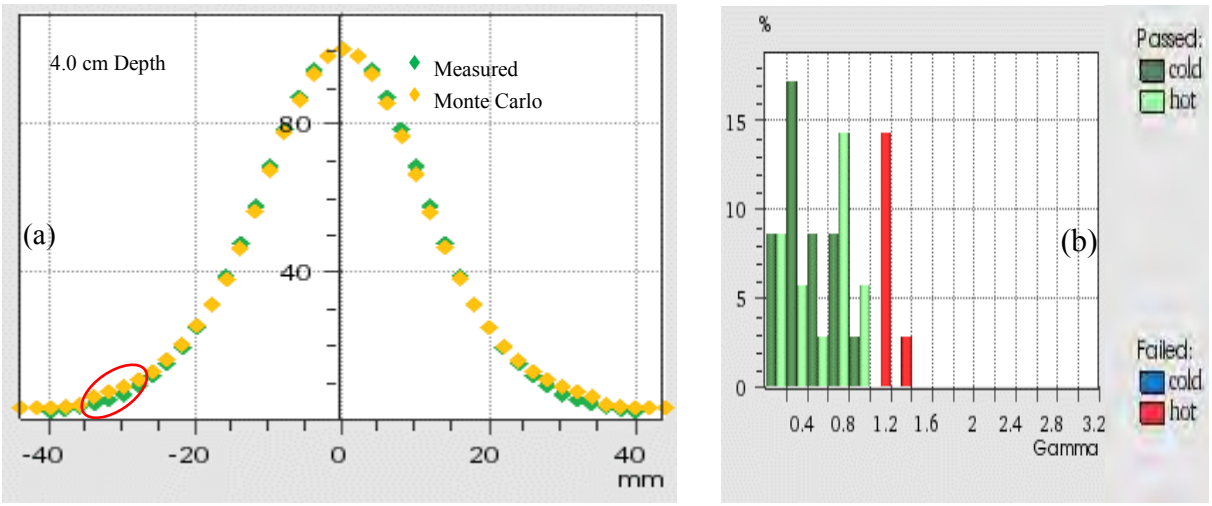

Figure 6.20 Comparison of measured and MC profiles at 4.0 cm depth for 12 MeV 19 mm IORT Open Cone: (a) Profile (b) Gamma Index histogram

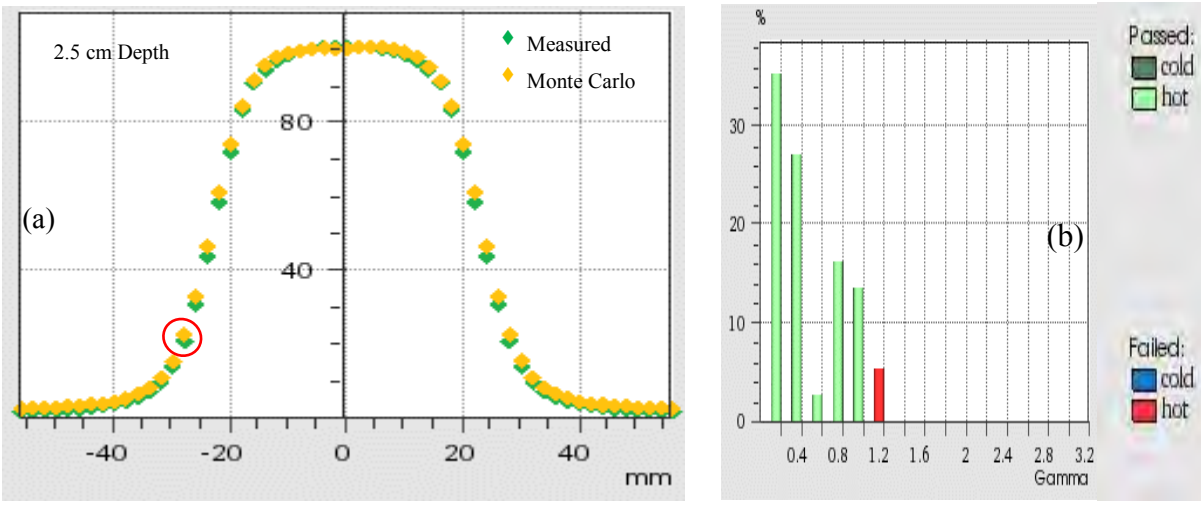

Figure 6.21 Comparison of measured and MC profiles at 2.5 cm depth for 12 MeV 45 mm IORT Open Cone: (a) Profile (b) Gamma Index histogram

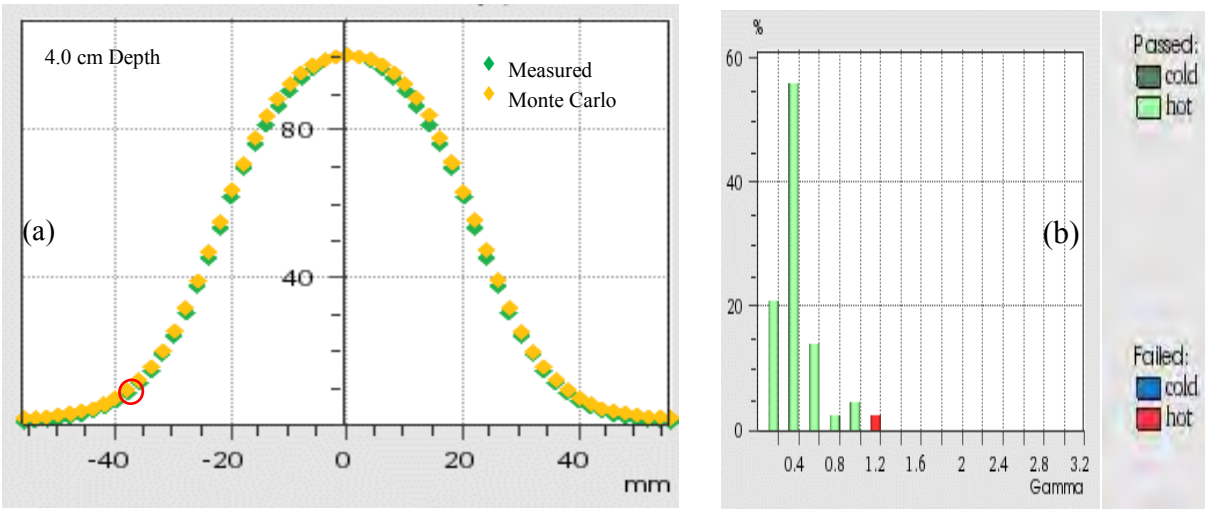

Figure 6.22 Comparison of measured and MC profiles at 4.0 cm depth for 12 MeV 45 mm IORT Open Cone: (a) Profile (b) Gamma Index histogram

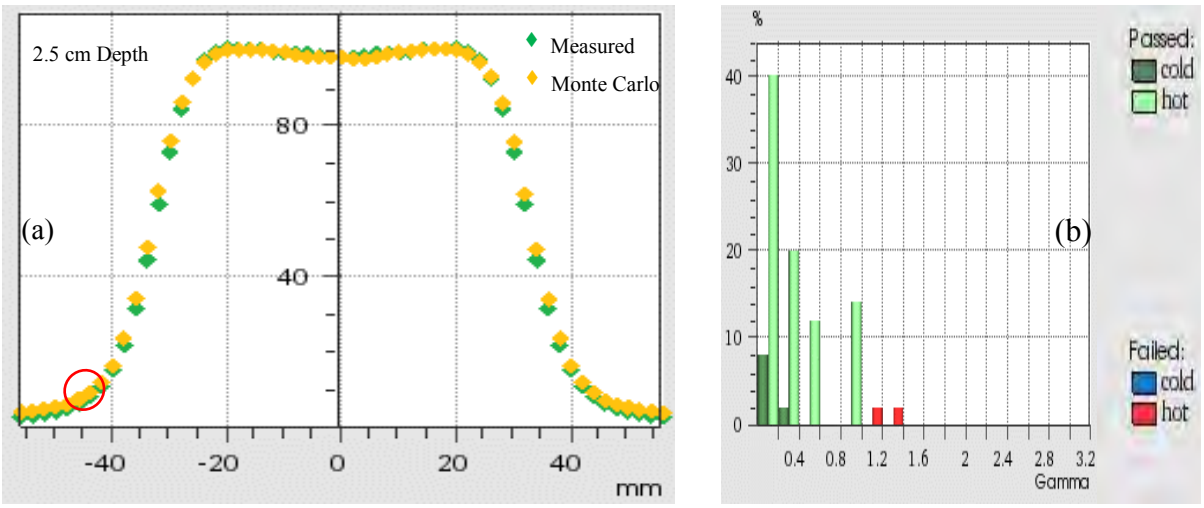

Figure 6.23 Comparison of measured and MC profiles at 2.5 cm depth for 12 MeV 64 mm IORT Open Cone: (a) Profile (b) Gamma Index histogram

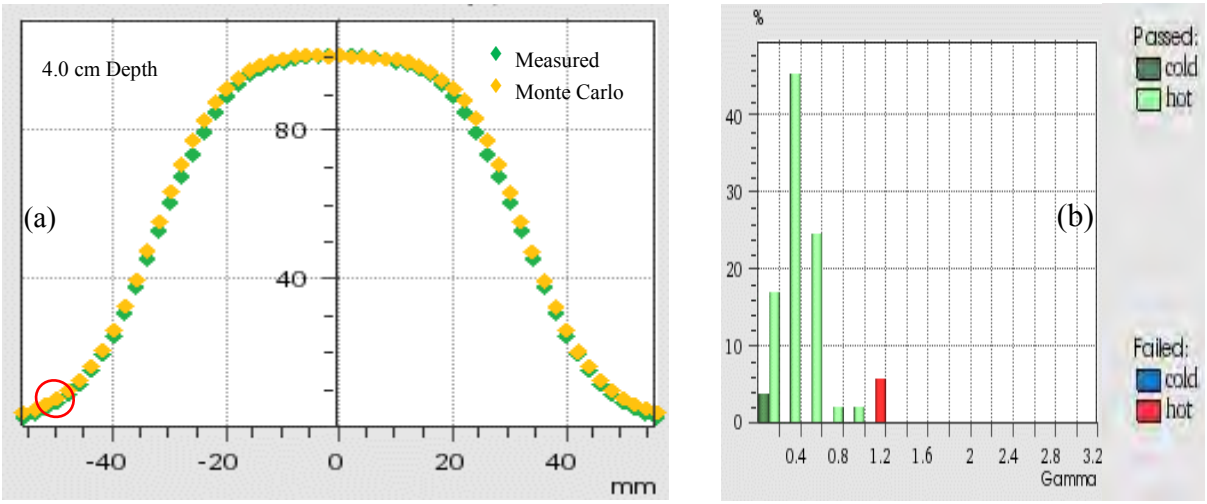

Figure 6.24 Comparison of measured and MC profiles at 4.0 cm depth for 12 MeV 64 mm IORT Open Cone: (a) Profile (b) Gamma Index histogram

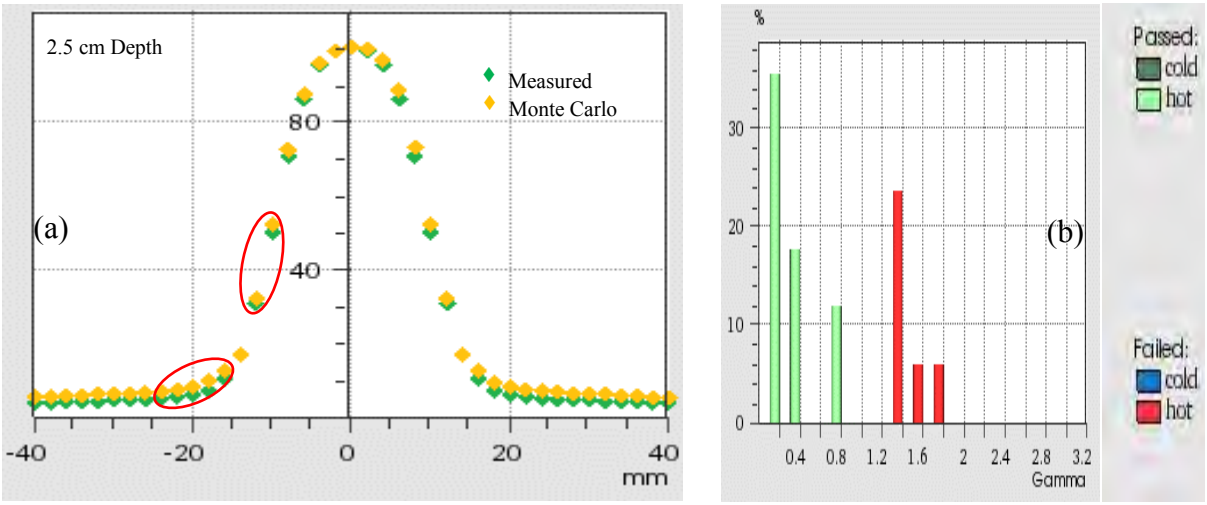

Figure 6.25 Comparison of measured and MC profiles at 2.5 cm depth for 18 MeV 19 mm IORT Open Cone: (a) Profile (b) Gamma Index histogram

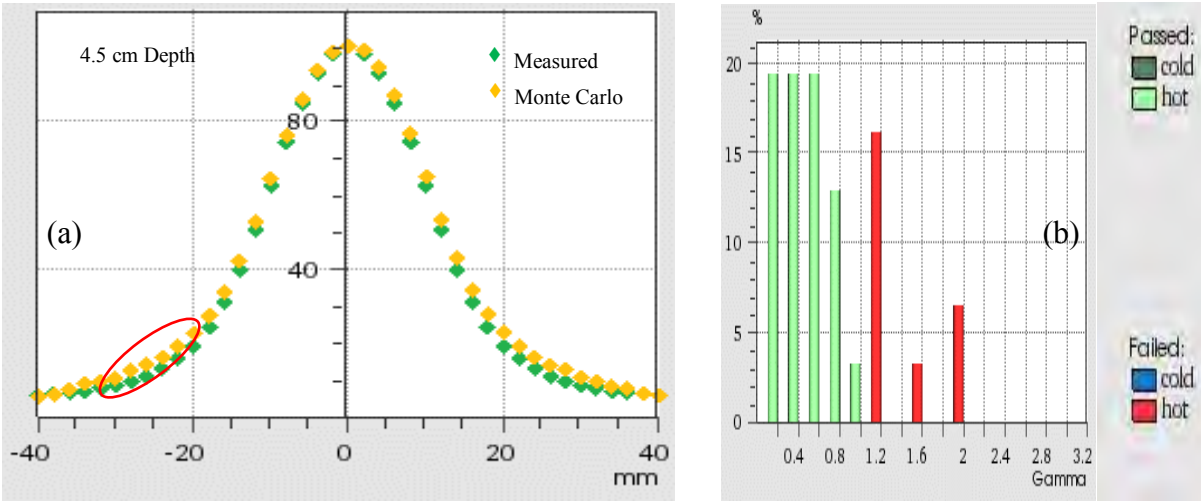

Figure 6.26 Comparison of measured and MC profiles at 4.5 cm depth for 18 MeV 19 mm IORT Open Cone: (a) Profile (b) Gamma Index histogram

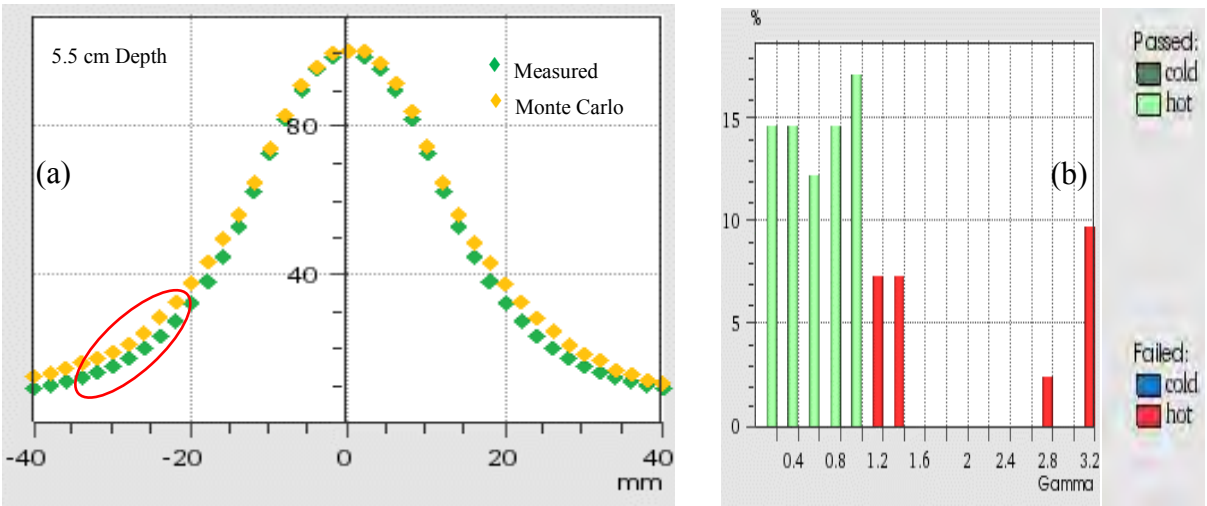

Figure 6.27 Comparison of measured and MC profiles at 5.5 cm depth for 18 MeV 19 mm IORT Open Cone: (a) Profile (b) Gamma Index histogram

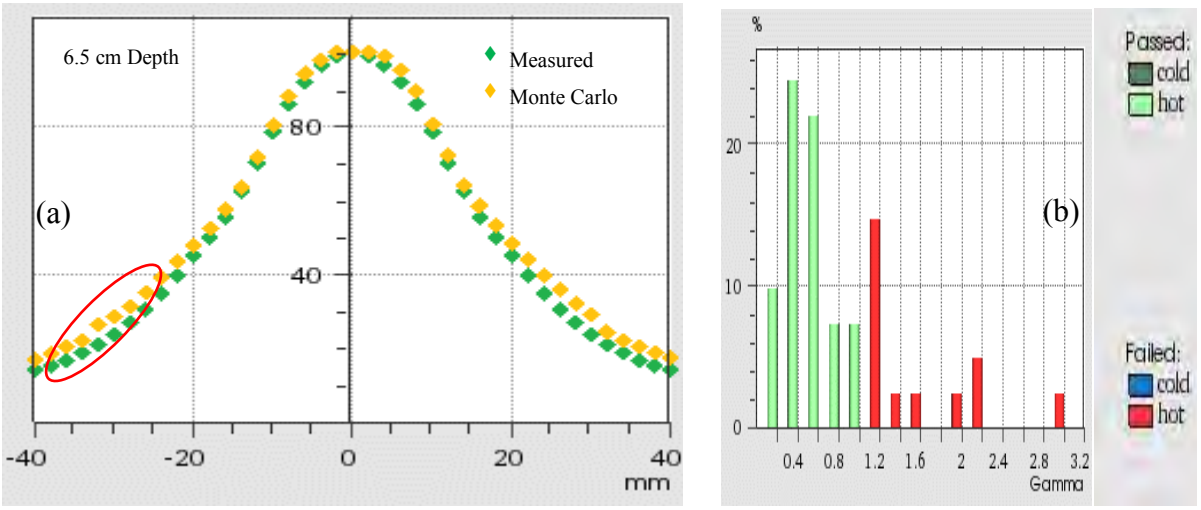

Figure 6.28 Comparison of measured and MC profiles at 6.5 cm depth for 18 MeV 19 mm IORT Open Cone: (a) Profile (b) Gamma Index histogram

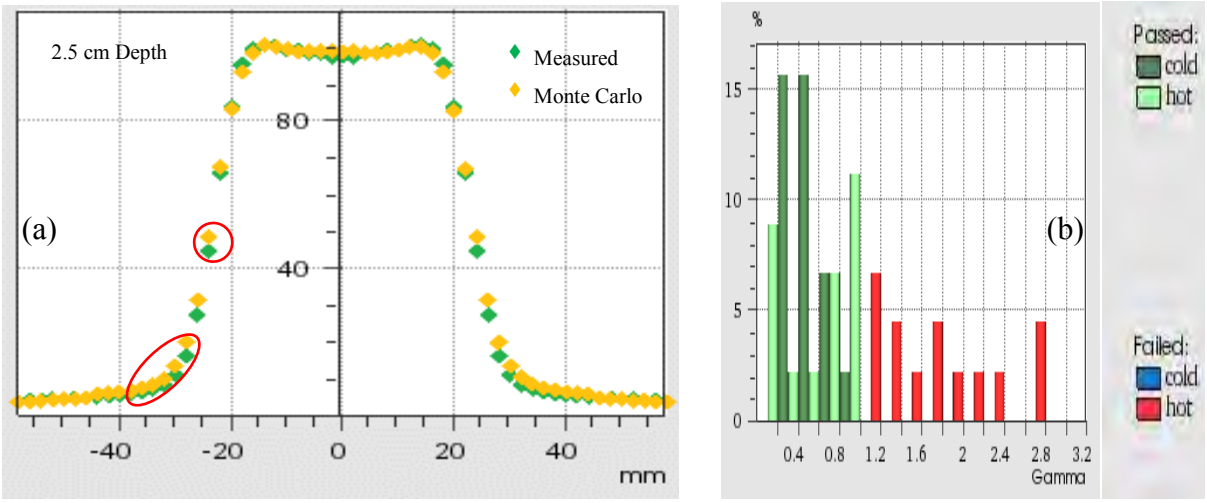

Figure 6.29 Comparison of measured and MC profiles at 2.5 cm depth for 18 MeV 45 mm IORT Open Cone: (a) Profile (b) Gamma Index histogram

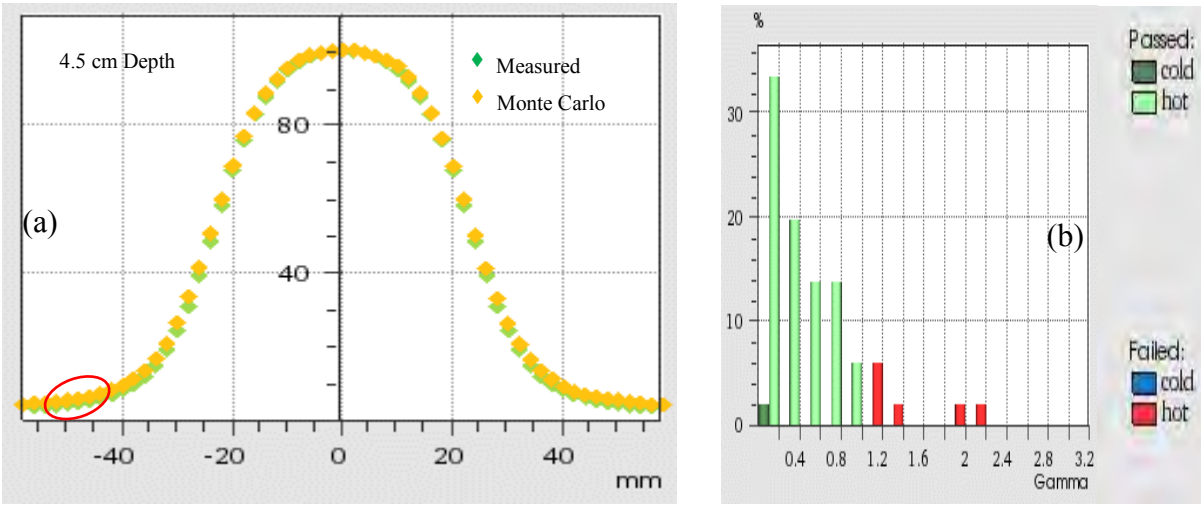

Figure 6.30 Comparison of measured and MC profiles at 4.5 cm depth for 18 MeV 45 mm IORT Open Cone: (a) Profile (b) Gamma Index histogram

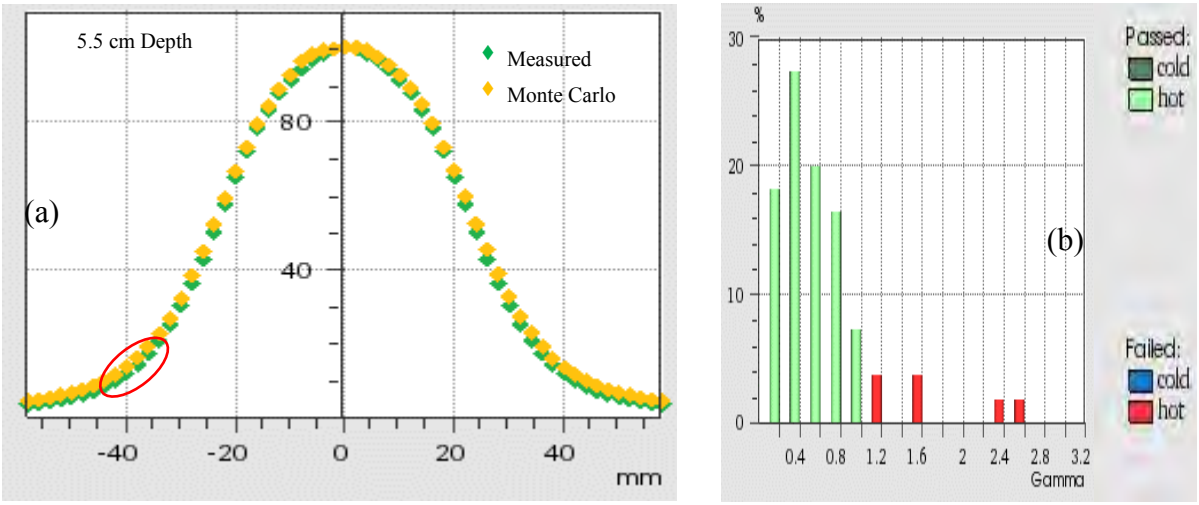

Figure 6.31 Comparison of measured and MC profiles at 5.5 cm depth for 18 MeV 45 mm IORT Open Cone: (a) Profile (b) Gamma Index histogram

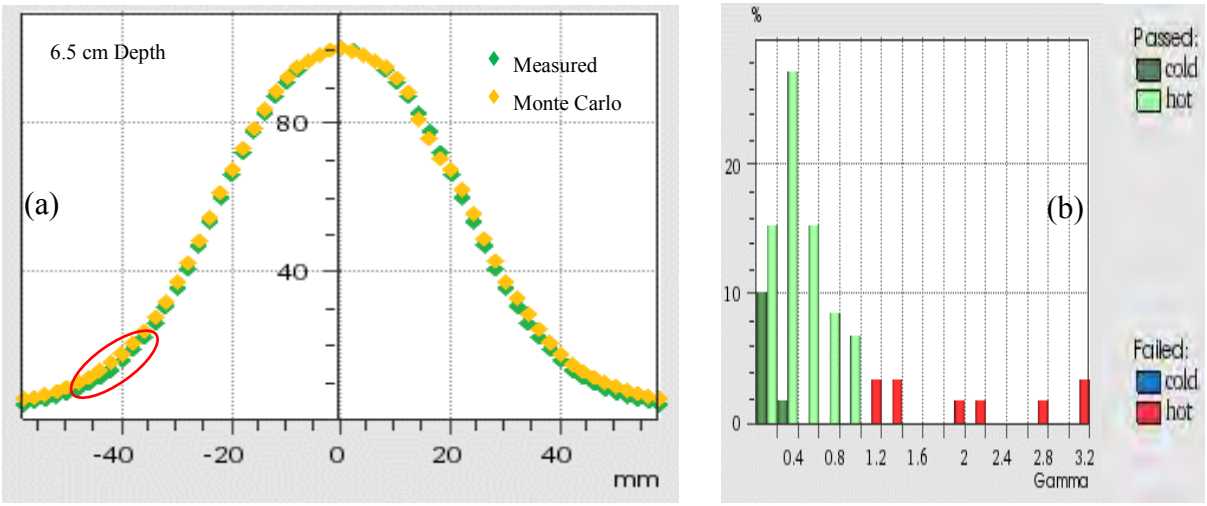

Figure 6.32 Comparison of measured and MC profiles at 6.5 cm depth for 18 MeV 45 mm IORT Open Cone: (a) Profile (b) Gamma Index histogram

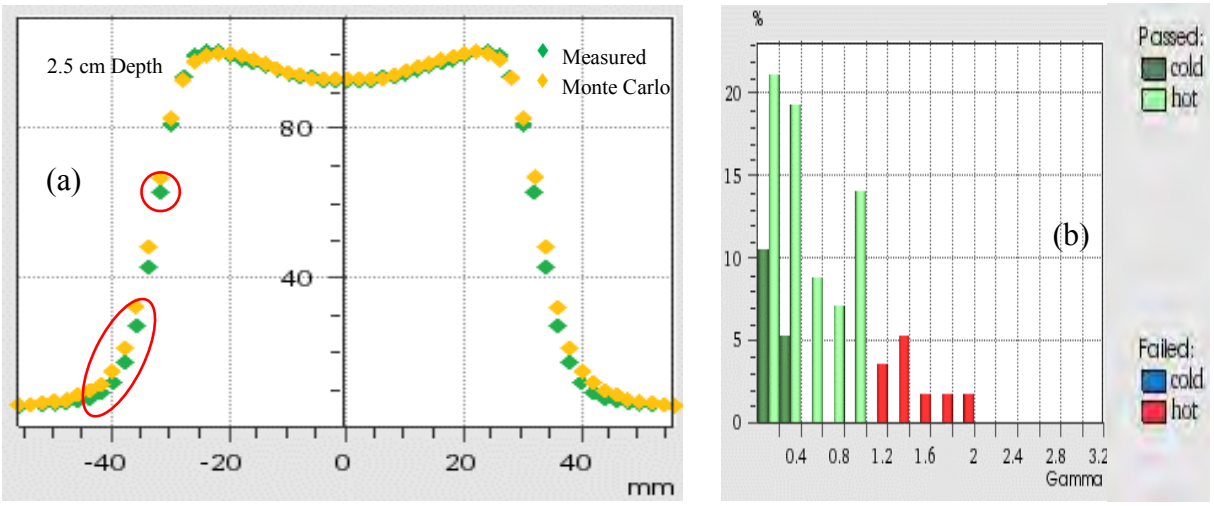

Figure 6.33 Comparison of measured and MC profiles at 2.5 cm depth for 18 MeV 64 mm IORT Open Cone: (a) Profile (b) Gamma Index histogram

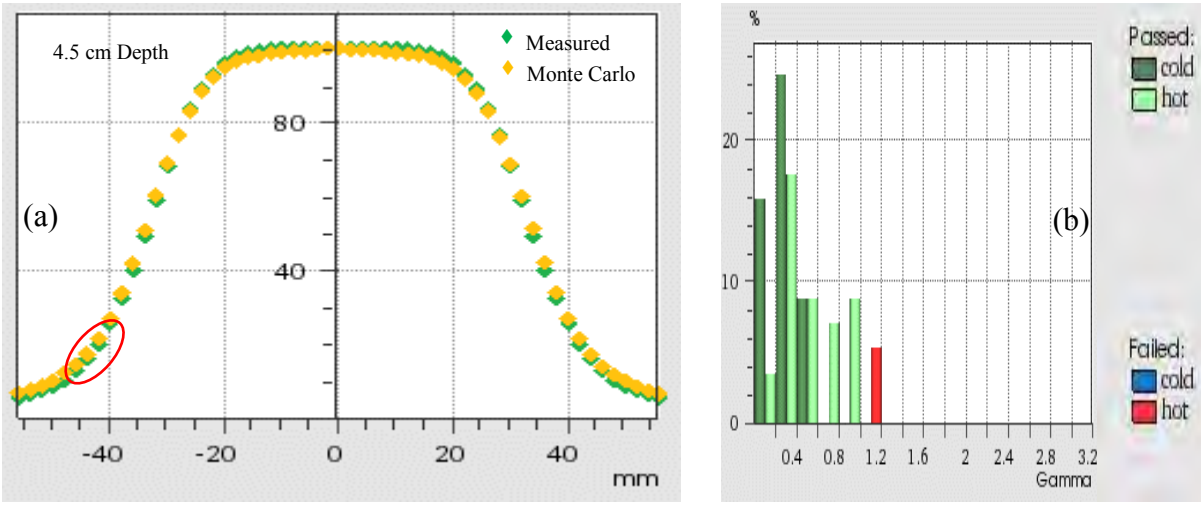

Figure 6.34 Comparison of measured and MC profiles at 4.5 cm depth for 18 MeV 64 mm IORT Open Cone: (a) Profile (b) Gamma Index histogram

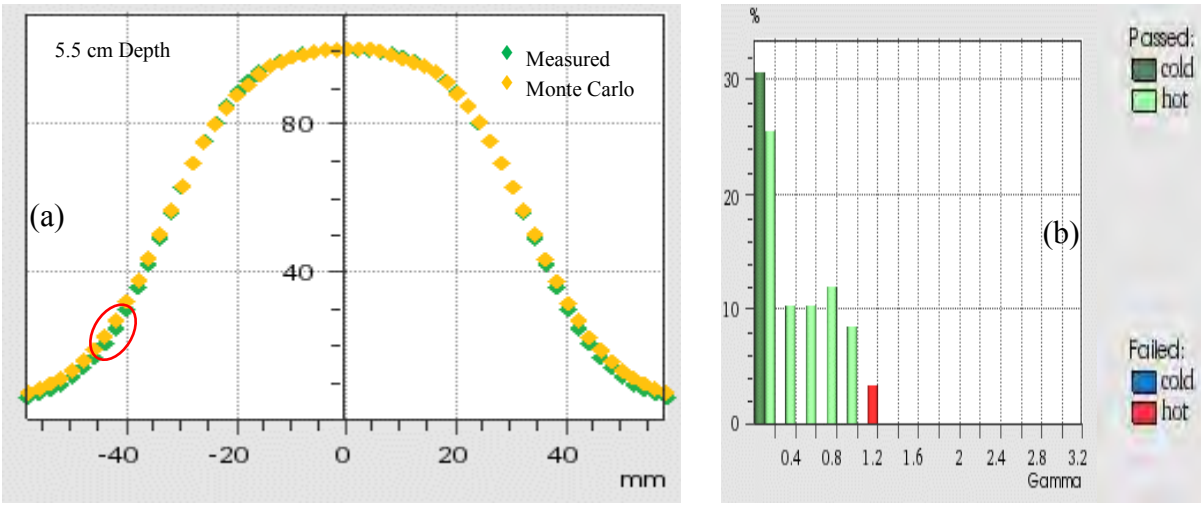

Figure 6.35 Comparison of measured and MC profiles at 5.5 cm depth for 18 MeV 64 mm IORT Open Cone: (a) Profile (b) Gamma Index histogram

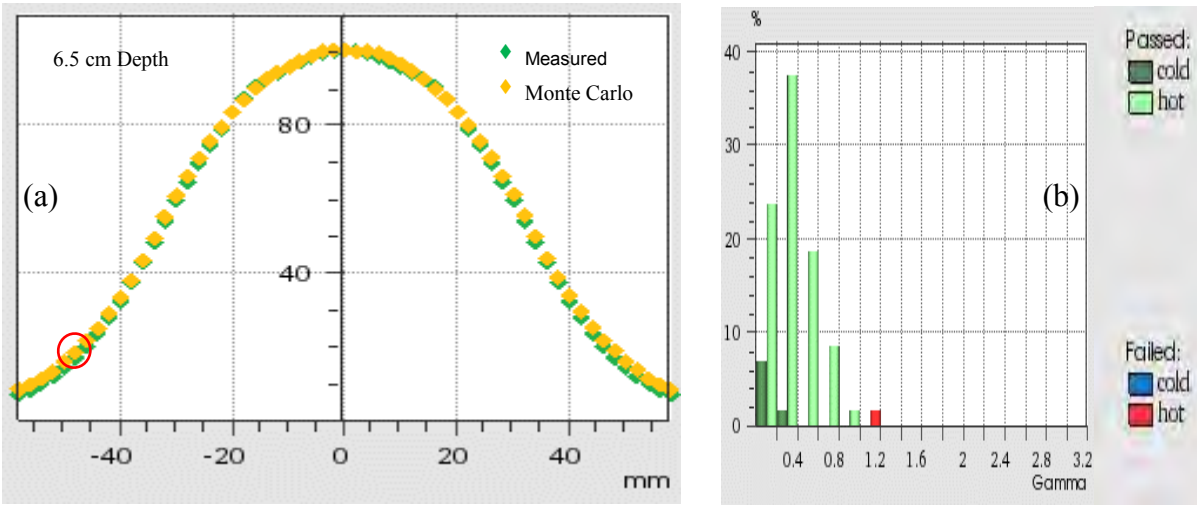

Figure 6.36 Comparison of measured and MC profiles at 6.5 cm depth for 18 MeV 64 mm IORT Open Cone: (a) Profile (b) Gamma Index histogram

6.3.2.1 Analysis

6 MeV 19 mm cone beam profile at 1.4 cm depth: Less than 10% of the points failed with a maximum γ of 1.6 in the high dose gradient range of 30% to 60% at lateral distance ranging from 7 mm to 12 mm, where the calculated points were lower than the measured points.
6 MeV 19 mm cone beam profile at 2.0 cm depth: Approximately 5% of the failed points had a maximum γ of 1.8 in the 0% to 10% dose region at lateral distance greater than 8 mm.

6 MeV 45 mm cone beam profile at 1.4 cm depth: Less than 3% of the points failed with a maximum γ of 2.2 in the high dose gradient range of 5% to 15% at lateral distance ranging from 28 mm to 32 mm, where the calculated points were higher than the measured points.
6 MeV 45 mm cone beam profile at 2.0 cm depth: Less than 3% of the points failed with a maximum γ of 2.0 in the high dose gradient range of 3% to 7% at lateral distance ranging from 28 mm to 32 mm, where the calculated points were higher than the measured points.

6 MeV 64 mm cone beam profile at 1.4 cm depth: Less than 10% of the points failed with a maximum γ of 1.4 in the high dose gradient range of 5% to 15% at lateral distance ranging from 35 mm to 40 mm, where the calculated points were lower than the measured points.
6 MeV 64 mm cone beam profile at 2.0 cm depth: Less than 3% of the points failed with a maximum γ of 1.6 in the high dose gradient range of 5% to 32% at lateral distance ranging from 35 mm to 40 mm, where the calculated points were higher than the measured points.

12 MeV 19 mm beam profile at 2.5 cm depth: A maximum of 5% of the failed points were hotter in the 0% to 10% dose range with γ of less than 1.8 at lateral distance of 18 mm to 25 mm.
12 MeV 19 mm beam profile at 4.0 cm depth: A maximum of 2% of the failed points were hotter in the 0% to 10% dose regions with γ of less than 1.4 at lateral distance ranging from 28 mm to 35 mm.

12 MeV 45 mm beam profile at 2.5 cm depth: Less than 5% of the failed points were hotter in the 20% dose region with γ of less than 1.2 at lateral distance of 28 mm.

12 MeV 45 mm beam profile at 4.0 cm depth: A maximum of 2% of the failed points were hotter in the 10% dose region with maximum γ of 1.2 at lateral distance ranging from 38 mm.

12 MeV 64 mm beam profile at 2.5 cm depth: Less than 2% of the failed points were hotter in the 10% dose region with γ of less than 1.4 at lateral distance of 45 mm.

12 MeV 64 mm beam profile at 4.0 cm depth: A maximum of 5% of the failed points were hotter in the 5% dose region with maximum γ of 1.2 at lateral distance ranging of 50 mm.

18 MeV 19 mm cone beam profile at 2.5 cm depth: A maximum γ of 1.8 for 6% of the points is observed in the 0% to 10% dose range at lateral distance ranging from 15 mm to 25 mm. Further failed point occurred in the high dose gradient region ranging from 30% to 50% at lateral distance of 20 mm.

18 MeV 19 mm cone beam profile at 4.5 cm depth: A maximum γ of 2.0 for 6% of the points is observed in the 20 mm to 30 mm range where calculated points were higher than measurement.

18 MeV 19 mm beam profile at 5.5 cm depth: A maximum γ of 3.2 for 8% of the points is observed in the 20% to 30% dose range at lateral distance ranging from 20 mm to 35 mm where calculated points were higher than measurement.

18 MeV 19 mm beam profile at 6.5 cm depth: A maximum γ of 3.0 for 3% of the points is observed in the 15% to 40% dose range at lateral distance ranging from 25 mm to 35 mm where calculated points were higher than measurement.

18 MeV 45 mm cone beam profile at 2.5 cm depth: A maximum γ of 2.8 for 4% of the points is observed in the 0% to 15% dose range at lateral distance ranging from 25 mm to 35 mm. A

further failed point occurred in the high dose gradient region at 45% at lateral distance of 25 mm.

18 MeV 45 mm cone beam profile at 4.5 cm depth: A maximum γ of 2.2 for 2% of the points is observed in the 42 mm to 52 mm range where calculated points were higher than measurement.

18 MeV 45 mm beam profile at 5.5 cm depth: A maximum γ of 2.6 for 2% of the points is observed in the 5% to 15% dose range at lateral distance ranging from 33 mm to 43 mm where calculated points were higher than measurement.

18 MeV 45 mm beam profile at 6.5 cm depth: A maximum γ of 3.2 for 3% of the points is observed in the 5% to 20% dose range at lateral distance ranging from 35 mm to 50 mm where calculated points were higher than measurement.

18 MeV 64 mm cone beam profile at 2.5 cm depth: A maximum γ of 2 for 4% of the points is observed in the 5% to 35% dose range at lateral distance ranging from 32 mm to 45 mm. A further failed point occurred in the high dose gradient region at 65% at lateral distance of 30 mm.

18 MeV 64 mm cone beam profile at 4.5 cm depth: A maximum γ of 1.2 for 5% of the points is observed in the 38 mm to 45 mm range where calculated points were higher than measurement.

18 MeV 64 mm beam profile at 5.5 cm depth: A maximum γ of 1.2 for 3% of the points is observed in the 15% to 30% dose range at lateral distance ranging from 40 mm to 45 mm where calculated points were higher than measurement.

18 MeV 64 mm beam profile at 6.5 cm depth: A maximum γ of 1.2 for less than 2% of the points is observed in the 15% to 20% dose range at lateral distance ranging from of 55 mm where calculated points were higher than measurement.

Further discussion and conclusions based on these results are reserved for the end of the chapter *(section 6.4).*

6.3.3 Cone Factors

The cone factors (CF) for the IORT open cones were determined in an analogous manner to the applicator output factor determination in section 5.4.2.3. The electron Dosimetry Diode E (PTW type T60017, Freiburg, Germany) was used to measure the cone factors for each of the cones each energy. Measurements were performed at d_{max} for each of the non-reference fields (19 mm, 45 mm and 64 mm cones) and the reference field ($10x10\ cm$ open applicator) for each energy. This depth varies with field size and energy *(IAEA 2000).* The resulting cone factors for each cone for each energy *(table 6.8)* was calculated as per equation 5.17 above.

The MC-calculated cone factors were obtained by analysing the 3-d dose distribution for each of the cones for each energy in STATDOSE and relating the doses at the respective d_{max} depths as per equation 2.4. A comparison between the measured and MC-calculated cone factors for the 19 mm, 45 mm and 64 mm cones appear in table 6.8 below, with the uncertainty in measurements being determined utilising equation 5.20. The statistical variance was less than 1% for all output factors determined by Monte Carlo calculations *(section 4.3.4)*.

Table 6.8 Comparison between the measured and MC-calculated cone factors for the 19 mm, 45 mm and 64 mm cones for energies 6 MeV, 12 MeV and 18 MeV electron beams

	6 MeV			12 MeV			18 MeV		
	Meas	**MC**	**%diff**	**Meas**	**MC**	**%diff**	**Meas**	**MC**	**%diff**
CF 19 mm Cone	0.445 ±0.004	0.463	4.04	0.877 ±0.004	0.912	3.99	1.083 ±0.003	1.115	2.95
CF 45 mm Cone	1.045 ±0.003	1.059	1.34	1.195 ±0.003	1.181	-1.18	1.204 ±0.003	1.211	0.59
CF 64 mm Cone	1.116 ±0.003	1.121	0.45	1.222 ±0.002	1.222	0.00	1.221 ±0.002	1.226	0.41

The variation of measured and calculated CF with cone size and variation of measured and calculated CF with energy is shown in figures 6.37 and 6.38 respectively.

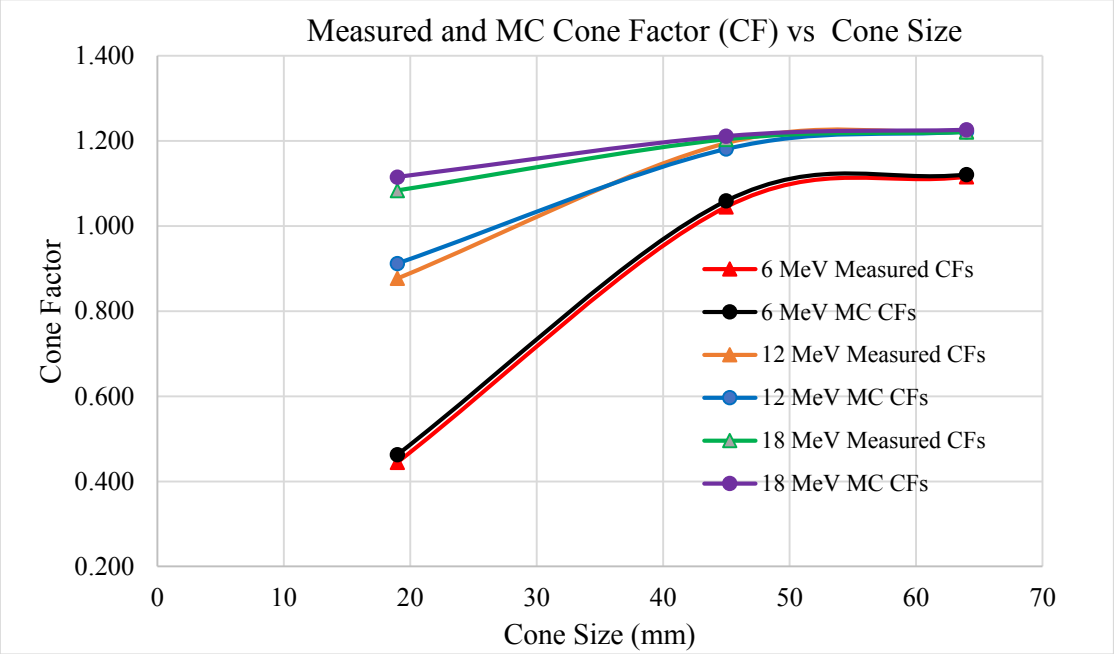

Figure 6.37 Plot of Measured and MC-calculated cone factors vs cone size for 6 MeV, 12 MeV and 18 MeV electron beams

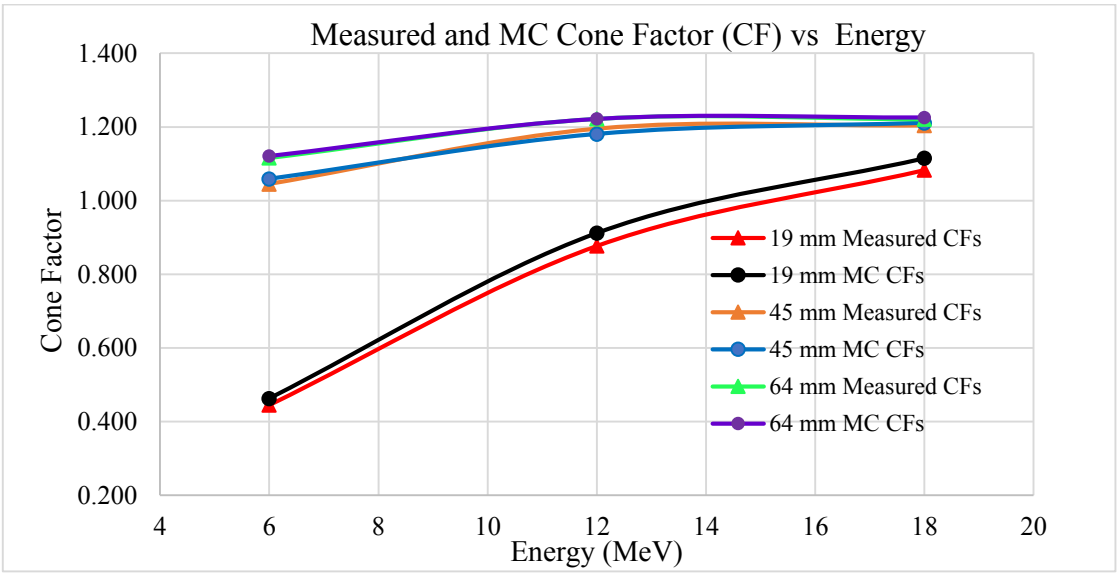

Figure 6.38 Plot of Measured and MC-calculated cone factors vs electron energy for 19 mm, 45 mm and 64 mm IORT open cones.

6.3.3.1 Analysis

The differences between calculated and measured cone factors were below 1.4% for the 45 mm and 64 mm cones for all the energies. Larger discrepancies were observed for the 19 mm

cone factors with the measured cone factors being 4.04%, 3.99% and 2.95% lower than calculation for the 6 MeV, 12 MeV and 18 MeV beams respectively.

As observed in figure 6.37, the cone factors increase with an increase in cone size for each energy. The difference in steepness in the gradient of the curves show that the lower the energy, the larger the effect of the change in cone size especially for the lower sizes. The cone factors level off as the cone size is increased further. Figure 6.38 shows a definite increase in cone factor with energy. Once again, the change is more pronounced for the smaller cone sizes.

6.4 Discussion and Conclusion

The focus of this chapter is to compare Monte Carlo calculated beam characteristics with measurements for the Siemens Primus LINAC for 6 MeV, 12 MeV and 18 MeV electron beams for the IORT open cones of diameters 19 mm, 45 mm and 64 mm. This was done in order to determine if the MC method may be used clinically for dose distribution calculations and for MU calculations from calculated cone factors. Acceptable comparisons with open cones would also justify the use of these cones for further collimation by the introduction of irregularly shaped cut-outs into the cone end to conform the shape of the beam to the treatment site.

The MC modelling task was accomplished by building the IORT cones in BEAMnrc *(section 6.1)* as a replacement for the standard applicators used for the commissioning process. The cone ends were situated at 99 cm from the source and the phantom surface was situated at 100 cm SSD (1 cm air gap). The phase space file from the BEAMnrc simulation was used as the input source for DOSXYZnrc. 3-d dose distributions were produced from which the relevant PDD and profiles were obtained for comparison with measured data.

Measurements were performed as described in section 6.2 with the same geometry (100 cm SSD, 1 cm air gap) described in the above paragraph.

The PDD comparison for the IORT cones proved to be favourable as direct comparison of R_{max}, R_{90}, R_{80}, and R_{50} yielded results of less than 1.5 mm, with the exception of the 18 MeV beam for 45 mm and 64 mm cones where there were differences of 9.5 mm and 4 mm in R_{max} respectively. The R_{90} and R_{80} values were also low for the 12 MeV 64 mm cone and exceeded the acceptance criteria. In general, these characteristic points were in good agreement with measurement.

Discrepancies in the surface doses (6 Mev 19 mm cone, 12 MeV 64 mm cone and 18 MeV 45 mm cone) showed a quick decline in the build-up region and differences reached 0% within the first 1.5 mm and would not have any appreciable effect on clinical outcomes. These differences may be attributed to inaccurate placement of the ionisation chamber during measurement. Studies have also shown *(Verhaegen et al 2001)* that MC modelling with an incorrect material composition in the applicator may lead to up to 10% error in dose in the build-up region. The surface dose increase with cone size observed in this study has been reported in other studies *(Hu et al 2008).*

The differences in the PDD curves at the surface and in the build-up regions are generally attributed to scattered electrons from the phantom, chamber type, and the choice of the effective point of measurement *(Omer 2012).* Discrepancies may also be due to inaccurate determination of the true zero depth. The effective point of measurement for the pinpoint chamber was taken into account for all measurements *(section 4.2).* The equivalent thickness of the chamber wall was determined to be 0.23 mm *(section 4.2)* and was not taken into account in detector positioning for the PDDs as it was deemed to be negligible *(IAEA 2000)*. Inclusion of this parameter would have decreased the measured surface doses, thereby

decreasing the differences between measurement and calculation. Scanning above the water surface was not an option with the cones in place for fear of collision of the stem of the pinpoint with the applicator. It may be noted that despite the mismatch at these points, the differences in general are within the 3%/3 mm range.

The comparisons in the therapeutic range and from R_{90} to R_{20} satisfied the acceptance criteria for all the beams with the exception of the 12 MeV beam for the 64 mm cone. The discrepancies observed at dose levels below 10% may be ignored since this portion of the curve is attributed to contaminant photons (bremsstrahlung), falls well beyond the therapeutic range, and is not clinically significant. Discrepancies in the bremsstrahlung tail mat be attributed to incorrect scattering foil dimension supplied by the vendor *(Bieda et al 2001)*. Care must however be taken to ensure that critical structures at the distal end of the beam are avoided. The PDD comparisons showed acceptable results satisfying the GI criteria in this portion of the beam.

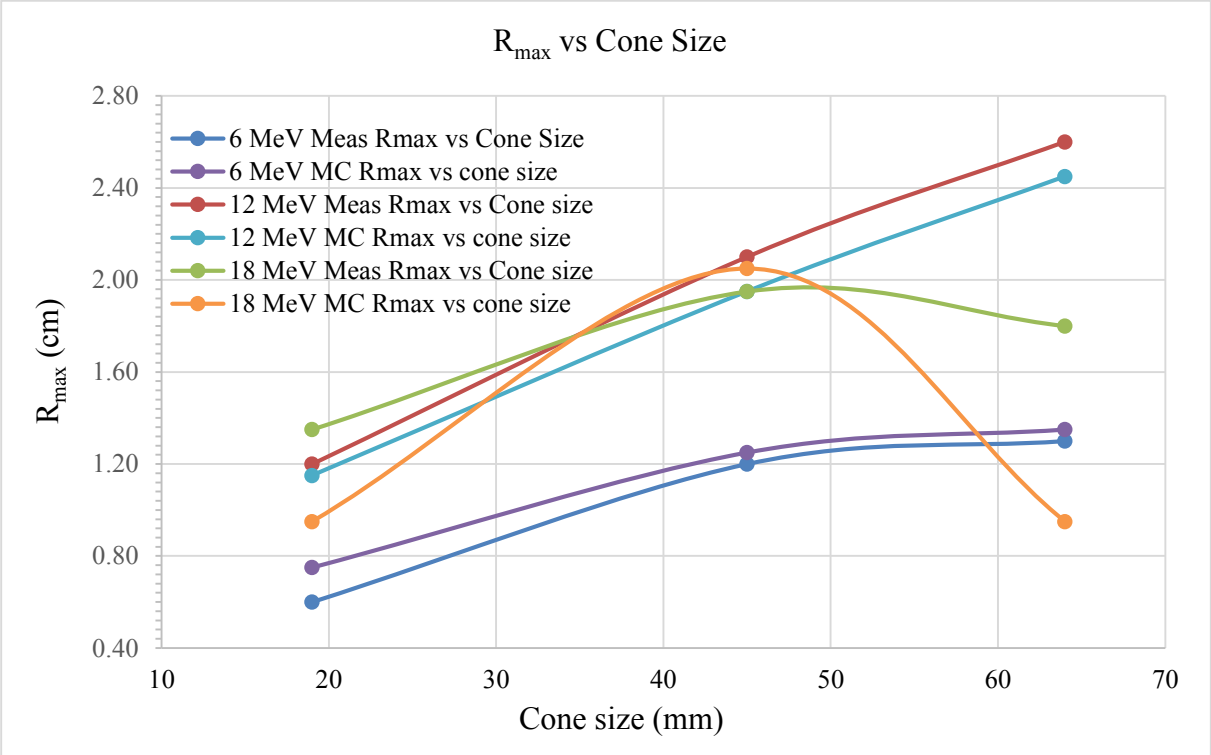

Figure 6.39 Plot of measured and MC-calculated R_{max} points for each energy for the IORT open cone sizes of 19 mm, 45 mm and 64 mm

For both measured and MC-calculated values, R_{max} increased with increasing cone size, with the exception of the 18 MeV beam where R_{max} decreased for the 64 mm cone. Note that this point for the 18 MeV beam considerably exceeded tolerance and may be regarded as being an outlier. If this point is excluded, the trends observed in this study are the same as that observed in similar studies *(Fraas et al 1985, Verhaegen et al 2001)*. For the 6 MeV beam, the shift in R_{max} is 0.50 cm when changing from the 19 mm cone to the 45 mm cone and is 0.10 cm when moving from the 45 mm cone to the 64 mm cone. For the 12 MeV beam, the shift in R_{max} is 0.80 cm when going from the 19 mm cone to the 45 mm cone and is 0.50 cm when changing to the 64 mm cone. It may be concluded that as the cone size increases, the magnitude of the shift in R_{max} decreases. Identical results were observed by Verhaegen et al 2001.

For all the cones and all the energies, a common discrepancy in the profile comparisons is observed at and beyond the edge of the field *(figures 6.13 to 6.36)*. In a few instances discrepancies were observed in the high dose gradient region where accurate chamber placement is critical. It is important to note that almost all points in the central 80% of the beam satisfied the acceptance criteria for all energy/cone combinations. The beam profiles for the IORT cones was therefore deemed to be acceptable as discrepancies were within the acceptance criteria and occurred beyond the field edge and would have little or no impact clinically.

With respect to the cone factor comparisons, the largest discrepancies were observed for the 19 mm cone with a maximum of 4.04% for the 6 MeV beam. Other studies *(Zhang et al 1999, Cygler et al 2004)* have shown that MC calculated output factors may agree with measurements to within 1% to 2%.

Cone factors increased with an increase in cone size for each energy, as observed in various other studies *(Cygler 1997, Turian 2004, Palta et al 1995, Biggs et al 1981)*. The lower the energy, the larger the effect of the change in cone size especially for the lower sizes. Cone factor also increased with energy. Once again, the change is more pronounced for the smaller cone sizes. With the exception of the 45 mm cone for 12 MeV, measured values were lower than calculated values.

It has been reported *(Verhaegen et al 2001)* that low measured values may be due to the fact that small fields do not have a flat dose distribution near the central axis and is not uniform at the point of measurement *(Turian et al 2004)*. Dose measurements with a detector of finite lateral dimensions therefore gives an average dose that is too low compared to the actual dose on the central axis, which seems to be the case for this study. A lack of lateral scatter equilibrium is also absent for small fields *(Shiu 1994)*. MC calculation with suitably-small voxel sizes and sufficient histories is therefore recommended as being the most accurate method of output factor determination for small fields *(Kapur et al 1998, Ma&Jiang 1999, Chetty et al 2007)*.

Output factors for clinical electron beams vary with electron energy, geometry of the jaws, applicator/cone and any field-defining cut-out *(Verhaegen et al 2001)*. Empirical analytical models have been developed to improve the ability to predict output factors for clinical electron beams *(Mills et al 1982, McParland 1989, Chen 2001)*. Monte Carlo methods have also been investigated in calculation of output factors *(Zhang et al 1999, Antolak et al 2002, Kapur et al 1998)*. The conclusions was that MC methods have the greatest potential of calculating output factors accurately *(Ma & Jiang 1999)*.

The results for the MC modelling of the open IORT cones have proved to be within acceptable tolerances with measured data. Furthermore, various studies *(Zhang et al 1999,*

Antolak et al 2002, Kapur et al 1998, Turian et al 2004) have shown that MC calculation of the cone factors are the most accurate method of CF determination especially for the smaller sizes and should be considered as a replacement for measurements for small fields.

The conclusion is that the Monte Carlo calculations of dose distribution and output factors with the IORT open cones may be used clinically.

CHAPTER 7

COMPARISON OF MC SIMULATIONS AND MEASUREMENTS WITH IRREGULARLY-SHAPED CUT-OUTS IN THE IORT OPEN CONES

The inclusion of beam modifiers in electron beams affects the resulting dose distributions significantly by changing the particle energy distribution, spatial distribution and angular distributions. Monte Carlo simulation is the most accurate method for beam modifier simulation *(Li 2002)*. Li stated further that it is more convenient and efficient to combine beam modifier simulation with dose calculation and that beam modifiers should be simulated. In this chapter, small irregularly-shaped cut-outs that may be necessary to modify the shape of the IORT beam, so that it conforms to the shape of the treatment site, are inserted into the cone. Monte-Carlo simulations of the beam are then performed and compared to measurements to ascertain the validity of MC calculations for these small fields.

7.1 Manufacture of the irregularly–shaped cut-outs

The custom-made irregularly-shaped cut-outs were manufactured with the assistance of the Par Scientific Block Cutting software and associated hotwire cutter (Par Scientific A/S, Odense, Denmark). After manual entry of the indices of the cut-outs for each of the IORT cones (19 mm, 45 mm and 64 mm) used in this study, the information was sent to the block-cutter. The outer dimensions of the cut-out was equivalent to the inner diameter of each cone mentioned above. Molten low melting point alloy (Cerrobend) was then poured into the cut-out and allowed to cool. Each cut-out was made to be 2 cm in thickness. The cut-outs were then inserted into their respective cones, ensuring that the bottom end of the cut-out was flush with the open end of the cone.

The cut-out dimensions for each cone appear in figures 7.1 to 7.3.

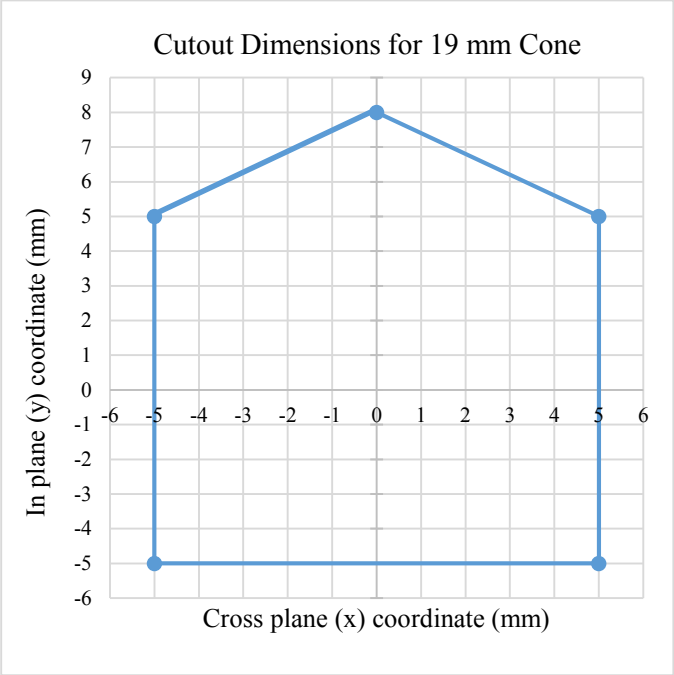

Indices (x,y) in mm for the 19 mm cut-out

(0, 8)
(5, 5)
(5, -5)
(-5, -5)
(-5, 5)

Figure 7.1 Representation of the dimensions and orientation of the cut-out in the 6 MeV, 12 MeV and 18 MeV beams for the 19 mm IORT cone

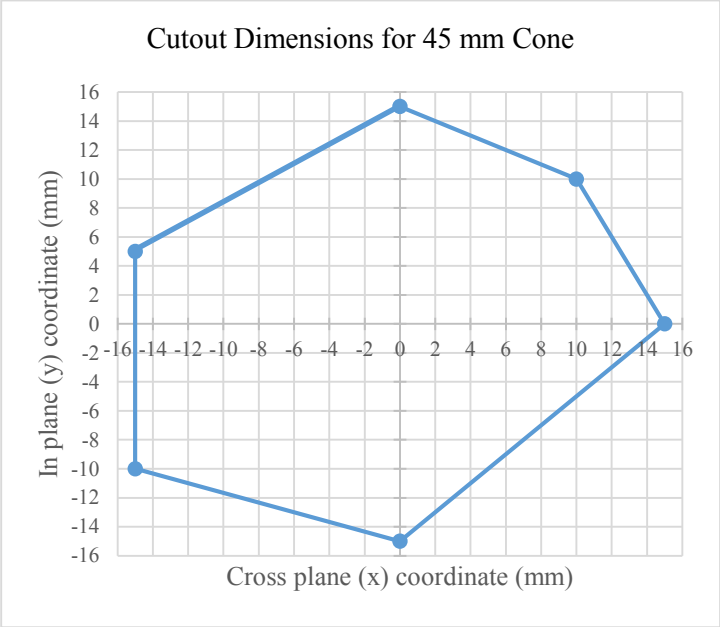

Indices (x,y) in mm for the 45 mm cut-out

(0, 15)
(10, 10)
(15, 0)
(0, -15)
(-15, -10)
(-15, 5)

Figure 7.2 Representation of the dimensions and orientation of the cut-out in the 6 MeV, 12 MeV and 18 MeV beams for the 45 mm IORT cone

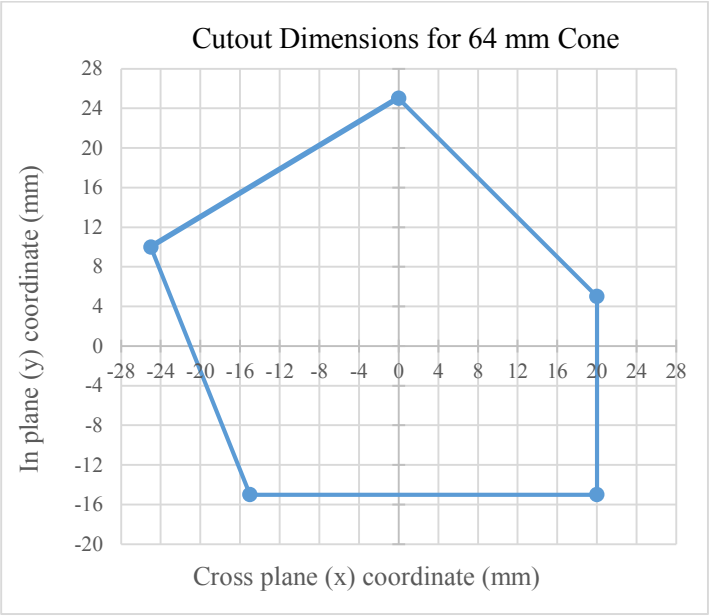

Indices (x,y) in mm for the 64 mm cut-out

(0, 25)
(20, 5)
(20, -15)
(-15, -15)
(-25, 10)

Figure 7.3 Representation of the dimensions and orientation of the cut-out in the 6 MeV, 12 MeV and 18 MeV beams for the 64 mm IORT cone

7.2 BEAMnrc modelling of the IORT accelerator with cut-outs

The input source for each of the 3 energies simulated was the same as that used for the MC simulations for the $10x10\ cm$ applicator and open cones, which was deemed to be the reference source for each energy *(sections 5.4.4.1 and 6.1)*.

The same main input parameters *(table 5.1)* and EGSnrc parameters *(table 5.2)* as for the $10x10\ cm$ applicator case was used as input for the IORT cones with cut-outs. Use of these sources produced PDDs *(section 5.3.2)* and beam profiles *(section 5.3.3)* for the $10x10\ cm$ applicator that compared favourably with measured data and were thus deemed to be acceptable for further investigations.

The exact same primary scattering foil for each energy, primary collimator, secondary scattering foil, chamber and mirror modelled for the $10x10\ cm$ applicator case and IORT cone cases was used to model the accelerators with the respective cut-outs in place.

The FLATFILT CM was once again used to build the cones with their respective cut-outs in BEAMnrc. Each cone still consisted of 9 layers with varying numbers of conical sections in each layer. The difference was that the cones for these cases were made to end at 97 cm instead of 99 cm. This was so that the respective cut-out could be added into the final 2 cm of each cone.

The BLOCK CM was used to model the cut-out. Modelling of the cut-out required input of the z distance of the front (97 cm) and back (99 cm) of the cut-out. The z coordinate from the focal point was chosen as -10^7 which implied a non-divergent block edge for the inner faces of the cut-outs. The BLOCK CM in BEAMnrc allows for only rectangular outer boundaries of the block being modelled, whereas the actual outer boundaries of each block were circular and equivalent to the inner diameter of each cone. The positive x and y and negative x and y coordinates of the outer rectangular boundaries were chosen to be equal in magnitude to the radius of each cone being used in the simulation. In a previous study *(Verhaegen et al 2001)*, it was suggested that only a 1 mm 'skin' (for 6 MeV to 12 MeV beams) of cerrobend be used around the aperture to improve efficiency of the MC calculations. This 'skin' thickness increases to 25 mm for 20 MeV. It is therefore safe to assume that for this study, any particles striking the additional cerrobend that exists off axis beyond 1 mm would have been effectively stopped by the initial 1 mm of cerrobend for the lower energies. Accurate input of the geometry of the cut-out was accomplished by entering the x and y coordinates of the indices *(figures 7.1, 7.2 and 7.3)* of each defining point of the cut-out.

The same PEGS4 datatset, main input parameters and EGSnrc input parameters as for the $10x10\ cm$ applicator, $5\ cm$ circle applicator and IORT cone cases were used for the cut-outs inserted into the IORT cones.

The same jaw settings (Y = 19.0 cm and MLC(X) = 19.0 cm) used for the MC simulation for the $10x10\ cm$ applicator and IORT cone cases was used for each cut-out simulation.

The dimensions and material composition of the various components of the barrel assembly and cone remained unchanged, with the exception of the final 2 cm of the cone, which was replaced by the cut-outs in the build.

The cone was once again slid 1 cm into the barrel assembly so that the open end of the cone/cut-out was at a z distance of 99 cm, resulting in a 1 cm gap between the end of the cut-out and the isocentre.

Monte Carlo simulations were performed for each energy (6 MeV, 12 MeV and 18 MeV) for each cone (19 mm, 45 mm and 64 mm) with the respective cut-outs in place. Phase-space files were scored at the open end of the cut-out at z = 99 cm.

Each PSF was used, in turn, as the input source in DOSXYZnrc. The homogenous water equivalent phantom and source parameters were unchanged from the previous DOSXYZnrc simulations. 3-D dose distributions were obtained from the simulations for each energy/cone/cut-out combination.

Table 7.1 Summary of particles in the Phase-Space file for the 19 mm IORT cut-out

ENERGY (MeV)	Total number of particles	Total number of photons	% Photons	% electrons/positrons	Max kinetic energy (MeV)
6	12 376	10 134	81.9	18.1	7.880
12	43 326	37 735	87.1	12.9	15.26
18	80 025	74 095	92.6	7.4	21.415

Table 7.2 Summary of particles in the Phase-Space file for the 45 mm IORT cut-out

ENERGY (MeV)	Total number of particles	Total number of photons	% Photons	% electrons/positrons	Max kinetic energy (MeV)
6	92 114	69 956	75.9	24.1	8.122
12	307 210	265 782	86.5	13.5	15.466
18	503 505	464 315	92.2	7.8	21.358

Table 7.3 Summary of particles in the Phase-Space file for the 64 mm IORT cut-out

ENERGY (MeV)	Total number of particles	Total number of photons	% Photons	% electrons/positrons	Max kinetic energy (MeV)
6	544 618	402 020	73.8	16.2	8.116
12	627 439	539 727	86.0	14.0	15.838
18	995 259	913 646	91.8	18.2	21.635

7.3 Measured data of the IORT accelerator with cut-outs

The MP3 3-D therapy beam analyser (PTW, Freiburg, Germany) operated by Mephysto mc^2 software was used to acquire the relevant cut-out data for the 6 MeV, 12 MeV and 18 MeV electron beams for each IORT cone of diameter 19 mm, 45 mm and 64 mm. There was a 1 cm air gap between the cone end and the water surface, which was positioned at 100 cm SSD *(figure 6.3)*. The waterproof Pinpoint ionisation chamber (PTW type 31006, Freiburg, Germany) with a measuring volume of 0.015 cm^3 was used as the field chamber to minimise errors due to the small fields used in this study. The semi-flex chamber (PTW type 31010, Freiburg, Germany) with a nominal sensitive volume of 0.125 cm^3 was used as the reference chamber and was placed at the corner of the last scraper of the applicator *(figure 6.3)*.

Central axis percentage depth dose (PDD) curves were measured with 1 mm step size for each energy/cut-out combination.

In-plane and cross-plane profiles were measured with 2 mm step size at the depths specified in table 7.4 below.

Table 7.4 Profile depths acquired for 6 MeV, 12 MeV and 18 MeV beams for the IORT cut-outs

	Depth 1 (cm)	Depth 2 (cm)	Depth 3 (cm)
6 MeV	1.4	2.0	-
12 MeV	2.5	4.0	
18 MeV	2.5	4.5	5.5

7.4 Conversion of MC and measured data

The MC and measured data was modified and converted as detailed in chapter 4.

7.5 Results

7.5.1 Percentage Depth Dose (PDD) Results

For the PDD comparisons, the %dose difference, DoN (in % of normalization value of the reference matrix) parameter was used. The passing criteria set was DoN ≤ 3.0%. Green bars in the histogram represents the %pass at each %difference level (x axis). The associated DoN histograms appear adjacent to each set of plotted data.

Table 7.5 Absolute differences between measured and MC-calculated characteristic points on the PDD curve for the 19 mm IORT cut-out for energies 6, 12 and 18 MeV.

	6 MeV			12 MeV			18 MeV		
	Meas	**MC**	**Diff**	**Meas**	**MC**	**Diff**	**Meas**	**MC**	**Diff**
D_s (%)	95.4	95.1	**-0.3**	98.2	95.9	**-2.3**	94.9	95.5	**0.6**
R_{max} (cm)	0.50	0.45	**-0.05**	0.25	0.45	**0.20**	1.35	0.55	**0.20**
R_{90} (cm)	0.97	0.98	**0.01**	1.25	1.27	**0.02**	1.64	1.68	**0.02**
R_{80} (cm)	1.20	1.20	**0.00**	1.63	1.64	**0.01**	2.09	2.16	**0.07**
R_{50} (cm)	1.75	1.74	**-0.01**	2.49	2.53	**0.04**	3.28	3.32	**0.04**

Table 7.6 Absolute differences between measured and MC-calculated characteristic points on the PDD curve for the 45 mm IORT cut-out for energies 6, 12 and 18 MeV.

	6 MeV			12 MeV			18 MeV		
	Meas	**MC**	**Diff**	**Meas**	**MC**	**Diff**	**Meas**	**MC**	**Diff**
D_s (%)	85.3	86.7	**1.4**	93.4	91.6	**-1.8**	98.4	96.2	**-2.2**
R_{max} (cm)	1.10	1.05	**-0.10**	1.50	1.25	**-0.25**	0.95	1.15	**0.20**
R_{90} (cm)	1.67	1.62	**-0.05**	2.61	2.53	**-0.12**	3.00	3.00	**0.00**
R_{80} (cm)	1.89	1.82	**-0.07**	3.04	2.96	**-0.08**	3.73	3.75	**0.02**
R_{50} (cm)	2.37	2.33	**-0.04**	4.07	4.03	**-0.04**	5.23	5.24	**0.01**

Table 7.7 Absolute differences between measured and MC-calculated characteristic points on the PDD curve for the 64 mm IORT cut-out for energies 6, 12 and 18 MeV.

	6 MeV			12 MeV			18 MeV		
	Meas	**MC**	**Diff**	**Meas**	**MC**	**Diff**	**Meas**	**MC**	**Diff**
D_s (%)	84.3	82.2	**-2.1**	96.3	93.0	**-3.3**	98.3	96.1	**-2.2**
R_{max} (cm)	1.25	1.25	**0.00**	1.50	1.65	**0.15**	0.90	0.65	**-0.35**
R_{90} (cm)	1.76	1.74	**-0.02**	2.95	2.92	**-0.03**	3.45	3.46	**0.01**
R_{80} (cm)	1.96	1.93	**-0.03**	3.45	3.40	**-0.05**	4.35	4.33	**-0.02**
R_{50} (cm)	2.39	2.37	**-0.02**	4.50	4.45	**-0.05**	6.06	6.03	**-0.03**

The statistical variance was less than 1% for all Monte Carlo PDD calculations *(section 4.3.4)*.

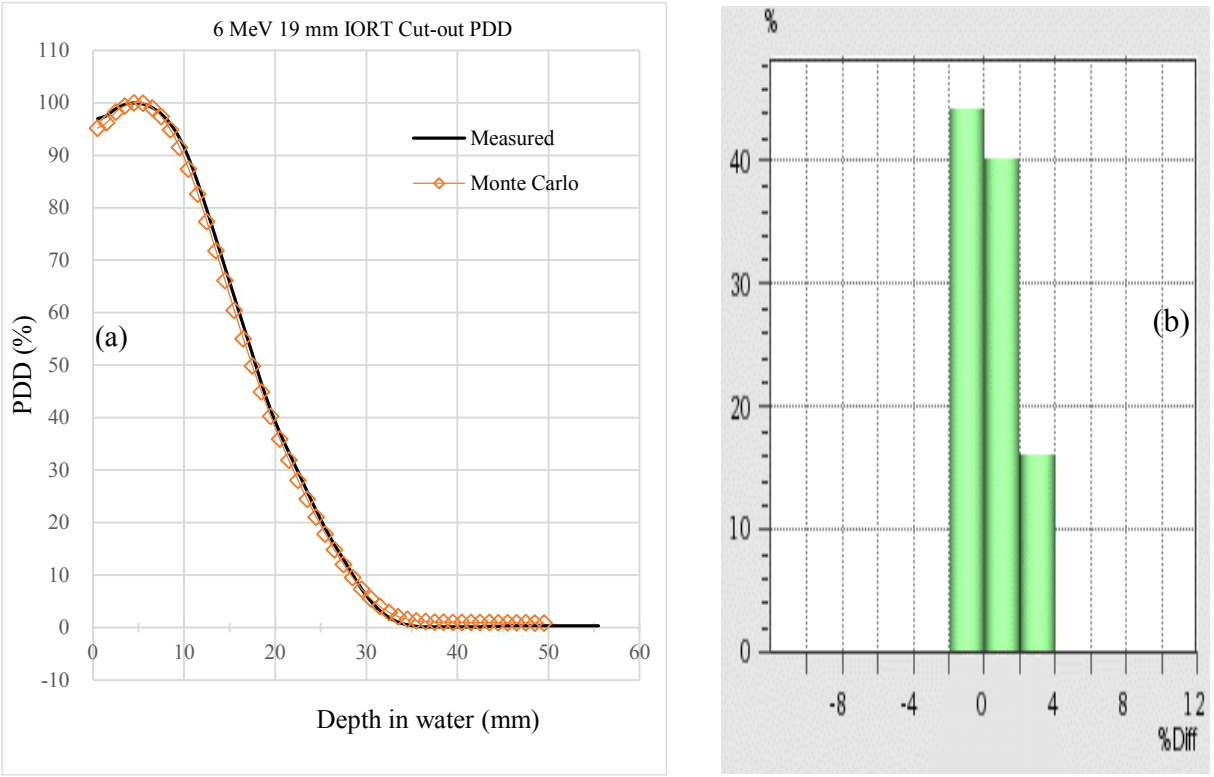

Figure 7.4 Comparison of measured and MC PDDs for 6 MeV 19 mm IORT Cone with Cut-out: (a) PDD (b) % dose difference histogram

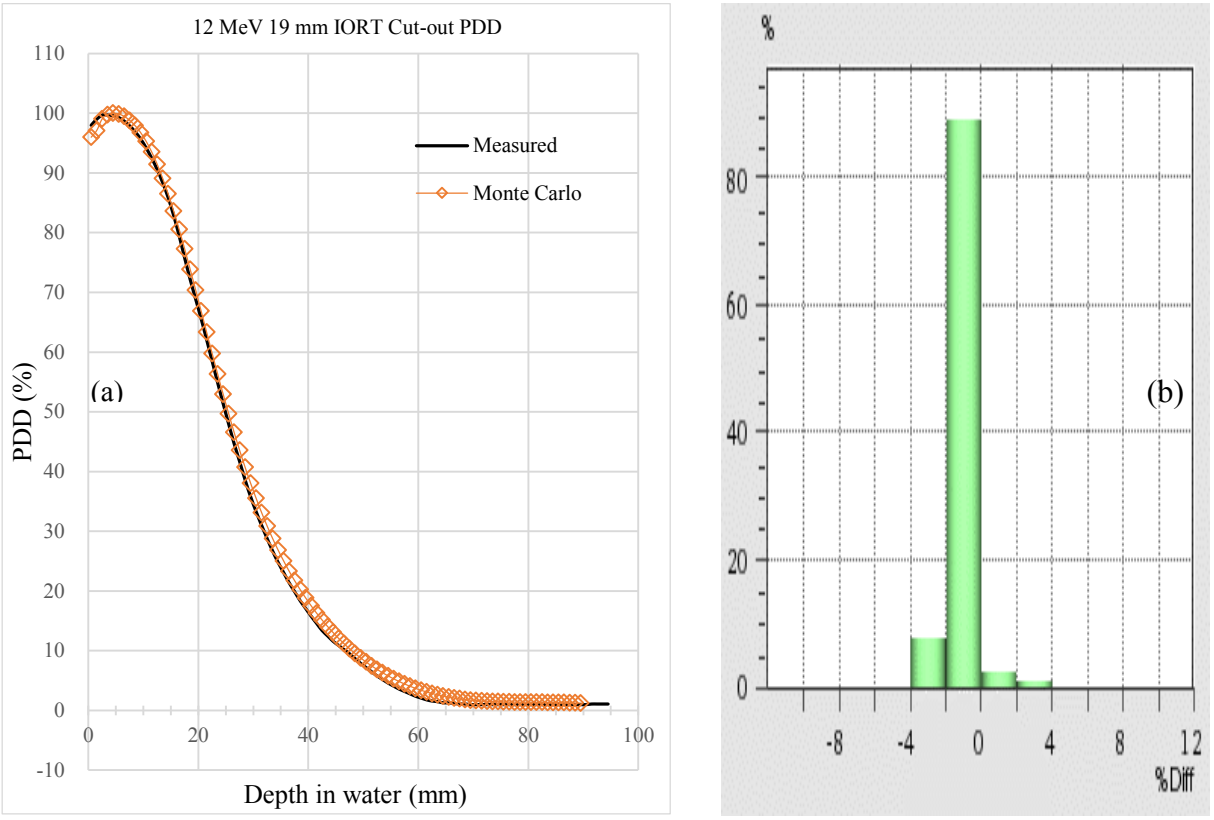

Figure 7.5 Comparison of measured and MC PDDs for 12 MeV 19 mm IORT Cone with Cut-out: (a) PDD (b) % dose difference histogram

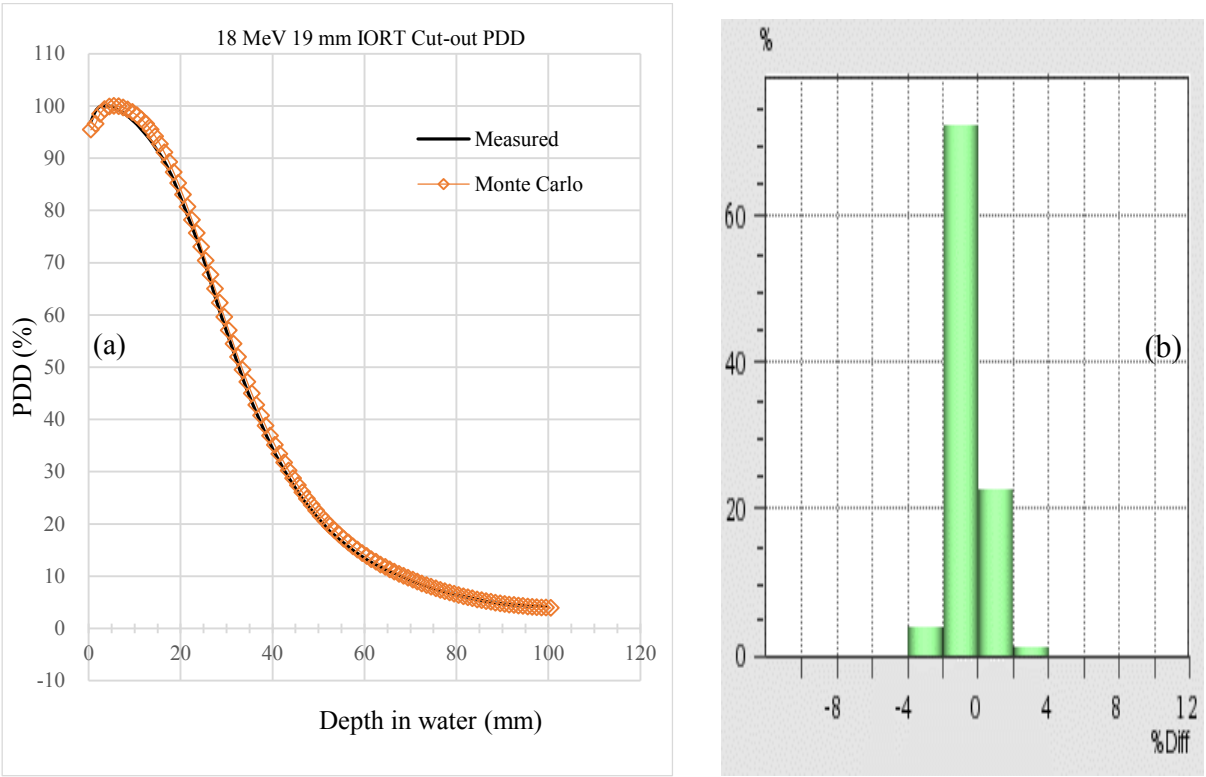

Figure 7.6 Comparison of measured and MC PDDs for 18 MeV 19 mm IORT Cone with Cut-out: (a) PDD (b) % dose difference histogram

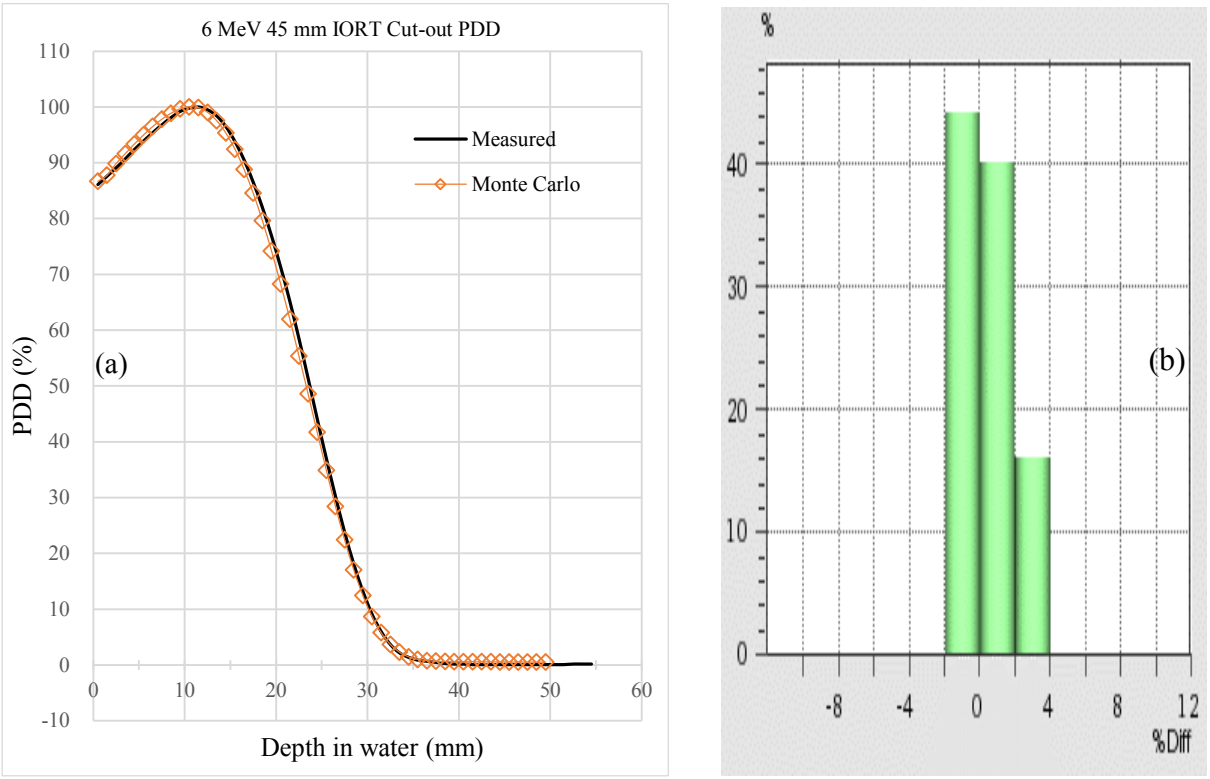

Figure 7.7 Comparison of measured and MC PDDs for 6 MeV 45 mm IORT Cone with Cut-out: (a) PDD (b) % dose difference histogram

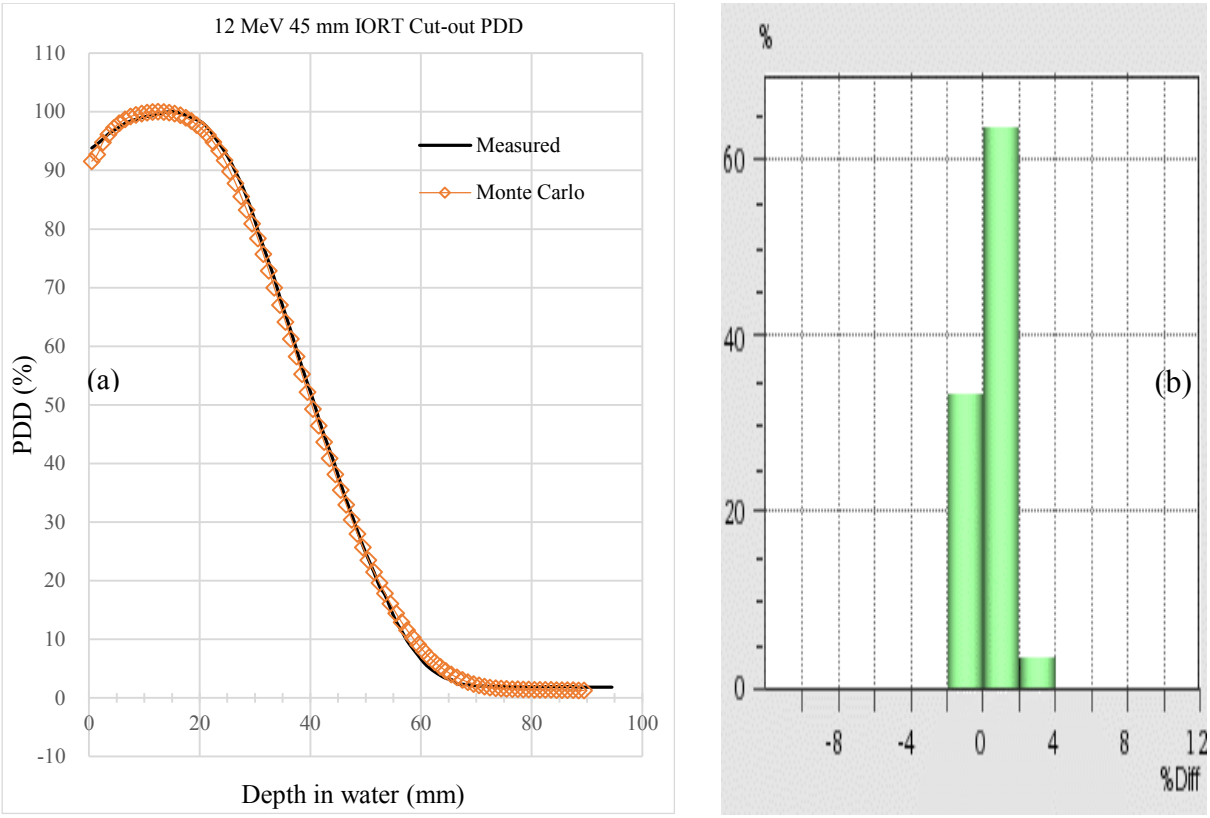

Figure 7.8 Comparison of measured and MC PDDs for 12 MeV 45 mm IORT Cone with Cut-out: (a) PDD (b) % dose difference histogram

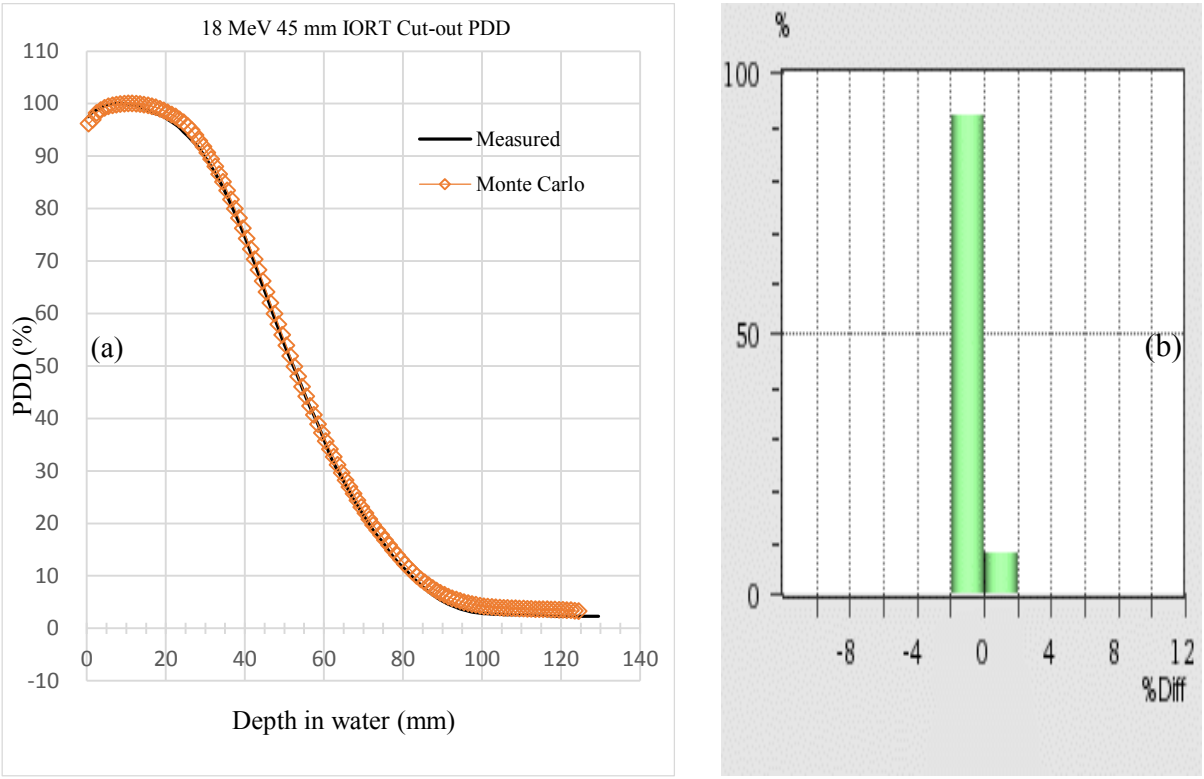

Figure 7.9 Comparison of measured and MC PDDs for 18 MeV 45 mm IORT Cone with Cut-out: (a) PDD (b) % dose difference histogram

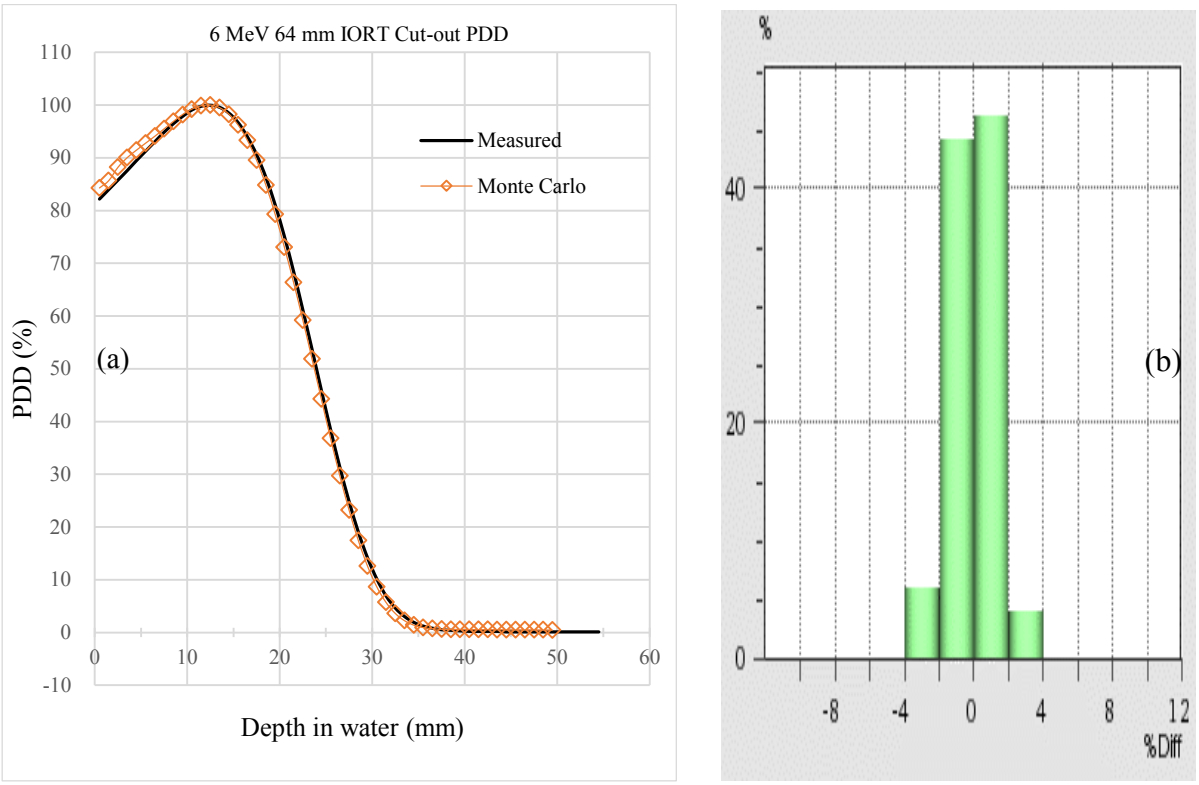

Figure 7.10 Comparison of measured and MC PDDs for 6 MeV 64 mm IORT Cone with Cut-out: (a) PDD (b) % dose difference histogram

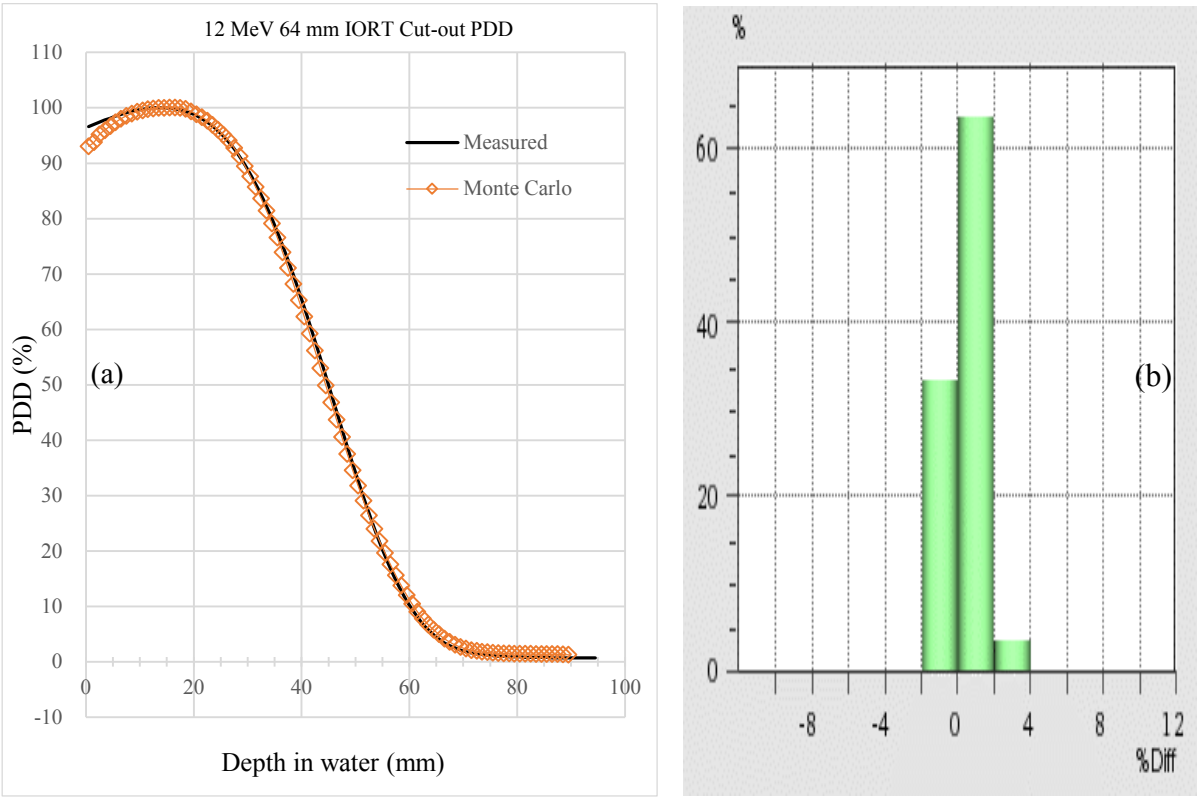

Figure 7.11 Comparison of measured and MC PDDs for 12 MeV 64 mm IORT Cone with Cut-out: (a) PDD (b) % dose difference histogram

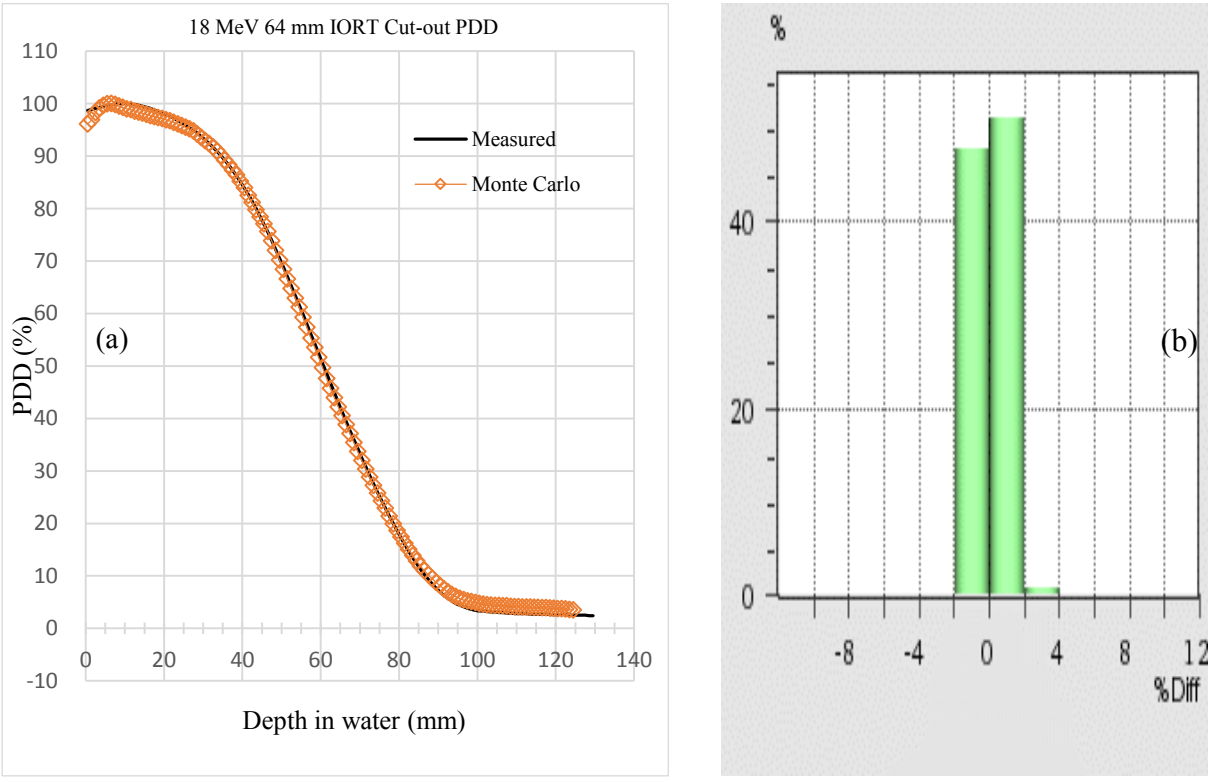

Figure 7.12 Comparison of measured and MC PDDs for 18 MeV 64 mm IORT Cone with Cut-out: (a) PDD (b) % dose difference histogram

7.5.1.1 Analysis

For the 19 mm IORT cone, direct comparison of the depths R_{max}, R_{90}, R_{80}, and R_{50} *(table 7.5)* show differences of less than 1.0 mm for all energies with the exception of R_{max} for the 12 MeV and 18 MeV beams which differed by 2 mm. All MC-calculated depths were equal to or larger than measurement for all the beams. All calculated surface dose values were lower than measurement with the surface dose for the 12 MeV beam displaying a difference of 2.3%. However, this dose difference decreased to 0% within the first 1.5 mm *(figure 7.5(a))* for this beam. The values between R_{max} and R_{20} for all energies compared favourably. The bremsstrahlung tail for the calculated curve is higher for all 3 energies but still fell within the acceptance criteria.

For the 45 mm IORT cone, direct comparison of the depths R_{max}, R_{90}, R_{80}, and R_{50} *(table 7.6)* show differences of less than 1.0 mm for all energies with the exception of R_{max} for the 12 MeV and 18 MeV beams which differed by 2.5 mm and 2.0 mm respectively, which was similar to the 19 mm cone cases.

The surface dose for the 18 MeV beam lower by 2.2%. However, this dose difference decreased to 0% within the first 1.5 mm *(figure 7.9(a))* for this beam. The values between R_{max} and R_{20} for all energies compared favourably.

The bremsstrahlung tail for the calculated curve is higher for the 6 MeV and 18 MeV beams but still fell within the acceptance criteria.

For the 64 mm IORT cone, direct comparison of the depths R_{max}, R_{90}, R_{80}, and R_{50} *(table 7.7)* show differences of less than 1.0 mm for all energies with the exception of R_{max} for the 12 MeV and 18 MeV beams, with the 18 MeV beam displaying a large difference of 3.5 mm. The surface dose for all the beams were lower than measurement with the 12 MeV beam displaying a difference of 3.3%. The values between R_{max} and R_{20} for all energies compared

favourably. The bremsstrahlung tail for the calculated curve is higher for all beams but still fell within the acceptance criteria.

7.5.2 Beam Profile Results

The comparison, with the MC simulation data, of the measured in-plane and cross-plane profiles at the depths specified in table 7.4 yielded similar results, so for brevity, only the cross-plane results are reported below.

The measured data was used as the reference matrix with the MC data as the secondary data set.

For the profile comparisons, the following 2D GI parameters were used:

3.0 mm Distance – To – Agreement (DTA)

3.0% Dose Difference with reference to local dose

Increased tolerance of 4.0 % Dose Difference for values below 3.0 %. This implies that for any dose points in the profile that is less than 3% of the maximum dose (extreme ends of the penumbra), the pass/fail GI criteria is increased to 4%.

The GI histograms appear adjacent to each set of plotted data. The percentage that satisfy the passing criteria of Gamma ≤ 1.0 are represented by light green and dark green bars for MC values greater than the measured values (hot) and for MC values less than the measured values (cold) respectively.

The percentage that fail and have Gamma > 1.0 are represented by red and blue bars for MC values greater than the measured values (hot) and for MC values less than the measured values (cold) respectively.

The red and blue ellipses on the plotted profile curves represent the point(s) on the curve that fail the GI criteria according to the colour nomenclature specified above.

The statistical variance was less than 1% for all Monte Carlo profile calculations *(section 4.3.4)*.

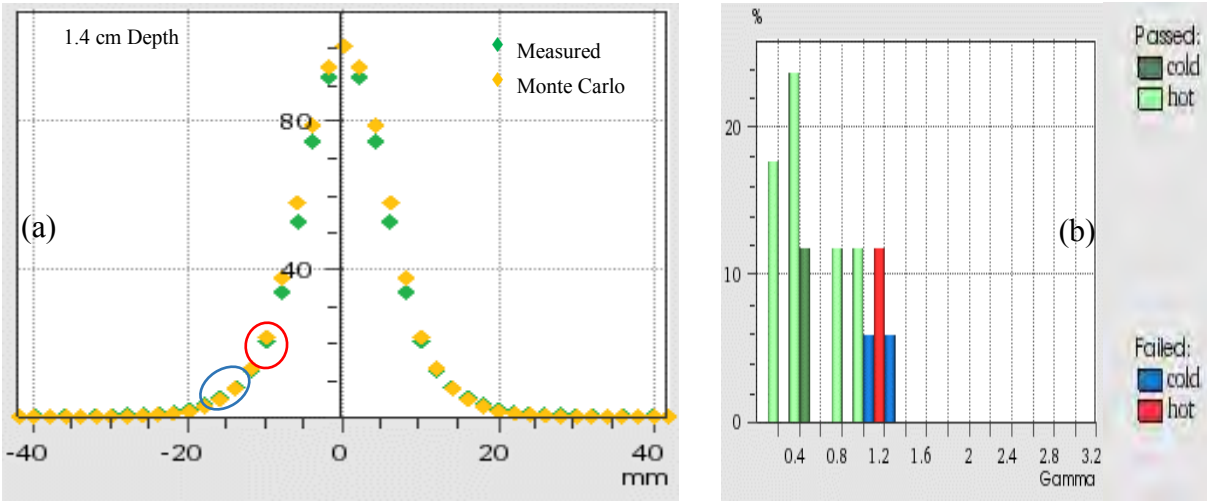

Figure 7.13 Comparison of measured and MC profiles at 1.4 cm depth for 6 MeV 19 mm IORT Cone with Cut-out: (a) Profile (b) Gamma Index histogram

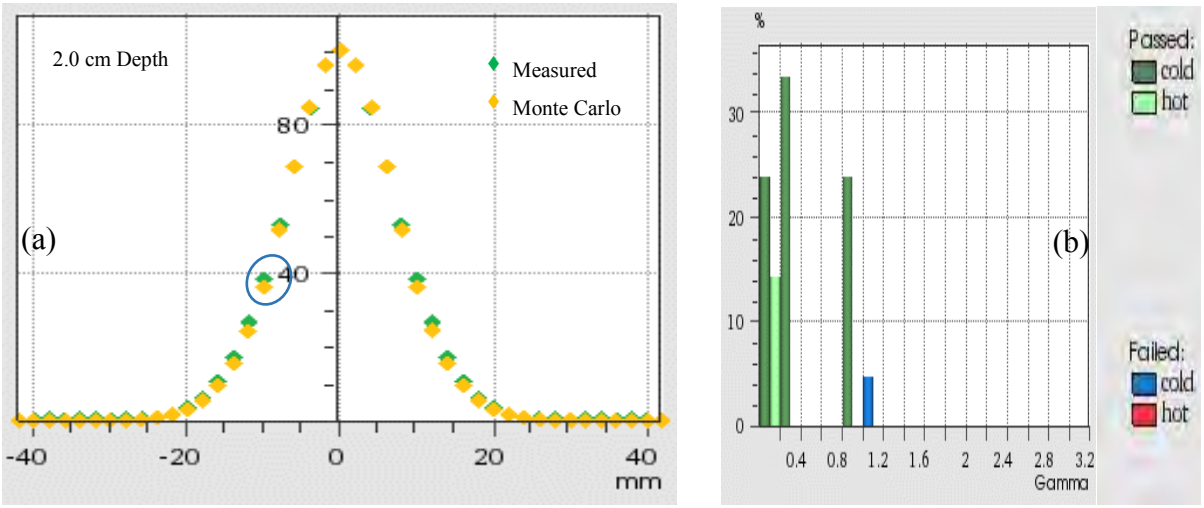

Figure 7.14 Comparison of measured and MC profiles at 2.0 cm depth for 6 MeV 19 mm IORT Cone with Cut-out: (a) Profile (b) Gamma Index histogram

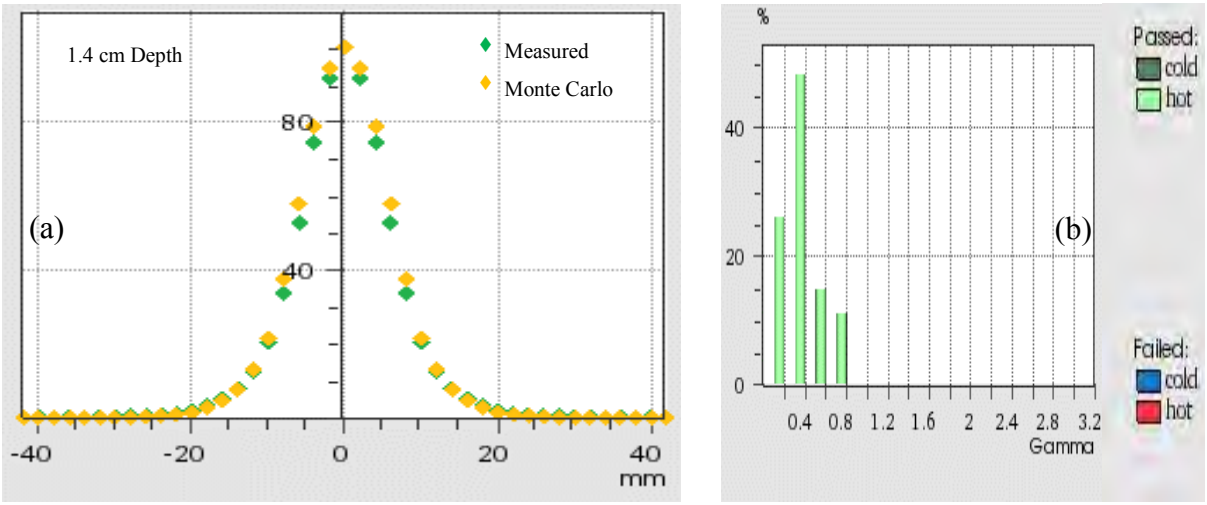

Figure 7.15 Comparison of measured and MC profiles at 1.4 cm depth for 6 MeV 45 mm IORT Cone with Cut-out: (a) Profile (b) Gamma Index histogram

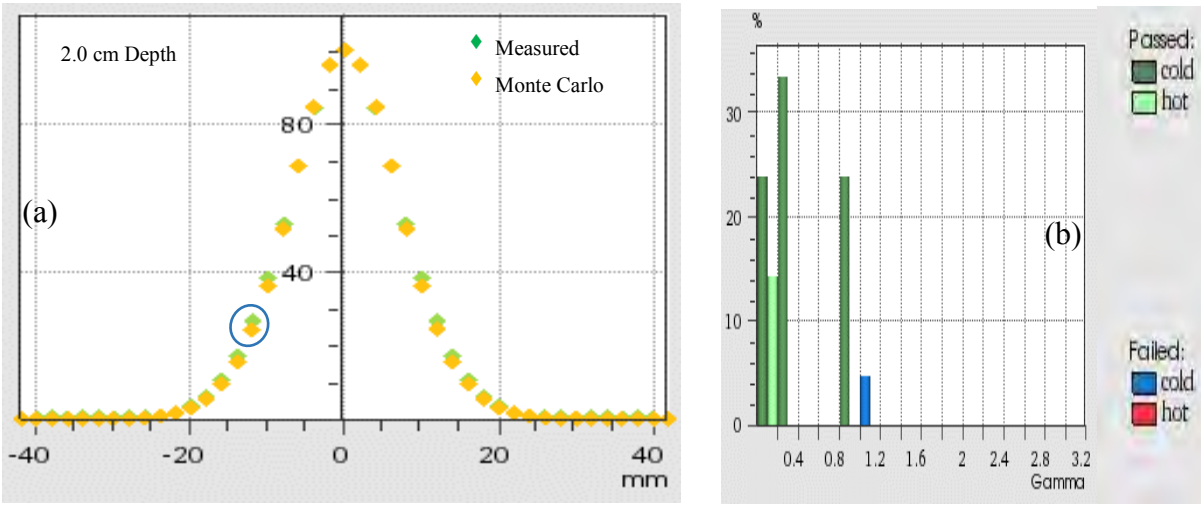

Figure 7.16 Comparison of measured and MC profiles at 2.0 cm depth for 6 MeV 45 mm IORT Cone with Cut-out: (a) Profile (b) Gamma Index histogram

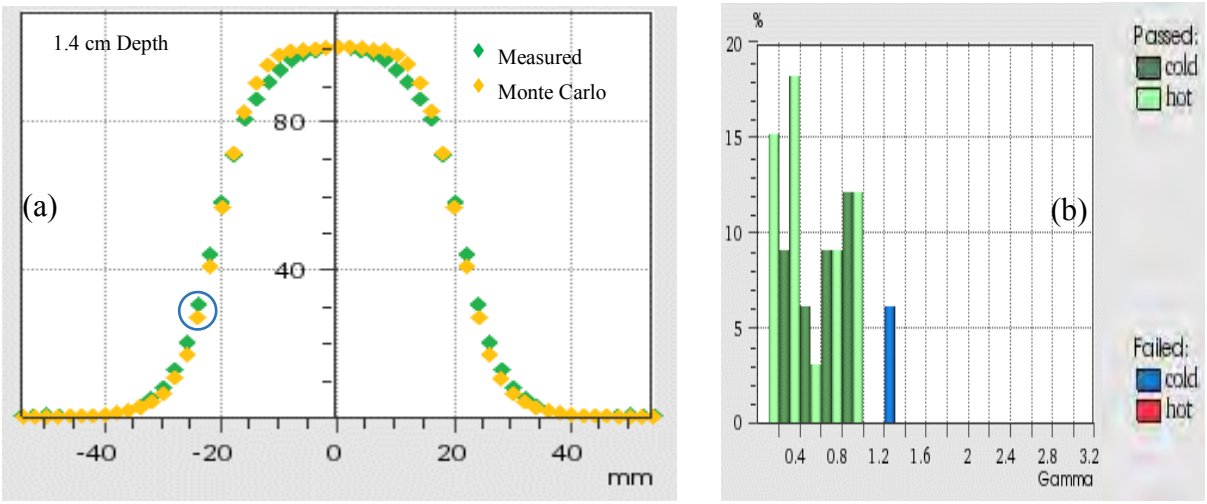

Figure 7.17 Comparison of measured and MC profiles at 1.4 cm depth for 6 MeV 64 mm IORT Cone with Cut-out: (a) Profile (b) Gamma Index histogram

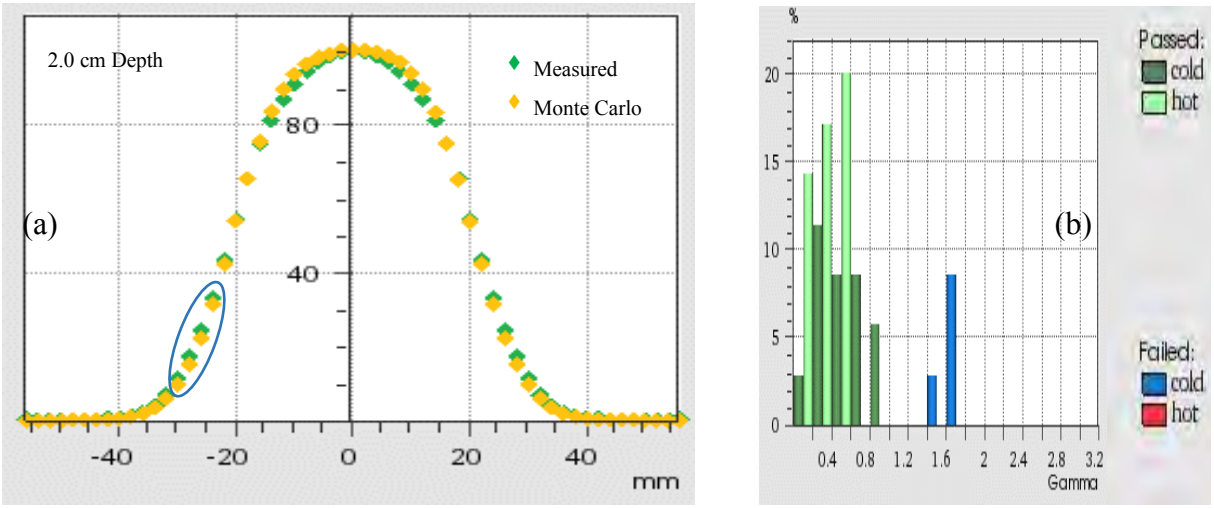

Figure 7.18 Comparison of measured and MC profiles at 2.0 cm depth for 6 MeV 64 mm IORT Cone with Cut-out: (a) Profile (b) Gamma Index histogram

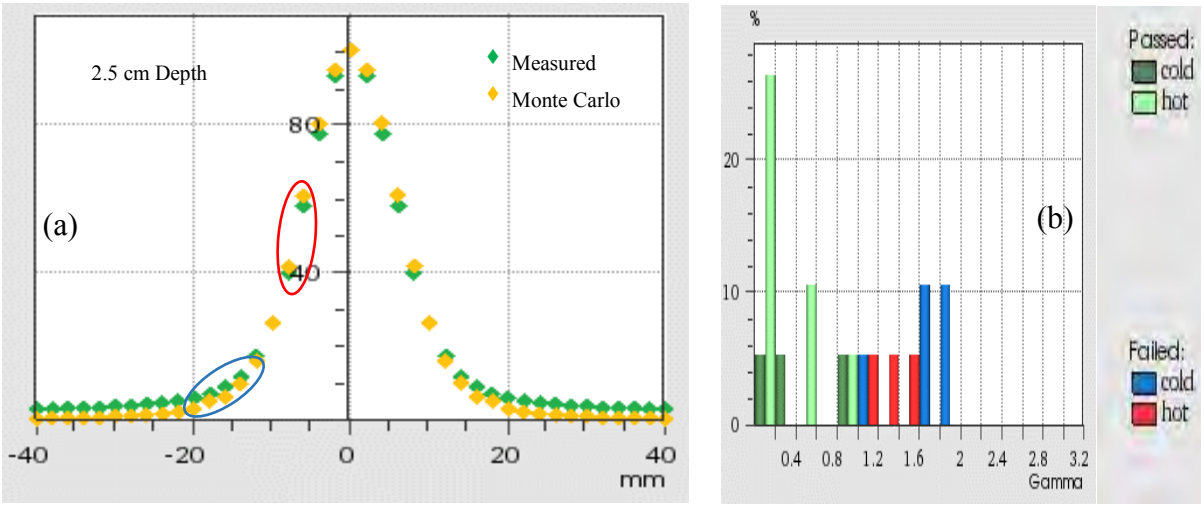

Figure 7.19 Comparison of measured and MC profiles at 2.5 cm depth for 12 MeV 19 mm IORT Cone with Cut-out: (a) Profile (b) Gamma Index histogram

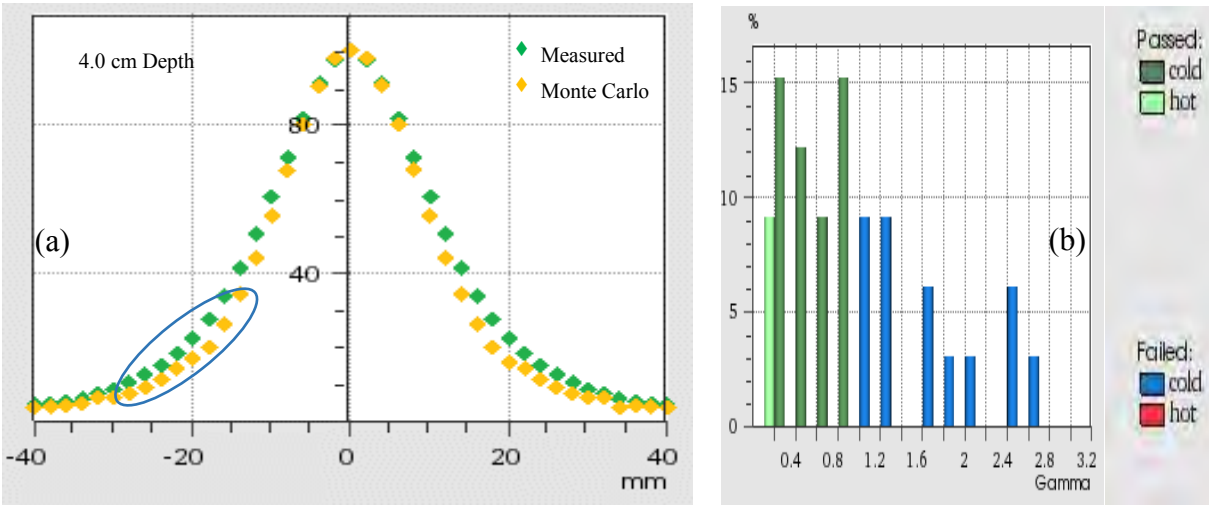

Figure 7.20 Comparison of measured and MC profiles at 4.0 cm depth for 12 MeV 19 mm IORT Cone with Cut-out: (a) Profile (b) Gamma Index histogram

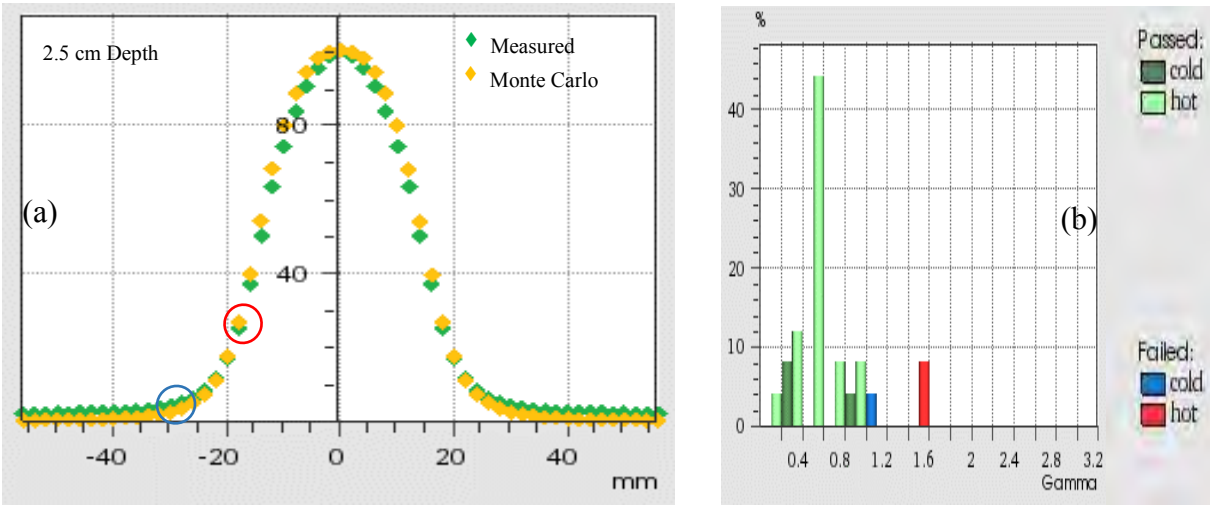

Figure 7.21 Comparison of measured and MC profiles at 2.5 cm depth for 12 MeV 45 mm IORT Cone with Cut-out: (a) Profile (b) Gamma Index histogram

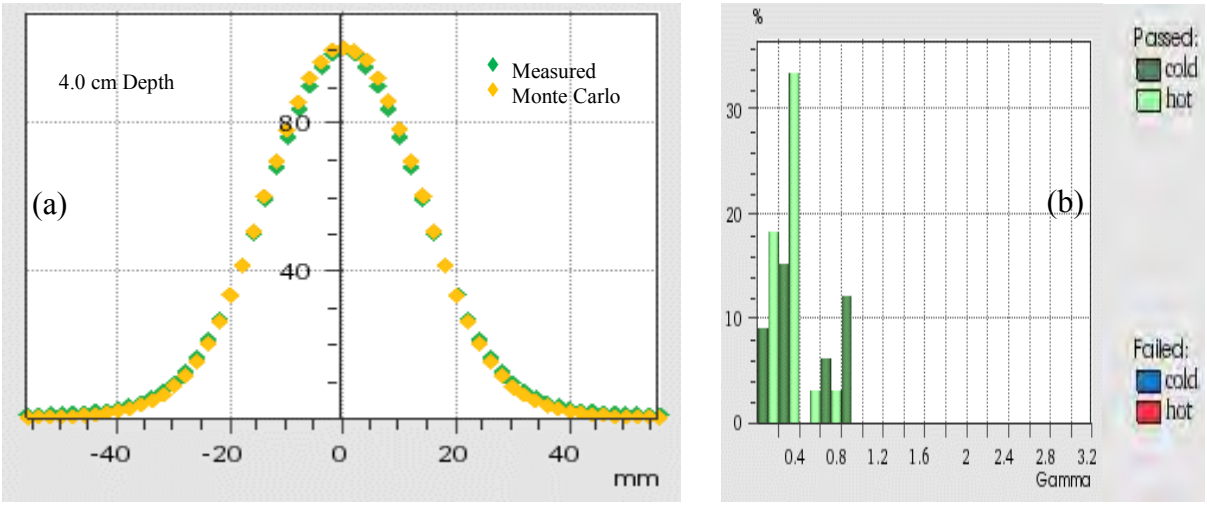

Figure 7.22 Comparison of measured and MC profiles at 4.0 cm depth for 12 MeV 45 mm IORT Cone with Cut-out: (a) Profile (b) Gamma Index histogram

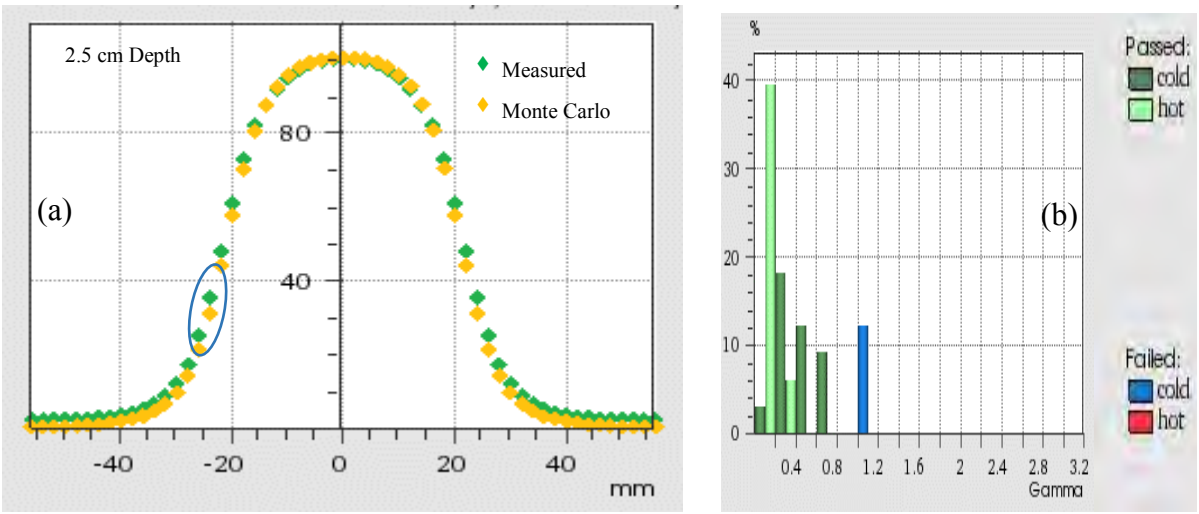

Figure 7.23 Comparison of measured and MC profiles at 2.5 cm depth for 12 MeV 64 mm IORT Cone with Cut-out: (a) Profile (b) Gamma Index histogram

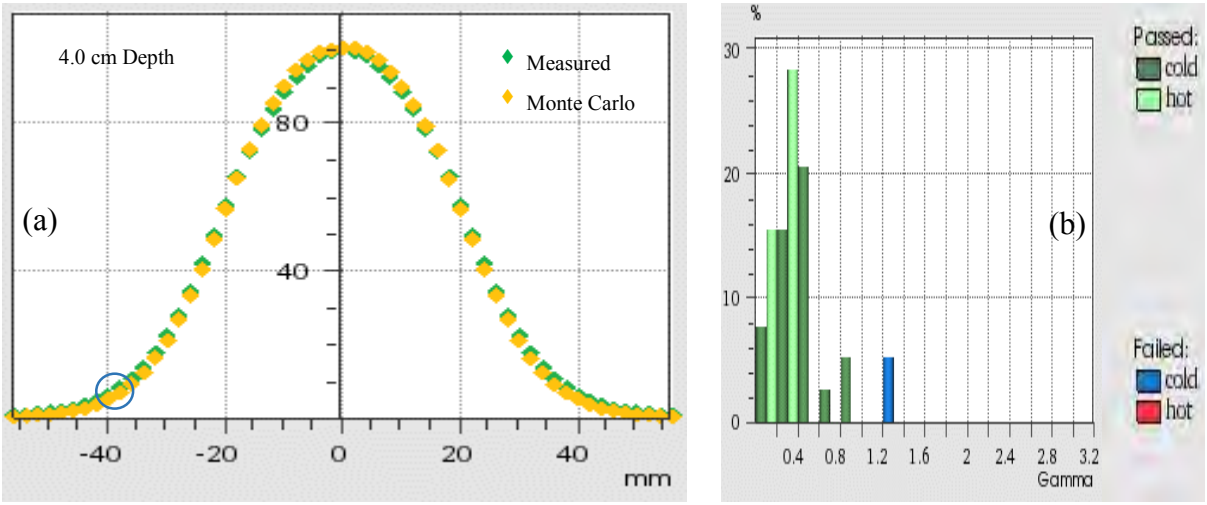

Figure 7.24 Comparison of measured and MC profiles at 4.0 cm depth for 12 MeV 64 mm IORT Cone with Cut-out: (a) Profile (b) Gamma Index histogram

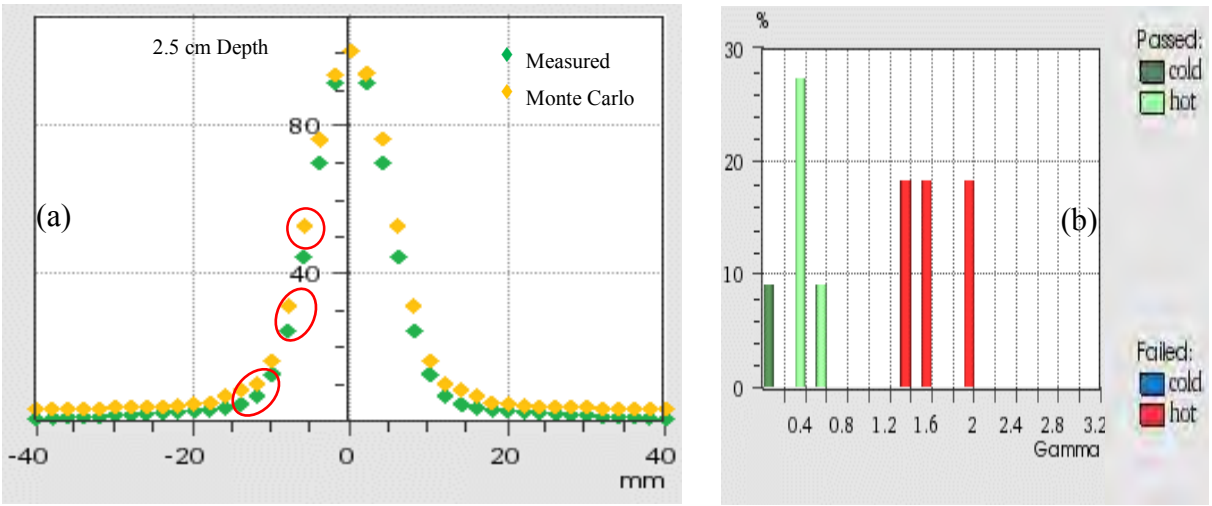

Figure 7.25 Comparison of measured and MC profiles at 2.5 cm depth for 18 MeV 19 mm IORT Cone with Cut-out: (a) Profile (b) Gamma Index histogram

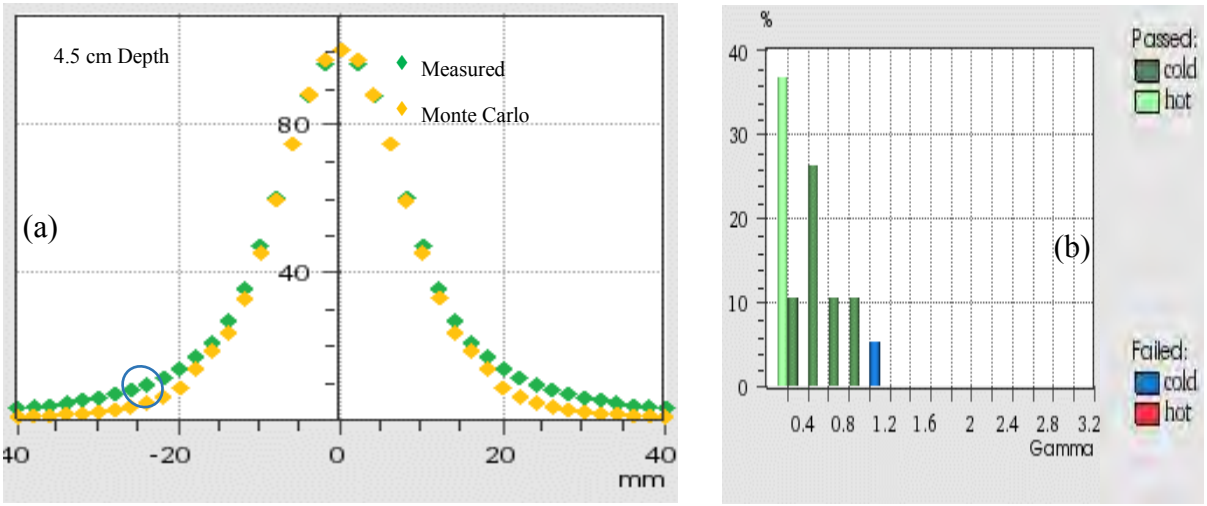

Figure 7.26 Comparison of measured and MC profiles at 4.5 cm depth for 18 MeV 19 mm IORT Cone with Cut-out: (a) Profile (b) Gamma Index histogram

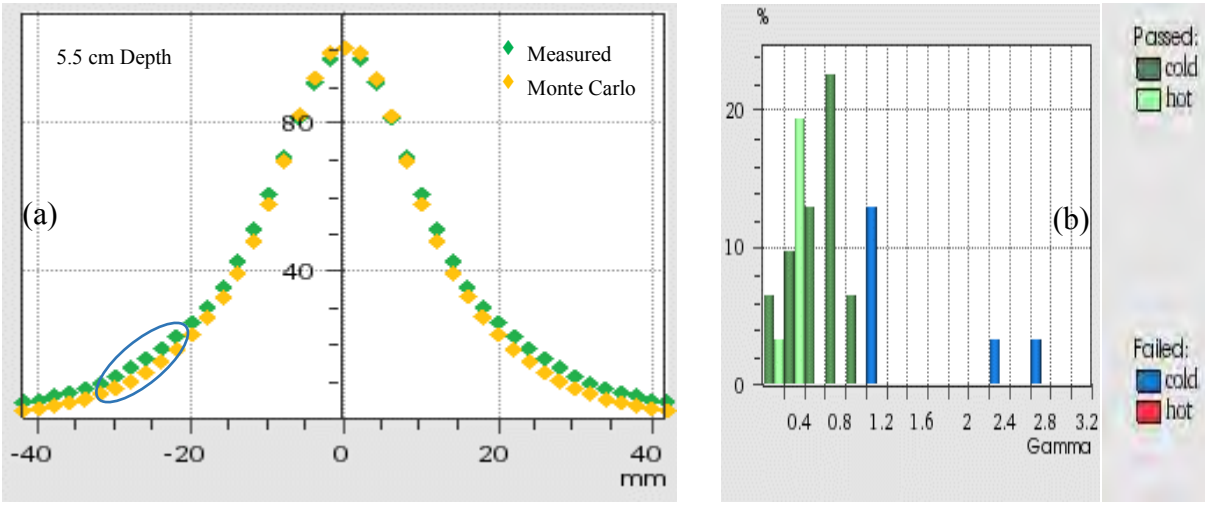

Figure 7.27 Comparison of measured and MC profiles at 5.5 cm depth for 18 MeV 19 mm IORT Cone with Cut-out: (a) Profile (b) Gamma Index histogram

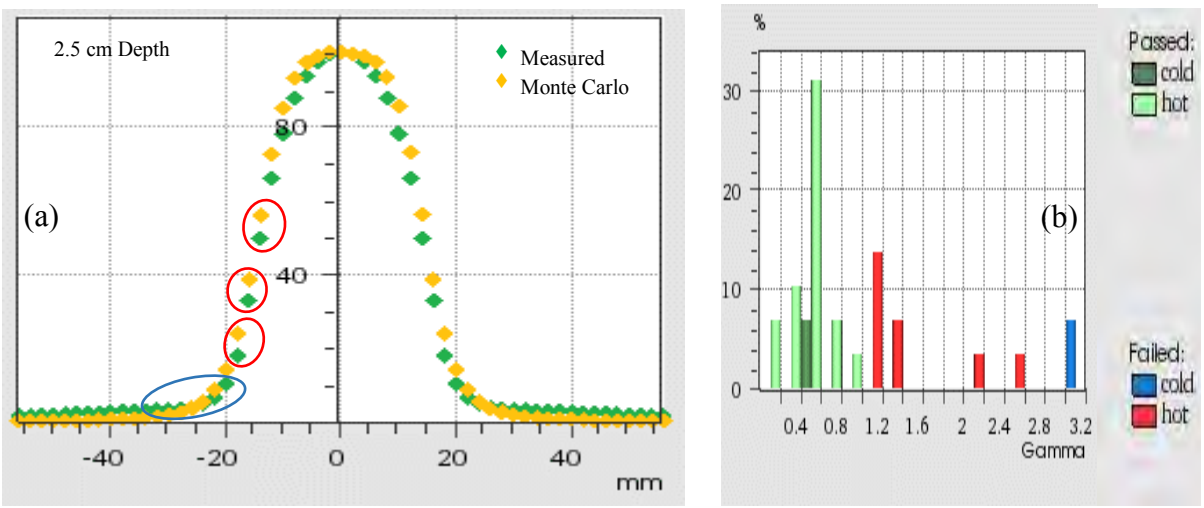

Figure 7.28 Comparison of measured and MC profiles at 2.5 cm depth for 18 MeV 45 mm IORT Cone with Cut-out: (a) Profile (b) Gamma Index histogram

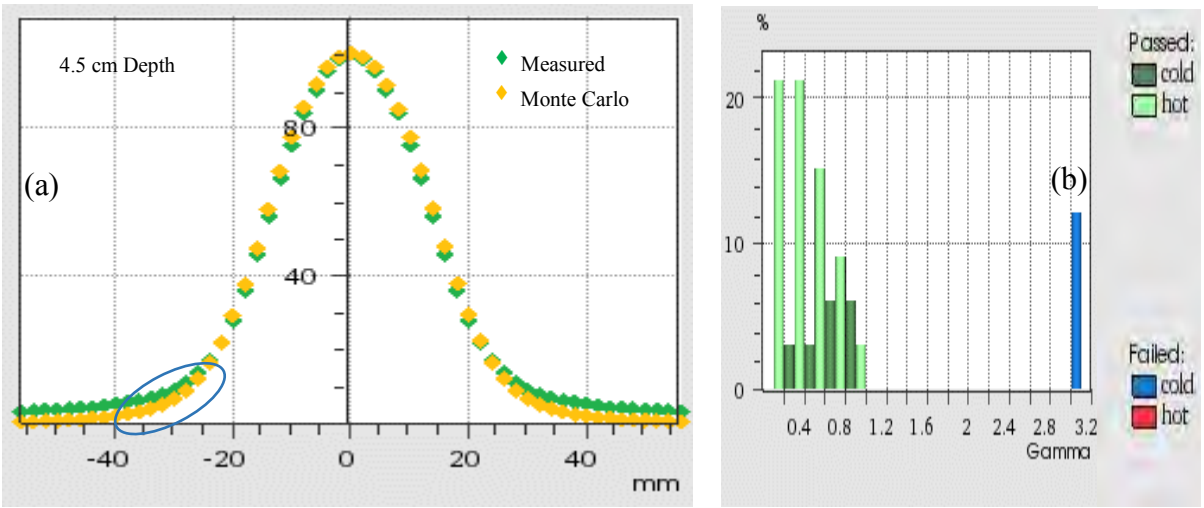

Figure 7.29 Comparison of measured and MC profiles at 4.5 cm depth for 18 MeV 45 mm IORT Cone with Cut-out: (a) Profile (b) Gamma Index histogram

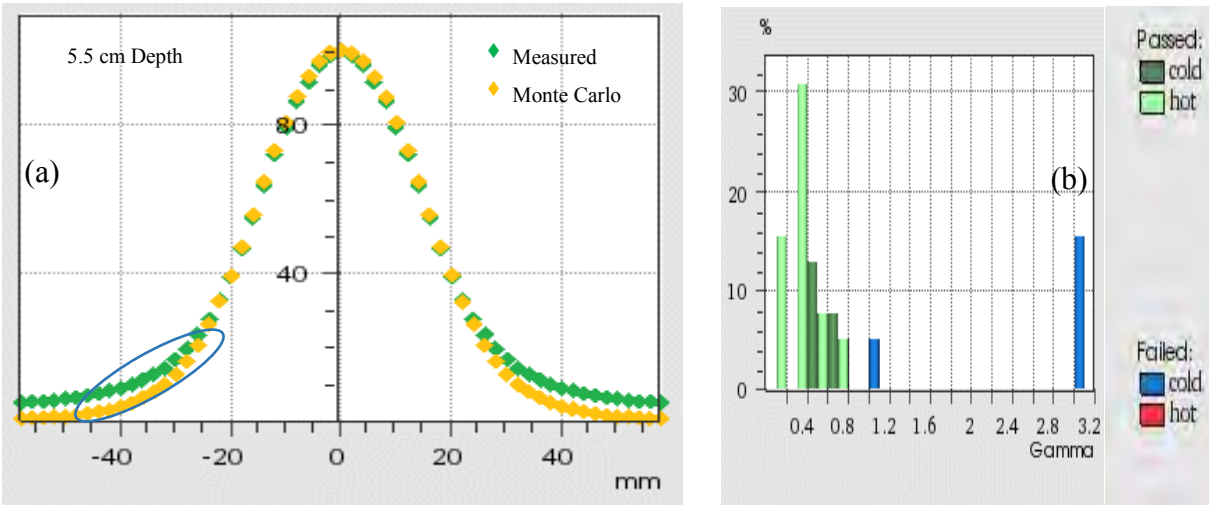

Figure 7.30 Comparison of measured and MC profiles at 5.5 cm depth for 18 MeV 45 mm IORT Cone with Cut-out: (a) Profile (b) Gamma Index histogram

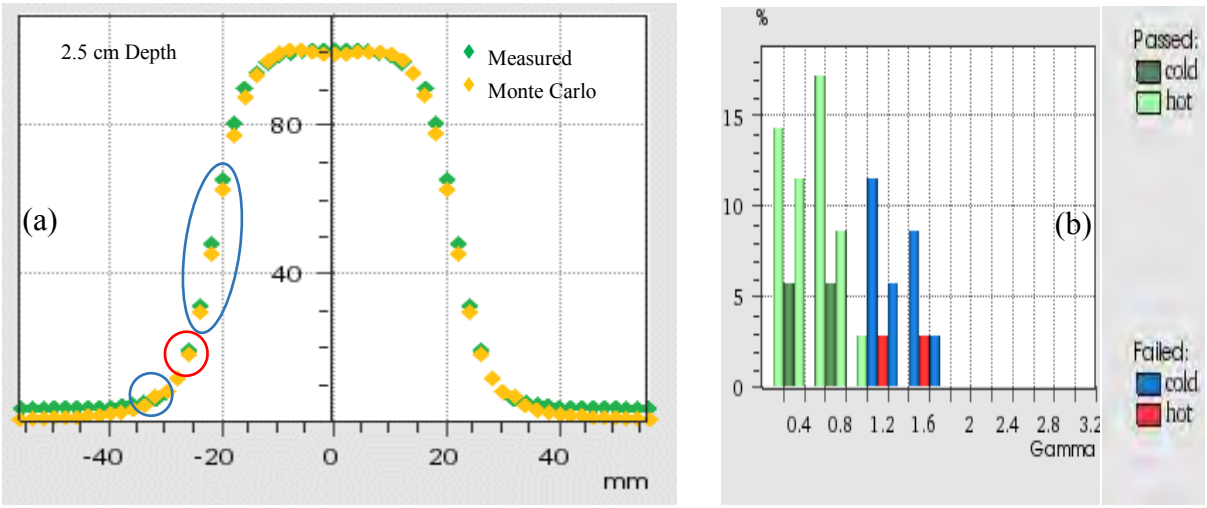

Figure 7.31 Comparison of measured and MC profiles at 2.5 cm depth for 18 MeV 64 mm IORT Cone with Cut-out: (a) Profile (b) Gamma Index histogram

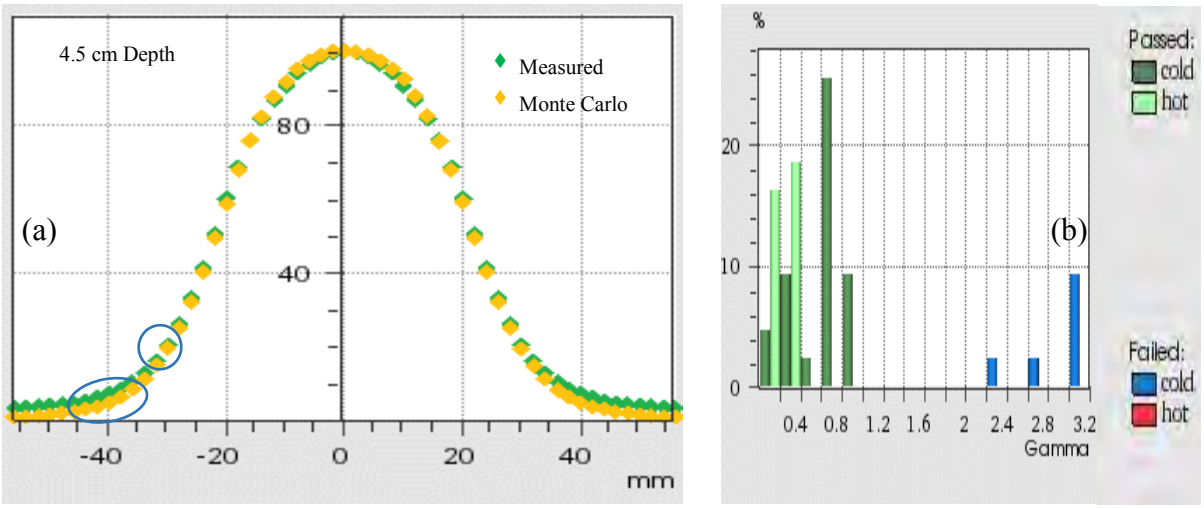

Figure 7.32 Comparison of measured and MC profiles at 4.5 cm depth for 18 MeV 64 mm IORT Cone with Cut-out: (a) Profile (b) Gamma Index histogram

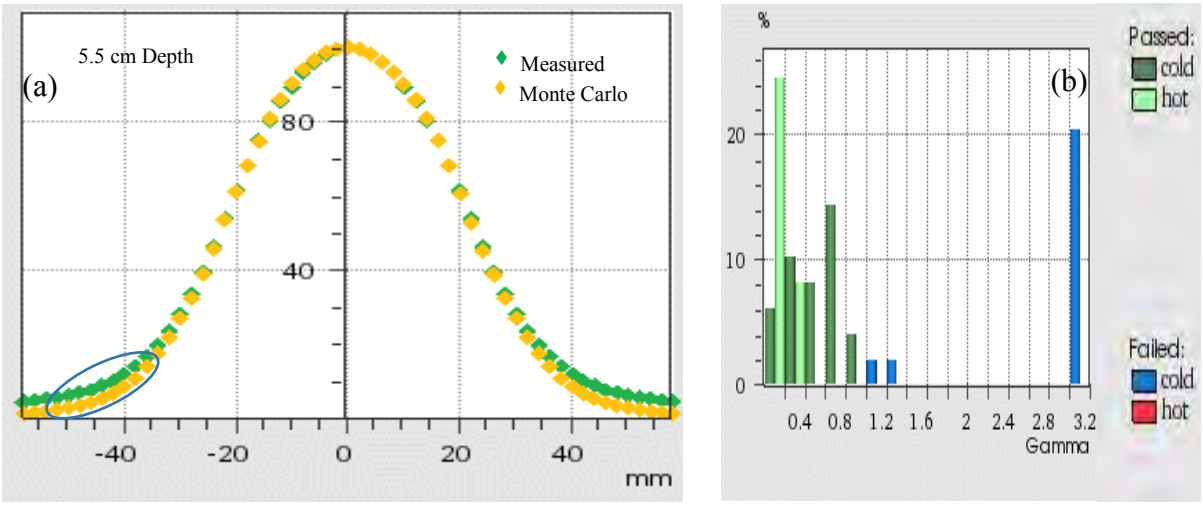

Figure 7.33 Comparison of measured and MC profiles at 5.5 cm depth for 18 MeV 64 mm IORT Cone with Cut-out: (a) Profile (b) Gamma Index histogram

7.5.2.1 Analysis

6 MeV 19 mm cone beam profile at 1.4 cm depth: 12% of the points failed with a maximum γ of 1.2 in the high dose gradient region of 20% at lateral distance of 10 mm, where the calculated points were higher than the measured points. A maximum γ of 1.4 is displayed at lateral distance ranging from 13 mm to 18 mm with the calculated doses being lower than measurement.

6 MeV 19 mm cone beam profile at 2.0 cm depth: Approximately 6% of the failed points had a maximum γ of 1.3 in the 40% dose region at lateral distance of 10 mm.

6 MeV 45 mm cone beam profile at 1.4 cm depth: There were no observable differences with all points meeting the acceptance criteria.

6 MeV 45 mm cone beam profile at 2.0 cm depth: Less than 4% of the points failed with a maximum γ of 1.1 in the high dose gradient region of 25% at lateral distance of 13 mm, where the calculated points were lower than the measured points.

6 MeV 64 mm cone beam profile at 1.4 cm depth: Less than 6% of the points failed with a maximum γ of 1.4 in the high dose gradient region of 30% at lateral distance of 22 mm, where the calculated points were lower than the measured points.

6 MeV 64 mm cone beam profile at 2.0 cm depth: Less than 7% of the points failed with a maximum γ of 1.7 in the high dose gradient range of 10% to 35% at lateral distance ranging from 22 mm to 30 mm, where the calculated points were lower than the measured points.

12 MeV 19 mm beam profile at 2.5 cm depth: A maximum of 10% of the failed points were hotter in the 40% to 60% dose range with γ of less than 1.6 at lateral distance of 10 mm. A maximum gamma of 1.6 was displayed in the low dose range of 0% to 10% at lateral distance ranging from 12 mm to 20 mm.

12 MeV 19 mm beam profile at 4.0 cm depth: the calculated beam was colder in the low dose range between 5% and 30% with a maximum γ of 2.7 at lateral distance ranging from 12 mm to 35 mm.

12 MeV 45 mm beam profile at 2.5 cm depth: Less than 8% of the failed points were hotter in the 25% dose region with γ of less than 1.6 at lateral distance of 18 mm. A colder spot was evident at lateral distance of 28 mm in the 3% dose region.

12 MeV 45 mm beam profile at 4.0 cm depth: All points satisfied the GI evaluation criteria.

12 MeV 64 mm beam profile at 2.5 cm depth: Less than 12% of the failed points were colder in the high dose gradient region of 20% to 40% with γ of less than 1.1 at lateral distance of 25 mm.

12 MeV 64 mm beam profile at 4.0 cm depth: Less than 12% of the failed points were colder in the low dose region of 5% with γ of less than 1.3 at lateral distance of 35 mm.

18 MeV 19 mm cone beam profile at 2.5 cm depth: A maximum γ of 2.0 for 18% of the points is observed in the 45%, 30% and 5% dose regions at lateral distance ranging from 5 mm to 15 mm.

18 MeV 19 mm cone beam profile at 4.5 cm depth: A maximum γ of 1.1 for 6% of the points is observed in the 25 mm to 32 mm range where calculated points were lower than measurement.

18 MeV 19 mm beam profile at 5.5 cm depth: A maximum γ of 3.0 for 15% of the points is observed in the 0% to 20% low dose range at lateral distance ranging from 25 mm to 45 mm where calculated points were higher than measurement.

18 MeV 45 mm cone beam profile at 2.5 cm depth: Calculated points were hotter in the high dose gradient region ranging from 18% to 55% with a maximum γ of 2.6 at lateral distance ranging from 12 mm to 18 mm. Further failed points occurred in the low dose region of 0% to 5% at lateral distances ranging from 20 mm to 35 mm.

18 MeV 45 mm cone beam profile at 4.5 cm depth: A maximum γ of 3.0 for 12% of the points is observed in the 25 mm to 40 mm range where calculated points were lower than measurement.

18 MeV 45 mm beam profile at 5.5 cm depth: A maximum γ of 3.0 for 14% of the points is observed in the 0% to 20% dose range at lateral distance ranging from 30 mm to 45 mm where calculated points were lower than measurement.

18 MeV 64 mm cone beam profile at 2.5 cm depth: A maximum γ of 1.8 for 3% of the points is observed in the high dose gradient region of 25% to 65% dose range at lateral distance ranging from 20 mm to 23 mm where calculated doses were lower than measurement. A further failed point occurred in the dose region of 15% at lateral distance of 30 mm with calculated point being higher than measurement.

18 MeV 64 mm cone beam profile at 4.5 cm depth: A maximum γ of 3.0 for 9% of the points is observed in the 20 mm to 45 mm range where calculated points were lower than measurement.

18 MeV 45 mm beam profile at 5.5 cm depth: A maximum γ of 3.0 for 20% of the points is observed in the low dose region of 0% to 12% dose range at lateral distance ranging from 35 mm to 50 mm where calculated points were lower than measurement.

Further discussion and conclusions based on these results are reserved for the end of the chapter *(section 7.6).*

7.5.3 Cut-out factors

The cut-out factors (COF) were determined in an analogous manner to the applicator output factor and cone factor determination in sections 5.4.2.3 and 6.3.3 respectively. The electron Dosimetry Diode E (PTW type T60017, Freiburg, Germany) was used to measure the cut-out factors for each of the cut-outs for each energy. Measurements were performed at d_{max} for each of the non-reference fields (19 mm, 45 mm and 64 mm cut-outs) and the reference field ($10x10\ cm$ open applicator) for each energy. This depth varies with field size and energy *(IAEA 2000).* The resulting cut-out factor for each cut-out for each energy *(table 7.8)* was calculated as per equation 5.17 above.

The MC-calculated cut-out factors were obtained by analysing the 3-d dose distribution for each of the cut-outs for each energy in STATDOSE *(chapter 4)* and relating the doses at the respective d_{max} depths as per equation 2.5. A comparison between the measured and MC-calculated cut-out factors for the 19 mm, 45 mm and 64 mm cones appear in table 7.8 below, with the uncertainty in measurements being determined utilising equation 5.20. The statistical variance was less than 1% for all output factors determined by Monte Carlo calculations *(section 4.3.4)*.

Table 7.8 Comparison between the measured and MC-calculated Cut-out factors (COF) for cut-outs inserted into the 19 mm, 45 mm and 64 mm cones for energies 6 MeV, 12 MeV and 18 MeV electron beams

	6 MeV			12 MeV			18 MeV		
	Meas	**MC**	**%diff**	**Meas**	**MC**	**%diff**	**Meas**	**MC**	**%diff**
COF 19 mm Cut-out	0.409 ±0.005	0.441	7.82	0.723 ±0.004	0.763	5.53	0.903 ±0.004	0.925	2.44
COF 45 mm Cut-out	0.992 ±0.004	1.046	5.44	1.188 ±0.003	1.192	0.34	1.270 ±0.003	1.263	-0.55
COF 64 mm Cut-out	1.120 ±0.003	1.131	0.98	1.203 ±0.003	1.207	0.34	1.276 ±0.003	1.271	-0.39

The variation of measured and calculated COF with cone size and variation of measured and calculated COF with energy is shown in figures 7.34 and 7.35 respectively.

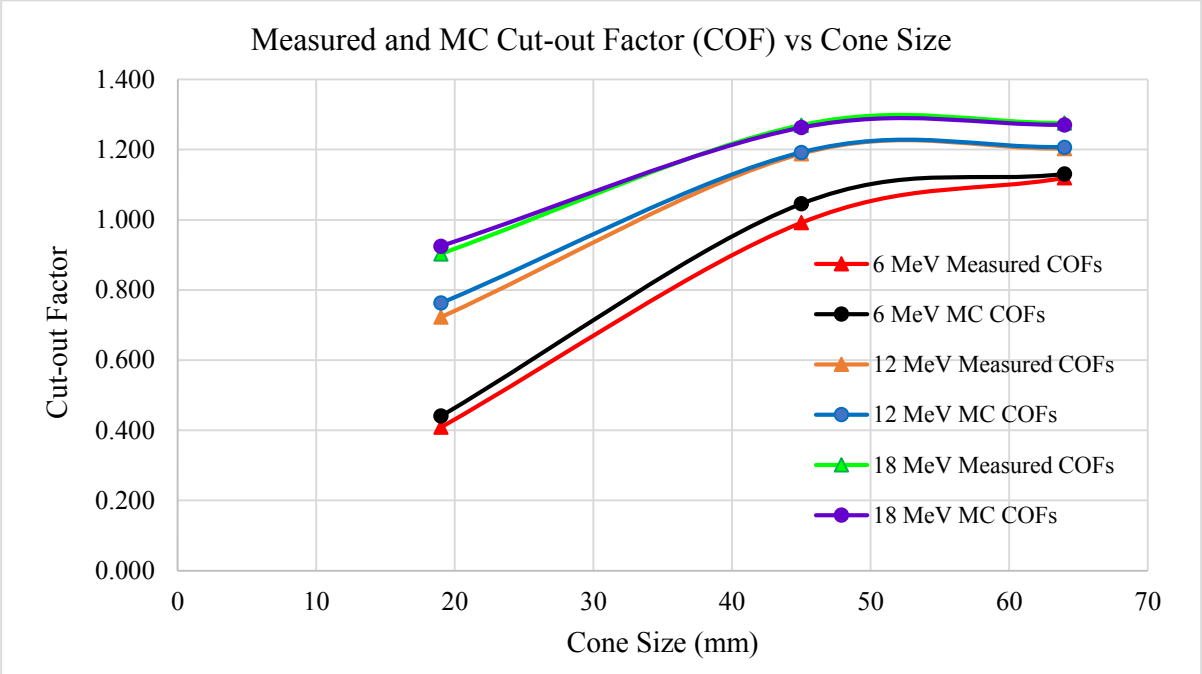

Figure 7.34 Plot of measured and MC-calculated cut-out factor vs cone size for 6 MeV, 12 MeV and 18 MeV electron beams

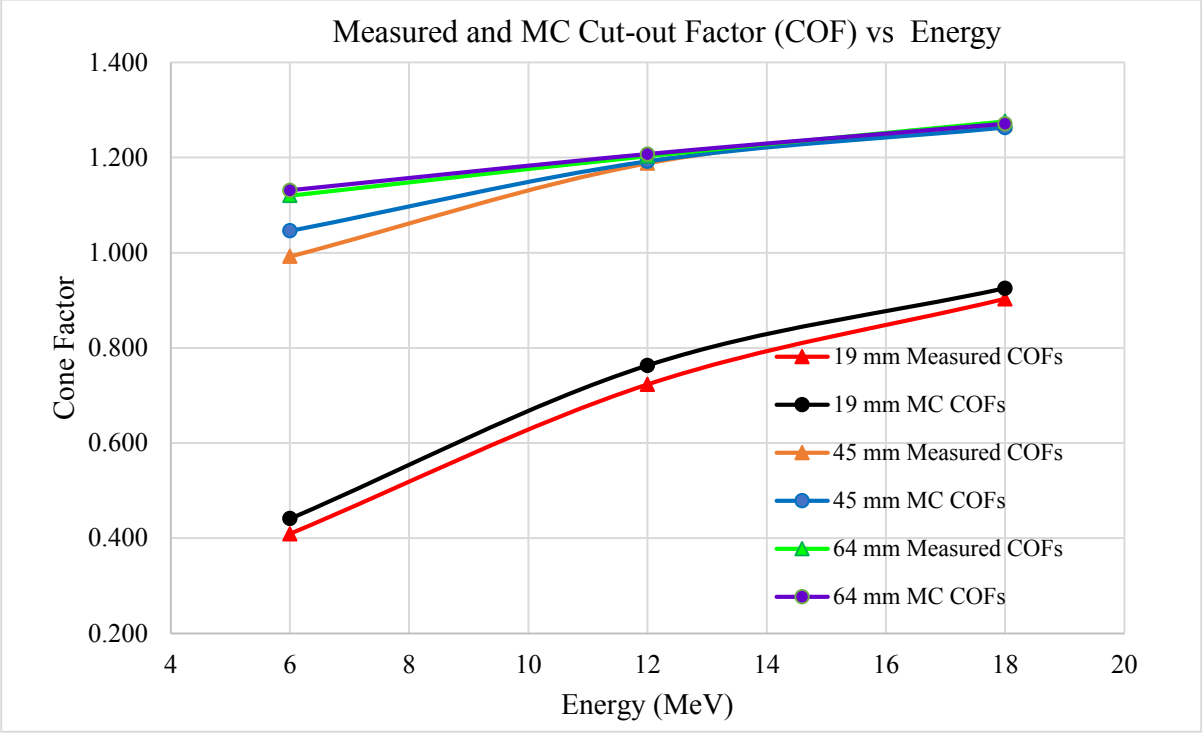

Figure 7.35 Plot of MC-calculated cut-out factors vs electron energy for 19 mm, 45 mm and 64 mm IORT cones.

7.5.3.1 Analysis

The differences between calculated and measured cut-out factors were below 1.22% for the 64 mm cone for all the energies as well as for the 12 MeV and 18 MeV 45 mm cut-outs. A larger discrepancy of 5.4% was observed for the 6 MeV 45 mm cut-out. Excessively large discrepancies were observed for all energies for the 19 mm cut-out with the differences decreasing with increasing energy (from 7.82% for 6 MeV to 2.44% for 18 MeV) with the calculated values being larger than measurement.

7.6 Discussion and Conclusion

Chapter 7 is dedicated to the comparison of measured and MC-calculated data for 6, 12 and 18 MeV beams with custom-made cut-outs inserted into the cones investigated in chapter 6. The objective is to determine if the MC method may be used clinically for dose distribution and MU calculations from calculated cut-out factors (COFs). The introduction of the

irregularly-shaped cut-outs may be deemed necessary to conform the shape of the beam to the dimensions of the treatment site to increase the therapeutic ratio *(section 1.1.2)*.

The cut-outs were 2 cm thick in the z-direction and were inserted in the cones at 97 cm from the source with the cut-out end being flush with the most distal end of the cone (99 cm). The phantom surface was situated at 100 cm SSD, implying a 1 cm air gap. The phase space file from the BEAMnrc simulation was used as the input source for DOSXYZnrc. 3-d dose distributions were produced from which the relevant PDD and profiles were obtained for comparison with measured data.

Measurements were performed as described in section 7.3 with the same geometry (100 cm SSD, 1 cm air gap) described in the above paragraph.

The PDD comparison for the IORT cut-outs proved to be favourable as direct comparison of R_{max}, R_{90}, R_{80}, and R_{50} yielded results of less than 1.5 mm, with a few exceptions for R_{max}. The 12 MeV beam for the 19 mm cut-out displayed the maximum difference of 2.5 mm for the 45 mm cut-out. Another exception was the 18 MeV beam for all the cut-outs where differences of 2.0 mm was observed for both the 19 mm and 45 mm cut-outs and 3.5 mm in R_{max} was observed for the 64 mm cone. It is worth noting that latter point also exceeded tolerance for the open cone case *(table 6.7)*. Comparisons of all other points satisfied the acceptance criteria. It may therefore be concluded that, in general, these characteristic points were in good agreement with measurement.

Discrepancies in the surface doses (12 MeV 19 mm cut-out, 18 MeV 45 mm cut-out and all energies for the 64 mm cut-out) showed a quick decline in the build-up region and differences reached 0% within the first 2.0 mm and would not have any appreciable effect on clinical outcomes. Various factors such as inaccurate surface determination and placement of the

detector would contribute to such discrepancies. These factors are critical in this portion of the beam. As mentioned in section 6.4, previous studies have shown *(Verhaegen et al 2001)* that MC modelling with an incorrect material composition in the applicator may lead to up to 10% error in dose in the build-up region. Simulations with inaccurate cerrobend composition would increase these errors for the simulations reported in this chapter.

The effective point of measurement for the pinpoint chamber was taken into account for all measurements *(section 4.2).* The equivalent thickness of the chamber wall was determined to be 0.23 mm *(section 4.2)* and was not taken into account in detector positioning for the PDDs as it was deemed to be negligible *(IAEA 2000)*. Inclusion of this parameter would have decreased the measured surface doses, thereby decreasing the differences between measurement and calculation. Scanning above the water surface was not an option with the cut-outs in place for fear of collision of the stem of the pinpoint chamber with the cone end. Despite the mismatch at these points, fewer and smaller differences are observed for the cut-outs than was observed for the open cones *(section 6.4)*.

The comparisons in the therapeutic range and from d_{90} to d_{20} satisfied the acceptance criteria for all the beams with the maximum difference being 1.2 mm in d_{90} for the 12 MeV 19 mm cut-out. The discrepancies observed at dose levels below 10% may be ignored since this portion of the curve is attributed to contaminant photons (bremsstrahlung), falls well beyond the therapeutic range, and is not clinically significant. Care must however be taken to ensure that critical structures at the distal end of the beam are avoided. The PDD comparisons showed acceptable results satisfying the GI criteria in this portion of the beam.

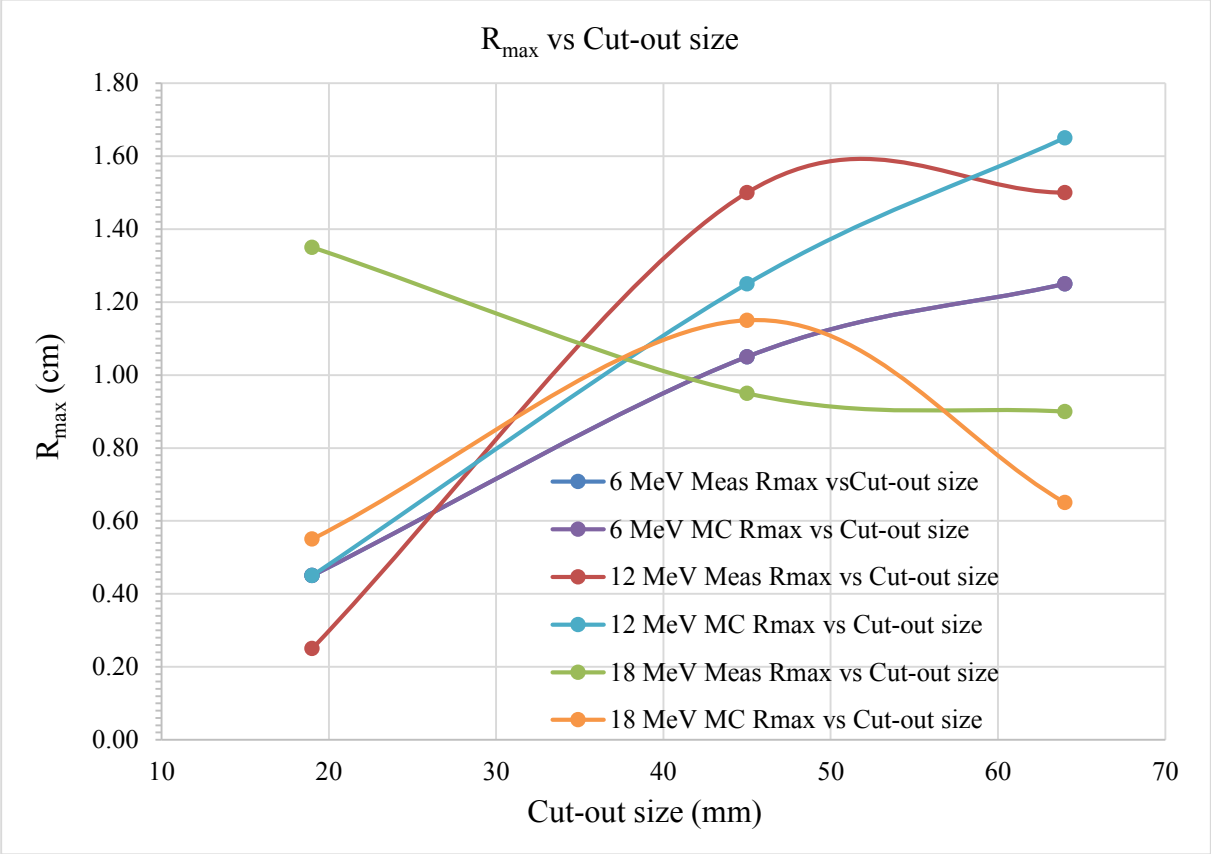

Figure 7.36 Plot of measured and MC-calculated R_{max} values vs cut-out size for each energy

Analysis of the MC-calculated values shows that for the 18 MeV beam, R_{max} is lower for the 64 mm cut-out than for the 45 mm cut-out *(figure 7.36)*. Note that this point for the 18 MeV beam exceeded tolerance for both the open cone and cut-out cases and may be regarded as being an outlier. The measured R_{max} values for the 64 mm cut-out is also lower than that for the 45 mm cut-out. By examination of the PDDs for the 18 MeV 45 mm and 64 mm cut-outs *(figures 7.9 and 7.12),* it is evident that there is a flattening of the PDD in the region of R_{max}. Due to the small variation in dose in this region, the R_{max} value obtained will be more sensitive to the accuracy of measurement and smoothing and averaging algorithms employed.

Therefore, with the exception of the 64 mm cut-out for the 18 MeV beam, the MC-calculated R_{max} values increase with an increase in cut-out size. The exact same trends have been observed in similar studies *(Cygler et al 1997, Fraas et al 1985, Verhaegen et al 2001, Turian et al 2004)*.

The differences and effects on R_{max} by the inclusion of the cut-out in each cone is shown in figure 7.37 below. These plots are meant to show the relationship between the change in R_{max} between the cut-outs and open cones for each cone size.

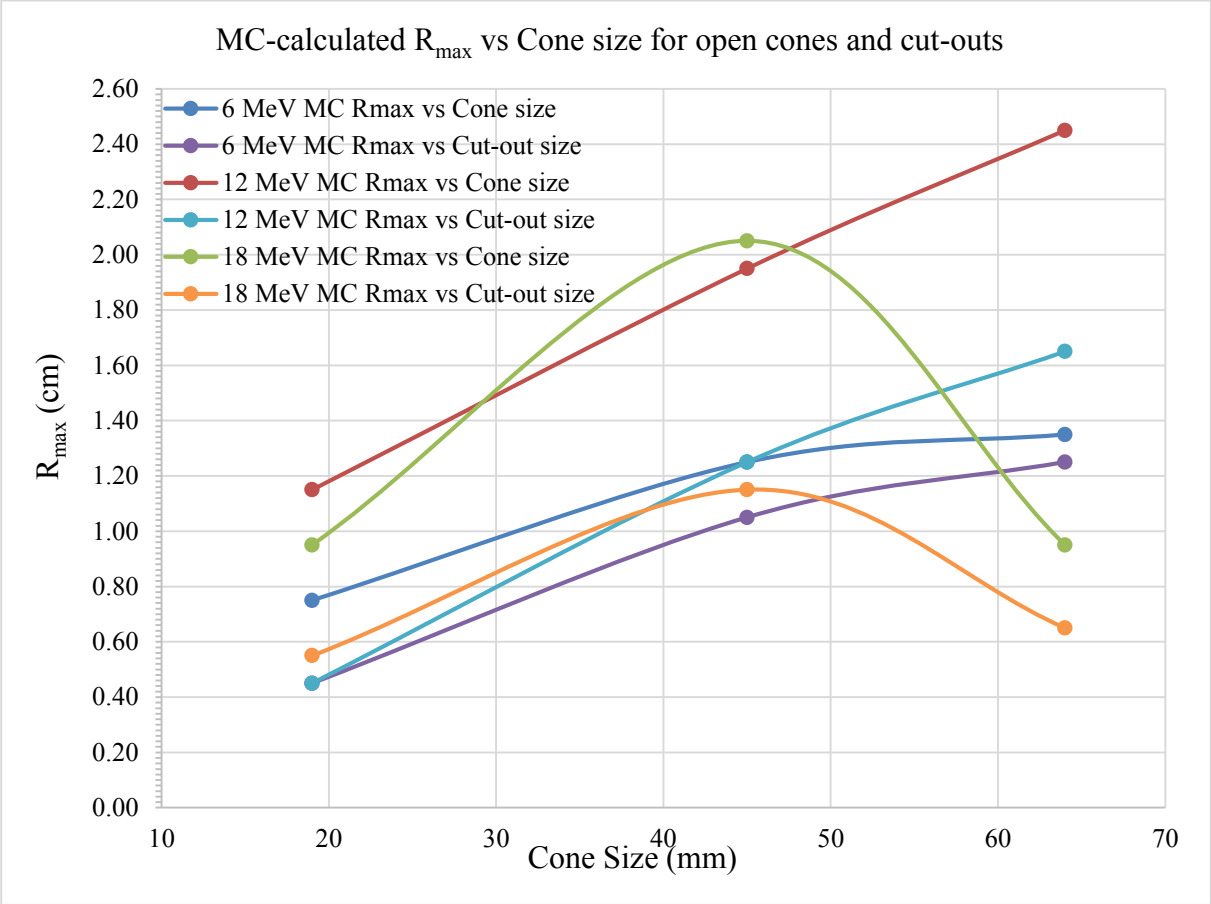

Figure 7.37 Plot of MC-calculated R_{max} points for each energy for the IORT cones and IORT cut-outs

The observation from figure 7.37 is that when the field aperture is reduced by the inclusion of a cut-out in the cone, R_{max} moves closer to the surface. This is observed for all energies and all cone sizes. The conclusion is that a further reduction in field size from the open cone cases reduces the depth of maximum dose for all energies. This shift of R_{max} closer to the surface with a decrease in aperture size is evident in a variety of studies *(Biggs et al 1981, Fraas et al 1985, Verhaegen et al 2001, Turian et al 2004)*

For all the cones and all the energies, the only discrepancies in the profile comparisons is observed in the high dose gradient regions and/or beyond the edge of the field *(figures 7.13 to*

7.33). Accurate chamber placement is critical for accurate measurements in the high dose gradient regions. It is important to note that almost all points in the central 80% of the beam satisfied the acceptance criteria for all energy/cut-out combinations. The beam profiles for the IORT cut-outs were therefore deemed to be acceptable as discrepancies were within the acceptance criteria and occurred beyond the field edge and would have little or no impact clinically.

Introduction of the cerrobend cut-outs introduces an additional source of possible inaccuracy in MC calculation. The material composition and associated densities has a large effect on the contribution of the direct electron component to the dose, whilst accurate construction of the cut-out shape affects the scattered component to a greater extent *(Turian et al 2004).*

As observed in figure 7.34, the cut-out factors increase with an increase in cone size for each energy, a trend that is validated by other studies *(Cygler 1997, Turian 2004, Palta et al 1995, Biggs et al 1981)*. The difference in steepness in the gradient of the curves show that the lower the energy, the larger the effect of the change in cut-out size. The cut-out factors level off as the cut-out size is increased further.

Figure 7.35 shows an increase in cut-out factor with energy. Once again, the change is more pronounced for the smaller cone sizes. The same trends were observed for the MC-calculated cone factors *(section 6.4)*.

Output factors for clinical electron beams vary with electron energy, geometry of the jaws, applicator/cone and any field-defining cut-out *(Verhaegen et al 2001).* As mentioned in section 6.4, empirical analytical models have been developed to improve the ability to predict output factors for clinical electron beams *(Mills et al 1982, McParland 1989, Chen 2001)*.

Monte Carlo methods have also been investigated in calculation of output factors *(Zhang et al 1999, Antolak et al 2002, Kapur et al 1998, Turian et al 2004)*. The conclusions were that MC methods have the greatest potential of calculating output factors accurately *(Ma & Jiang*

1999). Other studies *(Zhang et al 1999, Cygler et al 2004)* have shown that MC calculated output factors may agree with measurements to within 1% to 2%.

It has been reported *(Verhaegen et al 2001)* that low measured values may be due to the fact that small fields do not have a flat dose distribution near the central axis. Dose measurements with a chamber of finite lateral dimensions therefore gives an average dose that is too low compared to the actual dose on the central axis. This was observed for the open cone cases and also apply to the cut-outs used in this study. A lack of lateral scatter equilibrium is also absent for small fields *(Shiu 1994)*. MC calculation with small voxel sizes and more histories is therefore recommended as being the most accurate method of output factor determination for small fields *(Kapur et al 1998, Ma&Jiang 1999, Turian et al 2004, Chetty et al 2007)*.

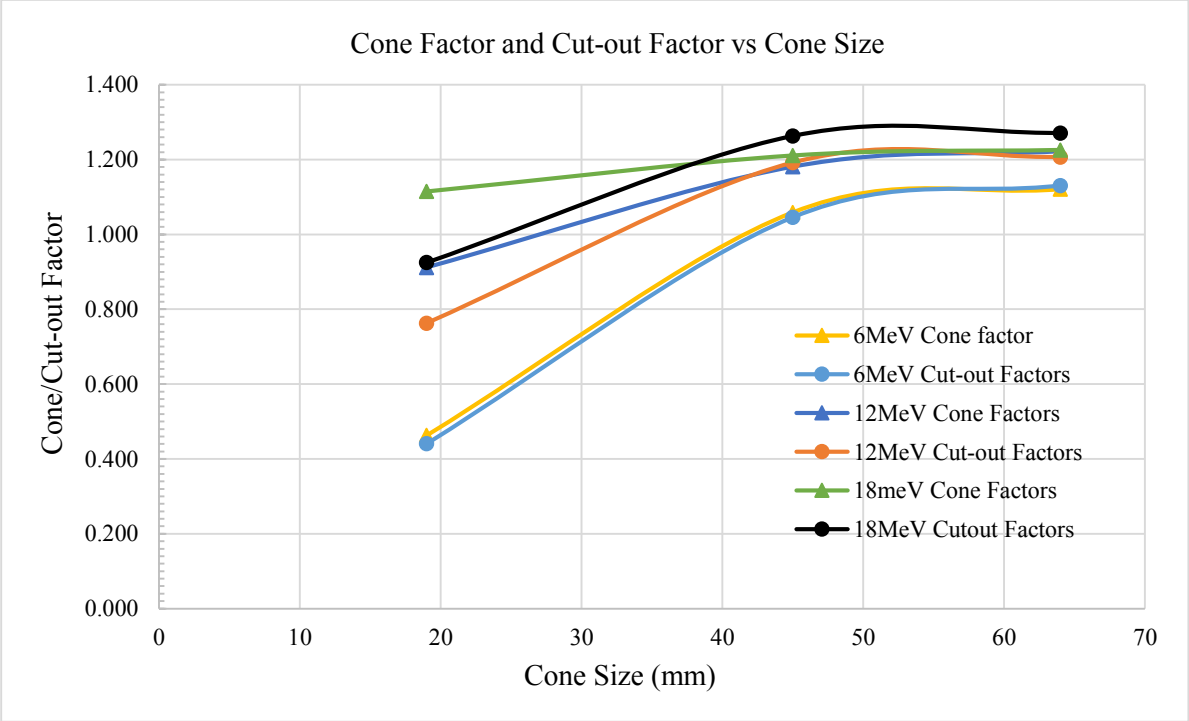

Figure 7.38 Plot of MC-calculated Cone and Cut-out factors vs cone size for 6 MeV, 12 MeV and 18 MeV electron beams

In figure 7.38, a direct relationship between the cut-out factors and the cone factors with respect to cone size for each energy is plotted to show the effect on output factor of inserting a

cut-out into each cone. Both CF and COF increase with increase in cone size. The 12 MeV 45 mm COF and 6 MeV 64 mm COF are both 0.9% higher than their respective cone factors. The 18 MeV 45 mm and 64 mm COFs are respectively 4% and 3.6% higher than the open CFs. All the other COFs are lower than their respective open cone counterparts.

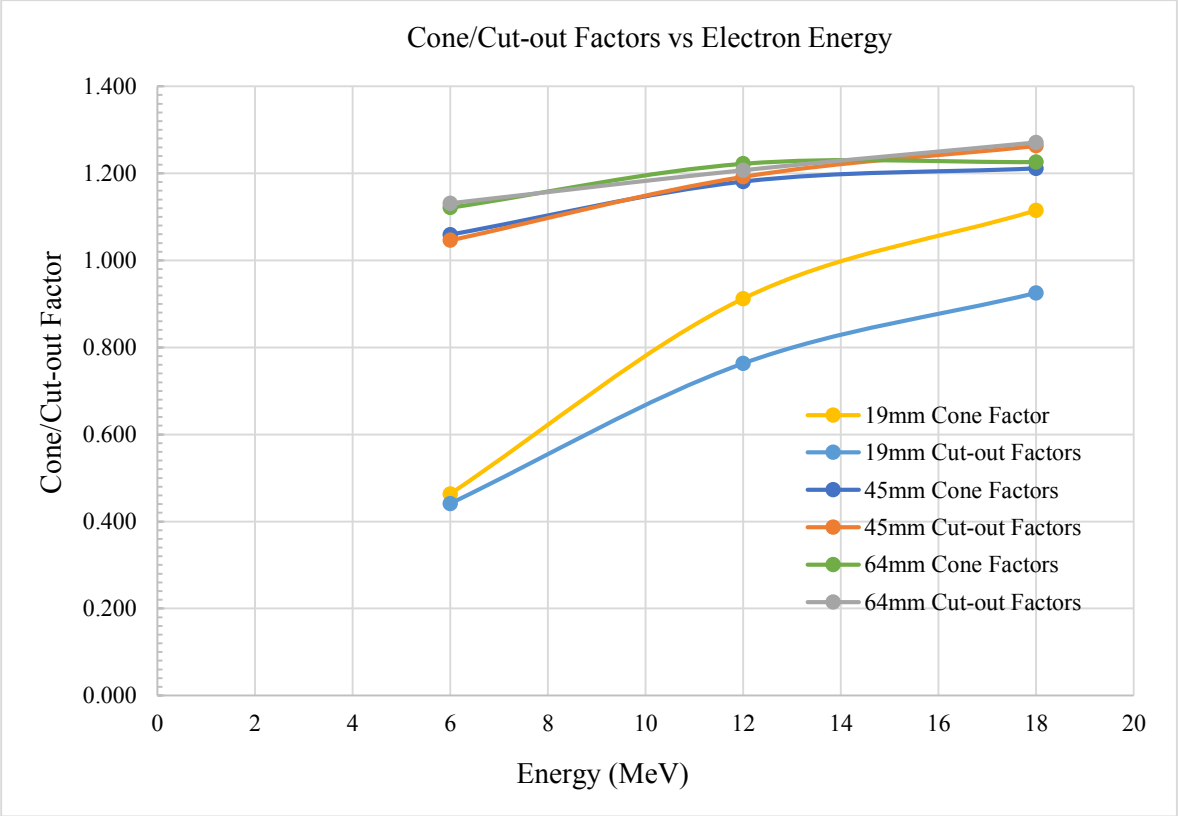

Figure 7.39 Plot of MC-calculated Cone and cut-out factors vs electron energy for 19 mm, 45 mm and 64 mm IORT cones.

In figure 7.39, a direct relationship between the cut-out factors and the cone factors with respect to energy for each cone with and without their respective cut-outs is plotted. It is easily observed that all CF and COFs increase with increase in energy. For all energies, the 19 mm CFs are larger than the COFs. For the 45 mm cone, it is only the 6 MeV beam in which CF exceeds COF (1.2%). For the 64 mm cone, it is only for 12 MeV that CF is higher than COF.

The results for the MC modelling of the IORT cut-outs have proved to be within acceptable tolerances with measured data with regards PDD and profile comparisons. Issues with

measurements of small fields with finite sized ionisation chambers have been well documented and were observed in the measurements of the COFs, where differences of up to 11.65% were seen.

The conclusion is that it is imperative that the introduction of an IORT programme clinically would require Monte Carlo calculations to be performed for the treatment fields, especially for small fields and for cone factor and cut-out factor determination.

Based on the results and comparisons presented in this and previous chapters, it may also be concluded that the Monte Carlo modelling of irregularly-shaped cut-outs performed in this study has been successful and may be used clinically.

CHAPTER 8

FUTURE WORK

8.1 Cone factor determination

MC simulations will be performed for all energy/open-cone combinations available so that a CF look-up table may be drawn up for the open cones. This will include energies 6, 9, 12, 15, 18 and 21 MeV and open cone sizes 19, 25, 32, 38, 45, 51, 57, 64, 70, 76, 83 and 95 mm.

8.2 Cut-out factor determination

It should be noted that the treatment site has to be exposed before the required cut-out dimensions are obtained. Approximately 30 min is required to manufacture and cool down the cut-out once it is poured. Whilst this might be an acceptable time period for the patient to be anaesthetised before treatment commences, MC calculation of the cut-out factor will need to be performed. Even if the PSF at z = 97 cm from the BEAMnrc simulation is kept on file, considerable time is required to perform the simulation of the cut-out, which starts at z = 97 cm and ends at z = 99 cm. Using the BLOCK CM for the cut-out extends the calculation time.

The PSF obtained at the distal end of the cut-out must then be used as the input source for DOSXYZnrc so that dose distributions may be obtained. The time required for this simulation depends greatly on the voxel dimensions of the phantom and on the size of the field. It has been found that a minimum of 1 hour is needed for this simulation.

Thereafter COF determination and verification using STATDOSE may require a further 10 minutes. It is therefore highly impractical for the patient to be lying on the treatment couch with the treatment site surgically exposed whilst waiting for MU calculations to be performed.

It is therefore envisaged that for each energy and cone mentioned above, MC simulations in BEAMnrc and DOSXYZnrc will be performed and kept on file for an appropriate range in

diameter of circular cut-outs that may be inserted into each cone. The calculated COF for each circular cut-out/energy combination will also be tabulated and available in the form of look-up tables. The COF for the circular cut-out that best approximates the clinical cut-out may then be used for the MU calculation to avoid delays once the treatment site is surgically exposed.

Determination of a full 3-d dose distribution is not necessary for treatment and may be performed subsequently for record purposes.

8.3 MC modelling of the 18 MeV beam

Further investigation is necessary in the MC modelling of the 18 MeV electron beam. Upon simulation of the $15\ x15\ cm$ applicator (not presented in this work), prominent discrepancies not observed for the $10x10\ cm$ applicator were observed in the high dose regions near the field edges of the beam profiles.

In a previous study *(Bieda et al 2001),* similar discrepancies were observed *(figure 8.1)* for the higher energy for large field sizes. By altering the manufacturer's specifications of the scattering foil, better agreement was achieved *(figure 8.1(a)).* Bieda's in-depth study concluded that MC calculations for higher energies and larger field sizes are more sensitive to the geometry of the scattering foil and revealed that the discrepancies were due to incorrect scattering foil information supplied by the vendor. Specifications of the treatment head components as supplied by vendors have been found in many cases to be unreliable *(Rogers et al 1995)* and sometimes incomplete *(Verhaegen 2001)*. This has been attributed mainly to the reluctance of vendors to divulge detailed specifications necessary for accurate MC modelling due to the commercial value of the accelerator parts *(Ma & Jiang 1999).*

Based on the similarity of the discrepancy in both studies *(figures 8.1 (a) and (b))*, it may be assumed that there are inaccuracies in the scattering foil configuration supplied for the Siemens Primus Linac for the 18 MeV beam, which ultimately led to the large differences near the field edges in the profile comparisons for the $15x15\ cm$ applicator.

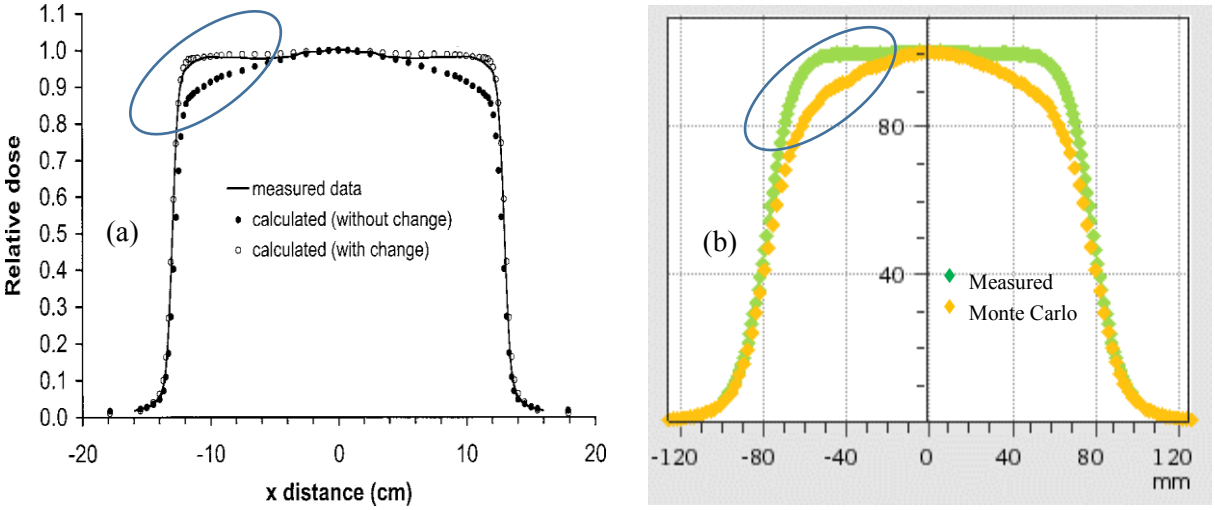

Figure 8.1 Representation of the similarities in discrepancies observed in a study by Bieda et al 2001 and by the investigator of this study (a) Comparison of measured and MC calculated cross-beam profile for the 20 MeV $25x25\ cm$ applicator before and after modification of the scattering foil specifications *(reprinted from Bieda et al 2001).* (b) Comparison of measured and MC calculated cross-beam profile for the 18 MeV $15x15\ cm$ applicator modelled by the author of this study.

This study involves the use of electron fields that are collimated to field sizes that are considerably smaller than that produced by the $15x15\ cm$ applicator. Since these discrepancies were not observed in the smaller $10x10\ cm$ applicator and the 19, 45 and 64 mm cones cases, it is hypothesised by this author that the inaccuracy in the build of the scattering foil is collimated out by these smaller field sizes.

It has therefore been decided that CF and COF calculations using Monte Carlo simulation of the 18 MeV beam will not be used clinically until the investigation is complete and yields acceptable results for the larger fields as well. It should be noted that IORT with dedicated mobile LINACs are successfully performed with a maximum available energy of 12 MeV at all institutions utilising this form of IORT treatment.

CHAPTER 9

SUMMARY AND CONCLUSION

A decision was made to implement an Intra-operative Radiation Therapy programme at the Inkosi Albert Luthuli Central Hospital for the treatment of a variety of treatment sites where the use of irregularly-shaped treatment fields may be necessary. Accurate dose distributions and monitor unit calculations are essential to all radiation therapy treatments. An extensive literature search revealed that accurate monitor unit calculations depended heavily on utilisation of accurate output factors. Whilst empirical analytical models have been developed to calculate output factors for clinical electron beams *(Mills et al 1982, McParland 1989, Chen 2001)*, Monte Carlo methods have also been investigated in calculation of output factors *(Zhang et al 1999, Antolak et al 2002, Kapur et al 1998, Verhaegen et al 2001)*. The conclusions from these investigations revealed that MC calculation methods have the greatest potential of calculating output factors accurately *(Ma & Jiang 1999)*.

There is no commercially available Monte Carlo treatment planning system that models the combination of LINAC (Siemens Primus), IORT cones and cut-outs that were to be used for this IORT programme. Over and above this, no studies were found that performed MC calculations for the same LINAC/cone system available at the institution. It was therefore decided to use an existing MC code system, EGSnrc *(Kawrakow & Rogers 2003)* with user codes BEAMnrc *(Rogers et al 1995)* and DOSXYZnrc *(Walters & Rogers 2005)* to obtain dose distributions and output factors for the LINAC/cone system in question so that the proposed IORT programme may be implemented.

The main objective of this project was therefore to validate the use of the EGSnrc MC code in producing dose distributions and providing output factors for the IORT open cones and cut-outs to be used for intra-operative treatments.

In order to achieve this goal, Monte Carlo commissioning of the LINAC was first performed. This process involved measurement of PDDs, profiles and output factors for comparison with MC calculations. The 6 MeV, 12 MeV and 18 MeV electron beams with standard $10x10\ cm$ and $5\ cm$ circle applicators were used for this purpose.

The various treatment head components, the specifications of which were supplied by the vendor on condition of non-disclosure, were modelled in BEAMnrc by accurately specifying their geometry and material compositions. Since characteristics of the electron source for the various electron energies are not known, mono-energetic sources were initially used. The PSF from the BEAMnrc simulation was used as the input source for DOSXYZnrc to obtain dose distributions in a phantom for comparison with the measurements. Since this did not satisfy the GI evaluation criteria set, appropriate electron spectrums that yielded acceptable comparisons were obtained and used as the input source for each energy. In-depth comparisons of the measured and MC-calculated dose PDDs and profiles were performed to confirm that the MC calculations produced dose distributions that were a true reflection of the beams emanating the treatment head.

Comparisons of characteristic points (D_s, R_{max}, R_{90}, R_{80}, and R_{50}) yielded acceptable results for both the $10x10\ cm$ and $5cm$ circle applicators, with a few points failing the acceptance criteria. Comparisons of the beam profiles were also found to be acceptable.

Similar measurements were then performed with the 19 mm, 45 mm and 64 mm IORT open cones for energies 6 MeV, 12 MeV and 18 MeV. Once again, detailed comparisons of measured and MC-calculated PDD and profiles yielded acceptable results. Whilst the effective point of measurement was taken into account for all measurements, inclusion of the chamber wall equivalent thickness would have reduced the differences between measurement and calculation of surface doses. In retrospect, the PDD scans should not have been included

in the same scan sequence as the profiles measurements. This would have made it possible to obtain PDD scans above the water surface (without fear of collision of the chamber stem with the cone end) so that the true surface could have been accurately determined.

The MC-calculated cone factors for the 19 mm cone were unacceptable and this was attributed to inaccuracies in measurement due to the small field size. Efficacy for the use of MC calculations of output factors, especially for the small fields used in this study, is provided by the results obtained and by previous MC studies performed *(Zhang et al 1999, Antolak et al 2002, Kapur et al 1998, Ma & Jiang 1999, Verhaegen et al 2001).*

Finally, a custom-built irregularly-shaped cerrobend cut-out was inserted into each of the cones and PDD and profile measurements were done for the 6 MeV, 12 MeV and 18 MeV beams for each of the cut-outs used in this study. The LINAC/cone/cut-out combination was modelled in BEAMnrc and dose distributions produced in DOSXYXnrc were compared to measurements. A detailed analysis and discussion of the comparisons is given in the relevant section *(section 7.5)*. The cone output factors did not compare favourably for the 19 mm cut-out. Once again, this was attributed to inaccurate measurement caused by the small field sizes used, which validated the need for the use of MC methods.

Reasons for lower measured values being obtained for the COFs for small fields is that the small fields do not have a flat dose distribution near the central axis and is not uniform at the point of measurement *(Turian et al 2004, Verhaegen et al 2001)*. The electron diode used for COF determination has finite lateral dimensions which would give an average dose that is too low compared to the actual dose on the central axis. A lack of lateral scatter equilibrium is also absent for small fields *(Shiu 1994)*. The lateral dimension of the cut-out inserted into the 19 mm cone was 10 mm *(figure 7.1)* and the lower values observed for the COFs for this

extremely small cut-out is in keeping with the observations made by the above-mentioned studies.

Monte Carlo methods have been extensively investigated in calculation of output factors *(Zhang et al 1999, Antolak et al 2002, Kapur et al 1998, Turian et al 2004)*. All these studies have concluded that especially for small fields, measurements are not trustworthy and that MC calculations have the greatest potential of calculating output factors accurately *(Ma & Jiang 1999)*. These studies have also recommended that output factor determination for the smaller sizes should be obtained utilising MC calculations as a replacement for measurements.

Differences between measurement and calculation for this study seem to be systematic as adequate histories were simulated and appropriate voxel sizes were chosen for calculations. The differences observed in the build-up region may be attributed to unreliable ionisation chamber measurements due to the high dose gradient in this portion of the beam *(Hosntalab et al 2012)*. Perturbation of the absorbed dose due to the finite size of the ionisation chamber is yet another source of error *(Siebers et al 1999)*.

The EGSnrc Monte-Carlo calculation method has been found to be an excellent tool for modelling of LINAC treatment head components and beam characteristics for the IORT programme envisaged. It is advised that Monte Carlo simulations be utilised in situations where there exists a greater possibility of inaccuracies in measurements or where measurements are impossible. This study is based on the situation whereby output factors for small irregularly-shaped fields were measured, which justifies the use of MC calculations. The main drawback is the computational time, which is being reduced rapidly by newer and faster computers and by use of appropriate variance reduction techniques. It is important that caution be exercised in the use of such research tools and software in clinical practice.

Based on the successful MC commissioning of the LINAC and on the acceptable comparisons between measurement and MC-calculated dose distributions and output factors for the open cones and for small irregularly-shaped IORT beams, it may be concluded that the Monte Carlo based dose calculation system evaluated in this study has been successfully validated and is acceptable for clinical implementation of the IORT programme.

REFERENCES

Abe M 1984, 'Intraoperative Radiotherapy – Past Present and Future', *Int. J. Radiat. Oncol. Biol. Phys.*, vol 10, pp 1987-1990.

Abe M, Takahashi M 1981, 'Intraoperative Radiotherapy: The Japanese experience', *Int. J. Radiat. Oncol. Biol. Phys.,* vol 7, no 7, pp 863 – 868.

Abe M, Takahashi M, Yabumoto E, Onoyama Y, Torizuka K, Tobe T, Mori K 1975, 'Techniques, Indications and Results of Intraoperative Radiotherapy of Advanced Cancers', *Therapeutic Radiology,* vol 116, no 3, pp 693 – 702.

Agostinelli S et al 2003, 'Geant4—a simulation toolkit', *Nuclear Instruments and Methods in Physics Research,* vol 3, pp 250 - 303.

Ali E S M, Rogers D W O 2007, 'Efficiency improvements of x-ray simulations in EGSnrc user-codes using bremsstrahlung cross-section enhancement (BCSE)', *Med Phys*., vol 34, no 6, pp 2143 – 2154.

Almond P R, Biggs P J, Coursey B M, Hanson W F, Saiful Huq M, Nath Ravinder, Rogers D W O 1999, 'AAPM's TG51 protocol for clinical reference dosimetry of high-energy photon and electron beams *Med. Phys.,* vol 26, pp 1847 – 1870.

Andreo P 1991, 'Monte Carlo techniques in medical radiation physics', *Phys. Med. Biol.*, vol 36 no 7, pp 861 – 920.

Antolak J A, Bieda M R, Hogstrom K R 2002, 'Using Monte Carlo methods to commission electron beams: A feasibility study', *Med. Phys.,* vol 29, no 5, pp 771 – 786.

Attix F H, 1986. 'Introduction to radiological physics and radiation dosimetry', J Wiley and sons, ISBN 0-471-01146-0.

Bakai A, Alber M, Nusslin F 2003, 'A revision of the gamma-evaluation concept for the comparison of dose distributions', *Phys. Med. Biol.*, vol 48, no 21, pp3543 – 3553.

Baro J, Sempau J, Fernandez-Varia J M, Salvat F 1995, 'PENELOPE: An algorithm for Monte Carlo simulation of the penetration and energy loss of electrons and positrons in matter', *Nuclear Instruments and Methods in Physics Research,* vol 100, pp 31 -46.

Beddar A S, Biggs P J, Chang S, Ezzel G A, Faddegon B A, Hensley F W, Mills M D 2006, 'Intraoperative radiation therapy using mobile electron linear accelerators: Report of AAPM Radiation Therapy Committee Task Group No. 72', *Med Phys.,* vol 33*,* no 5, pp 1476 – 1489.

Beddar A S, Krishnan 2005, 'Intraoperative radiotherapy using a mobile linear electron accelerator: A retroperitoneal sarcoma case', *J Appl Clin Med Phys*, vol 6, pp 95 – 107.

Berger M J 1963, 'Monte Carlo Calculation of the penetration and diffusion of fast charged particles', *'Methods in Computational Physics'*, eds Alder B, Fernbach S, Rotenberg M, vol 1, pp 135 – 215.

Berger M J, Wang R 1988, 'Multiple-scattering and angular deflections and energy-loss straggling', in *Monte Carlo transport of Electrons and Photons',* eds Jenkins T M, Nelson W R, Rindi A, Plenum Press NY p21.

Bieda M R, Antolak J A, Hogstrom K R 2001, 'The effect of scattering foil parameters on electron-beam Monte Carlo calculations', *Med. Phys.,* vol 28, no 12, pp 2527 - 2534.

Bielajew A F 2001, 'Fundamentals of the Monte Carlo method for neutral and charged particle transport', University of Michigan.

Bielajew A F, Mohan R, Chui C S 1989, 'Improved bremsstrahlung photon angular sampling in the EGS4 code system', National Research Council of Canada Report PIRS 0203.

Bielajew A F, Rogers D W O 1986, 'PRESTA-the Parameter Reduced Electron-Step Transport Algorithm for Electron Monte Carlo Transport', *Natl. Res. Council of Canada,* NRCC report PIRS 0042.

Biggs P et al 2001, 'AAPM Report 72: Basic Applications of Multileaf Collimators', Report of Task Group 50 Radiation Therapy Committee, *Medical Physics Publishing.*

Biggs P J 1985, 'The physics of intraoperative radiotherapy using high energy electron beams', *Nuclear Instruments and Methods in Physics Research Section B'*, Vol 10-11, part 2, pp 1102 – 1106.

Biggs P J, Epp E R, Ling C C, Novack D H, Michaels H B 1981, 'Dosimetry, field shaping and other considerations for intra-operative electron therapy', *Int. J. Radiat. Oncol. Biol. Phys.,*vol 7 pp 875 – 884.

Boyd R A, Hogstrom K R, Starkschall G 2001, 'Electron pencil-beam redefinition algorithm dose calculations in the presence of heterogeneities', *Med. Phys.,* vol 28, no 10, pp 2096 – 2104.

Brahme A 1975, 'Simple relations for the penetration of high energy electrons in matter' *S 10401 National Institute of Radiation Protection*, Stockholm, Sweden

Brahme A, 1988, 'Optimisation of stationary and moving radiation therapy techniques', *Radiother Oncol*., vol 12, pp 129 – 140.

Brahme A, Svensson H 1976, 'Specification of electron beam quality from the central-axis depth absorbed-dose distribution', *Med. Phys.*, vol 3, no 2, pp 95 – 102.

Briesmeister J, 2000, 'MCNP - A General Monte Carlo N-particle Transport Code, *'Technical report, Los Alamos National Laboratory'.*

Burns D T, Ding G X, Rogers D W O 1996, 'R 50 as a beam quality specifier for selecting stopping-power ratios and reference depths for electron dosimetry' *Med. Phys.,* vol 23, no 3, pp 383 – 388.

Calvo F A, Meirino R M, Orecchia R 2006, 'Intraoperative radiation therapy First part: rationale and techniques', *Clinical Reviews in Oncology/Haematology*, vol 59, pp 106 – 115.

Chen J Z, Van Dyk J, Lewis C, Battista J J 2001, 'A two-source model for electron beams: Calculation of relative output factors', *Med. Phys.,* vol 28, no 8, pp 1735

Chetty I J, Curran B, Cygler J E, DeMarco J J, Ezzel G, Faddegon B A, Kawrakow I, Keall P J, Liu H, Ma C-M, Rogers D W O, Seuntjies J, Sheikh-Bagheri D, Siebers J V 2007, 'Report of the AAPM Task Group No. 105: Issues associated with clinical implementation of Monte Carlo-based photon and electron external beam treatment planning', *Med Phys*., vol 34, no. 12, pp 4818 – 4853.

Chodos A and Ouellette J (eds.) 2001, 'This month in Physics History', *American Physical Society News,* vol. 10, no. 10 p2.

Crane H, Beddar A S, Evans D B 2003, 'The role of intraoperative radiotherapy in pancreatic cancer', Surg Oncol Clin N Am vol 12, pp 965 - 977

Cygler J, Li X A, Ding G X, Lawrence E 1997, 'Practical approach to electron beam dosimetry at extended SSD', *Phys. Med. Biol.*, vol 42 pp 1505 – 1514.

Cygler J E, Daskalov G M, Chan G H, Ging G X 2004, 'Evaluation of the first commercial Monte Carlo dose calculation engine for electron beam treatment planning', *Med Phys*., vol 31, no. 1, pp 142 - 153.

Dale R G 1985, 'The application of the linear-quadratic dose-effect equation to fractionated and protracted radiotherapy', *Br J Radiol*., vol 58 pp 515 – 528.

Das I J, Mcgee K P, Cheng C-W 1995, 'Electron-beam characteristics at extended treatment distances', *Med. Phys.,* vol 22, no 10, pp 1667 – 1674.

Das I J, Cheng C-W, Watts R J, Anesjo A, Gibbons J, Li X A, Lowenstein J, Mitra R K, Simon W E, Zhu T C 2008, 'Accelerator beam data commissioning equipment and procedures: Report of the TG-106 of the Therapy Physics Committee of the AAPM', *Med Phys*, vol 35, no 9, pp 4186 – 4215.

de Martel C, Ferlay J, Franceschi S, Vignat J, Bray F, Forman D and Plummer M 2012, 'Global burden of cancers attributable to infections in 2008: a review and synthetic analysis', *The Lancet Oncology* vol. 13, no. 6, pp 607-615.

del Carmen M G, Eisner B, Willet C G, Fuller A F 2003, 'Intraoperative radiation therapy in the management of gynecologic and genitourinary malignancies', Surg. Oncol. Clin. N. Am., vol 12, pp 1031 - 1042

Demchik V 2011, 'Pseudo-random number generators for Monte Carlo simulations on Graphics Processing Units', *Computer Physics Communications,* vol 182, no 3, pp 692 – 705.

Depuydt T, Van Esch A, Huyskens D P 2002, 'A quantitative evaluation of IMRT dose distributions: refinement and clinical assessment of the gamma evaluation', *Radiother. Oncol.* Vol 62, pp 309 – 319.

Ding G X, Rogers D W O, Mackie T R 1996, Mean energy, energy-range relationships and depth-scaling factors for clinical electron beams', *Med Phys*, vol 23, no 3, pp 361 – 376.

Ding G X 2002, 'Dose discrepancies between Monte Carlo calculations and measurements in the buildup region for high-energy photon beams', *Med. Phys,* vol 29, no 11, pp2459 – 2463.

du Plessis F C P, Willemse C A, Lotter M G 2001, 'Comparison of the Batho, ETAR and Monte Carlo dose calculation methods in CT based patient models', *Med. Phys.,* vol 28, no 4, pp 582 – 589.

du Plessis F C P, Leal A, Stathakis S, Xiong W, Ma C-M 2006, 'Characterization of megavoltage electron beams delivered through a photon multi-leaf collimator (pMLC)', *Phys. Med. Biol.*, vol 51 pp 2113 – 2129.

Eckhardt R 1987, 'Stan Ulam, John von Neumann, and the Monte Carlo Method', *Los Alamos Science*, Special Issue vol 15, pp 131 – 136.

Ehrman J R 1981, 'The Care and Feeding of Random Numbers', *SLAC VM Note Book Module 18*, in *The dosimetry of Ionizing Radiation'*, eds Kase K R, Bjarngaed, Attix F H, Academic Press.

Ellis R J, Nag S, Kinsella T J 2000, 'Alternative techniques of intraoperative radiotherapy', *Eur. J. Surg. Oncol.,*vol 26, suppl A, pp S25 – S27.

Emami B, Lyman J, Brown A, Coia L, Goitein M, Munzenrider J E, Shank B, Solin L J and Wesson M 1991 'Tolerance of normal tissue to therapeutic irradiation', *Int. J. Radiat. Oncol. Biol. Phys.*, vol 21, no. 1, pp 109 – 122.

Faddegon A, Blevis I 2000, 'Electron spectra derived fron depth dose distributions', *Med. Phys.,* vol 27, no 3, pp 514 -526.

Faddegon B, Balogh J, Mackenzie R, Scora D 1998, 'Clinical considerations of Monte Carlo for electron radiotherapy treatment planning, *Radiat. Phys. Chem*., vol 53, no 3, pp 217–227.

Faddegon B, Schreiber E, Ding X 2005, 'Monte Carlo simulation of large electron fields', *Phys. Med. Biol*., vol 50, no 5, pp 741 - 753.

Fantini M, Santoni F, Soriani A, Creton G, Benassi M, Begnozzi L 1997, 'IORT Novac7: a new linear accelerator for electron beam therapy,' *Front Radiat Ther Oncol*, vol 31, pp 54 - 59.

Farrell T J, Barbot D J, Rosato F E 1997, 'Pancreatic resection combined with intraoperative radiation therapy for pancreatic cancer', *Annals of Surgery,* vol 226, no 1, pp 66 – 69.

Fraass B A et al 1985, 'intraoperative Radiation Therapy at the National Cancer Institute: Technical Innovations and Dosimetry', *Int. J. Radiat. Oncol. Biol. Phys.,* vol 11, no 7, pp 1299 – 1311.

Garton GR, Gunderson LL, Webb MJ 1993, 'Intraoperative radiation therapy in gynecologic cancer: the Mayo Clinic experience', *Gynecol Oncol*, vol 48, pp 328 - 332

Giarratano J C, Duerkes R J, Almond P R 1975, 'Lead shielding thickness for dose reduction of 7 to 28 MeV electrons', *Med. Phys.,* vol 2, no 6, pp 336 – 337.

Goldson A L 1981, 'Past, present, and future prospects of intra-operative radiotherapy (IORT)', *Semin Oncol*, vol 8, pp 59 – 64.

Gunderson L L, Shipley W U, Suit H D, Epp E R, Nardi G, Wood W, Cohen A, Nelson J, Battit G, Biggs P J, Russel A, Rockett A, Clark D 1982, 'Intraoperative irradiation: a pilot study combining external beam photons with 'boost' dose intraoperative electrons', *Cancer*, vol 49, pp 2259–2266.

Gunderson L L, Nagorney D M, McIlrath D C, Fieck J M, Wieand H S, Martinez A, Pritchard D J, Sim F, Martenson J A, Edmonson J H, Donohue J H 1993, 'External beam and intraoperative electron irradiation for locally advanced soft tissue sarcomas', *Int J Radiat Oncol Biol Phys,* vol 25, pp 647 – 656.

Hall E J and Giaccia A J 2006 'Radiobiology for the Radiologist' 6th edition, Lippincott Williams & Wilkins.

Harms W B, Low D A, Wong J W, Purdy J A 1998, 'A software tool for the quantitative evaluation of 3D dose calculation algorithms', *Med Phys*., vol 25, no 10, pp 1830 – 1836.

Hartmann Siantar C L et al 2001, 'Description and dosimetric verification of the PEREGRINE Monte Carlo dose calculation system for photon beams incident on a water phantom', *Med. Phys.,* vol 28, no 7, pp 1322 – 1337.

Hendee W R, Ibbott G S, Hendee E G 2005, *Radiation Therapy Physics,* Hoboken (NJ) Wiley.

Hogstrom K R, Almond P R 2006, 'Review of electron beam therapy physics', *Phys. Med. Biol.*, vol 51, no 13, pp R455 – R489.

Hogstrom K R, Mills M D, Almond P R 1981, 'Electron beam dose calculations', *Phys. Med. Biol., vol* 26, no 3, pp 445 – 459

Hosntalab M, Mahdavi S R, Mostaar A, Motamedi M, Rezaeejam H, Shirazi A 2012, 'Conformal fields in prostate radiotherapy: A comparison between measurement, calculation and simulation', *Journal of Cancer Research and Therapeutics*, vol. 8, no. 1, pp 34-39

Hu Y A, Song H, Chen Z, Zhou S, Yin F-F 2008, Evaluation of an electron Monte Carlo dose calculation algorithm for electron beams', *J of App. Clin. Med. Phys.,* vol 9, no 3

IAEA 1997, 'Ionization Chambers in High-energy Electron and Photon Beams. An International Code of Practice for Dosimetry', *Technical Reports Series No. 381*, IAEA, Vienna

IAEA 2000, 'Absorbed Dose Determination in External Beam Radiotherapy: An International Code of Practice for Dosimetry Based on Standards of Absorbed Dose to Water', *Technical Report Series 398*, IAEA Vienna.

ICRU 24 1976, 'Determination of Absorbed Dose in a Patient Irradiated by Beams of X or Gamma Rays in Radiotherapy Procedures'.

ICRU 42 1988, 'Use of Computers in External Beam Radiotherapy Procedures with High-Energy Photons and Electrons'.

James F 1994, 'RANLUX: A Fortran implementation of the high-quality pseudorandom number generator of Lüscher', *Computer Physics Communications,* vol 79, no 1, pp 111 – 114.

Jiang S B, Kapur A, Ma C-M, 'Electron beam modeling and commissioning for Monte Carlo treatment planning', *Med. Phys.,* vol 27, no 1, pp 180 – 191.

Jiang S B, Sharp G C, Neicu T, Berbeco R I, Flampouri S, Bortfeld T 2006, *Phys. Med. Biol.,* vol 51, no , pp 759 – 776.

Johns H E, Cunningham J R 1983, 'The Physics of Radiology', 4th edition, Charles C Thomas publishers.

Kapur A, Ma C-M, Mok E C, Findley D O, Boyer A 1998, 'Monte Carlo calculations of electron beam output factors for a medical linear accelerator', *Phys. Med. Biol*., vol 43, no 12, pp 3479 – 3494.

Karzmark C J, Nunan C S, Tanabe E 1993, 'Medical Electron Accelerators', McGraw-Hill Inc.

Kawrakow I 2000, 'Accurate condensed history Monte Carlo simulation of electron transport. Part I. EGSnrc, the new EGS4 version', *Med Phys,* vol 27, no 3, pp 485 – 498.

Kawrakow I 2001, 'VMC++, Electron and Photon Monte Carlo Calculations Optimized for Radiation Treatment Planning', *'Advanced Monte Carlo for Radiation Physics, Particle Transport Simulation and Applications',* eds Kling A, Barao F J C, Nakagawa M, Tavora L, Vaz P, Springer-Verlag Berlin, chapter 7, pp 229 – 236.

Kawrakow I, Fippel M 2000, 'Investigation of variance reduction techniques for Monte Carlo photon dose calculation using XVMC', *Phys. Med. Biol*., vol 45, no 8, pp 2163 – 2183.

Kawrakow I, Fippel M, Friedrich K 1996, '3D electron dose calculation using a Voxel based Monte Carlo algorithm (VMC)', *Med. Phys.,* vol 23, no 4, pp 445 – 457.

Kawrakow I, Rogers D W O 2003, 'The EGSnrc Code System: Monte Carlo Simulation of electron and Photon Transport, *Natl. Res. Council of Canada,* NRCC report PIRS 701.

Khan F M, Doppke K P, Hogstrom K R, Kutcher G J, Nath R, Prasad S C, Purdy J A, Rozenfeld M, Werner B M 1991, 'Clinical electron-beam dosimetry: Report of AAPM Radiation Therapy Committee Task Group No. 25', *Med Phys.,* vol 18 no 1, pp 73 - 109

Khan F M 2003, 'The Physics of Radiation Therapy', 3rd edition, Lippincott Williams and Wilkins.

Klevenhagen S C 1985, 'Physics of Electron beam therapy: Medical Physics Handbook', Adam Higler Ltd.

Krämling H J, Willich N, Cramer C, Wilkowski R, Dühmke E, Schildberg FW 1997, 'Early results of IORT in the treatment of gastric cancer', *Front Radiat Ther Oncol*., vol 31, pp 157 - 160.

Li J 2002, 'Simulation of Beam Modifiers', Introduction to the Proceedings of the FCCC Short Course on Monte Carlo Treatment planning (MCTP), Fox Chase Cancer Centre.

Low D A, Harms W B, Mutic S, Purdy J A 1998, 'A technique for the quantitative evaluation of dose distributions', *Med. Phys.,* vol 25, no 5, pp 656 – 661.

Ma C-M, Faddegon B A, Rogers D W O, Mackie T R 1997, 'Accurate characterization of Monte Carlo calculated electron beams for radiotherapy, *Med. Phys.,* vol 24, no 3, pp 401 – 416.

Ma C-M, Jiang S B 1999, 'Monte Carlo modelling of electron beams from medical accelerators', *Phys. Med. Biol*., vol 44, no 12, pp R157 – R189.

Ma C-M, Jiang SB 1999, 'Monte Carlo modelling of electron beams from medical accelerators', *Phys. Med. Biol.*, vol 44, no 12, pp R157 – R189.

Ma C-M, Pawlicki T, Lee M C, Jiang S B, Li L S, Deng J, Yi B, Mok E, Boyer A L 2000, 'Energy- and intensity-modulated electron beams for radiotherapy', *Phys. Med. Biol.*, vol 45 pp 2293 – 2311.

Ma C-M, Rogers D W O 2005, 'BEAMDP Users' Manual', *NRCC Report PIRS 0509(C).*

Marks L B, Yorke E D, Jackson A, Ten Haken R K, Constine L S, Eisbruch A, Bentzen S, Nam J, Deasy J O 2010, 'Use of normal tissue complication probability models in the clinic', *Int. J. Radiat. Oncol. Biol. Phys.,* vol. 76, no. 3, Supplement, pp. S10–S19.

Mayles P, Nahum A E, RosenWald J C 2007 'Handbook of Radiotherapy Physics: theory and practice', Taylor and Francis, Boca Raton

Mayles WP, Lake R, McKenzie A, Macaulay EM, Morgan HM, Jordan TJ, Powley S K et al 1999, 'Physics aspects of quality assurance in radiotherapy', *The Institute of Physics and Engineering in Medicine (IPEM),* York.

McGowan H C E, Faggegon B A, Ma C M 2007, 'STATDOSE for 3D dose distributions', *NRCC report PIRS 0509(F)*, NRC publications archive.

McParland B J 1989, 'A method of calculating the output factors of arbitrarily shaped electron fields', *Med. Phys.,* vol 16, no 1, pp 88 - 93.

Metcalfe P, Kron T, Hoban P 2007, 'The Physics of Radiotherapy X-Rays and Electrons', *Medical Physics Publishing.*

Mihailescu D, Borcia C 2014, ' Monte Carlo Simulation of the electron beams produced by a linear accelerator for intraoperative radiotherapy', *Romanian Reports in Physics*, vol 66, no 1, pp 61 74.

Mills M D, Hogstrom K R, Almond P R 1982, 'Prediction of electron beam output factors', *Med. Phys.,* vol 9, no 1, pp 60 - 68.

Mohan R, Chui C, Lidofsky L 1985, 'Energy and angular distributions of photons from medical linear accelerators', *Med Phys,* vol 12, no 5, pp 592 – 597.

Nag S, Mills J, Martin E, Bauer C, Grecula J 1997, 'IORT using high-dose-rate brachytherapy or electron beam for colorectal carcinoma', *Front Radiat Ther Oncol,* vol 31**,** pp 238 – 242.

Nahum A E 2002, 'Monte-Carlo photon/electron transport (particle interactions, e- multiple scattering etc.)', Introduction to the Proceedings of the FCCC Short Course on Monte Carlo Treatment planning (MCTP), Fox Chase Cancer Centre.

Nelson W R, Hirayamal H, Rogers D W O 1985, 'The EGS4 Code System', Stanford Linear Accelerator Center report *SLAC 265.*

Neuenschwander H, Born E J 1992, 'A macro Monte Carlo method for electron beam dose calculations', Phys. Med. Biol., vol 37, no 1, pp 107 – 125.

Niemierko A, Goitein M 1991, 'Calculation of normal tissue complication probability and dose-volume histogram reduction schemes for tissues with a critical element architecture', *Radiotherapy Oncol.,* vol 20, no 3, pp 166 – 176.

Niemierko A, Goitein M 1993, 'Implementation of a model for estimating tumour control probability for an inhomogeneously irradiated tumor', *Radiother Oncol*., vol 29, no 2, pp 140 – 147

Nyerick C E, Ochran T G, Boyer A L, Hogstrom K R 1991, 'Dosimetry characteristics of metallic cones for intra-operative radiotherapy', *Int. J. Radiat. Oncol. Biol. Phys.*, vol 21, pp 501 - 510.

Omer H, Suleiman Abdelmoneim 2012, 'Simulation of ELEKTA SL18 beams for electron radiotherapy', *Asian Journal of Medical and Clinical Sciences,* vol 1, issue 2, pp 49 - 52.

Orton C G, Mondalek P M, Spicka J T, Herron D S, Andres L I 1984, 'Lung corrections in photon beam treatment planning: Are we ready?,' *Int. J. Radiat. Oncol. Biol. Phys.*, vol 10, no 12, pp 2191 – 2199.

Oxenberg J, Malhotra H K, Attwood K, Kane III J M, Salerno K 2014, 'Intraoperative radiation therapy for high risk soft tissue sarcoma resection margins', *Journal of Solid Tumors*, vol. 4, no. 4, pp 25 – 35.

Palta J R, Biggs P J, Hazle J D, Huq M S, Dahl R A, Ochran T G, Soen J, Dobelbower R R and McCullough E C 1995, 'Intraoperative Electron Beam Radiation Therapy: Technique, Dosimetry, and Dose Specification: Report of Task Group 48 of the Radiation Therapy Committee, American Association of Physicist in Medicine' *Int. J. Radiat. Oncol. Biol. Phys.*, vol 33, no 3, pp 725-746.

Palta J R, Suntharalingam N 1989, A nondocking intraoperative electron beam applicator system', *Int. J. Radiat. Oncol. Biol. Phys.*, vol 17, pp 411 - 417.

Papanikolaou N et al 2004, 'Tissue inhomogeneity corrections for megavoltage photon beams', *AAPM report 85*, Report of TG 65 of the AAPM.

Podgorsak E B (ed) 2005, 'Radiation Oncology Physics: A handbook for teachers and students', IAEA, Vienna.

Poon E, Verhaegen F 2005, 'Accuracy of the photon and electron physics in GEANT4 for radiotherapy applications', *Med. Phys*., vol 32, no 6, pp 1696 – 1711.

Powlis W D, Smith A R, Cheng E, Galvin J M, Villari F, Bloch P, Kligerman M M 1993, 'Initiation of multi-leaf collimator conformal radiation therapy', *Int. J. Radiat. Oncol. Biol. Phys.,* vol 25, no 2, pp 171 – 179.

Raeside D E 1976, 'Monte Carlo principles and applications', *Phys. Med. Biol*., vol 21, no 2, pp 181-197.

Reynaert N, van der Marck S C, Schaart D R, Van der Zee W, Van Vliet-Vroegindeweij C, Tomsej M, Jansen J, Heijmen B, Coghe M, De Wagter C 2007, 'Monte Carlo treatment planning for photon and electron beams', *Radiation Physics and Chemistry*, vol 76, pp 643–686.

Rich T A, Cady B, McDermott W V, Kase K R, Chaffey J T, Hellman S 1984, 'Orthovoltage intraoperative radiotherapy: a new look at an old idea', *Int. J. Radiat. Oncol. Biol. Phys.*, vol 10 pp 1957 – 1965

Rogers D W O 2006, 'Fifty years of Monte Carlo simulations for medical physics', *Phys. Med. Biol*., vol 51, pp R287 – R301.

Rogers D W O, Bielajew A F 1990, 'Monte Carlo Techniques of Electron and Photon Transport for Radiation Dosimetry', *The dosimetry of Ionizing Radiation'*, eds Kase K R, Bjarngaed, Attix F H, Academic Press, chapter 5, vol III, pp 427 – 540.

Rogers D W O, Faddegon B A, Ding G X, Ma C-M, Wei J, Mackie T R 1995, 'BEAM: A Monte Carlo code to simulate radiotherapy treatment units', *Med Phys*, vol 22, no 5, pp 503 – 524.

Rogers D W O 2002, 'Monte Carlo Techniques in Radiotherapy', *Physics in Canada, Medical Physics Special Issue*, vol 58, no 2, pp 63 - 70

Rogers D W O, Kawrakow I, Seuntjens J P, Walters B R B, Mainegra-Hing E 2011, 'NRC User Codes for EGSnrc', National Research Council of Canada Report PIRS-702 (rev C).

Rogers D W O, Walters B, Kawrakow 2005, 'BEAMnrc Users Manual', National Research Council of Canada, PIRS 0509A.

Seltzer S 1991, 'Electron-photon Monte Carlo calculations: The ETRAN code', *Intl. J. Appl. And Instr. Part A*, in Applied Radiation and Isotopes, Vol 42, no 10 PP 917 – 941.

Sempau J 1, Wilderman S J, Bielajew A F 2000, 'DPM, a fast, accurate Monte Carlo code optimized for photon and electron radiotherapy treatment planning dose calculations', *Phys. Med. Biol*., vol 45, no 8, pp 2263 - 2291.

Sempau J, Sánchez-Reyes A, Salvat F, Oulad ben Tahar H, Jiang S B, Fernández-Varea J M 2001, 'Monte Carlo simulation of electron beams from an accelerator head using PENELOPE', *Phys. Med. Biol*., vol 46, no 4, pp 1163 - 1186

Sheikh-Bagheri D, Rogers D W O 2002(b), 'Sensitivity of megavoltage photon beam Monte Carlo simulations to electron beam and other parameters', *Med. Phys*. vol 29, no 3, pp 379 - 390.

Sheikh-Bagheri D, Rogers D W O 2002(a), 'Monte Carlo calculation of nine megavoltage photon beam spectra using the BEAM code', *Med. Phys*. vol 29, no 3, pp 391- 402.

Shiu A S, Hogstrom K R 1991, 'Pencil beam redefinition algorithm - for electron dose distributions', *Med. Phys.,* vol 18, no 7 pp 7- 18.

Shiu A S, Tung A S, Nyerick C E, Ochran T G, Otte V A, Boyer A L, Hogstron K R 1994, 'Comprehensive analysis of electron beam central axis dose for a radiotherapy linear accelerator', *Med. Phys.,* vol 21, no 4, pp 559 - 566.
Siebers JV, Keall PJ, Libby B, Mohan R, 'Comparison of EGS4 and MCNP4B Monte Carlo codes for generation of photon phase space distributions for a Varian 2100C 1999', *Phys Med Biol*, vol 44, no 12, pp 3009 – 3026.

Steel G G, 2002 'Basic Clinical Radiobiology', 3rd edition, Arnold, London

Stewart B W and Wild C P (eds.) 2014, *World Cancer Report 2014*, International Agency for Research on Cancer, World Health Organisation.

Teoh M, Clark C H, Wood K, Whitaker S, Nisbet A 2011, 'Volumetric modulated arc therapy: a review of current literature and clinical use in practice', *Br J Radiol*., vol 84 pp 967 – 996.

Thwaites D I, DuSautoy A R, Jordan T, McEwen M R, Nisbet A, Nahum A E, Pitchford W G 2003, 'The IPEM code of practice for electron dosimetry for radiotherapy beams of initial energy from 4 to 25 MeV based on an absorbed dose to water calibration', *Phys. Med. Biol*., vol 48, no 18, pp 2929–2970

Thwaites D I, Tuohy J B 2006, 'Back to the future: the history and development of the clinical linear accelerator', *Phys. Med. Biol.*, vol 51 no 13, pp 343 - 362.

Turian J Y, Smith B D, Bernard D A, Griem K L, Chu J C 2004, 'Monte Carlo calculations of output factors for clinically shaped electron fields', Journal of App. Clin. Med. Phys., Vol5, no 2, pp 42 – 63.

Udale M 1988, 'A Monte Carlo investigation of surface doses for broad electron beams' *Phys. Med. Biol.*, vol 33, no 8, 939 – 954.

Van Dyk J, Barnett R B, Cygler J E, Shragge P C 1993, 'Commissioning and quality assurance of treatment planning computers', Int. J. Radiat. Oncol. Biol. Phys., vol 26, pp 261 – 273.

Venselaar J, Welleweerd H, Mijnheer B 2001, 'Tolerances for the accuracy of photon beam dose calculations of treatment planning systems', *Radiother Oncol*, vol 60, no 2, pp 191 – 201

Verellen D, de Ridder M, Storme G 2008, 'A (short) history of image-guided radiotherapy', *Radiother Oncol*., vol 86, no 1, pp 4 – 13.

Verhaegen F, Mubata C, Pettingell J, Bidmead M 2001, 'Monte Carlo calculation of output factors for circular, rectangular, and square fields of electron accelerators (6-20 MeV)', *Med. Phys.,* vol 28, no 6, pp 938 – 949.

Veronesi U, Orecchia R, Luini A, Gatti G, Intra M, Zurrida S, Ivaldi G, Tosi G, Ciocca M, Tosoni A, De Lucia F 2001, 'A preliminary report of intraoperative radiotherapy (IORT) in

limited-stage breast cancers that are conservatively treated' *Eur. J. Cancer*., vol 37, no 17 pp 2178 - 2183

Walters B R B, Kawrakow I, Rogers D W O 2002, 'History by history statistical estimators in the BEAM code system', *Med. Phys.,* vol 29, no 12, pp 2745 – 2752.

Walters B, Kawrakow I, Rogers D W O 2005, 'DOSXYZnrc User's Manual', *NRCC report PIRS 794(B)*.

Walters B R B, Kawrakow I 2007, 'A "HOWFARLESS" option to increase efficiency of homogeneous phantom calculations with DOSXYZnrc', *Med. Phys.,* vol 34, no 10, pp 3794 – 3807

Webb S I, Nahum A E 1993, 'A model for calculating tumour control probability in radiotherapy including the effects of inhomogeneous distributions of dose and clonogenic cell density', *Phys. Med. Biol.*, vol 38, no 6, pp 653 – 666.

Wiig J N, Poulsen J P, Tveit K M, Olsen D R, Giercksky K E 2000, 'Intra-operative irradiation (IORT) for primary advanced and recurrent rectal cancer. a need for randomised studies', *Eur J Cancer,* vol 36, no 7, pp868 - 874

Zhang G G, Rogers D W O, Cygler J E, Mackie T R 1999, 'Monte Carlo investigation of electron beam output factors versus size of square cutout', *Med. Phys.,* vol 26, no 4, pp 743 - 750

A1

PATIENT CASE

It is proposed that patient X be treated with IORT using a 12 MeV beam, 45 mm IORT cone and irregularly-shaped cut-out *(figure A1).* The prescription is 10 Gy to the depth of the 80%.

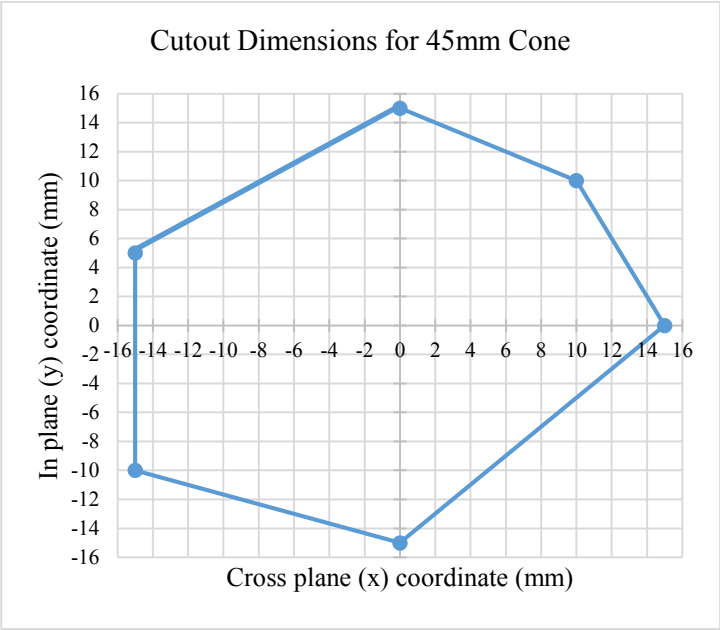

Figure A1 Representation of the dimensions and orientation of the cut-out for the 45 mm IORT cone for patient X.

The absorbed dose to water at R_{max} for the 12 MeV beam is calibrated to be 1.00 cGy/MU.

The objective of the exercise is to determine the monitor units that must be set to deliver 10 Gy to the 80% depth in tissue.

The cut-out factor as determined from MC calculation described in this report is found to be 1.192.

The MU required to deliver the prescribed dose at depth z with the IORT cut-out in place may then be calculated using the following equation

$$MU = \frac{Prescribed\ dose\ (Gy) * 100\ MU/Gy}{COF * PDD_z} \qquad \text{(A1.1)}$$

where prescribed dose is the prescription dose of 10 Gy at depth z for the cut-out and PDD_z is the $PDD/100$ at depth z (where PDD is obtained from the calculated PDD curve if the prescription depth instead of percentage is given). COF is the cut-out factor = 1.192

In this case, $PDD_z = 0.80$

From equation A1.1,

$$MU = \frac{10\ Gy * 100\ \ MU/Gy}{1.192 * 0.80}$$

$$= 1049\ MU$$